

DEVELOPMENT OF SLOPE MONITORING DEVICE USING
ACCELEROMETER

ALIFF RIDZUAN BIN BUNAWAN

UNIVERSITI TEKNOLOGI MALAYSIA

UNIVERSITI TEKNOLOGI MALAYSIA**DECLARATION OF THESIS / UNDERGRADUATE PROJECT REPORT AND
COPYRIGHT**

Author's full name : ALIFF RIDZUAN BIN BUNAWAN

Date of Birth : 01 FEBRUARY 1989

Title : DEVELOPMENT OF SLOPE MONITORING DEVICE USING
ACCELEROMETER

Academic Session : 2019/2020 - 2

I declare that this thesis is classified as:

CONFIDENTIAL(Contains confidential information under the
Official Secret Act 1972)***RESTRICTED**(Contains restricted information as specified by
the organization where research was done)***OPEN ACCESS**I agree that my thesis to be published as online
open access (full text)

I acknowledged that Universiti Teknologi Malaysia reserves the right as follows:

The thesis is the property of Universiti Teknologi Malaysia

The Library of Universiti Teknologi Malaysia has the right to make copies for the
purpose of research only.

The Library has the right to make copies of the thesis for academic exchange.

Certified by:

SIGNATURE OF STUDENT

PKA 153026

MATRIC NUMBER

Date: 3 August 2020



SIGNATURE OF SUPERVISORAssoc. Prof. DR. AHMAD
SAFUAN A RASHID

NAME OF SUPERVISOR

Date: 3 August 2020

NOTES : If the thesis is CONFIDENTIAL or RESTRICTED, please attach with the letter from
the organization with period and reasons for confidentiality or restriction

*

3 August 2020

Librarian
Perpustakaan UTM
UTM, Skudai
Johor

Sir,

CLASSIFICATION OF THESIS AS RESTRICTED

DEVELOPMENT OF SLOPE MONITORING DEVICE USING ACCELEROMETER
ALIFF RIDZUAN BIN BUNAWAN

Please be informed that the above mentioned thesis entitled "*Development of Slope Monitoring Device using Accelerometer*" be classified as RESTRICTED for a period of three (3) years from the date of this letter. The reasons for this classification are

- (i) The research would prefer its findings are kept confidential as the design of the system is sensitive to be open to the public for the time being.

Thank you. Sincerely yours,

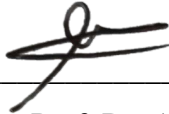


Associate Prof Dr Ahmad Safuan A Rashid
School of Civil Engineering,
Faculty of Engineering,
Universiti Teknologi Malaysia,
81310, Johor Bahru, Johor.
☎ : +(6)0197201279 Fax. : +(6)07-5538699
✉ : ahmadsafuan@utm.my


NOTES:

If the thesis is CONFIDENTIAL or RESTRICTED, please attach with the letter from the organization with period and reasons for confidentiality or restriction.

“We hereby declare that we have read this thesis and in our opinion this thesis is sufficient in term of scope and quality for the award of the degree of Doctor of Philosophy in Civil Engineering”

Signature : 
Name of Supervisor I : Assoc. Prof. Dr. AHMAD SAFUAN A RASHID
Date : 3 AUGUST 2020

Signature : _____
Name of Supervisor II : Prof. Ir. Dr. AZMAN BIN KASSIM
Date : 3 AUGUST 2020

Signature : 
Name of Supervisor II : Ir. Dr.-Ing. MOHD NAZRI BIN MOHD NASIR
Date : 3 AUGUST 2020

BAHAGIAN A - Pengesahan Kerjasama*

Adalah disahkan bahawa projek penyelidikan tesis ini telah dilaksanakan melalui kerjasama antara _____ dengan _____

Disahkan oleh:

Tandatangan :

Tarikh :

Nama :

Jawatan :

(Cop rasmi)

** Jika penyediaan tesis atau projek melibatkan kerjasama.*

BAHAGIAN B - Untuk Kegunaan Pejabat Sekolah Pengajian Siswazah

Tesis ini telah diperiksa dan diakui oleh:

Nama dan Alamat Pemeriksa Luar :

Nama dan Alamat Pemeriksa Dalam :

Nama Penyelia Lain (jika ada) :

Disahkan oleh Timbalan Pendaftar di SPS:

Tandatangan :

Tarikh :

Nama :

DEVELOPMENT OF SLOPE MONITORING DEVICE USING
ACCELEROMETER

ALIFF RIDZUAN BIN BUNAWAN

A thesis submitted in fulfilment of the
requirements for the award of the degree of
Doctor of Philosophy (Civil Engineering)

School of Civil Engineering
Faculty of Engineering
Universiti Teknologi Malaysia

AUGUST 2020

DECLARATION

I declare that this thesis entitled “*Development of Slope Monitoring Device using Accelerometer*” is the result of my own research except as cited in the references. The thesis has not been accepted for any degree and is not concurrently submitted in candidature of any other degree.

Signature :

Name : ALIFF RIDZUAN BIN BUNAWAN

Date : 3 AUGUST 2020

DEDICATION

To my beloved family

Rohaida Affandi

Alyssandra

Papa Bunawan Sagi

Mama Rozlinawati Mohd Aris and

Mak Eneho Ahmad Zaidi

Not all heroes wear capes

ACKNOWLEDGEMENT

In the name of ALLAH, the most Gracious and most Merciful. Alhamdulillah with His blessing, the thesis was successfully accomplished.

I would like to express my deepest and sincerest gratitude to my supervisor, Associate Professor Dr Ahmad Safuan bin A Rashid for his continuous support; technically and morally, his motivation, enthusiasm, guidance and also for his critics and suggestions throughout the completion of this research. I am extremely grateful for the time and energy spent on empowering me throughout my journey. It was a great honour and privilege to have worked and studied under his guidance. A role model.

My sincerest thanks also go to Prof. Ir. Dr Azman Kassim and Dr Mohd Nazri Mohd Nasir for their insights to their respective area of expertise which I had just nose-dived headfirst without a clue. Their guidance helped me broaden my spectrum of understanding of the engineering field. I am also grateful for the extended family that we had with the Geotechnical Laboratory team. I am grateful to be surrounded by people who empower, believe, support, uplift, motivate and appreciative towards one another.

I would also like to fully acknowledge Universiti Teknologi Malaysia (UTM) and Ministry of Higher Education (MOSTI) for the research funds which was made available to conduct this research.

Last but not least, it is whole-heartedly appreciated to my parents, lovely wife Rohaida and daughter Alyssandra for always giving encouragement, love and joy towards the success of this PhD journey.

ABSTRACT

There are numerous sorts of instruments that have been utilized to monitor the high-risk slopes as a preventive precaution should a slope fail. Unfortunately, fewer instruments are installed directly into the slope as a detection unit before the slope fails. Automatic Wireless Accelerometer Monitoring System (AWAM) is an innovation in the slope monitoring system and will be introduced in this research. By determining the limitations of previous monitoring systems in slope monitoring; AWAM will overcome problems such as geomorphology limitations, physical obstructions, different climate conditions and concurrent works at a site. In addition, minimal human interaction is required since the sensors are automatic and placed on the slope. This study demonstrates the AWAM system to monitor slope failures and the effectiveness of the system as an early warning sign. It was presented in two parts; consist of physical modelling calibration of the device and loading test in the laboratory to numerical modelling of the model simulated by using softwares such as Slope/W and MatLab. The monitoring device was confirmed to be able to be used as a monitoring system of soil movements given that the device is moving in tilting modes. Physical modelling presented promising results in correlation with the numerical modelling and the system test will continue with a full-scale modelling test. The AWAM system site performance was validated to monitor slope movements on a full-scale site test for a whole year with minimum maintenance.

ABSTRAK

Terdapat banyak jenis peranti yang telah digunakan untuk memantau cerun yang berisiko tinggi sebagai langkah pencegahan sebelum cerun gagal. Kajian mendapati hanya sebilangan peranti yang dipasang terus ke cerun sebagai alat pengesanan sebelum cerun gagal. Automatic Wireless Accelerometer Monitoring System (AWAM) merupakan sebuah inovasi dalam sistem pemantauan cerun dan akan diperkenalkan dalam penyelidikan ini. Dengan mengenal pasti kelemahan pada sistem pemantauan yang terdahulu, AWAM akan mengatasi masalah seperti halangan geomorfologi, halangan fizikal, keadaan iklim yang berbeza dan kerja yang serentak di tapak. Di samping itu, pengendalian manusia yang minimum diperlukan memandangkan peranti alat pengesanan adalah automatik dan diletakkan pada cerun. Penyelidikan ini menunjukkan keberkesanan sistem AWAM sebagai peranti pemantau kegagalan cerun dan kebolehan sistem tersebut untuk memberi amaran awal. Penyelidikan ini dipersembahkan dalam dua bahagian; kalibrasi permodelan fizikal peranti dan pengujian fizikal di makmal hingga ke bahagian kedua iaitu permodelan berangka model yang disimulasi dengan menggunakan perisian seperti Slope/W dan MatLab. Peranti pemantauan ini telah disahkan untuk digunakan sebagai sistem pemantauan pergerakan tanah disebabkan terdapat pengesanan pergerakan pada peranti apabila peranti bergerak dalam berkeadaan condong. Pemodelan fizikal menunjukkan hasil yang memuaskan apabila di korelasi dengan pemodelan berangka dan ujian sistem akan diteruskan dalam ujian pemodelan berskala besar di tapak. Sistem peranti pemantauan cerun AWAM telah disahkan untuk memantau pergerakan cerun di tapak ujian selama satu tahun dengan penyelenggaraan yang minimum.

TABLE OF CONTENTS

	TITLE	PAGE
	DECLARATION	ii
	DEDICATION	iii
	ACKNOWLEDGEMENT	iv
	ABSTRACT	v
	ABSTRAK	vi
	TABLE OF CONTENTS	vii
	LIST OF TABLES	xv
	LIST OF FIGURES	xvii
	LIST OF ABBREVIATIONS	xxxiv
	LIST OF SYMBOLS	xxxvii
	LIST OF APPENDICES	xxxix
CHAPTER 1	INTRODUCTION	1
1.1	Introduction	1
1.2	Problem Statement	3
1.3	Research Objectives	4
1.4	Scope of Study	5
1.5	Research Significance	5
1.6	Thesis Outline	6
CHAPTER 2	LITERATURE REVIEW	9
2.1	Introduction	9
2.2	Slope Monitoring	9
2.2.1	Geodetic (Surveying) Technique	10
2.2.1.1	Theodolite and Prism	10
2.2.1.2	Laser Monitoring	16
2.2.1.3	Global Positioning System (GPS)	22
2.2.1.4	Synthetic Aperture Radar (SAR)	27

2.2.1.5	Ground Based Interferometric Synthetic Aperture Radar (GBInSAR)	36
2.2.1.6	Automated Robotic Station for Slope Monitoring	42
2.2.2	Geotechnical Instrumentation Technique	45
2.2.2.1	Extensometer	45
2.2.2.2	Inclinometer/ Tiltmeter	47
2.2.2.3	Piezometers	50
2.2.2.4	Intelligent System for Slope Monitoring	51
2.2.2.5	Acoustic Emission Monitoring of Soil Slope	56
2.3	Automated Wireless Accelerometer Monitoring System (AWAM)	57
2.4	Particle Image Velocimetry (PIV)	60
2.4.1	Principles of PIV	60
2.4.2	Application of PIV	63
2.5	Numerical Modelling of Slope Failure using GeoStudio	75
2.5.1	Application of Geostudio on Slope Failure Simulation	76
2.6	Concluding Remarks	83
CHAPTER 3	PHYSICAL MODELLING OF SLOPE MONITORING DEVICE SIMULATIONS	85
3.1	Introduction	85
3.2	Research Plan	85
3.3	Materials for Testing	86
3.3.1	Site Selection	86
3.3.2	Soil Properties	87
3.3.3	Determination of Soil Water Characteristic Curve (SWCC)	89
3.4	Equipment for Testing	90
3.4.1	Loading Frame	90
3.4.2	Testing Chamber	91

3.4.3	Pneumatic Cylinder	92
3.4.4	Rigid Footing	93
3.4.5	Rain Simulator	94
3.4.6	Alignment Box	96
3.5	Measurement Method	97
3.5.1	Data Logging and Acquisition	97
3.5.1.1	Loading Stage Physical Modeling	97
3.5.1.2	Tensiometer Soil Suction Measurement	100
3.5.1.3	AWAM Device	102
3.5.2	Digital Camera	103
3.6	Model Preparation	105
3.6.1	Laterite Mixing	105
3.6.2	Slope Construction	106
3.6.2.1	Testing Chamber Preparations, Filling and Compaction	106
3.6.2.2	Model Trimming	108
3.7	Model Soil Test	109
3.7.1	Test Notation	110
3.7.2	Model Test Procedure	110
3.8	Particle Image Velocimetry (PIV)	113
3.8.1	Introduction	113
3.8.2	Pre-PIV Analysis	113
3.8.3	Running Procedures of the PIV Analysis	115
3.8.3.1	Inspection of Subroutines	115
3.8.3.2	Running regimlistgen	116
3.8.3.3	Running fmeshing	116
3.8.3.4	Running GeoPIV8	117
3.8.3.5	led_launcher Processing and Running regimlistgen Command for targetmarker Folder	118
3.8.3.6	Running geoCENTROID8	118

3.8.3.7	Running fmeshing and GeoPIV8 on the targetmarker Folder	119
3.8.3.8	Running consolidate8	120
3.8.3.9	Running geoCALIBRATE8(uvdata) (Calibration with the targetmarker)	120
3.8.3.10	Running qq.m (Vector Result)	121
3.8.3.11	Running cntr (Contour Mapping)	121
3.8.3.12	Plotting Shear Strain	122
3.8.4	Repetition of Steps for Subsequent Set of Analysis	123
3.9	Concluding Remarks	123
CHAPTER 4	CALIBRATION OF SLOPE MONITORING DEVICE	125
4.1	Introduction	125
4.2	Calibration Equipment	127
4.2.1	Automated Wireless Accelererometer Monitoring (AWAM) device	127
4.2.2	Linear Variable Displacement Transducer (LVDT)	128
4.2.3	DXL360 Digital Protractor Inclinometer Level Box	128
4.3	Calibration Procedures	129
4.3.1	Initial Calibration	129
4.3.2	Primary Calibration Procedure	132
4.3.3	Additional Calibrations (Flip Test)	138
4.4	Concluding Remarks	143
CHAPTER 5	EXPERIMENTAL RESULT	145
5.1	Introduction	145
5.2	Materials	145
5.2.1	Materials Description and Properties	145
5.2.2	Soil Water Characteristic Curve (SWCC)	147
5.2.3	Hydraulic Conductivity Function	148
5.2.4	Rainfall Patterns	149

5.3	Laboratory Model Result	149
5.3.1	Laboratory Infiltration Test on the Homogenous Soil Layer	150
5.3.2	Loading Test	155
5.3.3	Slope Deformation Result	157
5.3.4	AWAM Readings	164
5.3.4.1	Test 1:2 Slope with 1 Hour Rain (Case A)	165
5.3.4.2	Test 1:2 Slope with 1 Hour Rain (Case B)	167
5.3.4.3	Test 1:2 Slope without Rain (Case C)	169
5.3.4.4	Test 1:1 Slope with 1 Hour Rain (Case D)	172
5.3.4.5	Test 1:1 Slope with 24 Hour Rain (Case E)	174
5.3.4.6	Test 1:1 Slope without Rain (Case F)	177
5.3.4.7	Concluding Notes	179
5.3.5	PIV Result	183
5.4	Concluding Remarks	197
CHAPTER 6	NUMERICAL MODELLING OF SLOPE FAILURE SIMULATION	199
6.1	Introduction	199
6.2	Modelling of Materials	200
6.3	Modelling Geometry and Simulation Methods	200
6.3.1	General Setting	201
6.3.2	Initial Condition SEEP/W	202
6.3.3	Transient Seepage of Rainfall Simulations	203
6.3.4	Slope Stability with Load Simulations using SLOPE/W	204
6.4	Result of Slope Modelling	207
6.4.1	Pore-water Pressure vs. Depth	207
6.4.2	Factor of Safety (FOS) vs. Time	211

6.5	Comparison of Results from Numerical and Physical Modelling	213
6.6	Concluding Remarks	215
CHAPTER 7	SITE WORK OF AUTOMATED WIRELESS ACCELEROMETER MONITORING (AWAM) SYSTEM	217
7.1	Introduction	217
7.2	Site Work Plan	217
7.3	Automatic Wireless Accelerometer Monitoring (AWAM) System Development	219
7.3.1	Introduction	219
7.4	Equipment for Site Work	223
7.4.1	Outdoor Capabilities	224
7.4.1.1	Power Station Casing	224
7.4.1.2	Sensor Casing	226
7.4.1.3	Power Station Column	227
7.4.1.4	Base Plate	228
7.4.2	Power Supply	229
7.4.2.1	Solar Charge Controller	229
7.4.2.2	Solar Panel	230
7.4.2.3	Solar Cable	232
7.4.2.4	Battery	234
7.4.2.5	Power Relay	235
7.4.3	Step Down Module	236
7.4.4	Data Logging	238
7.4.4.1	Controller Display	238
7.4.4.2	Wireless Transmitter	239
7.4.4.3	Wireless Transmitter Controller	241
7.4.5	Date and Time Module	242
7.4.6	Security System	244
7.4.7	Sensors	246
7.4.8	Server and Web Hosting	248

7.5	Site Work	250
7.5.1	Site Selection	250
7.5.2	Soil Properties	252
7.5.2.1	Mackintosh Probe Test	253
7.5.3	Modelling of the Site Slope Stability Analysis	254
7.5.3.1	Modelling of Site Materials	254
7.5.3.2	Modelling of the Site Geometry	255
7.5.3.3	Modelling of the Site Initial Condition	257
7.5.3.4	Transient Seepage of the Rainfall Simulation for the AWAM Site	258
7.5.3.5	Factor of Safety (FOS) vs. Time Simulations for the AWAM Site	259
7.5.3.6	Concluding Notes for the Simulations of the AWAM Site	262
7.6	Measurement And Warning System Notifier of Slope Monitoring System Through awam.my	264
7.6.1	awam.my Index Page	265
7.6.2	awam.my Components	266
7.6.3	awam.my Admin Privilege Page	267
7.6.4	awam.my Limiting Value Page	268
7.6.5	awam.my User Management Page	268
7.7	Installation of AWAM System on the Field	269
7.8	Slope Monitoring Result	271
7.8.1	Slope Monitoring Result for the M47 Site	272
7.8.2	Slope Monitoring Result for the CICT Site	274
7.9	Concluding Remarks	276
CHAPTER 8	SUMMARY, CONCLUSION AND RECOMMENDATIONS	279
8.1	Summary	279
8.2	Conclusion	282
8.2.1	Establishing the AWAM System Mechanics	283
8.2.2	Failure Signal Determination for Early Warning Detection	284

8.2.3	Field Testing of AWAM System	285
8.3	Recommendation for Future Study	285
	REFERENCES	287
	Appendices	296 - 339

LIST OF TABLES

TABLE NO.	TITLE	PAGE
Table 2.1:	The strength and limitations of slope monitoring devices	84
Table 3.1:	Nikon D5100 digital camera specifications	105
Table 3.2:	Test scheme for experiments	110
Table 4.1:	Summary result of calibration setup	131
Table 4.2:	Summary Result of Calibration Test with Different Angles	134
Table 4.3:	Accelerometer readings respective to the degree change and standard deviation value for AWAM1	141
Table 4.4:	Accelerometer readings respective to the degree change and standard deviation value for AWAM2	141
Table 5.1:	Summary of soil properties of the Grade VI of Balai Cerapan	147
Table 5.2:	SWCC parameters of the ground model	148
Table 5.3:	Modelling rainfall patterns	149
Table 5.4:	The maximum stress load on the model tests	156
Table 5.5:	AWAM device results summary	182
Table 6.1:	Summary of soil properties	200
Table 6.2:	Modelling scheme for numerical modelling	201
Table 6.3:	Pre-cursor movement FOS compared to the final failure load	213
Table 7.1:	Power station casing specifications	225
Table 7.2:	Sensor casing specifications	226
Table 7.3:	Power station column specifications	227
Table 7.4:	Base plate specifications	228
Table 7.5:	Solar charge controller specifications	230
Table 7.6:	Solar panel specifications	232
Table 7.7:	Solar cable specifications	233
Table 7.8:	Solar battery specifications	235

Table 7.9:	Power relay specifications	236
Table 7.10:	Step down module specifications	238
Table 7.11:	Controller display specifications	239
Table 7.12:	Wireless transmitter specifications	241
Table 7.13:	Wireless transmitter controller specifications	242
Table 7.14:	Date and time module specification	244
Table 7.15:	Screw caps specifications	245
Table 7.16:	APM 2.8 flight controller sensor specifications	248
Table 7.17:	Web server specifications	250
Table 7.18:	Physical and mechanical properties of soil samples	255
Table 7.19:	Anchor depth summary for AWAM hinged foundation installations	264

LIST OF FIGURES

FIGURE NO.	TITLE	PAGE
Figure 2.1:	Location of Instrumentation (Angeli et al., 2000).	11
Figure 2.2:	Displacement Monitored by EDM from June 1996 to October 1999 (Rizzo, 2002).	12
Figure 2.3:	Theodolites and Prism Network on the Sandlout Open-Pit (Little, 2006).	12
Figure 2.4:	Geomorphological sketch of the landslide study in Portalet, Spain (Herrera et al., 2009)	13
Figure 2.5:	a) Prism installed b) Position of 6 prisms with XYZ axes (Khan et al., 2010).	14
Figure 2.6:	Levelling network base point made of stainless steel situated in stable structures (Fastellini et al., 2011)	14
Figure 2.7:	Contour map of vertical displacement resulted from high precision levelling network (Fastellini et al., 2011)	15
Figure 2.8:	Schematic of ROX system (Blair et al., 1997)	16
Figure 2.9:	Measuring principle of pulse and CW-lasers (Wehr and Lohr, 1999)	17
Figure 2.10:	Progressing Palmer Scan (Wehr and Lohr, 1999)	18
Figure 2.11:	The shore and shallow of Friedrichskoog, Germany by ScarLARS laser scanner (Wehr and Lohr, 1999)	18
Figure 2.12:	Object classification result (Hug and Wehr, 1997)	19
Figure 2.13:	a) Laser Installation b) Laser Point Showing a Side View of the Pit Slope (Little, 2005).	20
Figure 2.14:	LIDAR data from Big Sur, California USA (NOAA, 2018)	21
Figure 2.15:	Risk map for TSR study (Jamaluddin and Hussein, 2006).	21
Figure 2.16:	GPS Method of Measuring (Gili et al., 2000).	22
Figure 2.17:	Vallcebre Landslide Monitoring Network Data (Gili et al., 2000).	23
Figure 2.18:	i) GPS Fixed Point ii) GPS Moving Point (Malet et al., 2002)	23

Figure 2.19:	Displacement Obtained by GPS, Vectors Show the Movement of Flow Slide (Rizzo, 2002).	24
Figure 2.20:	Periodic GPS survey result of Valoria Landslide (Bertacchini et al., 2009)	24
Figure 2.21:	GPS setup on a stainless-steel rod on a fixed point (Fastellini et al., 2011)	26
Figure 2.22:	Displacement vector map of Assisi Town, Italy from 1995 to 2001 (Fastellini et al., 2011)	26
Figure 2.23:	Displacement vector map of Assisi Town, Italy from 1995 to 2001 (Fastellini et al., 2011)	27
Figure 2.24:	SAR imaging acquisition (Bamler and Hartl, 1998)	27
Figure 2.25:	Shuttle radar Topography mission flight system configuration. Antennae reside in shuttle's cargo bay are extended on a 60 m long boom, 45 degrees from the horizontal mapping plane (Rosen et al., 1998)	28
Figure 2.26:	Maratea Valley geology highlighting Sackung morphology (Berardino et al., 2003)	29
Figure 2.27:	Available data from previous researches on Maratea Valley (Berardino et al., 2003)	30
Figure 2.28:	DiffSAR displacement map in comparison to GPS measurement and locations of reference points (Berardino et al., 2003)	31
Figure 2.29:	Map of instability modelled at Maratea Vally (Berardino et al., 2003)	32
Figure 2.30:	Geometry of CRs and the Application in DInSAR Technique (Crosetto et al., 2013)	33
Figure 2.31:	Map of Vellecebre and the Displacement Monitored (Crosetto et al., 2013)	33
Figure 2.32:	Location of study in Asisi, Italy. Blue shades indicate ancient landslide while red is the recently occurring landslide (Calo et al., 2014)	34
Figure 2.33:	Diagram of SBAS implementation (Berardino et al., 2002)	34
Figure 2.34:	Deformation mean displacement velocity (A) December 2009 to February 2012 (B) April 1992 to November 2010 (Calo et al., 2014)	35
Figure 2.35:	3D View of Terrain a) Before Landslide b) After Landslide c) Both Terrain Fused for Landslide Detection (Jebur et al., 2014)	36

Figure 2.36:	Technical Scheme for the GBInSAR System (Tarchi et al., 2003).	37
Figure 2.37:	GBInSAR Analysis of the Tessina Landslide (Tarchi et al., 2003).	38
Figure 2.38:	Operation scheme of the radar (Pierraccini et al., 2001)	39
Figure 2.39:	Photograph of the test site viewed by the radar installation (Pieraccini et al., 2003)	39
Figure 2.40:	Cumulative Displacement Maps from 14 Hours of Monitoring until the 46th Hour. Displacements are Shaded Accordingly (Pieraccini et al., 2003).	40
Figure 2.41:	3D Projected Displacement Monitoring of the Site (Pieracini et al., 2003).	40
Figure 2.42:	Monitoring System GBInSAR of the Site (Bozzano et al., 2010).	41
Figure 2.43:	Displacement of Slope Overlain by the Line of Sight Map (Bozzano et al., 2010).	41
Figure 2.44:	Total displacement measurements of GBSAR between the months of October to November 2006 (Herrera et al., 2009)	42
Figure 2.45:	The map and view of Valoria Landslide, Italy (Bertacchini et al., 2009)	43
Figure 2.46:	Reflectors of total station points (Bertacchini et al., 2009).	43
Figure 2.47:	Solar powered GPS rover (Bertacchini et al., 2009)	44
Figure 2.48:	Displacements of slope movements (Bertacchini et al., 2009)	44
Figure 2.49:	Landslide recording result of Total Station during continuous measurement (Bertacchini et al., 2009)	45
Figure 2.50:	Typical Extensometer Applications (Ding et al., 2000).	46
Figure 2.51:	Layout of the Extensometer Device (Angeli et al., 2000).	46
Figure 2.52:	Two Boreholes with Extensometers Installed on Mine Slope (Ding et al., 2000).	47
Figure 2.53:	Basic Principal of Inclinometers (Ding et al., 2000).	48
Figure 2.54:	Estimated border of the landslide obtained from a geological -geotechnical point of view (Fastellini et al., 2011)	48

Figure 2.55:	Inclinometer readings for the Portalet landslide, Italy from June 2005 until August 2005 (Herrera et al., 2009)	49
Figure 2.56:	Inclinometer readings of 4 points in Asisi landslide (Calo et al., 2014)	50
Figure 2.57:	Diagram of Intelligent Monitoring System (Ding et al., 2000).	51
Figure 2.58:	The Torgiovannetto landslide localization (Intrieri et al., 2012)	52
Figure 2.59:	Schematic view of the monitoring system of the Torgiovannetto landslide (Intrieri et al., 2012)	53
Figure 2.60:	Displacement data from extensometer with cumulative rainfall data collection (Intrieri et al., 2012)	53
Figure 2.61:	The photograph of Torgiovannetto landslide detail on sliding surfaces and tension cracks (Intrieri et al., 2012)	54
Figure 2.62:	Warning criteria of EWSs for Torgiovannetto landslide (Intrieri et al., 2012)	55
Figure 2.63:	Velocity vs. time for 2 sets of extensometers with the threshold value (Intrieri et al., 2012)	55
Figure 2.64:	Schematic of AE Detection on Slope (Dixon et al., 2014).	56
Figure 2.65:	RDC Rate, Rainfall and Displacement vs Time Behavior in Early 2013 (Dixon et al., 2014).	56
Figure 2.66:	Concept of the accelerometer in X-axis	57
Figure 2.67:	Data collection by the accelerometer in place (Ravi et al., 2005)	58
Figure 2.68:	X-axis readings from accelerometers on different movement criteria (Ravi et al., 2005)	58
Figure 2.69:	Diagram Process of AWAM System	59
Figure 2.70:	Image manipulation during PIV analysis (White et al., 2003)	61
Figure 2.71:	Evaluation of displacement vector from correlation plane plane, $R_n(s)$: (a) correlation function $R_n(s)$; (b) highest correlation peak; (c) sub-pixel interpolation using cubic fit over ± 1 pixel of integer correlation (White et al., 2003)	62
Figure 2.72:	Object-space and image-space coordinate system (White et al., 2003)	63
Figure 2.73:	Photogrammetric target (White et al., 2003)	63

Figure 2.74:	Displacement field around plane strain displacement in pile; (a) mesh of PIV patches, (b) displacement vector field, (c) magnitude of displacement vectors (White et al., 2003)	64
Figure 2.75:	Experimental setup; (a) elevated view, (b) plan view (Ni et al., 2010)	65
Figure 2.76:	Displacement vectors: (a) incremental from $L = 9.5R$ to $L = 10R$; (b) accumulated, from $L = 0R$ to $L = 10R$ (Ni et al., 2010)	66
Figure 2.77:	Automated foundation test set-up: 1- camera, 2- PC, 3- signal transmission unit, 4- pneumatic loading unit, 5- support beam, 6- load test plate with rod, 7- plexiglass wall with stiffener, 8- pressure control unit (Boldyrev et al., 2012)	67
Figure 2.78:	Vertical displacement isolines at 8 mm plate settlement: 1- compaction; 2- uplift (Boldyrev et al., 2012)	67
Figure 2.79:	Volume strain isolines at 8 mm plate settlement (Boldyrev et al., 2012)	68
Figure 2.80:	Shear strain isolines at 16 mm plate settlement (Boldyrev et al., 2012)	68
Figure 2.81:	16 mm plate loading. Shear strain isolines for one layer of reinforcements (Boldyrev et al., 2012)	69
Figure 2.82:	16 mm plate loading. Shear strain isolines for three layers of reinforcements (Boldyrev et al., 2012)	69
Figure 2.83:	Plate settlement versus loads plot; 1- unreinforced; 2,3,4- 1,2,3 layers of reinforcements; A and B -PIV measurement points (Boldyrev et al., 2012)	69
Figure 2.84:	The trapdoor apparatus; (a) overview, (b) stress sensor arrangements (Khatami et al., 2019)	70
Figure 2.85:	Elements in DIC; (a) target marker with 28 mm spacing, (b) typical image of the general specimen, (c) close-up of speckle pattern of the soil and (d) typical subset and Area of Interest (AOI) for the DIC analysis (Khatami et al., 2019)	71
Figure 2.86:	Horizontal displacement in a trapdoor apparatus with no surcharge; (a) 1 mm and (b) 3 mm yielding (Khatami et al., 2019)	72
Figure 2.87:	Vertical displacement in a trapdoor apparatus with no surcharge; (a) 1 mm and (b) 3 mm yielding (Khatami et al., 2019)	72

Figure 2.88:	Horizontal displacement in a trapdoor apparatus with surcharge; (a) 1 mm and (b) 3 mm yielding (Khatami et al., 2019)	73
Figure 2.89:	Vertical displacement in a trapdoor apparatus with surcharge; (a) 1 mm and (b) 3 mm yielding (Khatami et al., 2019)	73
Figure 2.90:	Vertical strains in a trapdoor apparatus with no surcharge for (a) 1 mm and (b) 3 mm yield of the trapdoor (Khatami et al., 2019)	74
Figure 2.91:	Vertical strains in a trapdoor apparatus with 5 kPa surcharge for (a) 1 mm and (b) 3 mm yield of the trapdoor (Khatami et al., 2019)	75
Figure 2.92:	Idealised vertical strain of the arching effect illustration (Khatami et al., 2019)	75
Figure 2.93:	Geometry of the homogenous slope used (Tsaparas et al., 2002)	77
Figure 2.94:	Summary of soil parameters used in the study (Tsaparas et al., 2002)	77
Figure 2.95:	Comparison of pore-water pressure profiles at the crest of the slope by the end of rainfall; (a) rainfall over 16 h (intensity 15 mm/h) and (b) rainfall over 2 h (intensity 120 mm /h) (Tsaparas et al., 2002)	78
Figure 2.96:	Development of the factor of safety (FOS) with time for different distributions of antecedent rainfall for the case of $k_{sat} = 10^{-5}$ m/s, initial pore-water pressure -25 kPa and initial groundwater table at the toe of the slope; (a) the whole simulation and (b) during major rainfall event (Tsaparas et al., 2002)	79
Figure 2.97:	Geometry of analysis listing element meshes and boundary condition of the model (Lee et al., 2009)	80
Figure 2.98:	Suction distribution from several durations of major rainfall; (a) sand-gravel, (b) silty gravel, (c) sandy silt and (d) silt (kaolin) (Lee et al., 2009)	80
Figure 2.99:	Slope model for seepage and slope stability analysis parametric studies (slope height =15 m and slope angle = 27°) (Kristo et al., 2017)	81
Figure 2.100:	Variations of the factor of safety (FOS) during and after rainfall for years 2003, 2050 and 2100 (Kristo et al., 2017)	82
Figure 3.1:	Flow chart of the research	86

Figure 3.2:	Location of the sample site; Balai Cerap, Universiti Teknologi Malaysia (UTM), Malaysia.	87
Figure 3.3:	Air drying soil sample in the laboratory	87
Figure 3.4:	Triaxial compression test	88
Figure 3.5:	Pressure plate extractor setup in UTM	90
Figure 3.6:	Loading frame housing a testing chamber in physical modelling tests	91
Figure 3.7:	Testing chamber used to mould the model ground for physical testing (without soil)	92
Figure 3.8:	Tensiometer holes on the other side of the testing chamber	92
Figure 3.9:	Pneumatic cylinder; (a) cylinder body and (b) pneumatic cylinder connected to a loading shaft and applying pressure to the model ground	93
Figure 3.10:	Loading plate pushed into the ground model to distribute loading	94
Figure 3.11:	Rainfall simulator in the Geotechnical Laboratory Universiti Teknologi Malaysia (UTM)	95
Figure 3.12:	Rainfall flow nozzles each with its regulators	96
Figure 3.13:	Target marker displayed in front of a ground model	97
Figure 3.14:	LVDT used to measure displacement units equipped with a magnet coupler	98
Figure 3.15:	Load cell transducer made by VMC California USA used in the study	99
Figure 3.16:	Portable data logger TML TDS-303 for loading stage data acquisition	99
Figure 3.17:	Calibration of load cell commencing in the UTM laboratory	100
Figure 3.18:	The data logger by Campbell Scientific model CR800 used by tensiometers data logging with protruding labelled wires connected to all the tensiometers used in the study	101
Figure 3.19:	12 units of tensiometers with wires connecting to the data logging system	101
Figure 3.20:	Calibration of tensiometer readings are being carried out with an Ammeter milliamp (mA) reading of tensiometer on the multiplexor used in the study	102

Figure 3.21:	The two AWAM devices on top of a ground model being powered by a Power Bank clamped to the testing chamber during loading stages	103
Figure 3.22:	AG GPS Reader program used to monitor readings from the AWAM device installed onto a personal computer	103
Figure 3.23:	Canon D5100 on an aluminium tripod used in the research	104
Figure 3.24:	Slowly pouring distilled water into the mixer	106
Figure 3.25:	Filling the gaps between the testing chamber acrylic sides with silicone rubber	107
Figure 3.26:	Manual compaction of the ground model using a hand tool	107
Figure 3.27:	The compaction of the ground model being modelled into 5 layers and shaped with formwork whilst the first layer being layered with 50 mm gravel.	108
Figure 3.28:	Reshaping the ground model onto its intended shape with hand tools	109
Figure 3.29:	Finished ground model setup ready for testing	109
Figure 3.30:	12 units of tensiometer installation into the ground model	110
Figure 3.31:	AWAM device location on the model ground	112
Figure 3.32:	Camera Setup for PIV data acquisition	112
Figure 3.33:	Screenshot of a proper finished preparation folder, ready for PIV analysis that contains folders for a result, target marker and subroutines from the GeoPIV8 module	114
Figure 3.34:	XYCoordinate file example placed in the Targetmarker folder	114
Figure 3.35:	led_launcher file adjusted to suit the location of image files	115
Figure 3.36:	registered_propics_list file generated after running regimlistgen command	116
Figure 3.37:	Meshing of the target image	117
Figure 3.38:	Several files named 'PIV_DSC_XXXX_DSC_XXXY' that is generated by entering the GeoPIV8 command	117
Figure 3.39:	Tagging physical target marker prompting red squares and numbering on the centre of the black dots of the target image	119

Figure 3.40:	The subroutine geoCENTROID8 running to find the centroid of each dot on the target marker	119
Figure 3.41:	The highlighted file of led_launcher to be selected during geoCALIBRATE8 step that is in the target marker folder	120
Figure 3.42:	Vector for testX simulated after qq.m command	121
Figure 3.43:	The code customized for the subroutine 'cntr.m' used in the PIV analysis	122
Figure 3.44:	The 'plotstrain.m' the subroutine that plots the strain for the PIV analysis	123
Figure 4.1:	Example of the Box-Flip raw data output (Evans et al., 2014)	126
Figure 4.2:	AG GPS reader program developed by the research to interpret AWAM device readings on a personal computer	127
Figure 4.3:	Dual axis digital protractor model DXL360 manufactured by Shenzhen Capital Electronics Co., Ltd. checked for flat surface readings using a bubble level	128
Figure 4.4:	Initial calibration setup	129
Figure 4.5:	AWAM reading vs LVDT measurement Test 1	130
Figure 4.6:	AWAM reading vs LVDT measurement Test 2	130
Figure 4.7:	AWAM reading vs LVDT measurement Test 3	131
Figure 4.8:	Analysis of AWAM value against LVDT movement for all test in the x-axis	132
Figure 4.9:	Dual-axis accelerometer with one axis of tilt (Baranilingesan and Rajesh, 2018)	133
Figure 4.10:	Calibration AWAM device setup	133
Figure 4.11:	Output acceleration vs angle of inclination for dual axis sensing; a) overall angle, b) angle of -50° until 50° for the x-axis showing linear approximation (Fisher, 2010).	134
Figure 4.12:	Calibration result of the AWAM devices on the x-axis	135
Figure 4.13:	Calibration result of the AWAM devices on the z-axis	136
Figure 4.14:	Output acceleration vs degree of angle	137
Figure 4.15:	Orientation of axes; (A) from the AWAM device orientation, (B) previous researcher axes orientation	137
Figure 4.16:	Modified accelerometer readings vs degree of angle for AWAM device	138

Figure 4.17:	Flip test calibration procedures	139
Figure 4.18:	Accelerometer calibration value vs time AWAM1	142
Figure 4.19:	Accelerometer calibration value vs time AWAM2	142
Figure 4.20:	Tilting device interpretation using difference of angle from x and z-axis	144
Figure 5.1:	Particle size distribution of the model soil	146
Figure 5.2:	The soil-water characteristic curves (SWCC) of the ground model	147
Figure 5.3:	Hydraulic conductivity of residual soil using Genutcten's method (1980)	148
Figure 5.4:	Intensity-Duration-Frequency (IDF) curve of Johor Bahru, Malaysia (Kassim, 2011)	149
Figure 5.5:	Tensiometer sensor locations for 27° slope angle cases (Cases A and D)	150
Figure 5.6:	Tensiometer sensor locations for 45° slope angle cases (Cases B and E)	151
Figure 5.7:	Pore water pressure vs. time for Case A (27° slope angle and 1-Hour rain)	151
Figure 5.8:	Pore water pressure vs. time for Case B (27° slope angle and 24-Hour rain)	152
Figure 5.9:	Pore water pressure vs. time for Case D (45° slope angle and 1-Hour rain)	152
Figure 5.10:	Pore water pressure vs. time for Case E (45° slope angle and 24-Hour rain)	153
Figure 5.11:	Pore water pressure vs. Elevation for model tests; (A) 27° slope angle and 1-Hour rain, (B) 27° slope angle and 24-Hour rain, (C) 45° slope angle and 1-Hour rain and (D) 45° slope angle and 24-Hour rain	154
Figure 5.12:	Stress vs. strain for the model tests	156
Figure 5.13:	Slope deformation of the ground model for Case A; (A) initial state (B) significant AWAM device reading and (C) final condition after maximum loading	158
Figure 5.14:	Slope deformation of the ground model for Case B; (A) initial state (B) significant AWAM device reading and (C) final condition after maximum loading	159

Figure 5.15:	Slope deformation of the ground model for Case C; (A) initial state (B) significant AWAM device reading and (C) final condition after maximum loading	160
Figure 5.16:	Slope deformation of the ground model for Case D; (A) initial state (B) significant AWAM device reading and (C) final condition after maximum loading	161
Figure 5.17:	Slope deformation of the ground model for Case E; (A) initial state (B) significant AWAM device reading and (C) final condition after maximum loading	162
Figure 5.18:	Slope deformation of the ground model for Case F; (A) initial state (B) significant AWAM device reading and (C) final condition after maximum loading	163
Figure 5.19:	AWAM1 (1A) & AWAM2 (2A) result of degree change overtime data for Case A	165
Figure 5.20:	Degree of slope change over a minute for AWAM1 case A	166
Figure 5.21:	Degree of slope change over a minute for AWAM2 case A	166
Figure 5.22:	AWAM1 (1B) & AWAM2 (2B) result of degree change overtime data for Case B	167
Figure 5.23:	Degree of slope change over a minute for AWAM1 case B	168
Figure 5.24:	Degree of slope change over a minute for AWAM2 case B	168
Figure 5.25:	AWAM1 (1C) & AWAM2 (2C) result of degree change overtime data for Case C	170
Figure 5.26:	Degree of slope change over a minute for AWAM1 case C	170
Figure 5.27:	Degree of slope change over a minute for AWAM2 case C	171
Figure 5.28:	AWAM1 (1D) & AWAM2 (2D) result of degree change overtime data for Case D	172
Figure 5.29:	Degree of slope change over a minute for AWAM1 case D	173
Figure 5.30:	Degree of slope change over a minute for AWAM2 case D	173
Figure 5.31:	AWAM1 (1E) & AWAM2 (2E) result of degree change overtime data for Case E	174

Figure 5.32:	Degree of slope change over a minute for AWAM1 case E	175
Figure 5.33:	Degree of slope change over a minute for AWAM2 case E	175
Figure 5.34:	AWAM1 (1F) & AWAM2 (2F) result of degree change overtime data for Case F	177
Figure 5.35:	Degree of slope change over a minute for AWAM1 case F	178
Figure 5.36:	Degree of slope change over a minute for AWAM2 case F	178
Figure 5.37:	Downward movement as x^0 increases and z^0 decreases	180
Figure 5.38:	Slope displacements for Case A (27° Degree and 1-Hour rain)	183
Figure 5.39:	Slope displacements for Case B (27° Degree and 24-Hour rain)	184
Figure 5.40:	Slope displacements for Case C (27° Degree and 0-Hour rain)	184
Figure 5.41:	Slope displacements for Case D (45° Degree and 1-Hour rain)	184
Figure 5.42:	Slope displacements for Case A (45° Degree and 24-Hour rain)	185
Figure 5.43:	Slope displacements for Case A (45° Degree and 0-Hour rain)	185
Figure 5.44:	Contours of cumulative vertical displacement for Case A (27° Degree and 1-Hour rain)	186
Figure 5.45:	Contours of cumulative horizontal displacement for Case A (27° Degree and 1-Hour rain)	187
Figure 5.46:	Contours of shear strain for Case A (27° Degree and 1-Hour rain)	187
Figure 5.47:	Contours of cumulative vertical displacement for Case B (27° Degree and 24-Hour rain)	188
Figure 5.48:	Contours of cumulative horizontal displacement for Case B (27° Degree and 24-Hour rain)	189
Figure 5.49:	Contours of shear strain for Case B (27° Degree and 24-Hour rain)	189

Figure 5.50:	Contours of cumulative vertical displacement for Case C (27° Degree and 0-Hour rain)	190
Figure 5.51:	Contours of cumulative horizontal displacement for Case C (27° Degree and 0-Hour rain)	190
Figure 5.52:	Contours of shear strain for Case C (27° Degree and 0-Hour rain)	191
Figure 5.53:	Contours of cumulative vertical displacement for Case D (45° Degree and 1-Hour rain)	191
Figure 5.54:	Contours of cumulative horizontal displacement for Case D (45° Degree and 1-Hour rain)	192
Figure 5.55:	Contours of shear strain for Case D (45° Degree and 1-Hour rain)	192
Figure 5.56:	Contours of cumulative vertical displacement for Case E (45° Degree and 24-Hour rain)	193
Figure 5.57:	Contours of cumulative horizontal displacement for Case E (45° Degree and 24-Hour rain)	193
Figure 5.58:	Contours of shear strain for Case E (45° Degree and 24-Hour rain)	194
Figure 5.59:	Contours of cumulative vertical displacement for Case F (27° Degree and 0-Hour rain)	194
Figure 5.60:	Contours of cumulative horizontal displacement for Case F (45° Degree and 0-Hour rain)	195
Figure 5.61:	Contours of shear strain for Case F (45° Degree and 0-Hour rain)	195
Figure 6.1:	Modelling scheme for slope 1:2 ratio (27° slope)	202
Figure 6.2:	Modelling scheme for slope 1:1 ratio (45° slope)	202
Figure 6.3:	SEEP/W initial condition after 84,600 seconds of simulation	203
Figure 6.4:	Rainfall intensity (blue arrow) was added to the model via boundary condition setup	204
Figure 6.5:	‘KeyIn Analysis’ tab of the Geostudio depicting the overall analysis done throughout the simulations	205
Figure 6.6:	Checked box drawn to simulate the loading conditions of the SLOPE/W loading condition whilst red line representing entry and exit boundary for slip surface	206
Figure 6.7:	Example of a SLOPE/W analysis resulting in a value of FOS	206

Figure 6.8:	Pore water simulations result for SEEP/W; (A) case A and (B) case B	207
Figure 6.9:	Pore water simulations result for SEEP/W for; (A) case D, (B) case E	208
Figure 6.10:	Draw graph sub-option to graphically interpret depth vs. pore-water pressure	209
Figure 6.11:	Compilation of the Depth vs. PWP for all cases; A) case A, B) case B, D) case D and E) case E	210
Figure 6.12:	Factor of Safety (FOS) of the ground model vs. time for all cases	211
Figure 6.13:	Vertical pore-water profile comparison for physical model and simulated readings for both cases; A) 1-hour rain and B) 24-hour rain	214
Figure 7.1:	Flowchart of AWAM development	218
Figure 7.2:	Diagram Process of AWAM System	220
Figure 7.3:	Proposed site installation	221
Figure 7.4:	United States Geological Survey (USGS) open-canopy rain gauge on-site (Reilly et al, 2017)	221
Figure 7.5:	Typical rain gauge installation including an enclosed datalogger and temperature sensor assembly (Smith et al., 2017)	222
Figure 7.6:	Production stages	222
Figure 7.7:	Overview of the overall system assembly for the AWAM site device	223
Figure 7.8:	Power station housing of the AWAM system	224
Figure 7.9:	The overview of the waterproof enclosure box of the AWAM system in site conditions	225
Figure 7.10:	Enclosure box of the casing for the sensors of the AWAM system	226
Figure 7.11:	Column supporting the power stations enclosure box	227
Figure 7.12:	Steel base plate supporting the base of the power station	228
Figure 7.13:	Solar charge controller of the power supply	229
Figure 7.14:	Solar panel installed on top of the power station on the AWAM device	231
Figure 7.15:	Dual-core solar cable used in the AWAM system for transferring current as of the power source	233

Figure 7.16:	GP Seal Lead Acid (SLA) rechargeable battery used in the power capacity of the AWAM system	234
Figure 7.17:	Sample of the power relay used to control the current powering the system	236
Figure 7.18:	The step-down module used in the power management of the AWAM system	237
Figure 7.19:	Controller display for the data logging status display of the AWAM system	239
Figure 7.20:	Wireless transmitter module manufactured by Arduino Uno for the data transmitting apparatus of the AWAM system	240
Figure 7.21:	The controller board to control the wireless transmitter process used in the AWAM system	242
Figure 7.22:	The on-board data and time management board for the date and time specifications of the AWAM system	243
Figure 7.23:	The casing of the power station and sensor casings assembled with tightening screw caps to ensure onboard systems are protected.	245
Figure 7.24:	The label and hoarding of the research in progress tagging the AWAM system on site	246
Figure 7.25:	ArduPilot Mega (APM) flight controller used as the sensor mechanism in the AWAM system	247
Figure 7.26:	Hinged foundation mechanism of the AWAM system sensor case	248
Figure 7.27:	Web page Hostinger.com used to host the AWAM system data storage and analysis output algorithms	249
Figure 7.28:	Satellite view of AWAM device installation sites through Google maps	251
Figure 7.29:	Exact location of AWAM device installation inside UTM	251
Figure 7.30:	The aerial overview of the surroundings for the AWAM2.	252
Figure 7.31:	The surrounding location of the AWAM4 and AWAM5	252
Figure 7.32:	Mackintosh Probe test on site of the AWAM system prepared by research assistants	253
Figure 7.33:	Overview of the M47 site layout	255
Figure 7.34:	Overview of the CICT site layout	256
Figure 7.35:	Site M47 geometry and boundary conditions	256

Figure 7.36:	Site CICT geometry and boundary conditions	256
Figure 7.37:	SEEP/W initial condition of M47 site	257
Figure 7.38:	SEEP/W initial condition of CICT site	257
Figure 7.39:	Transient seepage simulation condition of M46 site	258
Figure 7.40:	Transient seepage simulation condition of CICT site	259
Figure 7.41:	SLOPE/W factor of safety analysis of M46 site at 0 hour (initial)	260
Figure 7.42:	SLOPE/W factor of safety analysis of M46 site after 4 hours	260
Figure 7.43:	SLOPE/W factor of safety analysis of M46 site after 8 hours	260
Figure 7.44:	SLOPE/W factor of safety analysis of M46 site after 20 hours	260
Figure 7.45:	SLOPE/W factor of safety analysis of CICT site at 0 hour (initial)	261
Figure 7.46:	SLOPE/W factor of safety analysis of CICT site after 4 hours	261
Figure 7.47:	SLOPE/W factor of safety analysis of CICT site after 8 hours	262
Figure 7.48:	SLOPE/W factor of safety analysis of CICT site after 20 hours	262
Figure 7.49:	Relationship between safety factor and rain period simulations	263
Figure 7.50:	AWAM monitoring system webpage	265
Figure 7.51:	awam.my displaying all the healthy status of the AWAM system	266
Figure 7.52:	awam.my extensive data table display	266
Figure 7.53:	AWAM system data sample downloaded from the awam.my website	267
Figure 7.54:	a) admin login page and b) settings menu for administration	267
Figure 7.55:	AWAM device data limiting value management	268
Figure 7.56:	User management navigation list for awam.my personnel	269
Figure 7.57:	Preliminary installation stages	270

Figure 7.58:	Setup of the AWAM system on site	270
Figure 7.59:	Completed installations of the AWAM system for slope monitoring on site	271
Figure 7.60:	AWAM1 device accelerometer readings for the year 2019	272
Figure 7.61:	AWAM2 device accelerometer readings for the year 2019	273
Figure 7.62:	AWAM3 device accelerometer readings for the year 2019	274
Figure 7.63:	AWAM4 device accelerometer readings for the year 2019	275
Figure 7.64:	AWAM5 device accelerometer readings for the year 2019	276

LIST OF ABBREVIATIONS

3D	-	3 Dimension
AC	-	Alternate Current
AE	-	Acoustic Emission
Ah	-	Ampere-hour
ALOS-PALSAR	-	Phased Array type L-band Synthetic Aperture Radar
ALS	-	Airborne Laser Scanning
APM	-	Ardupilot Mega
ASTM	-	American Society of Testing Method
AWAM	-	Automatic Wireless Accelerometer Monitoring
BS	-	British Standard
BSCS	-	Biological Sciences Curriculum Study
CCD	-	Charge-Couple Device
CICT	-	Centre for Information and Communication
CIU	-	Consolidated Isotropic Undrained
CMOS	-	Complementary Metal Oxide Semiconductor
CSK	-	COSMO-SkyMed satellite
CW-SF	-	Continuous-Wave-Step-Frequency
DC	-	Direct Current
DEM	-	Digital Elevation Model
DGPS	-	Differential Global Positioning System
DIC	-	Digital Image Correlation
DiffSAR	-	Differential Interferometric Synthetic Aperture Radar
DMG	-	Department of Mineral and Geoscience
EDM	-	Electronic Distance Meter
EEPROM	-	Electrically erasable programmable read-only memory
ERS	-	European Remote Sensing
ESA	-	European Space Agency
FPS	-	Frames per Second
FOS	-	Factor of Safety
GBInSAR	-	Ground Based Interferometer Synthetic Aperture Radar

GB-SAR	-	Ground Based Synthetic Aperture Radar
GPRS	-	General Packet Radio Services
GPS	-	Global Positioning System
GSM	-	Global System for Mobile communication
IDF	-	Intensity-Duration-Frequency
IGM	-	Italian Instituto Geografico Militare
IoT	-	Internet of Things
IR	-	Infrared
ISO	-	International Standards Organisation
JKR	-	<i>Jabatan Kerja Raya</i>
JPEG	-	Joint Photographic Experts Group
kHz	-	Kilohertz
LCD	-	Liquid Crystal Display
LDO	-	Low Noise Linear
LED	-	Light Emitting Diode
LIDAR	-	Light detection and Ranging
LL	-	Liquid Limit
LVDT	-	Linear Variable Displacement Transducer
MACRES	-	Centre of Remote Sensing
mAh	-	mili Ampere-hour
MDD	-	Maximum Dry Density
MF	-	Manual Focus
MHz	-	Megahertz
MP	-	Megapixel
MPBX	-	Multi-Point Borehole Extensometer
MUX	-	Multiplexer
NOAA	-	National Oceanic and Atmospheric Administration
OMC	-	Optimum Water Content
PDF	-	Portable Document Format
PHP	-	Hypertext Pre-processors Language
PI	-	Plasticity Index
PIV	-	Particle Image Velocimetry
PL	-	Plastic Limit
PV	-	Photovoltaic

PVC	-	Polyvinyl Chloride
PWD	-	Public Works Department
PWP	-	Pore Water Pressure
RTC	-	Real Time Clock
SAR	-	Synthetic Aperture Radar
SBAS	-	Small Baseline Subset
SLA	-	Seal Lead Acid
SMS	-	Short Message Service
SOP	-	Standard of Procedure
SSPM	-	Shallow Strain Path Method
SWCC	-	Soil Water Characteristic
UMTS	-	Universal Mobile Telecommunications Service
USGS	-	United States Geological Survey
UTM	-	University Teknologi Malaysia
UV	-	Ultraviolet
WLAN	-	Wireless Local Area Network
XLPE	-	Cross-linked Polyethylene

LIST OF SYMBOLS

%	-	Percent
°	-	Degree
A	-	Ampere
A_{ev}	-	Air entry value
c	-	Cohesion
e	-	Bulk density of soil
E	-	East
e	-	Void ratio
E	-	Young Modulus
g	-	Acceleration = 9.81m/s ²
G_s	-	Specific Gravity
h	-	Hour
h_w	-	Initial depth of groundwater levels
J	-	JKR probe blow
k	-	Hydraulic conductivity
K	-	Permeability
k_{sat}	-	Saturated coefficient of permeability
N	-	No of Blows
N	-	North
ϕ	-	Friction angle
q	-	Bearing Capacity
q	-	Unit flux
Q	-	Water flow
R^2	-	Linear regression models
S_u	-	Undrained Shear Strength
u_a	-	Air pressure
u_w	-	Pressure of water phases
u_w	-	pressure of water phases
V	-	Volt
w	-	Moisture content of soil

w_{opt}	-	Optimum moisture content
γ_b	-	unit weight
θ	-	Volumetric water content
θ_r	-	Residual Water Content
θ_s	-	Saturated Volumetric Water Content
ρ	-	Density
ρ_d	-	Dry density of soil
ρ_{dmax}	-	Dry density of soil
ϕ	-	Shear resistance angle
ϕ^b	-	Shear strength relative to suction
ψ_{min}	-	Minimum Suction at Residual Water Content
e	-	Porosity

LIST OF APPENDICES

APPENDIX	TITLE	PAGE
Appendix A	Calibration of Instrumentation	287
Appendix B	MatLab Program for PIV	297
Appendix C	awam.my datalogging for AWAM system for the year 2019	307

CHAPTER 1

INTRODUCTION

1.1 Introduction

Slope stability is an uprising problem in geotechnical engineering where slope failure occurrences impose risks on human lives and property (Ahmed et al., 2011). Many fatalities have occurred due to slope failure (Chowdhury et al., 2009). Even when there is no injury, there is a high cost effect due to construction delay, structural damages, loss of production and often damaged equipment. Malaysia has had several landslide incidents which had tremendous effects on the livelihoods of its residents. Among the highlights of these incidents were recorded in the Highland Tower disaster in the state of Selangor, Malaysia in December of 1993 (Jamaludin and Hussein, 2006). An estimated toll of 48 people lost their lives to the incident when one of the buildings collapsed after suffering slope failure. The slope failure was investigated by the authorities and was revealed to have been originated by the poorly maintained construction project of Bukit Antarabangsa in the neighbouring vicinity. Heavy rains unmitigated by proper channelling poured over the unstable natural slope contributed heavily to the disaster. Several follow-up landslides did occur in several places around the area that was also reported to have human casualties.

Gue and Tan (2006) reported that based on the 49 individual slope failure cases investigated, 60 % of the failure is caused by man-made slopes. This is due to the weakness design, for instance the design exceeds the maximum angle of slope construction, underestimating rainfall condition and lack of maintenance. In addition; poor workmanship, quality of materials and lack of site supervision contributed to the total cases of landslides during constructions work.

Some typical signs of landslide danger could be foretold such as the appearance of water overflowing near the toe or base surface of a slope or retaining walls (Flooding

of water in hilly areas). It shows that the water is not flowing along a proper channel, and instead pools in unexpected areas. It also indicates that water is seeping into the slope and flowing out at the base (seepage problems). Sudden change in colour (from clear to muddy) of water flowing from slopes or retaining walls is also a clear indicator of slope failure. Fences, trees and retaining structures on slopes are going to tilt or move. It shows that there is ground movement on the slopes. In addition, there would be the emergence of large cracks and ground settlement occurring in slopes, retaining walls or along road pavements. Such occurrences are illustrated by the development of horizontal cracks that appears at the top of the slope where parts of the soil and rock layer break away from the main slope (Bunawan et al., 2016).

The risk of these tragedies repeating could be minimized if a monitoring system for a slope failure was implemented. The previous early warning methods are implemented by using rain gauges and surface monitoring devices as the instrumentations. It is difficult to determine the effectiveness of these tools as they monitor only the surface of potential fail slopes. As of today, surveying on slope movement (monitoring system) can be performed by several methods. A common technique to determine slope stability is to monitor the small precursory movements such as deformations, which occur prior to collapse. A wide variety of instruments were employed to monitor slope deformations. Readily available measuring apparatus such as inclinometer, theodolite, electronic distance meter (EDM), or tiltmeter (Angeli et al., 2000) have gained the most accredited slope monitoring tools. Inclinometers were instrumental in quantifying lateral movements of a slope body including retaining walls, high-risk landslide area and also embankments. In addition, deflection measurements of retaining walls and piles underneath loading were also possible. A number of studies are previously done to create alternatives to slope monitoring systems.

Ding et al. (2000) proposed automatic monitoring of slope deformation using geotechnical instruments equipped with self-contained power supply system consists of solar power and rechargeable batteries, data logger and alarm system at the sloping site. Various commercial sensors (extensometer, tiltmeter, strain and stress gauge, and piezometer) were used to provide the deformation data. All the site information will

then be transferred to central computer software by using a wireless system (Ding et al., 2000). Bozzano et al. (2010) conducted continuous monitoring on slope structure for 23 months using an integrated platform with a ground-based SAR interferometer (GBInSAR), a weather station, and an automatic camera. This method could provide the opportunity to analyze the response of an unstable slope to the different phases of work. The deformational behaviour of both the natural slope and the man-made structures were recorded and interpreted in relation to the working stages and the rainfall conditions during the whole monitoring period (Bozzano et al., 2010). Khan et al. (2010) measured hill-slope movement of the Gunung Pass, Cameron Highland, Pahang, Malaysia slope site using theodolite and collection of rainfall data. Prisms and theodolite were employed to measure ground displacement. The other method is based on remote sensing techniques such as Synthetic Aperture Radar (SAR) data with differential information, while some are based on Global Positioning System (GPS) (Gili et al., 2000, Malet et al., 2002, Megawati et al., 2005). These methods have each advantage and disadvantages to oversee deformation monitoring.

Hence, the research opted to develop an innovative system that offers an economical, user-friendly and highly effective alternative to the current array of systems readily on the market. The system is to be named Automatic Wireless Accelerometer Monitoring System (AWAM). AWAM system was implemented as an early warning slope failure system that can relay real-time slope conditions while also notifying the system users and authorities if the slope condition changes. In other words, the system would act as a risk management system of a particular slope. A small-scale physical laboratory testing was structured to calibrate the system capabilities and detect the precursor movement of the slope prior to failure. The laboratory result then was validated using Numerical Analysis software (Geostudio). Furthermore, the system was tested in full-scale test on site.

1.2 Problem Statement

Continuous monitoring of slope requires a huge budget and manpower which is currently lacking for developing countries such as Malaysia. Traditional slope

monitoring limitations include the lack of accessibility to some slope monitoring sites due to harsh logistic conditions, a disruptive ambience of surrounding areas and climate diversity hindrance. In addition, the slope monitoring system may require a stable power supply which is scarce in remotely located sites. Furthermore, the data transmission and recordings would also be hindered by physical complications present on slope sites. Some systems opted the use of manual data collection through observations which are highly susceptible to human error. All these factors would undoubtedly affect the ability of a slope monitoring system to properly assess risk conditions of an intended slope thus incurring the unnecessary cost of additional manpower to properly maintain the system.

Due to such limitations, the research sought out various combinations of innovative modification onto established instrumentation and monitoring systems and assembles a complete monitoring system to monitor potentially high-risk slopes. A series of physical model test at the laboratory scale was performed to test out the AWAM system on detecting the failure of the ground. After that, the performance of the system would be put to the test in the field.

1.3 Research Objectives

The objectives of this study are to:

- (a) To develop a fully Automatic Wireless Accelerometer Monitoring System (AWAM) used for slope monitoring
- (b) To determine the failure signal of the accelerometer by conducting a calibration test and small-scale physical modelling.
- (c) To investigate the performance of the system by conducting a full-scale test

1.4 Scope of Study

This research would focus on:

- (a) Monitoring instrumentation for slope engineering based on the deformation that is occurring on the slope.
- (b) Laterite soil was used to prepare the slope model with three rain conditions simulating the slope condition in the tropical climate.
- (c) The slope tested would be defined as a finite slope with two sets of slopes with the inclinations of 27° and 45° , respectively.
- (d) Numerical model used in this study is two-dimensional limit equilibrium (Geostudio) focusing on SLOPE/W and SEEP/W to validate the physical modelling test for slope stability analysis.
- (e) Full-scale monitoring of slope in the site was conducted to test a prolong exposure to real field conditions.

1.5 Research Significance

This research is envisioned to be an innovative alternative to the monitoring instrumentation for slope engineering. Automatic Wireless Accelerometer Monitoring System (AWAM) would overcome most of the limitations for the current slope monitoring systems implemented. The device would traverse geomorphology limitations, climate conditions, isolated sites and improbable site conditions for slope monitoring. It was designed to be operable with minimal cost, accommodating to new users and bridges the public with readings from the monitoring.

1.6 Thesis Outline

The thesis produced from the research comprises of eight chapters. The current chapter contains the introductory statement on the approach that was done to tackle current slope monitoring practices. The research objectives clarify the goals of the research to develop an improved and innovative system to monitor slope stability. The scope of the study was detailed out to put on perspective the development approach and limitations of resources imposed on the study. The importance and implications of the developed system to improve slope stability monitoring was emphasized.

Chapter 2 explicitly detail out the concepts and techniques that were implemented on slope monitoring. Application, strength and weaknesses are thoroughly researched as a strong foundation to develop an advanced and innovative approach to monitoring slope stability. Key aspects of Particle Image Velocimetry (PIV) and numerical modelling (GeoStudio) was also discussed to develop interpretations of the newly developed system as compared to the existing slope monitoring systems.

Chapter 3 contains the physical modelling aspect of the research. The materials, equipment, measuring method, model preparation and soil testing are extensively presented. In addition, the PIV testing on the slope model was also described.

Chapter 4 portrays the calibrations done to the newly developed slope monitoring system in accordance with previous researchers. The equipment, preparations and procedure were detailed out accordingly. The research also explained the difference in data interpretation in contrast to the preceding study. A calibration unit is vital in interpreting the data acquisition outcome of the system.

Chapter 5 illustrates the experimental result of the physical modelling done throughout the research. Material properties, Soil Water Characteristic Curve (SWCC), hydraulic conductivity function and rainfall patterns were determined to properly assess the physical model that would later be simulated through numerical

modelling. Infiltration results from the rainfall simulations were prepared to measure pore water pressure according to depth. Stress-strain relationship of the conducted physical modelling tests was carried out accompanied by the slope deformation of the model tests. The main result obtained from the sensors of the slope monitoring system was translated onto a slope movement per minute to properly determine the magnitude of the slope movement. In accordance with the objectives set out in the research, the trigger value to quantify precursor movement prior to slope failure was determined. Furthermore, the sensors movement orientation was explained thoroughly. In addition, PIV results obtained from physical modelling was also prepared.

Chapter 6 focuses on the cross-referencing of physical modelling with numerical modelling. Numerical modelling approach using the limit equilibrium software (Geostudio) was illustrated step by step to determine to factor of safety (FOS) of the slope model from initial condition until failure. The comparison data from the numerical and physical model was defined to prove the concept of numerical analysis in properly predicting the outcome of the physical modelling.

Chapter 7 comprises of the development of the on-site slope monitoring system components. On-site application of the newly developed slope monitoring system was meticulously discussed starting from the system components, data acquisition procedure, site preliminary investigations, system installations and finally slope monitoring results. The slope monitoring system capabilities and outcomes were highlighted.

Chapter 8 represents the conclusion of the overall research, emphasizing the research outcomes and contributions while also remarking on future recommendations to develop an even advance slope failure alarm system for the benefit of mankind.

CHAPTER 2

LITERATURE REVIEW

2.1 Introduction

In this chapter, the concepts of slope monitoring techniques are reviewed. Previous applications, strengths and weaknesses are extensively researched for comparison and future references. Automated Wireless Accelerometer Monitoring system (AWAM) developed in the study will be briefly described for its functionality and capabilities. Particle Image Velocimetry (PIV) and numerical modelling (GeoStudio) was discussed since the present research employs said analysis.

2.2 Slope Monitoring

Slope stability is the ability of slope-forming materials to withstand movement. Instability of both man-made and natural slopes has a significant impact on the built environment and infrastructure of cities and the people relying on the stability of slopes. Despite careful planning and design to minimize the risk of slope instability, accidents such as landslides, subsidence and earthquake can always happen (Angeli et al., 2000). Consequently, there is a need for a real-time monitoring device to measure the soil movements, conduct risk assessments, and provide an early warning system for instability detection (Dixon et al., 2015).

Geotechnical investigations have been carried out since the 1960s, in order to detect the instability of slopes. The aim of monitoring systems in natural geotechnical phenomena is to understand the process of the accidents and to minimize the risk of slope instability towards the community and infrastructure by proposing a mitigation plan (Angeli et al., 2000; Lacasse and Nadim, 2009). Basically, methods of monitoring systems are divided into two categories, which are geodetic (surveying) and

geotechnical instrumentation techniques (Ding et al., 2000). Ding et al., (2000) explained how surveying techniques include surveying tools such as level, theodolites, total stations, and Global Positioning System (GPS) to measure differences of a certain point in a specific location repeatedly over a certain period of time. Other than that, the geotechnical techniques are said to require geotechnical instruments in determining both the physical and the geotechnical parameters of the assigned location.

It is well known that in the past, manual reading and recording of data was used for slope monitoring systems. However, recent studies and developments in the geotechnical world have led to several advancements in the slope monitoring system. Data can be now be collected automatically and computerized for the most part to be of greater assistance in managing risks of slope instability. Interpreting the collected data in real-time could be the deciding factor in the safety or the evacuation of people and property (Malet et al., 2002).

Evolution of slope monitoring systems has involved numerous innovations in order to create the most user friendly, cost-effective, and reliable system for monitoring slopes. From a combination of conventional ground displacement monitoring sensors to space-borne radar remote sensing, researchers have come a long way in understanding geological hazards threatened by terrain movements (Calo et al., 2014). The following chapter reviews the progress, key features detailing the strengths and limitation of several researches on slope monitoring devices to provide an understanding of the future demands.

2.2.1 Geodetic (Surveying) Technique

2.2.1.1 Theodolite and Prism

A theodolite is a surveying instrument to measure horizontal and vertical angles and can be used as an automatic topographic system for measuring surface movement. Angeli et al. (2000) reported that since as early as 1960 in the Tessina region in Italy, an automatic topographic system has been used to detect surface

movement of the aftermath of a landslide as shown in Figure 2.1. A motorized Wild TM3000V theodolite with 30 reflecting prisms was used at 1 to 3-hour interval to measure angles and distances in the site. Data was transferred into a central monitoring station in order to define possible dangerous situations.

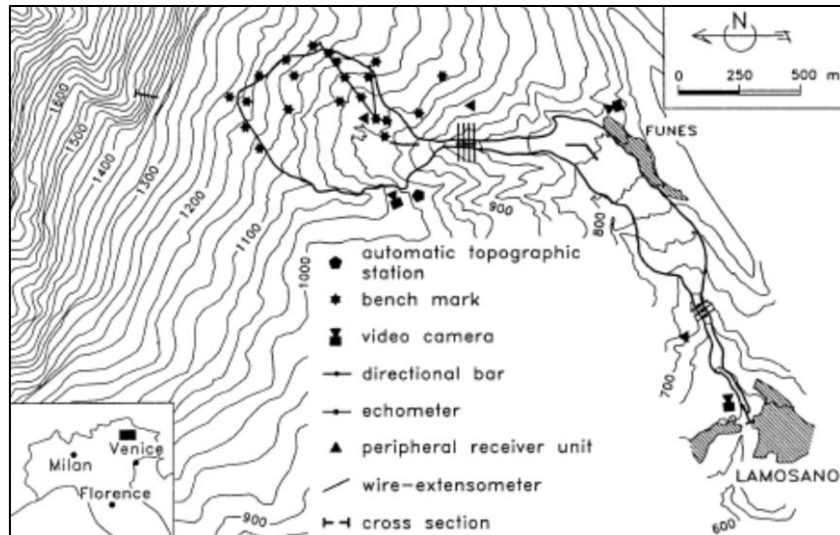


Figure 2.1: Location of Instrumentation (Angeli et al., 2000).

From 1996 to 1999, Rizzo (2002) updated the benchmark of the infrared distance-meter instrument (EDM) in Maratea valley in Italy to monitor the casual distance difference in the site. About 50 existing benchmarks were updated that had been used along with further 73 points to monitor the Maratea valley. The system measured displacements of about 1.5 to 4.5 cm per year that had occurred during the mentioned period of time as shown in Figure 2.2. These values were similar to the previously monitored value at the site.

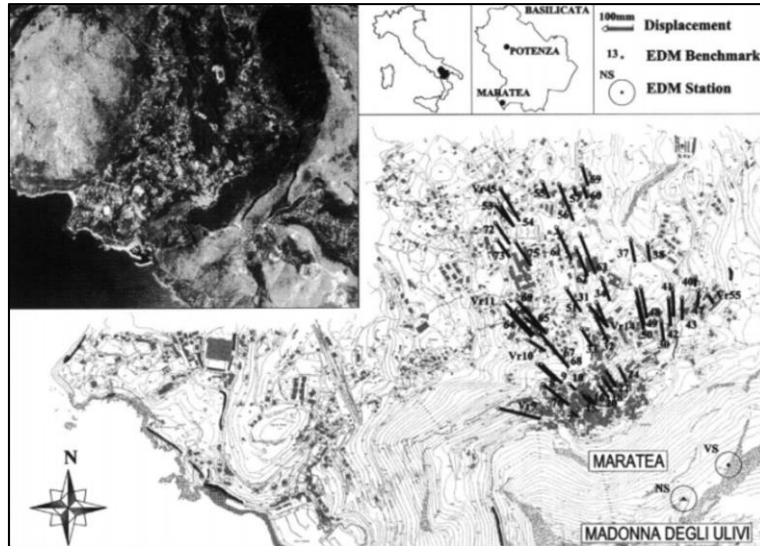


Figure 2.2: Displacement Monitored by EDM from June 1996 to October 1999 (Rizzo, 2002).

A study was conducted by Little (2006) in October 2003 to use automated theodolites and prisms as an early monitoring system in an open-pit mine in South Africa as shown in Figure 2.3. The prisms positions were measured every 4 hours by automated theodolites positioned on the crest of the open-pit mine. The theodolites were encased in steel casings to protect them from surrounding hazards. Data from the theodolites were transferred via radio link to an office computer for analysing purposes. The collected data were used to measure the displacements and produce vectors of movements for the prisms.

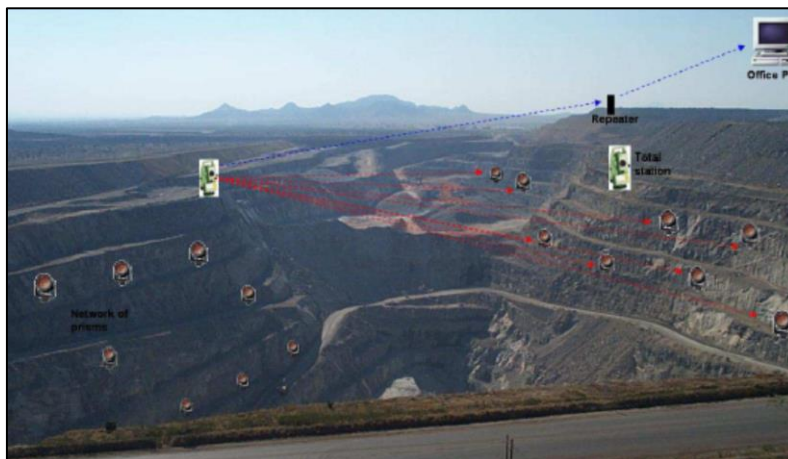


Figure 2.3: Theodolites and Prism Network on the Sandloot Open-Pit (Little, 2006).

Herrera et al. (2009) reported the utilization of total station in measuring several active landslides in Portalet, Spain. A total of seven total stations were deployed in the initial monitoring campaigns performed from December 2004 until March 2005. Figure 2.4 shows the sketch of the studied landslide area with total stations measurements are highlighted within the landslide body. Total displacement of about 510 mm was monitored (0.5 mm per day).

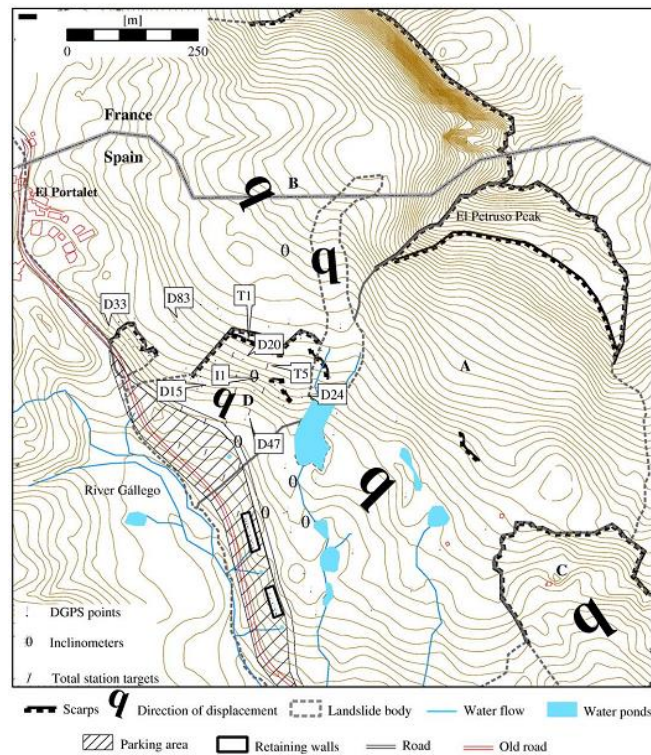


Figure 2.4: Geomorphological sketch of the landslide study in Portalet, Spain (Herrera et al., 2009)

Another case study on landslide hazard was conducted in Malaysia by Khan et al. (2010) to monitor the Gunung Pass hill-slope movement using theodolites and prisms, after a series of landslides occurred in 2007 (Figure 2.5). Six prisms mounted on concrete footing were placed on the ground and were used to monitor the site within 293 days overlooking two rainy seasons. The study assumed that changes in the position of the prisms are correlated with the ground movement. Rainfall data were also collected to be studied in conjunction with the ground movement. After heavy rainfall in March 2007, the slope had become saturated and failed subsequently. The monitoring device was capable of recording ground movements after the failure occurred.

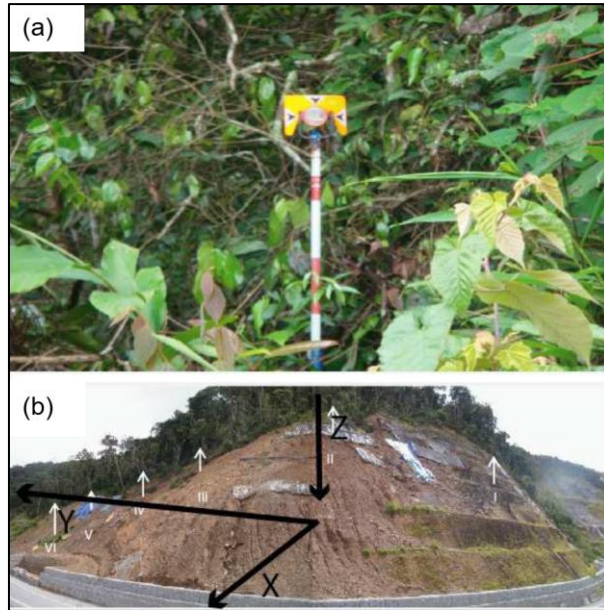


Figure 2.5: a) Prism installed b) Position of 6 prisms with XYZ axes (Khan et al., 2010).

In the year 1999, Fastellini et al. (2011) reported that a high precision levelling network has been setup in Assisi, Italy to monitor a known landslide movement. A total length of 12 km and 200 markers are utilized for the monitoring. Figure 2.6 shows the stainless-steel rods for levelling network installed all over the proposed area (walls, buildings, and concrete structures). A total of seven measuring campaigns were calculated with a standard deviation of 1 mm.



Figure 2.6: Levelling network base point made of stainless steel situated in stable structures (Fastellini et al., 2011)

Fastellini et al. (2011) noted that by utilizing levelling campaigns for monitoring purposes resulted in numerous advantages including the ability to operate on long time periods, relatively low-cost monitoring providing more dense control points distribution even though the base result is only vertical components of the motion (1-dimensional data). Figure 2.7 highlights the result of high precision levelling of vertical displacements from 1999 to 2008. The campaign projected estimations of 5 to 6 mm per year velocity. Maximum displacement was calculated about 53 mm in 9 years duration shown in the centre of the landslide body. The result of the research is reported to be crucial in the design of technical mitigation plan for the landslide area.

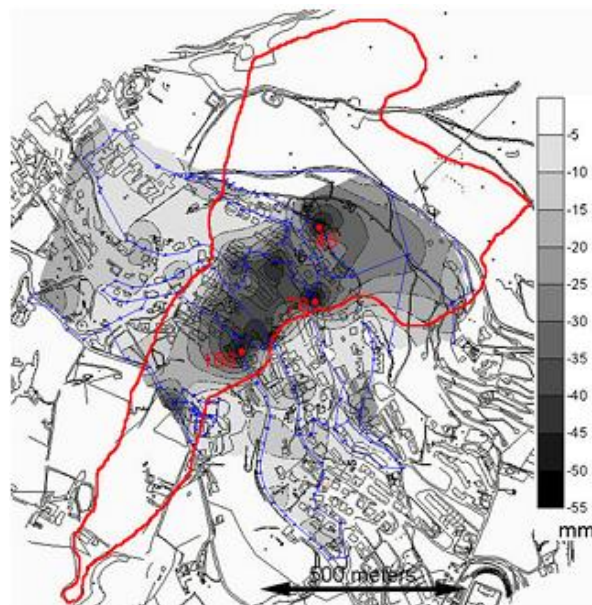


Figure 2.7: Contour map of vertical displacement resulted from high precision levelling network (Fastellini et al., 2011)

Although the monitoring devices managed to measure the movements during the failure, however, several limitations were identified from this method. Among the limitations of using a theodolite and prism, monitoring is its dependence on the geomorphology of the area, physical obstacles, climate factor, and also whether the monitoring site is an active construction site or not. Sufficient manpower is also needed for setting out the monitoring devices to cover a large-scale site.

2.2.1.2 Laser Monitoring

Blair et al. (1997) developed an optical extensometer that measures distance using modulated laser beams. The laser monitoring instruments are divided into two parts. The first part consists of an electro-optic module that contains a laser distance measuring device, controlled by a computer, that lets the laser determine the laser intensity, records data and additional data and control function. In addition, the second part is the reflectors of said laser beams installed at the desired measuring points (Figure 2.8). Blair monitored the Yucca Mountain, Nevada, USA for a period of 6 months from August 1996 measuring distances up to 2.5 meters and 4.3 meters. The measuring conducted its monitoring although being situated in close proximity to continuous mining operations such as drilling, blasting and mechanical excavation works.

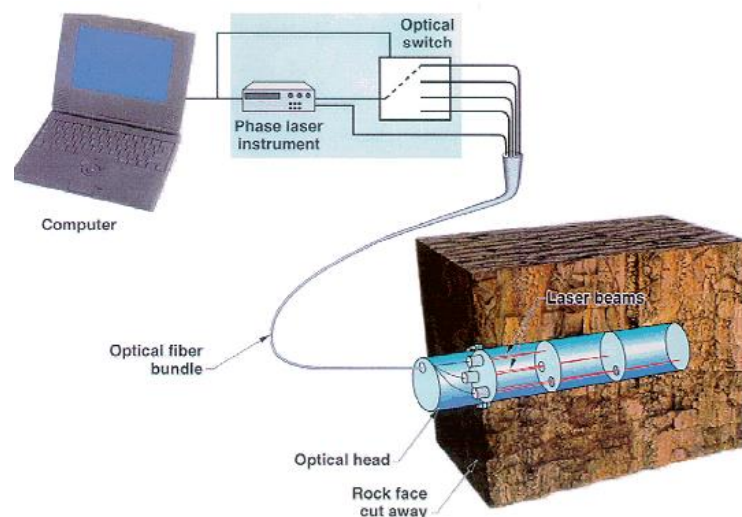


Figure 2.8: Schematic of ROX system (Blair et al., 1997)

Blair et al. (1997) reported that several problems arose from the laser monitoring prototype, firstly the precision of the laser monitoring data are disappointing. In addition, the return beam signals of further located anchors are too weak to be captured. It seems the laser powers are in need of reinforcements. Other than that, condensed heated moisture from the cracks and muddy mist from nearby mining blast fogged the laser beam lenses and reflectors. However, the research was

positive that the monitoring system was still under development and several modifications are hoped to improve the overall system performance.

Wehr and Lohr (1999) reported on the overview of the airborne laser scanning (ALS) principles to measure reflection and range of the earth's surface. Basic principles of laser monitoring are the recording of the mean distance between the sensor and the illuminated spot on the ground. This distance is calculated by measuring the travel time between the emitted and received pulse (Figure 2.9).

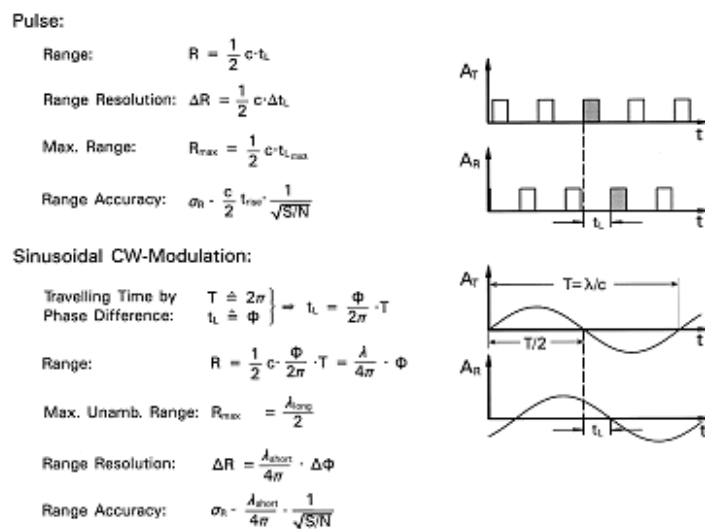


Figure 2.9: Measuring principle of pulse and CW-lasers (Wehr and Lohr, 1999)

Wehr and Lohr (1999) reported that the airborne laser scanning (ALS) is dependent on several factors such as scan patterns flight directions, speeds and the terrain topography involved. An example of the progression of a Palmer scan is shown in Figure 2.10, to obtain accurate readings of the range measurement, a laser scanner system must be integrated with a coordinate system such as position and orientation system. Such orientation and position system would require a time synchronization of the Differential Global Positioning System (DGPS) and laser scanner data.

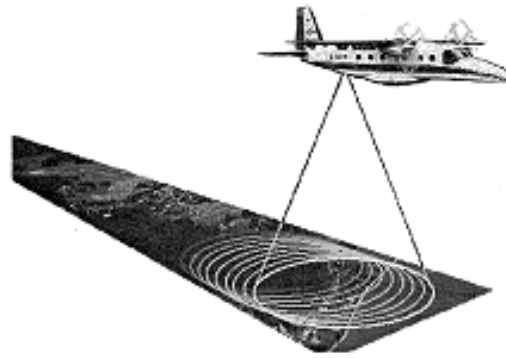


Figure 2.10: Progressing Palmer Scan (Wehr and Lohr, 1999)

Figure 2.11 shows an example of the image production using a scanner of the shore of Friedrichskoog, Germany. Figure 2.12 also shows that the visualization of the scene can also be improved by applying filtering, removal, classification and also a separation of the objects available in the data (Hug and Wehr, 1997). The research lists a few applications for ALS including, high accuracy and dense measurements for floods, open-pit mines, roads and modelling. In addition, Rapid Mapping and damage assessment post-natural disasters such as tornadoes, earthquakes and landslides are also encouraged.

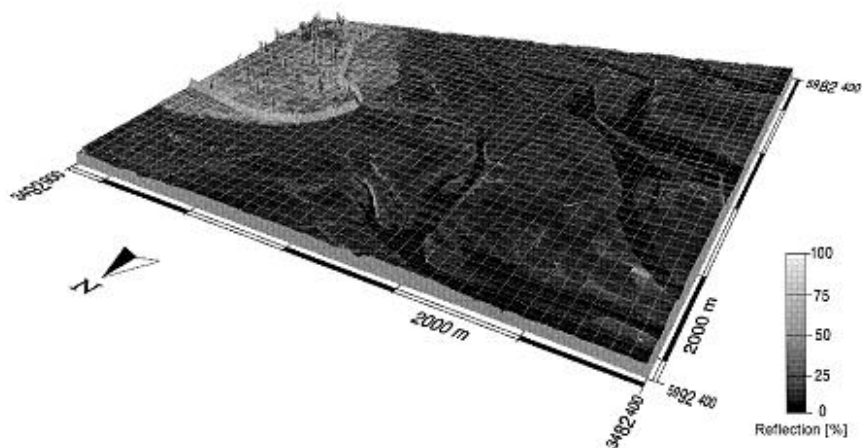


Figure 2.11: The shore and shallow of Friedrichskoog, Germany by ScarLARS laser scanner (Wehr and Lohr, 1999)

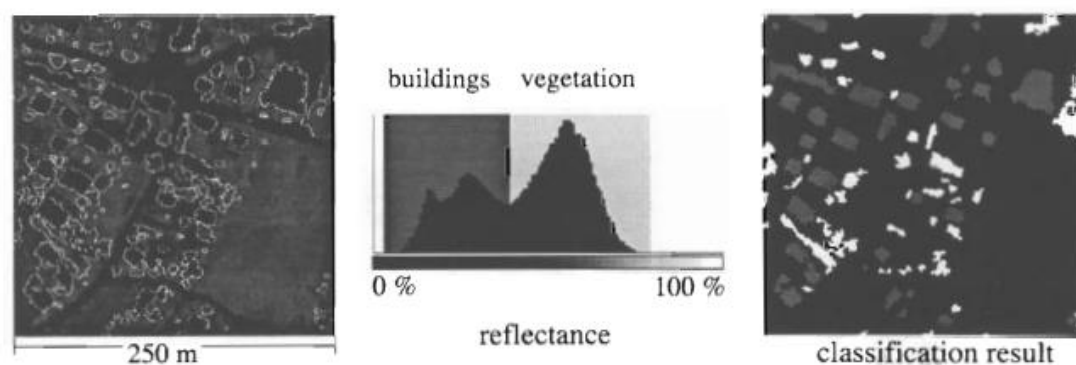
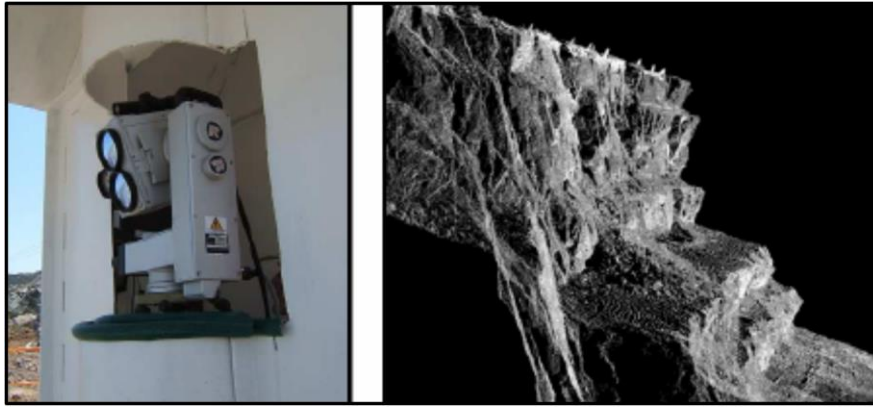


Figure 2.12: Object classification result (Hug and Wehr, 1997)

However, laser monitoring does have its limitations such as the range of monitoring is proportional to its signal power (higher range equals more power needed), ground radiation and also physical obstruction of the line-of-sight. Furthermore, all the readings are susceptible to noises but are toned down using post image processing programs.

Laser monitoring was employed in 2005 to monitor slope movements in Sandsloot and Zwartfontein South, South Africa by using two Riegl LPM-2K laser scanners (Little, 2005). These lasers are eye-safe, battery operated and require no levelling to operate as shown in Figure 2.13a. The exact x, y and z coordinates were programmed into Site Monitor software and acted as a ‘virtual prism’. An area of 2 km long and 100 m deep had been scanned with a 9-hour interval. The laser data was transmitted by radio to a computer in the survey office where it was used in slope movement analysis (Figure 2.13b). Although the laser monitoring system had advantages over using the theodolite and prism method, it required quite a substantial amount of resources to be maintained and the data interval gap between the readings was very large (9 hours), especially considering some rapid changes in climate condition may trigger a landslide in a short amount of time.



(a)

(b)

Figure 2.13: a) Laser Installation b) Laser Point Showing a Side View of the Pit Slope (Little, 2005).

Light detection and Ranging (LIDAR) are produced after the invention of lasers around the 1960s and was first used by the American National Centre for Atmospheric Research to measure the clouds. Since then, LIDAR also known as laser scanning has been known to map large areas of land to identify orientation and schematics of the surface of the Earth. LIDAR fires rapid pulses of laser light such as ultraviolet (UV) or Infrared (IR) at any surface (land, seafloor or riverbed) and when the light hits the target, the reflection from its intended target bounces back with the speed of light if the bounce calculated. The result is three-dimensional (3D) information of the intended target and its surface characteristics (Taylor-Smith, 2019). The instrument principally consists of a laser, a scanner and GPS receiver. Helicopters and Airplanes are the most commonly used platforms for LIDAR utilization (Figure 2.14). LIDAR system allows researchers to examine the surface of the Earth with accuracy, precision and flexibility. LIDAR assists in mapping shorelines, elevation models in the geographic information system, emergency response operation mapping and many other applications (NOAA, 2018).

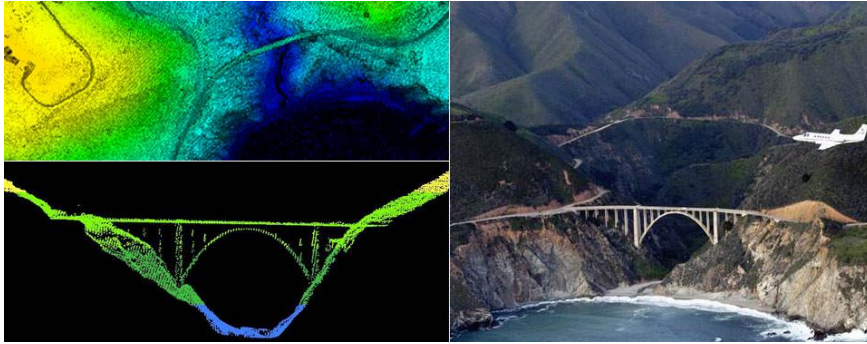


Figure 2.14: LIDAR data from Big Sur, California USA (NOAA, 2018)

Jamaludin and Hussein (2006) reported on the landslide hazard and risk assessment and mapping, mitigation measure and warning systems in Malaysia. According to Jamaluddin and Hussein, the development of slope assessment system in Malaysia has started in the early 1990s to anticipate landslide occurrences. Several parties are involved in this assessment including the Public Works Department (PWD), Department of Mineral and Geosciences (DMG) and Centre of Remote Sensing (MACRES). In 2004, the PWD Malaysia has issued a study of slope management system for the Tamparuli-Sandakan, Sabah, Malaysia roads. The study uses spatial data taken from a LIDAR system. The result is a typical risk map for the entire section of the road (Figure 2.15).

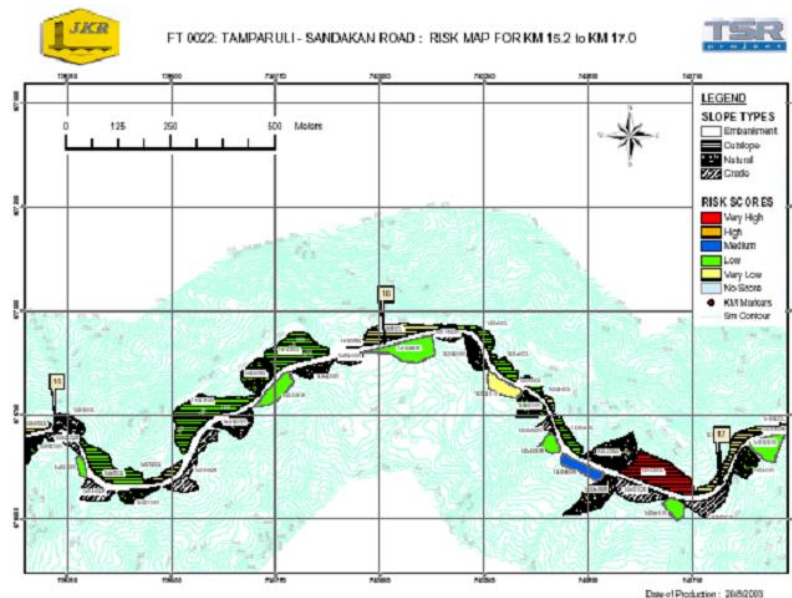


Figure 2.15: Risk map for TSR study (Jamaluddin and Hussein, 2006).

2.2.1.3 Global Positioning System (GPS)

The basic principle of GPS is to provide radio navigation, timing and positioning in air, sea and terrestrial area. These navigations are done by tracking the electromagnetic waves that are sending by satellite to the earth, thus the system can obtain the positioning of a target in terms of longitude, latitude and height as shown in Figure 2.16. Ever since 2000, GPS has become fully operational worldwide with the aid of at least four satellites operating in their orbits. As a result, GPS has evolved into numerous applications in the geotechnical world such as control points for remote sensing images, positioning of boreholes, environmental studies, and natural resources management (Gili et al., 2000). This system is also used in monitoring tasks and geological mapping.

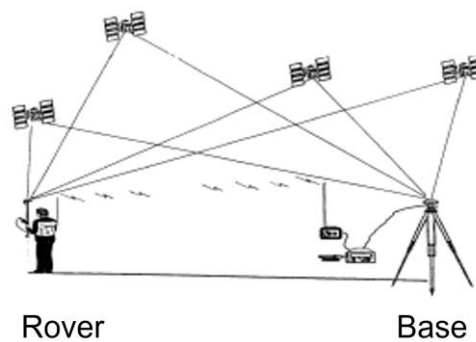


Figure 2.16: GPS Method of Measuring (Gili et al., 2000).

Gili et al. (2000) selected a test site in Vallcebre located in Barcelona, Spain to monitor ground displacements using GPS as shown in Figure 2.17. From July 1994 to February 1998, more than 30 points of observation was implemented in the site consisting of one survey per 2 months, approximately. All the surveys produced displacement graphs on X-Y axes that showed displacements in a range of 3 to 13 cm per month. They concluded that although the GPS system used for monitoring ground displacements have its flaws such as low number of satellite data, hindered data collection from physical obstruction, and quite low precision, but it is applicable without extensive training, the price of GPS receivers are affordable, and the technique benefits from cost to benefit ratio overlarge observational areas.

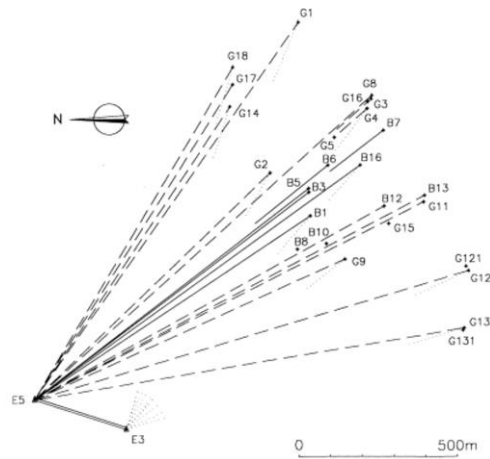


Figure 2.17: Vallcebre Landslide Monitoring Network Data (Gili et al., 2000).

Malet et al., (2002) monitored the Super-Sauze earthflow in Alpes-de-Haute-Provence, France using GPS monitoring system from March to October in 1999. Six dual-frequency Ashtech Z-XII receivers were utilized in their study with 2 reference and 4 remote stations distributed on the flow areas (Figure 2.18). Displacements of up to 0.2 cm per day were successfully detected by employing the GPS with an hourly temporal resolution, which was a significant improvement compared with classic surveying measurements.

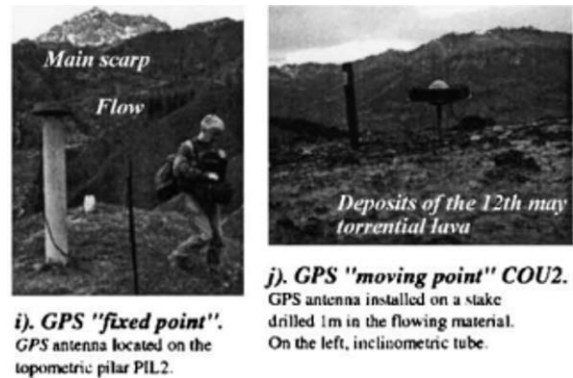


Figure 2.18: i) GPS Fixed Point ii) GPS Moving Point (Malet et al., 2002)

In a study conducted by Rizzo (2002), a network of 40 points of GPS monitoring system was setup to monitor the movement of flow-slide in Maratea, Italy for the period of June 1997 until March 2000 as shown in Figure 2.19. Rizzo (2002) also concluded that the GPS measuring system provides high precision data and is reliable in monitoring ground displacements.

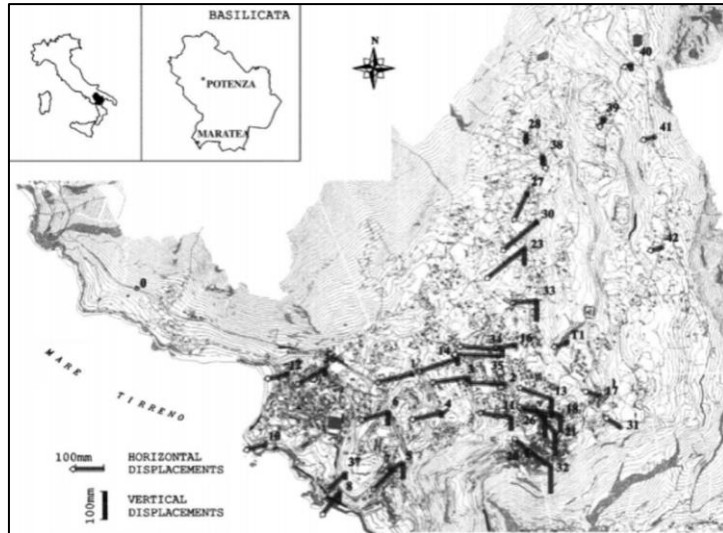


Figure 2.19: Displacement Obtained by GPS, Vectors Show the Movement of Flow Slide (Rizzo, 2002).

In the period of 3 months from November 2007 until January 2008, Bertacchini et al. (2009) did three periodic GPS survey of the Valoria Landslide in Italy made every two weeks. The research employs a double frequency GPS receiver (GMX902 Leica) with AX1202 Leica antenna covering up to 3.5 km long and 0.7 km wide area. The GPS utilizes 11 points of measurement on the landslide detecting movements as shown in Figure 2.20.

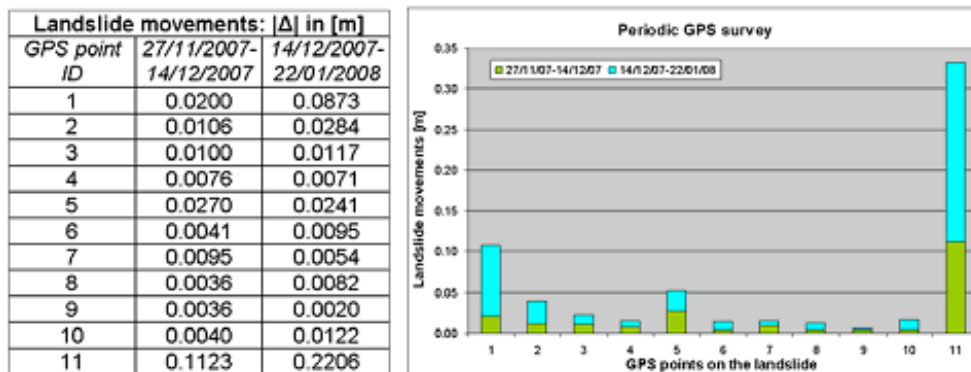


Figure 2.20: Periodic GPS survey result of Valoria Landslide (Bertacchini et al., 2009)

Herrera et al. (2009) reported in the year 2006 to 2007, a total of 93 points (a combination of rock block drawings and metal bars) including a few stable reference point was used in the Differential Global Positioning System (DGPS) data collection

in Portlet, Spain (Figure 2.4). The data was collected from May 2006 to July 2007. Total displacement of 62 cm was observed for 426 days (0.13 cm per day).

Fastellini et al. (2011) reported a monitoring activity on the Assisi landslide in Italy by the University of Perugia starting with 1995, utilizing a Global Positioning System (GPS) control network. The research mentioned the advantages of GPS monitoring, including reduced cost, a three-dimensional coordinate determination, free from operator human error, high accuracy (with good visibility), rapid execution and also is not affected by intervisibility between network points.

The GPS survey was done periodically (once a year) due to being suitable to measure a slow-motion rate of displacement (a few centimetres per year) and the object of just to understand the landslide dynamics, having an effective description of the field of movements and to propose proper mitigation plan to halt landslide progress.

The GPS erection was installed in a steel casing on a concrete base such as shown in Figure 2.21. The first setup was done in May 1995 consisting of 20 control points (6 known to be fixed reference points and 14 points scattered inside the landslide vicinity). The survey continued for 6 years (each survey per year) until 2002 when the surveying stopped due to lack of funds. However, in 2006 the project reinstated and an additional 16 points were introduced to get a better result and also substituting damaged points. Several GPS receivers including Trimble 4000 SSI and Topcon Legacy GGD are fitted with a number of antennas such as Trimble, Topcon Legacy and Leica RX1210T (Blume, 2014). All observations were done in static mode with 2 hours minimum session at 5 seconds per sampling.

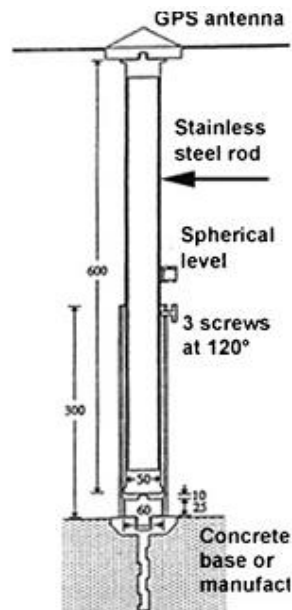


Figure 2.21: GPS setup on a stainless-steel rod on a fixed point (Fastellini et al., 2011)

Figure 2.22 and Figure 2.23 show the GPS displacement vectors for campaigns from 1995 to 2001 and 1995 to 2008 respectively. The estimated velocities are up to 1 centimetre per year for points with maximum displacements.

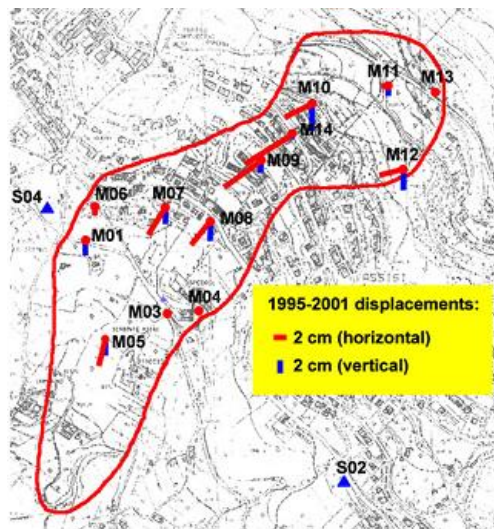


Figure 2.22: Displacement vector map of Assisi Town, Italy from 1995 to 2001 (Fastellini et al., 2011)

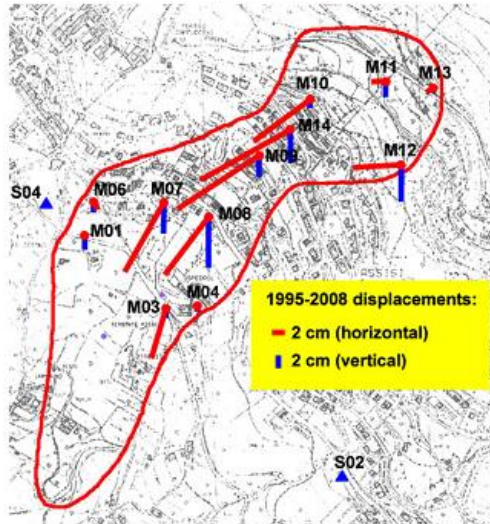


Figure 2.23: Displacement vector map of Assisi Town, Italy from 1995 to 2001 (Fastellini et al., 2011)

2.2.1.4 Synthetic Aperture Radar (SAR)

Synthetic Aperture Radar (SAR) is a remote sensing technique used to collect data all day and night through all weather conditions by satellite imagery. This technique employs continuous monitoring of the Earth's surface by data from remote sensing satellites such as European Remote Sensing (ERS) ERS1 and ERS2. An example of the SAR acquisition is shown in Figure 2.24 and Figure 2.25.

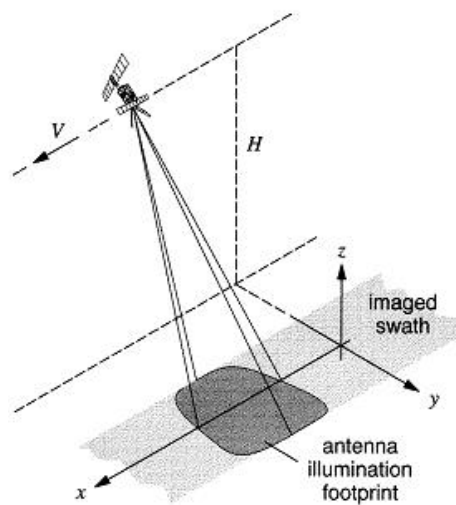


Figure 2.24: SAR imaging acquisition (Bamler and Hartl, 1998)

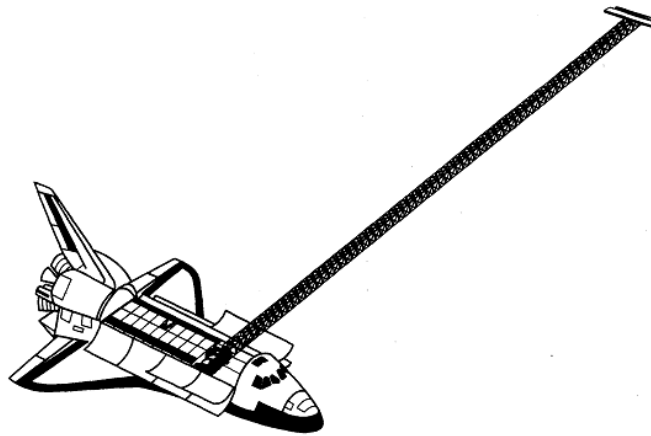


Figure 2.25: Shuttle radar Topography mission flight system configuration. Antennae reside in shuttle's cargo bay are extended on a 60 m long boom, 45 degrees from the horizontal mapping plane (Rosen et al., 1998)

Berardino et al. (2003) referred to Franceschetti and Lanari (1999) defining Differential Synthetic SAR interferometric as DiffSAR as a technique to measure ground movements over time. This was later renamed as Differential Interferometric Synthetic Aperture Radar (DInSAR) by Crosetto et al. (2013) defining it as a technique whereby it measures changes of characteristics of the surface imaging two SAR images at different times in the same area.

DiffSAR has been researched since the 1990s and is widely accepted to assess geological hazards (landslides, earthquakes, subsidence and volcanic activity) (Zebker et al., 1994; Achache et al., 1995; Carnec et al., 1996; Rosen, 1998). The basic concept of DiffSAR is the phase difference of two complex SAR images with the exact location in relation to topography and ground displacement having accurate readings in the range of centimetres (Bamler and Hartl, 1998).

Limitations of SAR technique are well known throughout the field experts. Noises from terrain reflectability and random fluctuation of the atmospheric refraction plague SAR techniques. In need of stable and isolated structures also affects SAR technique as decorrelation noises put a heavy toll on its accuracy. Berardino et al. (2002,2003) overcome decorrelation noise with utilizing phase unwrapping technique developed by Rosen et al. (1998) by performing temporal analysis of the deformation in DiffSAR, allowing sparse data to be processed and simultaneously reduce the

impact of atmospheric noise (Berardino, 2002, 2003; Franceschetti and Lanari 1999, 2018).

In 2003, Berardino et al. (2003) researched the Maratea Vally, Italy, spanning an area of 4 km². The whole valley is a tectonically active area, subjected to large complex gravitational phenomena and Sackung-type morphologies (Figure 2.26). Berardino et al. (2003) report that the first schematic mapping and modelling of the slope instability was proposed by Rizzo (1997, 2002). Early researches include obtained their data by using extensometers and crack gauges. In addition, Rizzo (1997) carried their research by using inclinometers. Between 1997 and 1999-2001, Rizzo (2002) produced GPS data of the Maratea Vally by utilizing 42 benchmarks scattered across the valley. The available data from previous researches are employed as a basis for comparison in the Berardino et al. (2003) research (Figure 2.27).

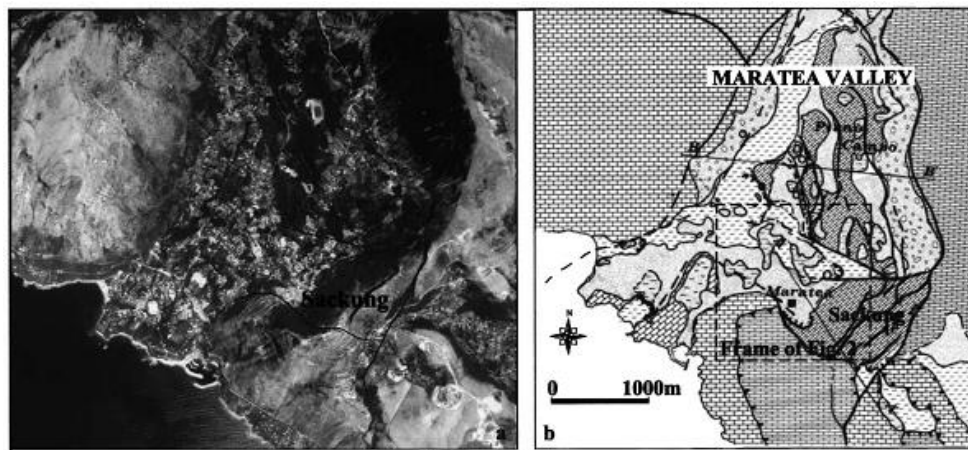


Figure 2.26: Maratea Valley geology highlighting Sackung morphology (Berardino et al., 2003)

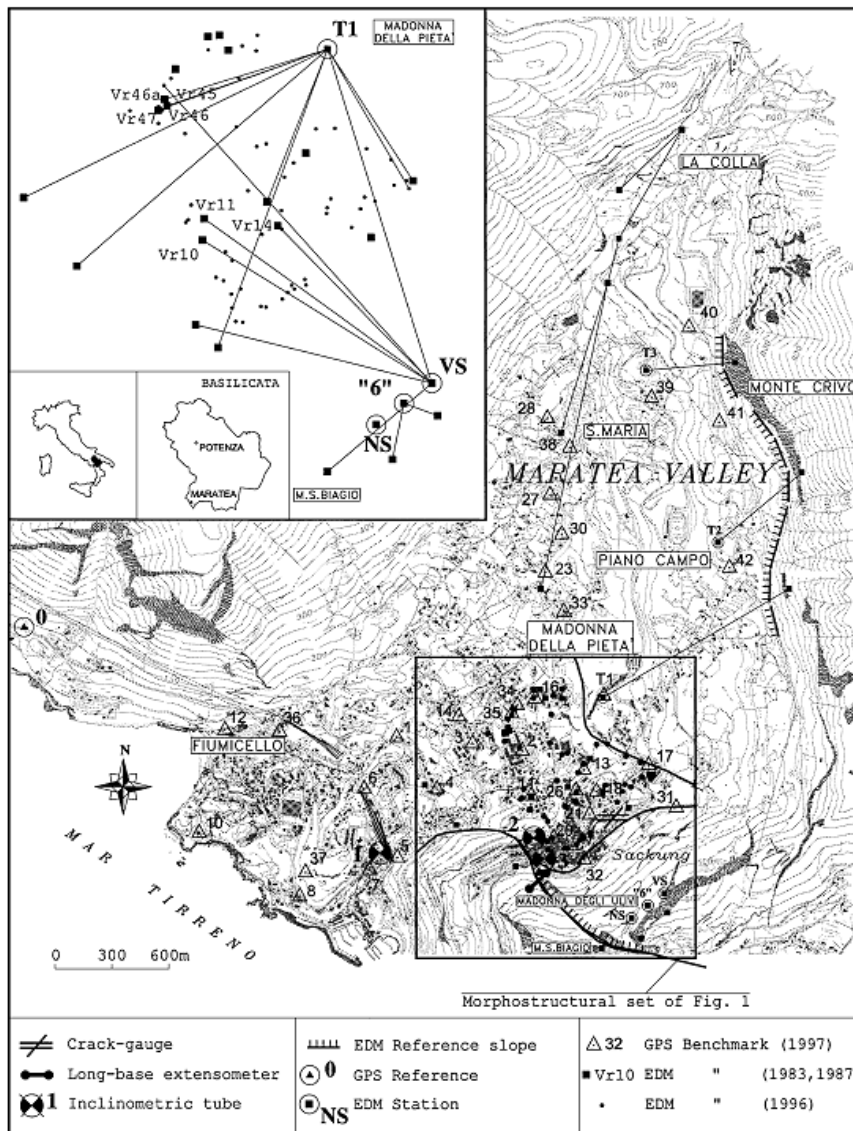


Figure 2.27: Available data from previous researches on Maratea Valley (Berardino et al., 2003)

Berardino et al. (2003) produced a displacement map from an interferometric pair provided by the Italian Istituto Geografico Militare (IGM) and orbit data by European Space Agency (ESA) by undergoing careful selection mapping of the interferometric pair, unwrapping algorithm from Rosen et al. (1998) and displacement value conversion. Berardino et al. (2003) displacement map were also modelled by the sum of true displacement value, atmospheric noise and topography noise. Figure 2.28 shows the combination of all obtained interferograms. A reference point outside of Maratea Valley that was known to be unaffected by the slope instability was used as a reference point to map the displacements.

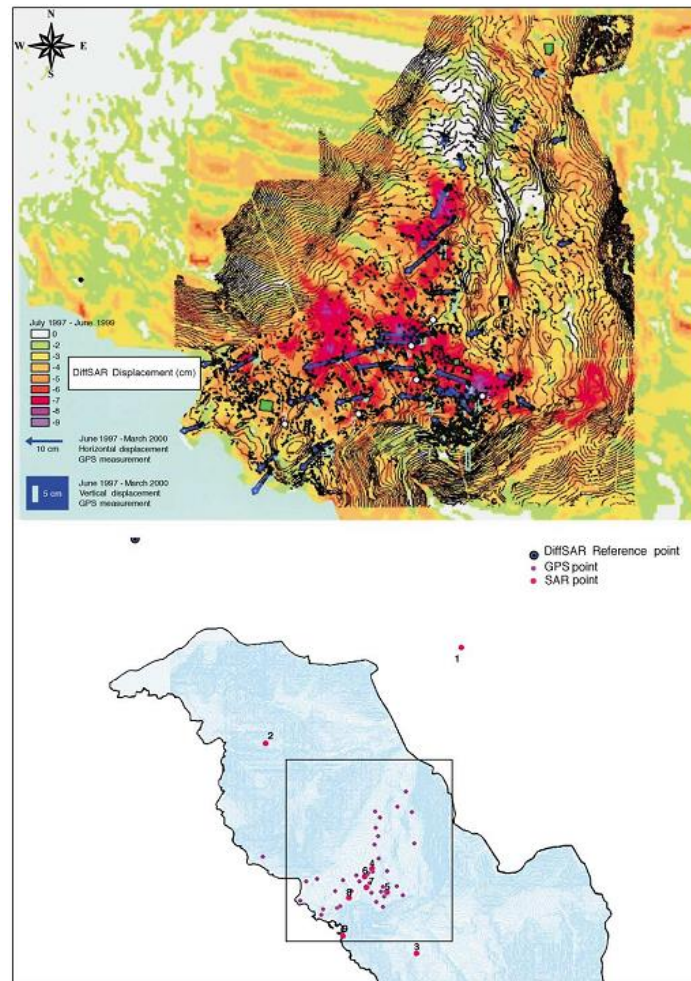


Figure 2.28: DiffSAR displacement map in comparison to GPS measurement and locations of reference points (Berardino et al., 2003)

Although some issues arose in comparing GPS measurements, including incoherence reference points and different time interval, the DiffSAR measurement was successfully corrected producing a difference in value smaller than 2.5 cm confirming that the DiffSAR distribution of displacement was consistent with the result of the GPS measurement. Berardino et al. (2003) reported the margin of difference is the result of the DiffSAR values are interpreted as an average displacement value over a rather large area compared to the GPS data of strictly referring to every single point. DiffSAR is not useful to measure the exact displacement of a particular area but only as to understand the overall kinematics of slope instability. Figure 2.29 shows the integration of DiffSAR and GPS data of Maratea Valley. Five regions of different kinematic were modelled: (1) low movement

0.5 cm per year, (2) intense movement 2-4 cm per year, (3) only horizontal movement 2-4 cm per year, (4) no movement but tectonic, (5) stable slope.



Figure 2.29: Map of instability modelled at Maratea Vally (Berardino et al., 2003)

Crosetto et al. (2013) applied DInSAR on the Vallcebre landslide in Barcelona, Spain. From Figure 2.30, with the additional marking of corner reflectors (CRs), proper monitoring of earth displacement was conducted in the duration of 7 months from December 2006 until July 2007. Displacements from 1 to 11.95 cm were analysed during the mentioned duration and the goal of the study, to derive deformation estimation from the interferometric phases of SAR imagery, was achieved (Figure 2.31).

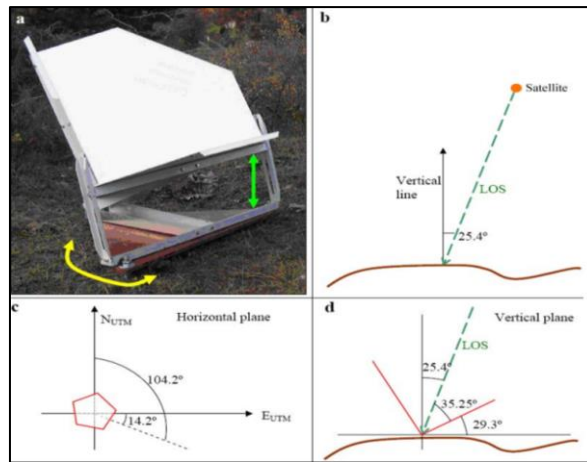


Figure 2.30: Geometry of CRs and the Application in DInSAR Technique (Crosetto et al., 2013)

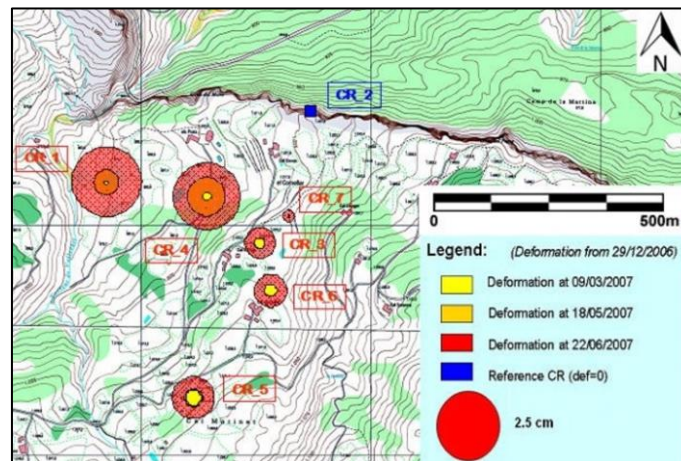


Figure 2.31: Map of Vellcebre and the Displacement Monitored (Crosetto et al., 2013)

Calo et al. (2014) studied on the Differential SAR interferometry (DInSAR) to measure landslides in Asisi, Italy (Figure 2.32). A very huge set of data set for the analyses were collected from April 1992 to Nov 2010 (ERS-1/2 and ENVISAT) and another set of December 2009 to Feb 2012 (COSMO-SkyMed (CSK)). An advanced DInSAR technique also known as Small Baseline Subset (SBAS) was utilized to produce a breakthrough of landslide area deformation time series, one of the first to produce deformation velocity map exceeding 18 years. Figure 2.33 shows that SBAS is a technique to limit noise effects, maximizing the number of points scatter in the image pairs by short temporal and spatial orbital separation (Berardino et al., 2002).

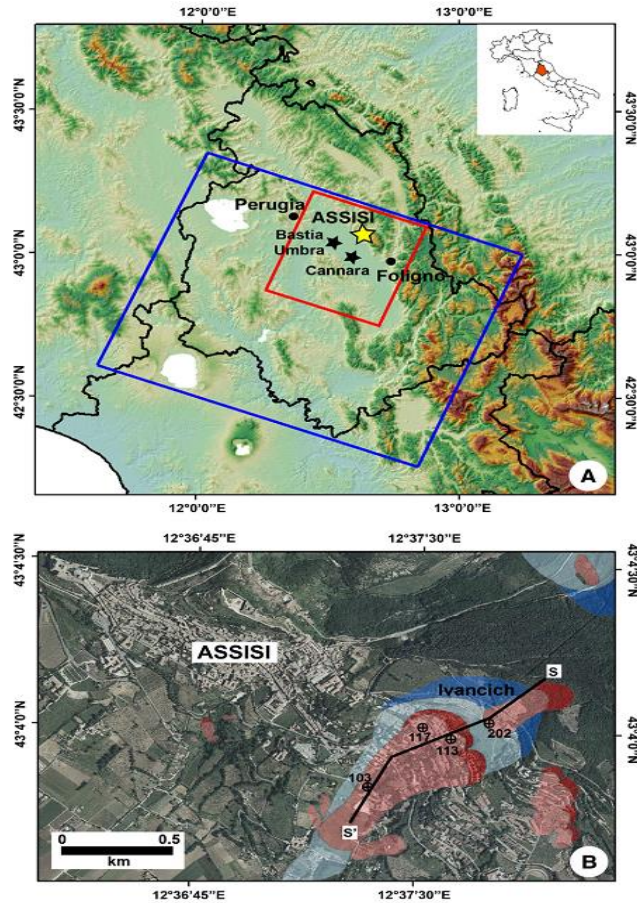


Figure 2.32: Location of study in Asisi, Italy. Blue shades indicate ancient landslide while red is the recently occurring landslide (Calo et al., 2014)

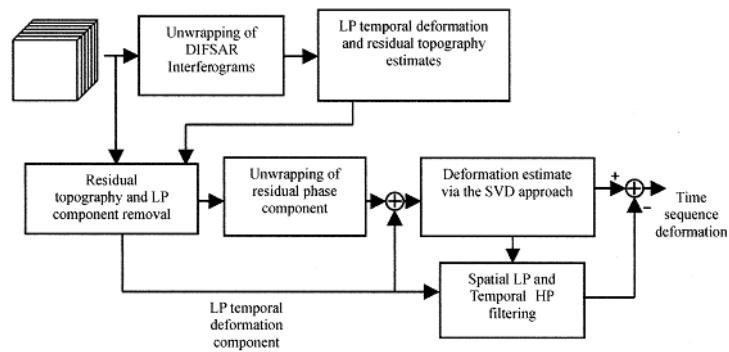


Figure 2.33: Diagram of SBAS implementation (Berardino et al., 2002)

The mean displacement velocity resulted from the Calo et al. (2014) research are shown in Figure 2.34. The research reported the difference of CSK dataset analysis with ERS-1/2 data sets in terms of density of coherence, CSK capturing 30,000 coherent points in comparison to 2000 coherent point by the ERS-1/2 seeing an

increase of 1500%. As seen in the figure, several patterns of deformations are unseen in Figure 2.34B as compared to Figure 2.34A. This clearly demonstrates the ability of CSK to offer a more effective remedial measurement that is limited previously.

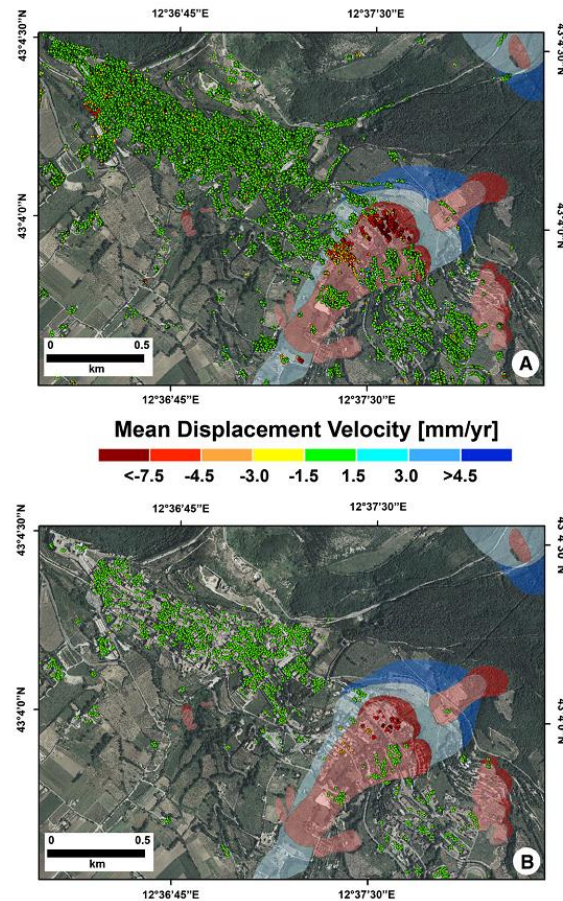


Figure 2.34: Deformation mean displacement velocity (A) December 2009 to February 2012 (B) April 1992 to November 2010 (Calo et al., 2014)

Calo et al. (2014) reported that long term characterization of landslides was quantified and unstable sectors prone to fail can be identified even though they underwent various deformation dynamics. By understanding long term kinematics of a given landslide occurrence, an improved understanding of the relationship of meteorological triggers, varied climate conditions and the movement of deep-seated landslides.

Jebur et al. (2014) conducted a study on detection of vertical slope movement in Gunung Pass, Malaysia landslide using an L-band InSAR technique. The data was collected from Phased Array type L-band Synthetic Aperture Radar (ALOS-

PALSAR), an active microwave sensor that is cloud-free and offers day-and-night observation (ALOS, 1997). The data collected was filtered and analysed, resulting in the measurement of the movements and thus recognition of the slope failure. A 3D advance processing of the image was done to calculate the volume of landslide afterwards as shown in Figure 2.35.

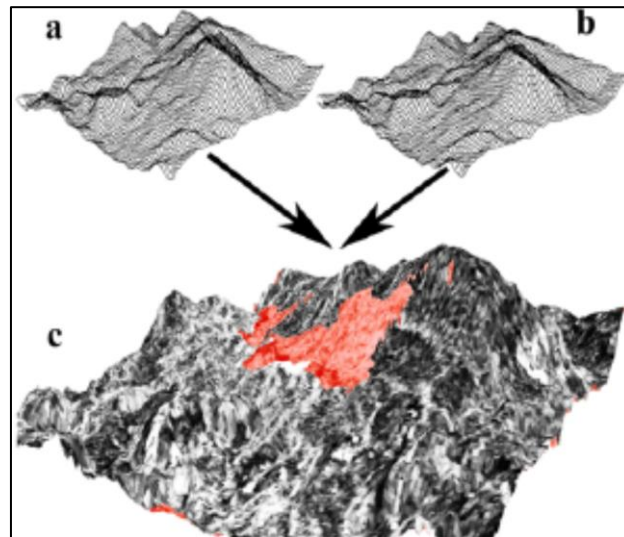


Figure 2.35: 3D View of Terrain a) Before Landslide b) After Landslide c) Both Terrain Fused for Landslide Detection (Jebur et al., 2014)

Based on the research outcomes, Jebur et al. (2014) concluded that the L-band of SAR data can be used in a densely vegetated tropical area to provide accurate results. However, getting the data from the high-resolution satellite images can be costly and time-consuming. In addition, bad weather can delay the data enquiry for the movement of slope in a specifically allocated time.

2.2.1.5 Ground Based Interferometric Synthetic Aperture Radar (GBInSAR)

An unstable slope situated in an on-going construction stage poses numerous problems to both the project and on-site workers, including accumulation of excavation debris of the sloping site and problems with installation of reinforcements of the structure (Bozzano et al., 2010). These problems can lead to slope failure and are needed to be monitored. In these situations, installation of geotechnical monitoring

equipment (inclinometers, strain gauges, crack meters, and GPS) and conventional geodetic techniques (theodolite and prism) may not be effective as they are affected by on-going construction work.

To overcome such problems, a Ground-based SAR interferometry (GBInSAR) can be employed whereby it follows the same principle of satellite SAR interferometry but the imaging is conducted by an antenna moving along a rail on the ground. Though the range of observations is limited compared to the satellite imaging, the GBInSAR has been developed for landslide monitoring purposes. This system features superior characteristics such as constructing an analysis of the site is only a few minutes, remote monitoring that does not require installation on-site, operability under any weather conditions and continued monitoring of the site. GBInSAR is currently being utilized for monitoring open-pit mines.

Tarchi et al. (2003) studied the GBInSAR application in the Tessina region of Italy from September to October 2000. The technical scheme of the GBInSAR is shown in Figure 2.36. Data was collected with an interval of 14 minutes. All in all, a total of approximately 400 imaging was produced and arranged in continuous sequence. Area of maximum displacements was then identified showing a movement of approximately 36 mm/h as shown in Figure 2.37. The landslide evolution was able to be measured showing a constant pattern of displacement over the imaging time span.

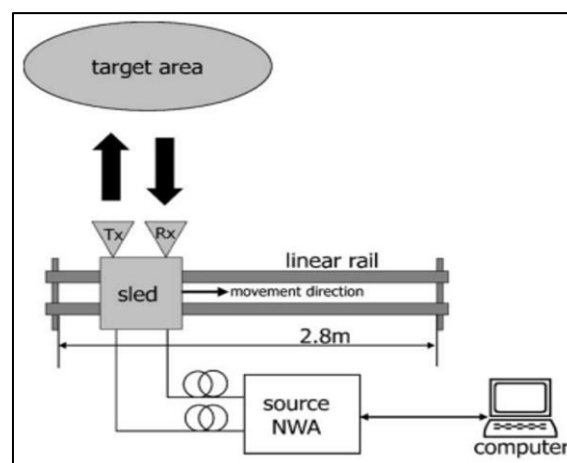


Figure 2.36: Technical Scheme for the GBInSAR System (Tarchi et al., 2003).

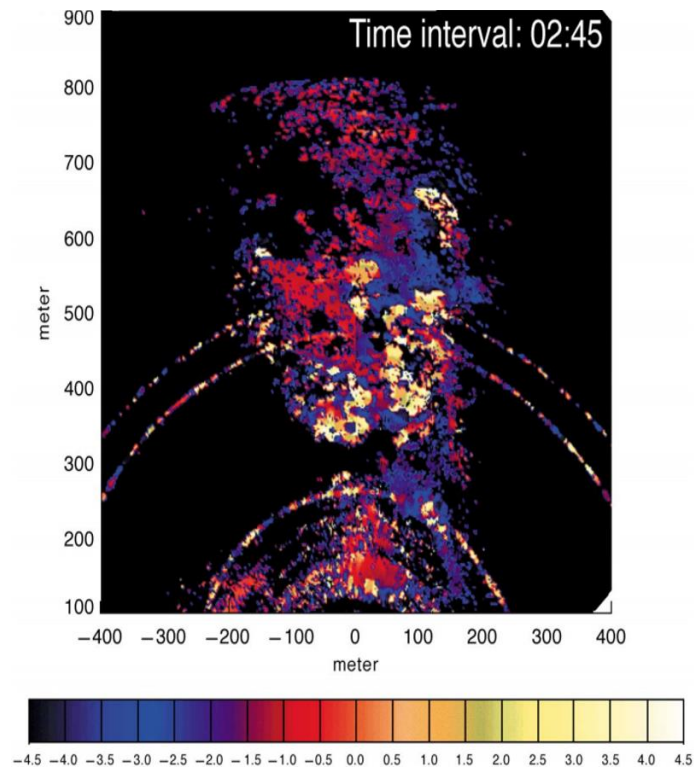


Figure 2.37: GBInSAR Analysis of the Tessina Landslide (Tarchi et al., 2003).

Pieraccini et al. (2003) studied the GBInSAR monitoring of the Valley of Arno River in Italy for 5 weeks from February 2001 until March 2001. Figure 2.38 shows continuous-Wave-Step-Frequency (CW-SF) radar that was used in the study (Pieraccini et al., 2001). Rainfall data were collected for the duration and a full scan of the site had been completed every 20 minutes. Pierrachini et al. (2003) mentioned that in comparison to a satellite sensor, GBInSAR has a much quicker and well described real-time images. Minimal human interaction was also noted and severe climate conditions were also not a problematic factor. Some disadvantages are also reported as GBInSAR needs a particular site condition such as the components monitored needed to be big enough to be detected along the GBInSAR's line of sight. Another significant difference is that the site covered by this method is rather small compared to a satellite's field of monitoring. Figure 2.39 shows the image example as viewed by the radar installation.

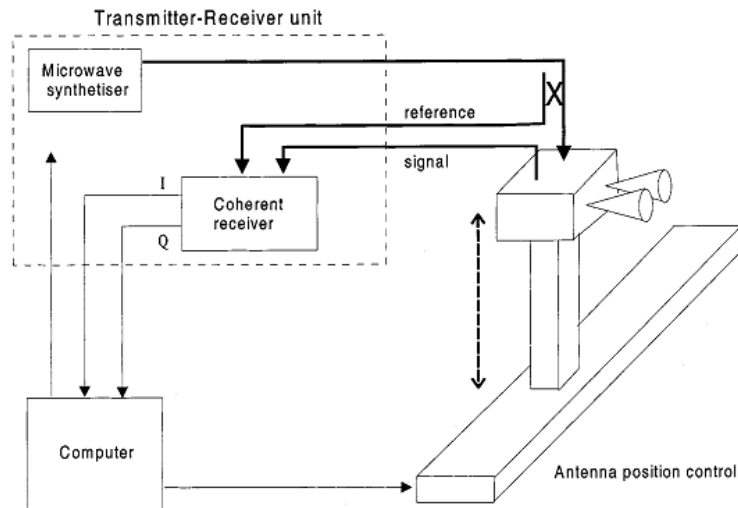


Figure 2.38: Operation scheme of the radar (Pierraccini et al., 2001)

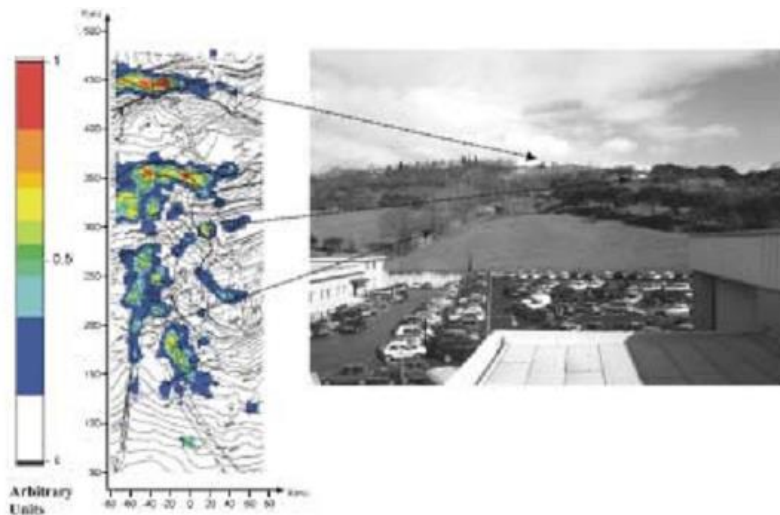


Figure 2.39: Photograph of the test site viewed by the radar installation (Pieraccini et al., 2003)

A map of displacement after 2 days of observation was produced based on the monitored displacement as shown in Figure 2.40. From Figure 2.41, it can be seen that the data was further enhanced with a Digital Elevation Model (DEM) to project a 3D display of the displacement. Point B and C are identified to be moving for 5.33 mm per hour and 3.96 km per hour respectively. The average movement of the site was recorded that revealed the motion of the landslide. Pierraccini et al. (2003) noted that the GBInSAR takes images in terms of minutes (long duration) thus are not capable of monitoring landslides during a collapse and saying that much faster instrumentation could probably be developed in the future.

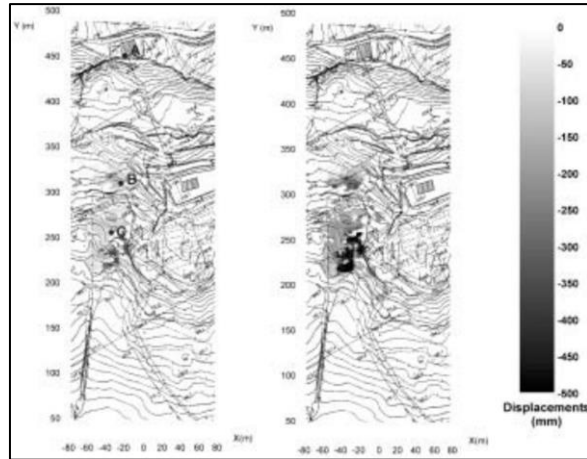


Figure 2.40: Cumulative Displacement Maps from 14 Hours of Monitoring until the 46th Hour. Displacements are Shaded Accordingly (Pieraccini et al., 2003).

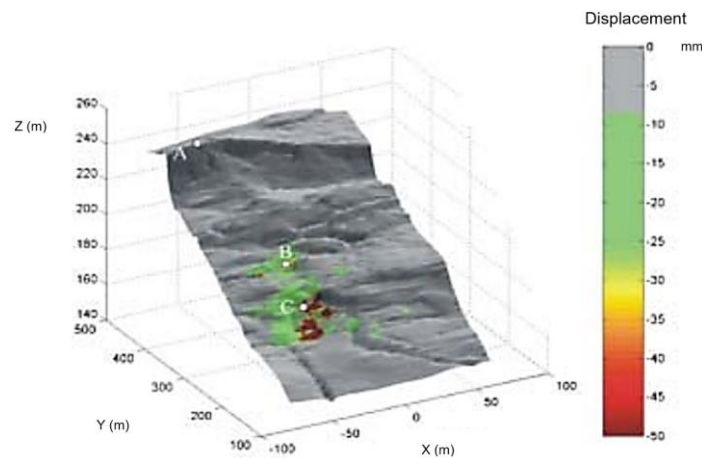


Figure 2.41: 3D Projected Displacement Monitoring of the Site (Pieracini et al., 2003).

Bozzano et al. (2010) reported that since 2007, 200,000 SAR images, 300,000 weather data, and 20,000 pictures have been collected in an unstable rock slope hosting a road construction in Italy as shown in Figure 2.42. Collected data has been analysed on a daily basis to measure the progression of the unsteady slope and displacement patterns are identified and recorded for future references. Bozzano et al. (2010) reported continuous monitoring of an earthflow interacting with a housing area and a pipeline, by a GBInSAR. As shown in Figure 2.43, displacements in a range from a few millimetres to 1 meter per day were measured. However, the effects were localized and the pipeline remained stable over the course of the 3 months of monitoring.



Figure 2.42: Monitoring System GBInSAR of the Site (Bozzano et al., 2010).

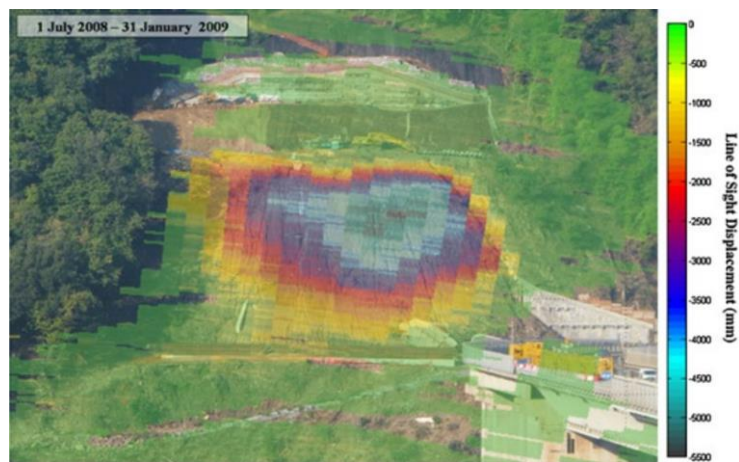


Figure 2.43: Displacement of Slope Overlain by the Line of Sight Map (Bozzano et al., 2010).

Herrera et al. (2009) studied the usage of Ground Based SAR (GB-SAR) technology to obtain data for field parameter that was later used to build a landslide prediction algorithm. The research focused on the Portlet landslide in Spain which was triggered by the construction of a big parking area on the toe of the slope. Datasets of 6 weeks from October 2006 to November 2006 are recorded once every hour. Over 1000 images were recorded and resulted in the total displacement measurements as shown in Figure 2.44. The value from GB-SAR was also validated using Differential Global Positioning System (DGPG) with 17 coherent pixels as a basis of comparison. As a result, a very close argument of datasets was founded with a maximum difference of 1.5 cm in one of the plots.

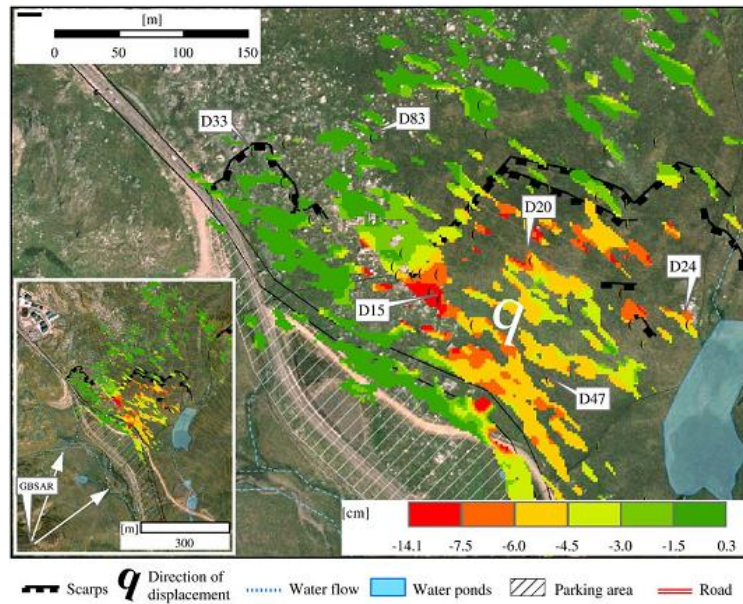


Figure 2.44: Total displacement measurements of GBSAR between the months of October to November 2006 (Herrera et al., 2009)

Herrera et al. (2009) pointed out that GB-SAR has several disadvantages that would hinder the monitoring including vegetated surface, absence of rock and rock blockage interfering with the pixilation analysis of the interferometry. In addition, noise originated from atmospheric propagation is a norm in the interpretation analysis.

2.2.1.6 Automated Robotic Station for Slope Monitoring

Bertacchini et al. (2009) integrate traditional geodetic instruments such as the automated total station to its more modern counterpart which is a satellite Global Positioning System (GPS) monitoring system. Some additional data from several geotechnical instrumentations including inclinometer and piezometer are also present. The case study was done in the Valoria Landslide, Italy ranging a span of about 1.6 km² for a period of 5 months from November 2007 to March 2008 (Figure 2.45). The landslide is well known for reactivation from time to time and causes major damages to roads and houses during 2001, 2005 and 2007. Reactivation was due to high cumulative precipitation from rainfall and snowfall recharging of groundwater in the slope (Borgatti et al., 2006; Ronchetti et al., 2007).

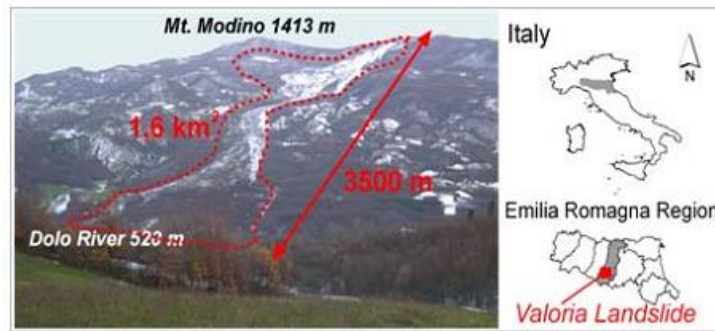


Figure 2.45: The map and view of Valoria Landslide, Italy (Bertacchini et al., 2009)

Bertacchini et al. (2009) performed landslide monitoring by measuring 45 points of prisms (39 points in the body of the landslide and 6 outside positioned on electric poles, houses etc. (Figure 2.46)) for the automated total station (TCA 2003) and 11 points of monitoring for the GPS. The system was designed to be self-sufficient to allow for continuous and near-real-time data processing. The power supply to the robotic station was supplied continuously by electric current and has a backup battery power in case of an outage that can last up to 2 hours while the GPS apparatus on the field was powered by solar panels (Figure 2.47). The data stream was transferred wirelessly to the master unit when the GNSS Spider software would create hourly and daily files for report purposes. An inclinometer was installed where the total station was located to measure the local displacement of the master GPS and total station. A special case of glass box was used to cover the total station for security purposes. The research assumed an allowable distortion to the values read by the total station due to the glass box but and justifies it to be neglected since the value is insignificantly small compared to the device's accuracy margin and the rather large displacement if the landslide.

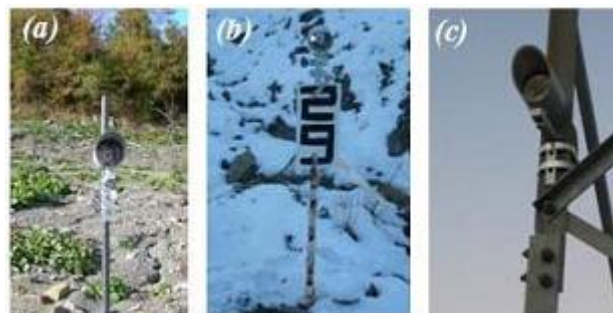


Figure 2.46: Reflectors of total station points (Bertacchini et al., 2009).



Figure 2.47: Solar powered GPS rover (Bertacchini et al., 2009)

The robotic station was superior to conventional inclinometer borehole system since the range of monitoring are millimetres to meters per day compared to the latter being decimated when displacement exceeds decimetres. The station was proved to be able to track slope movements and also produced a relationship between rainfall pattern and phases of the slope movement Figure 2.48. Figure 2.49 shows the result of the displacement during the 5 months of continuous monitoring. The most significant displacement happens in the autumn of 2007 where it is very wet at the time.

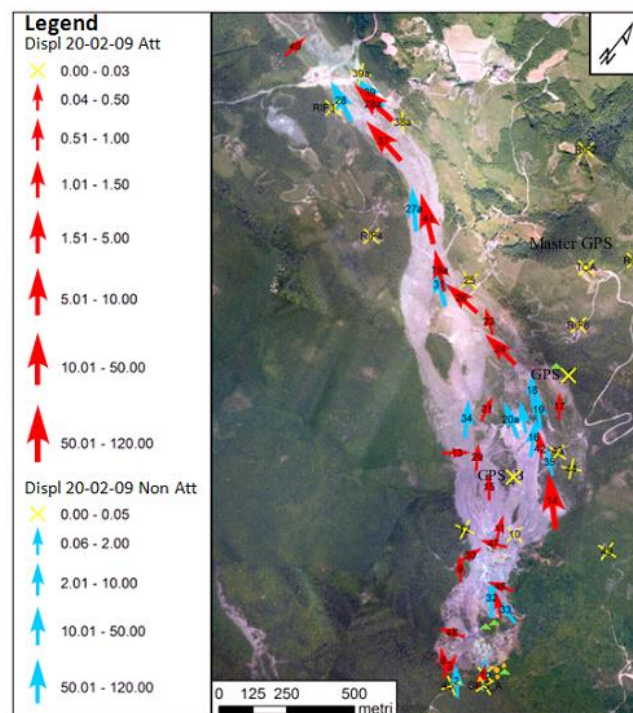


Figure 2.48: Displacements of slope movements (Bertacchini et al., 2009)

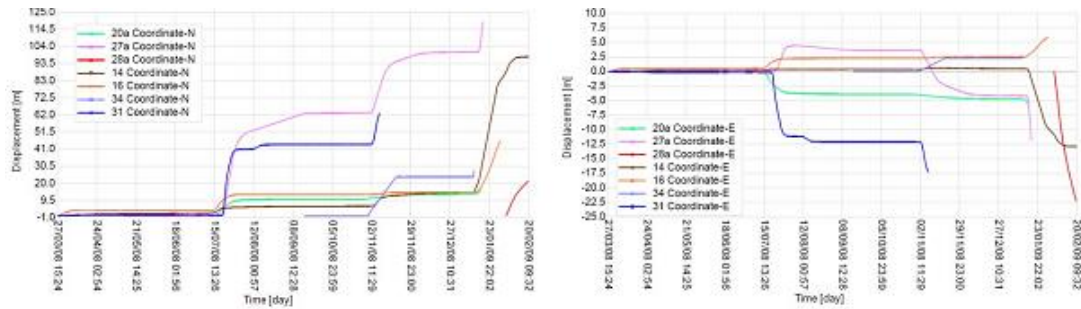


Figure 2.49: Landslide recording result of Total Station during continuous measurement (Bertacchini et al., 2009)

Bertacchini et al. (2009) recommend future systems to have automated procedures for data interpretation of a threshold risk limit to produce an alert system for the landslide. The system designed by Bertacchini was still not completely automated since the system needed an operator to download the data, analysing it remotely and notifying authorities if ever a possible risk of a landslide occurring.

2.2.2 Geotechnical Instrumentation Technique

2.2.2.1 Extensometer

Extensometers are used to measure relative movements between points with materials made up from steel tapes and wires, tensioned or untensioned steel rods, and fibreglass (Blair et al., 1997; Ding et al., 2000). Distances from a few centimetres up to 180 meters can be measured with a digital readout across a discontinuity, in a borehole, or alongside a crest that can be stored in an electronic data logger as shown in Figure 2.50. Blair et al. (1997) mentioned that deformation using boreholes in the geotechnical field is often referred to as multi-point borehole extensometer (MPBX). Any movements connected to extensometers are also quantifiable using unit displacement transducers. Extensometers are economical, effective in defining relative movement, and easily hooked to a data logger and alarm system.

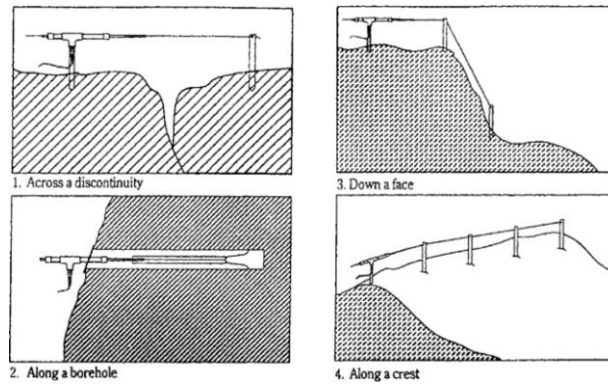


Figure 2.50: Typical Extensometer Applications (Ding et al., 2000).

Angeli et al. (2000) used extensometers in the monitoring of Tessina landslide in Italy. Two multiple based wire-extensometer units capable of measuring 280 and 390 m lengths were installed in the upper section of the landslide as shown in Figure 2.51. Displacements of up to 19 m were recorded and a graph correlating with the rainfall was plotted. The test showed that even when the site was going through climatic changes such as rainfall, fog, and snow, the observations could still continue. However, managing the apparatus which needs to be in a constant tension proves to be difficult, since the wire could snap and in this condition, the extensometer has to be reset to its initial setting. Intense movements have also taken its toll in the data transfer of the apparatus since the wire connected to the data logger could snap with the intense movement of the slide.

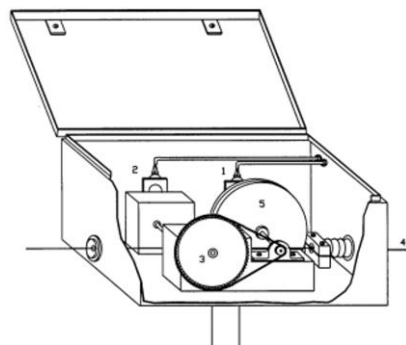


Figure 2.51: Layout of the Extensometer Device (Angeli et al., 2000).

Ding et al. (2000) studied the use of extensometer in a mining site in Western Australia to monitor the deformation of a sloping wall. Two 50 m boreholes were drilled into the wall and fitted with extensometers as shown in Figure 2.52. Readings were taken over a 5-day period and cyclic variations were obtained from the recorded

data. Later on, the monitoring extensometers were left at a place to record data for up to 4 years. It is shown that the extensometer is a robust device which could stand and monitor for a long period of time.

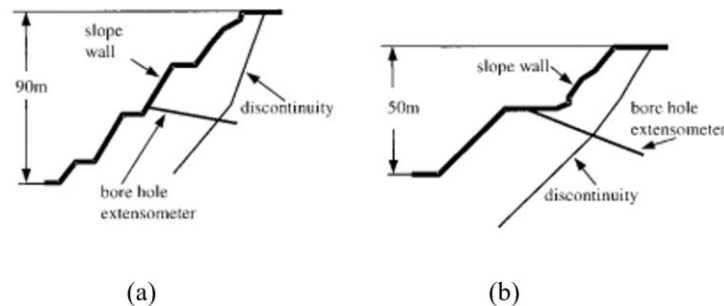


Figure 2.52: Two Boreholes with Extensometers Installed on Mine Slope (Ding et al., 2000).

Extensometers, in general, face a few problematic issues when applied on site (Blair et al., 1997). Issues such as heightened temperature would affect the accuracy of readings. The harsh environments of a particular site are also a limiting factor. Although modifications to an extensometer are indeed possible, the cost itself would cost a fortune.

2.2.2.2 Inclinometer/ Tiltmeter

Inclinometers are used to measure the lateral displacement of subsurface soil or rock. An electric probe is lowered into the near-vertical borehole and then pulled up while the inclination profile is recorded at certain intervals as shown in Figure 2.53. From these data, the profile of the borehole can be derived and reviewed (Ding et al., 2000). Boreholes of up to 200 m in depth can be measured using inclinometers. Commonly, inclinometers are lowered into a borehole into the stable ground to determine displacement and can be installed permanently to log data, indefinitely. In this setup, the inclinometer acts as a tiltmeter. Servo accelerometers are usually used as a sensor in the inclinometer. An accuracy of about 6 mm per 25 m casing could be achieved.

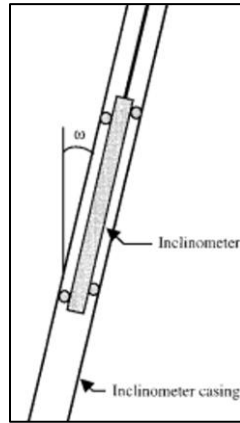


Figure 2.53: Basic Principal of Inclinometers (Ding et al., 2000).

Fastellini et al. (2011) wrote about the use of inclinometers, piezometers and total stations in Assisi Town, Italy during the 1970s until 1980s to monitor a known slope (of about 21% inclination) movement which damages local foundation (buildings, retaining wall, pipelines and street pavements). Figure 2.54 shows the estimated border of the landslide. Unfortunately, during the end of 1980s, the measuring activities were halted due to excessive cost and having to take difficult surveying in an urban area.

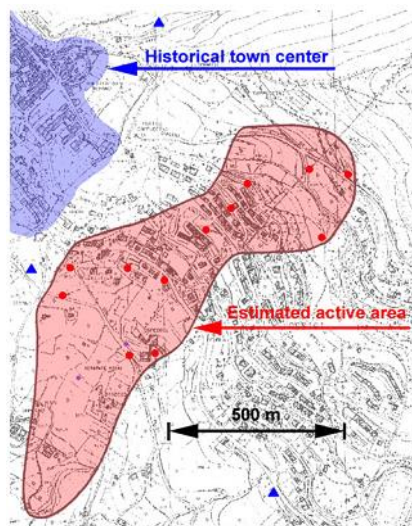


Figure 2.54: Estimated border of the landslide obtained from a geological - geotechnical point of view (Fastellini et al., 2011)

Ding et al. (2000) reported the application of inclinometers in open pit mines in Australia for pit deformation measurements. Tiltmeters are usually used to measure rotational deformation at a specific location of a sloping wall. An electronic tiltmeter

can measure 1.74 to 0.01 micro radians. However, due to the high cost of these instruments, they are not widely used in the field (Ding et al., 2000).

Herrera et al. (2009) indicated that in the Portalet landslide occurring in Spain between May to October of 2005, six boreholes were dug and later installed with inclinometers to measure slope surface depth (Figure 2.4). It was recorded that the sloped surface was identified to be around 7 to 16 metres in depth with displacements up to 80 mm in the space of 74 days (1 mm per day) as shown in Figure 2.55.

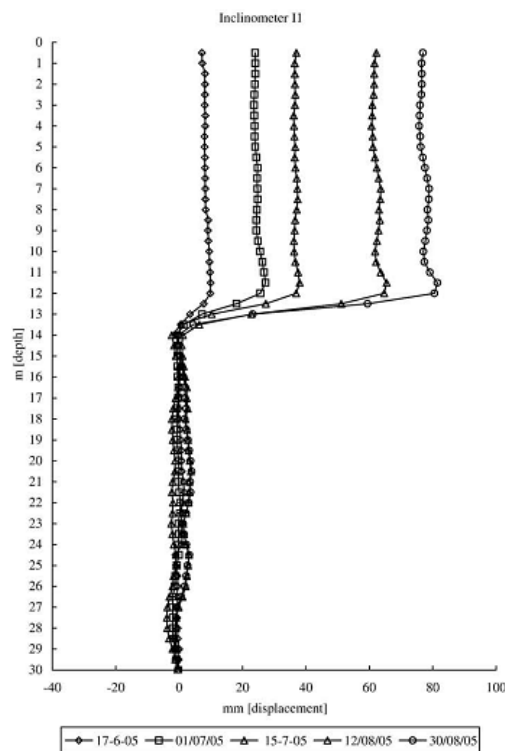


Figure 2.55: Inclinometer readings for the Portalet landslide, Italy from June 2005 until August 2005 (Herrera et al., 2009)

In the year 2014, Calo et al. (2014) presented inclinometer measurements of 4 points by a known active landslide in Assisi, Italy. The readings monitored the active landslide for a period of 10 years between 1998 and 2008 revealing that the shear zone separating the stable bedrock from the landslide material is relatively thin of about 2 meters as shown in Figure 2.56.

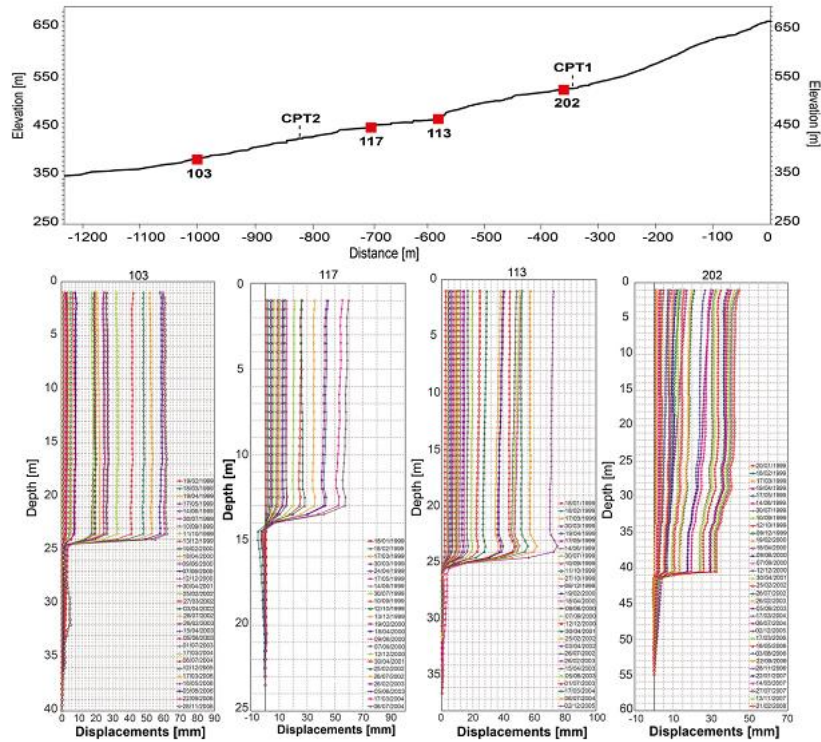


Figure 2.56: Inclinerometer readings of 4 points in Asisi landslide (Calo et al., 2014)

2.2.2.3 Piezometers

Piezometers are used to monitor groundwater levels as well as the pore-water pressure in the ground. Piezometers are commonly used for groundwater level and pressure measurement of most pit mines in Western Australia (Ding et al., 2000). However, they cannot measure immense pressure as the tube needs to be significantly extended in a vertical direction in order for it to measure high pressure. Little (2005) reported the use of piezometers to measure the groundwater flow in open pit mining in Sandloot, South Africa. In correlation to rainfall gauges, the piezometers were checked weekly for groundwater measurements.

Previous researches reported the usage of piezometer in correlation with a combination of other geotechnical instrumentation for supporting data (Angeli et al., 2000; Bertacchini et al., 2009; Fastellini et al., 2011).

2.2.2.4 Intelligent System for Slope Monitoring

Ding et al. (2000) proposed an intelligent system for slope monitoring using a combination of electronic sensors including extensometers, inclinometers, tiltmeters, piezometers, and temperature and humidity meters as shown in Figure 2.57. The system will be connected to a self-sufficient data logger which has a self-contained power-supply system and an alarm system for warning purposes. The system was tested in the Western Australian mining site for about 4 years. The system was able to measure the significant movement of the slope throughout the overall duration of the study, proved by detection of a significant movement of slope in the mid-1994. Among the advantages of this system is sustaining with little human involvement, working continuously for 24 hours a day under all weather conditions, and providing a reliable alarm control program. Other than that, the data is easily managed, since the system combines all the data in an extensive complete dataset.

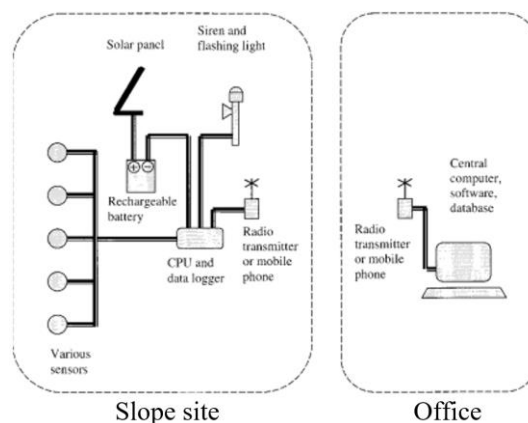


Figure 2.57: Diagram of Intelligent Monitoring System (Ding et al., 2000).

Intrieri et al. (2012) documented a design on early warning system to detect the Torgiovanetto landslide on the slope on Mount Subasio, Italy as shown in Figure 2.58. Intrieri et al. (2012) defined the early warning system (EWSs) as a risk mitigation tool, hindering especially people from dangerous areas of expected slope failure. Key points in a successful EWS are mentioned such as the identification of the elements of risk, hazards, vulnerability, lead time and residual risks (Medina-Cetina and Nadim, 2008).

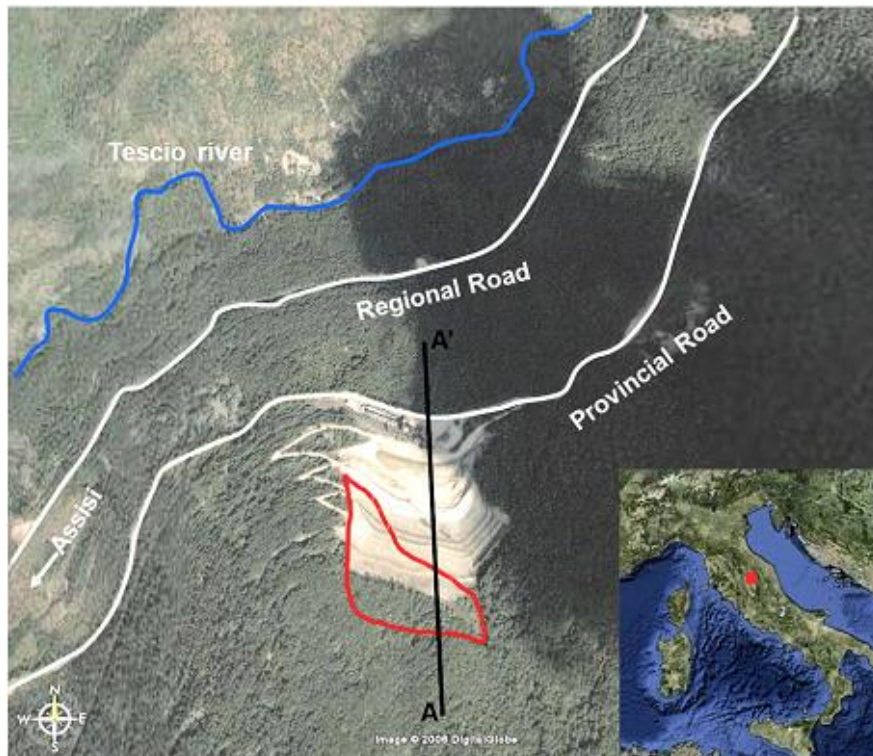


Figure 2.58: The Torgiovanetto landslide localization (Intrieri et al., 2012)

By indicating that the pinnacle of instability was the open fractures bounding unstable mass, the wire extensometer was selected as the prime sensor namely because of the ease of installation and employment, low vulnerability and high velocity. Designed to be wireless, but due to proven interference from strong obstacles, some of the systems are cable connected. The research conducted by Intrieri et al. (2012) presented data from July 2007 until January 2011 opting 12 extensometers, a thermometer, rain gauge station and also were equipped with video surveillance for visual confirmation of failure as shown in Figure 2.59. The network was also complemented with radio processors, transducers, analogue-digital converter, data logger, a gateway (to transmit via General Packet Radio Service (GPRS)) and powered by solar cells. Data acquisition is done every 60 seconds but transmitted to the data logger every 5 minutes in order to save energy.

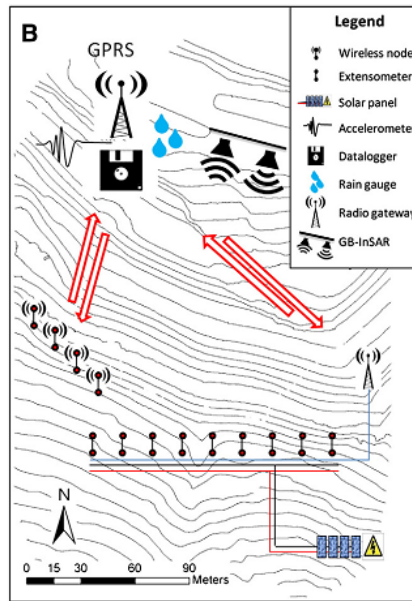


Figure 2.59: Schematic view of the monitoring system of the Torgiovanetto landslide (Intrieri et al., 2012)

Figure 2.60 shows the displacement versus time for 5 years that consist of extensometer reading and also rainfall collection. The highest movement recorded was on April 2008 (2.77 mm per day). From observation trends, the landslide was quite active from November to May and remains stable during the dry periods. Figure 2.61 provides a visual interpretation of the tension cracks monitored.

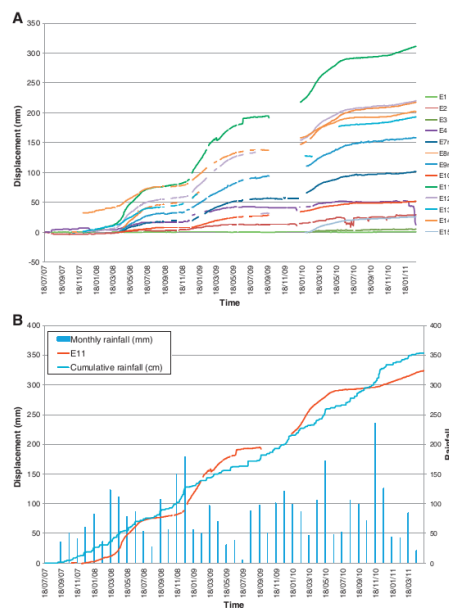


Figure 2.60: Displacement data from extensometer with cumulative rainfall data collection (Intrieri et al., 2012)

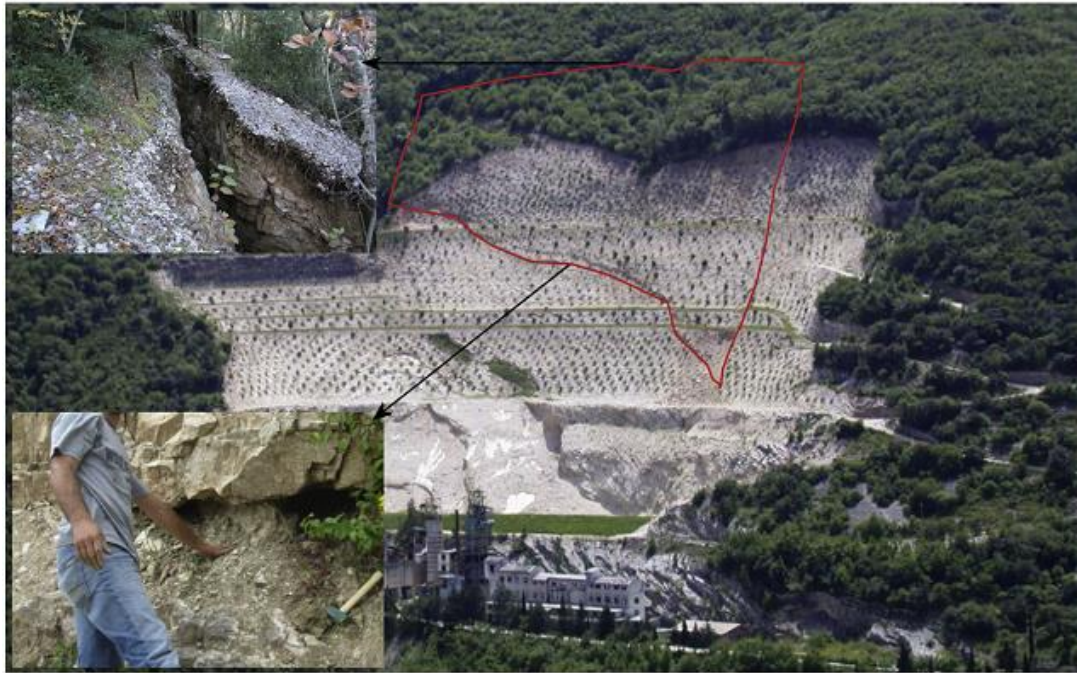


Figure 2.61: The photograph of Torgiovannetto landslide detail on sliding surfaces and tension cracks (Intrieri et al., 2012)

The warning system was designed to have 3 distinct warning labels as described in Figure 2.62. Intrieri et al. (2012) reported that a key issue to consider was that the landslide is expected to show an accelerating trend a few days before failure allowing safety interventions to take place. The velocity threshold value was set at 0.5 mm per day and 1.0 mm per day dependent on the respective displacement sensitivity recorded by the instrument such as shown in Figure 2.63. The velocity was checked manually daily while an automated check is executed every 8 hours. Whenever two or more sensors exceed their threshold, a notification would be sent to an operator pending confirmation. After confirmation, the operator would inform the monitoring team to raise the warning levels and subsequently proceed with the necessary response. During the whole 5 years of monitoring, only once was the warning level raised and it lasted for about a day only because of a heavy downpour. Apart from that, the system registered no worrying behaviour.

Warning level	Trigger	Definition	Response
Ordinary level	Default level	Normal activity encompassing, to some degree, seasonal variations	Data are checked daily. Monthly monitoring bulletin
Attention level	When 2 or more extensometers exceed their own velocity thresholds	Increased activity possibility due to prolonged rainfalls. Potentially dangerous	Data are checked more frequently. Daily monitoring bulletin. H24 personnel from each stakeholder are alerted. Preparing for alarm
Alarm level	Based on expert judgement and on the use of forecasting methods	Accelerating trend far beyond any seasonal fluctuation. Collapse is expected	Data are checked even more frequently. Two monitoring bulletins per day. The Provincial Street is closed

Figure 2.62: Warning criteria of EWSs for Torgiovannetto landslide (Intrieri et al., 2012)

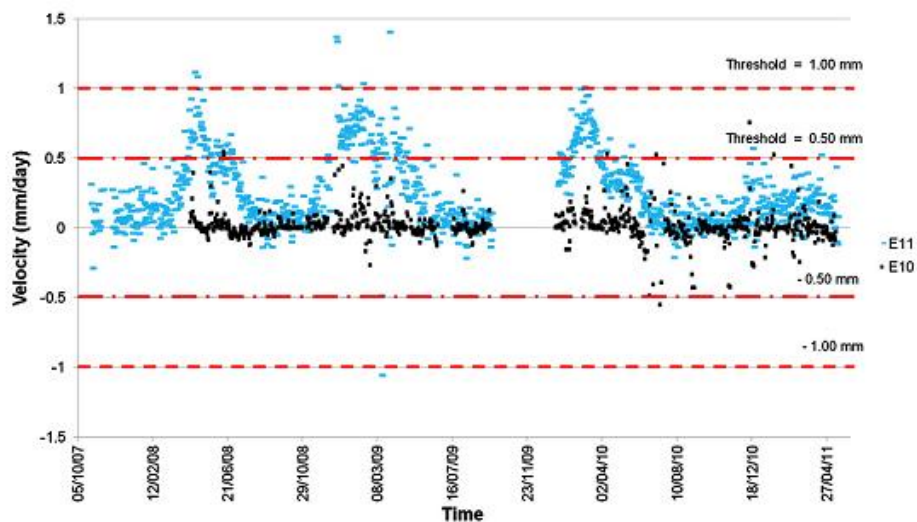


Figure 2.63: Velocity vs. time for 2 sets of extensometers with the threshold value (Intrieri et al., 2012)

The importance of reliable threshold setting, being careful not to produce false alarms as it would upset the integrity of the warning system (Lacasse and Nadim, 2009; Intrieri et al., 2012) Furthermore, the EWSs was programmed to have adjustable threshold values and adhere to background noise level (due to surrounding actions) to maintain a level of reliability. The maintenance of the system was also deemed important since an operator would have an assignment to maintain the order of the system from time to time.

2.2.2.5 Acoustic Emission Monitoring of Soil Slope

Dixon et al. (2014) studied on the need for an early continues real-time monitoring system to detect the risk of soil instability and proposed an approach by using acoustic emission (AE) monitoring and comparing its performance with conventional inclinometer data. Materials undergoing deformations generate AE from inter-particle friction that can be measured using transducer and an ALARMS acoustic sensor encased in a steel tube in the ground as shown in Figure 2.64. This concept is being used to monitor landslides displacements at North Yorkshire, UK since 2013 where the results are compared to a standard inclinometer measurement. Based on the comparison, they concluded that there is a direct relationship between AE and ground displacements. A relationship was developed for AE rate vs. time indicating that the device can provide continues real-time information on subsurface ground deformations as shown in Figure 2.65.

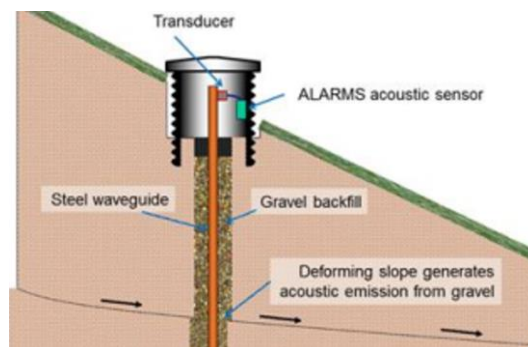


Figure 2.64: Schematic of AE Detection on Slope (Dixon et al., 2014).

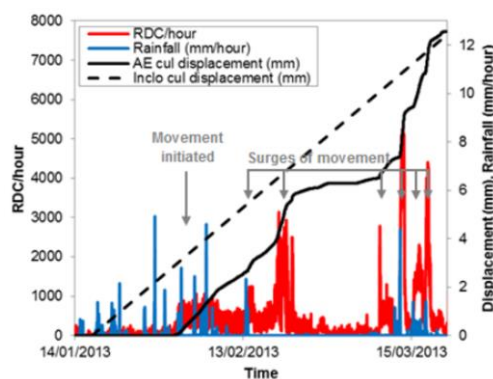


Figure 2.65: RDC Rate, Rainfall and Displacement vs Time Behavior in Early 2013 (Dixon et al., 2014).

2.3 Automated Wireless Accelerometer Monitoring System (AWAM)

Automatic Wireless Accelerometer Monitoring System (AWAM) is a new product proposed in this study for slope monitoring. The system is intended for monitoring the deformation automatically by using an accelerometer and requires minimal human input to function after initial setup.

The accelerometer is a device that measures proper acceleration with embedded electromechanical devices. As an example, an accelerometer in free fall will be subjected to the earth's gravity acceleration and will measure zero whilst when at rest would measure an acceleration $g = 9.81 \text{ m/s}^2$. The concept of the accelerometer is shown in Figure 2.66.

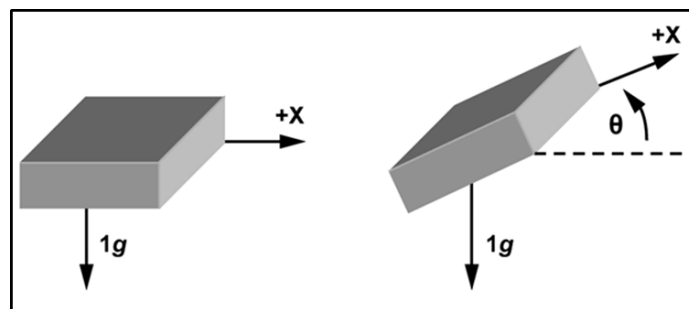


Figure 2.66: Concept of the accelerometer in X-axis

Consequently, this device can be used to provide the required data by measuring the motion, vibration, and speed of any movement in the slope body. The accelerometer would collect attributes such as time and acceleration along the x , y and z -axis. Figure 2.67 and Figure 2.68 shows the data collection apparatus and results obtained by the accelerometer conducted by previous researches (Ravi et al., 2005). The sensors can obtain readings although there are obstacles and climate conditions occurring. Transfer information/data by using this device are wireless and the power supply is generating from the solar energy. The cost of this device is also cheaper than the existing device in the market.

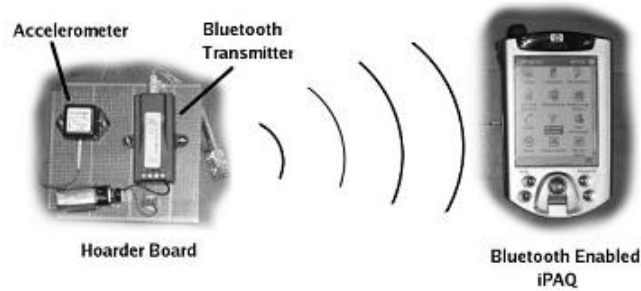


Figure 2.67: Data collection by the accelerometer in place (Ravi et al., 2005)

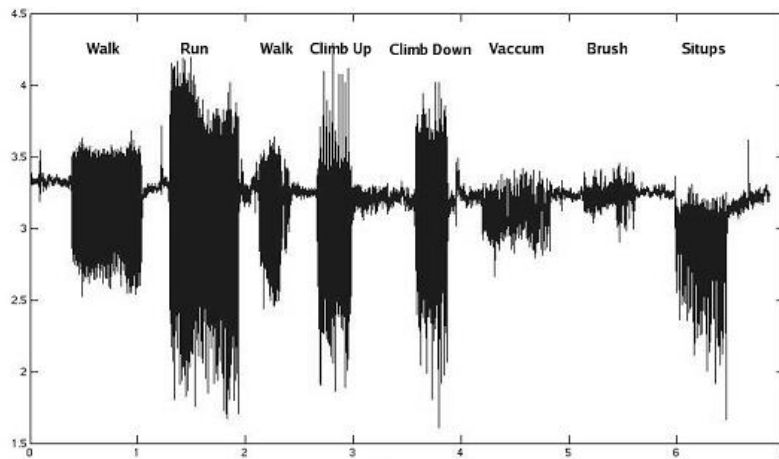


Figure 2.68: X-axis readings from accelerometers on different movement criteria (Ravi et al., 2005)

The range of monitoring between the sensors and the receiver of the device are within a few kilometres (depending on wiring lengths) and allows monitoring of each type of movements that affects the slope. Data from the receiver will be synchronized with a cloud server and simultaneously would be analysed by using software that has been designed to suit the function of this device. Wireless LAN (WLAN) and mobile communications (GSM / GPRS / UMTS Network) is a communication tool for data streaming between measuring receiver and the data acquisition software. The analysed data can be monitored directly through means of a mobile communication apparatus (Figure 2.69).



Figure 2.69: Diagram Process of AWAM System

Data acquisition and analysis software are including data management, analysis, and alarm systems. Data interpretations can be accessed directly via mobile devices including personal computer or laptop, and smartphones. These mobile devices are used to receive the required data from the monitoring system through any communication provider and allow the data acquisition and analysis software to work with the mobile device like an alarm system. The software is very important in the monitoring system for acquiring data from an accelerometer, a means of calculating threshold measurements and recording the results. Should the threshold value exceed its limitations, any person subscribed would be entitled to a critical signal failure (the limit deformation before failure).

With this system, it is expected that the critical slope monitoring can be operable with the price offered is lower than the existing tools with improved energy efficiency. The transmission and acquisition of more data would also be more accurate and faster.

2.4 Particle Image Velocimetry (PIV)

Soil deformation is the epitome of the safety design and analysis of slopes, piles and foundations in geotechnical engineering. While conventional measuring techniques are only able to display soil settlement on the ground surface, further developments in laboratory modelling and deformation measurement in geotechnical engineering have provided researchers more success in obtaining additional details on soil deformation. Particle Image Velocimetry (PIV) is a technique that uses processed digital images to determine field displacements.

In this section, an introduction to the PIV analysis method used by White (2002) was conveyed through literature studies. Along the years, PIV technique has undergone several modifications and presented with many designations such as block-matching (Michalowski and Shi, 2002) and Digital Image Correlation (DIC) (Liu and Iskander, 2004, Yan et al., 2018, Khatami, Deng and Jaksa, 2019).

2.4.1 Principles of PIV

PIV originated from the fluid and gas mechanics field for speed measuring back in 1991 (Adrian, 1991). It was White that established a modified approach of PIV for it to be used in the geotechnical field, gaining popularity in establishing geotechnical modelling. While fluid models needed seeded particles to create texture, in the geotechnical field natural sand has its own distinct texture while clay surface can be textured with dyed sand or ‘flock’ material. Since then, PIV has gained immense reputation for its time-saving technique and used to observe soil displacement during pile installation (White et al., 2003, Ni et al., 2010), seasonal moisture cycle in clay slope (Take, 2003), loading of circular and square footings in transparent soil (Iskander et al., 2002, Ganiyu, 2016) and reinforce and without the reinforcement of sand behaviour under loading (Boldyrev et al., 2012).

The PIV techniques is essentially a technique involving continuously capturing high resolution imaging of matter that is subjected to progressive deformation

(Khatami et al., 2019). These deformed images are then traced back to a reference image and the displacement pixels are identified.

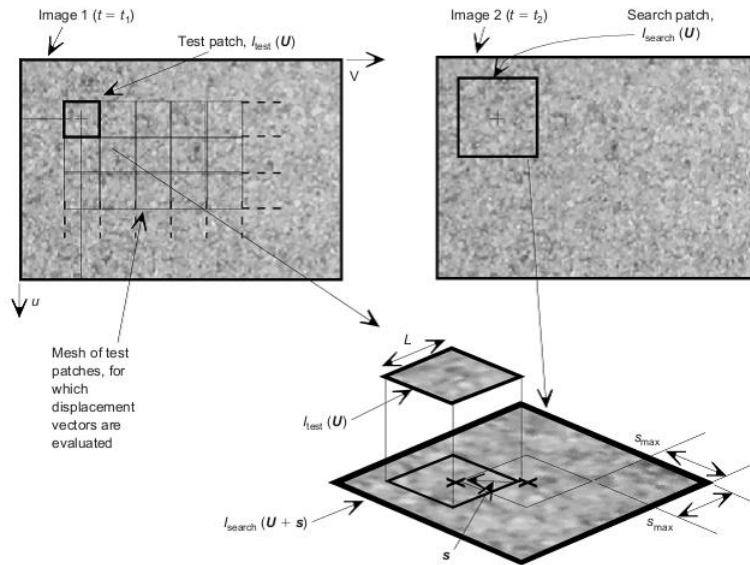


Figure 2.70: Image manipulation during PIV analysis (White et al., 2003)

Figure 2.70 illustrates the schematics on how the deformation during PIV analysis is quantified. The first image (t_1) is divided into grids of test patches. Each test patch (U) consists of an $L \times L$ pixel of an image matrix, $I(U)$. By using a search patch $I_{search}(U+S)$, extracted from the second image (t_2), the displacement of the test patch can be calculated. This search patch extends beyond the test patch by a distance, s_{max} in the u and v directions in the search for defining test patches. The resulting correlation plane was normalized, $R_n(s)$ by square rooting the sum of the squared value of $I_{search}(U+S)$ over the range of the occupied test patch to validate the ‘match’ between the test and search patches.

Figure 2.71(a) indicates the displacement vector, S_{peak} from the highest peak in the normalised correlation plane and then is enlarged in Figure 2.71(b). By using a bicubic interpolation to the surrounding region, the displacement vector is established in Figure 2.71(c). White et al., (2003) reported that the resolution greater than 0.005 pixels is unnecessary since most cases the errors are larger than that. These steps are continued with the subsequent image, (t_3) replacing t_2 and so on. When a correct correlation peak is drowned by random noise, these are called ‘wild’ vectors. ‘Wild’ vectors are minimised by updating the ‘initial’ image at each interval during analysis.

White et al., (2003) successfully converted image-space deformation recorded using PIV onto measurable object-space coordinates (mm) with corrective procedures suggested by Heikkila and Silven (1997) and Abdel-Aziz and Karara (1974) as shown in Figure 2.72. These corrective procedures cater to image distortions such as radial and tangential lens distortion, refraction of a viewing window and unparallelled charge-coupled device (CCD) plane of measurement. Figure 2.73 shows the grids of dots that were used as a reference field to determine transformational parameters using centroiding method.

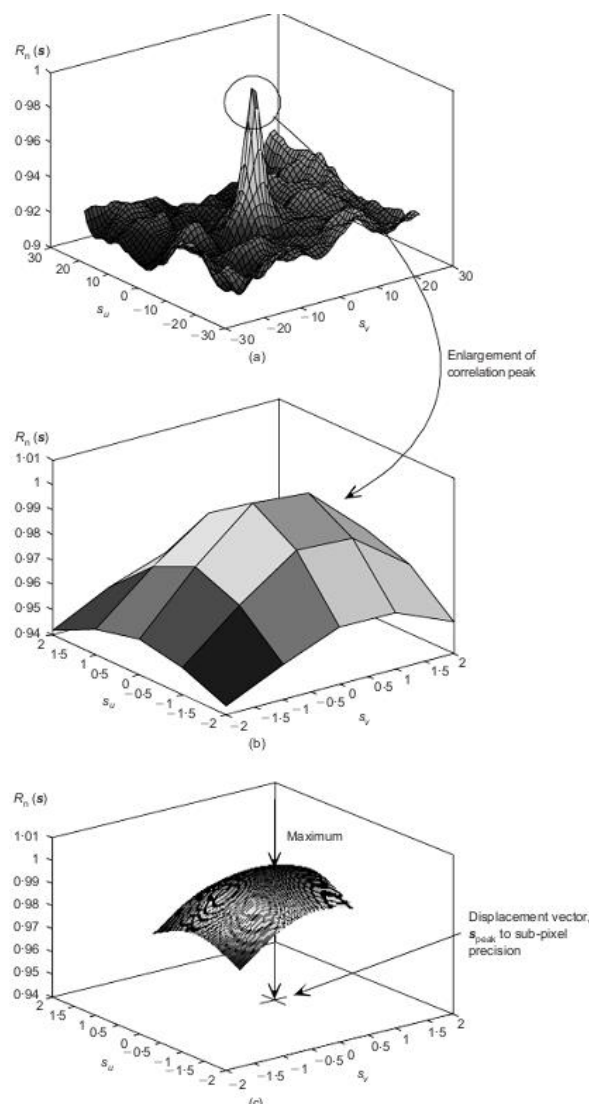


Figure 2.71: Evaluation of displacement vector from correlation plane plane, $R_n(s)$: (a) correlation function $R_n(s)$; (b) highest correlation peak; (c) sub-pixel interpolation using cubic fit over ± 1 pixel of integer correlation (White et al., 2003)

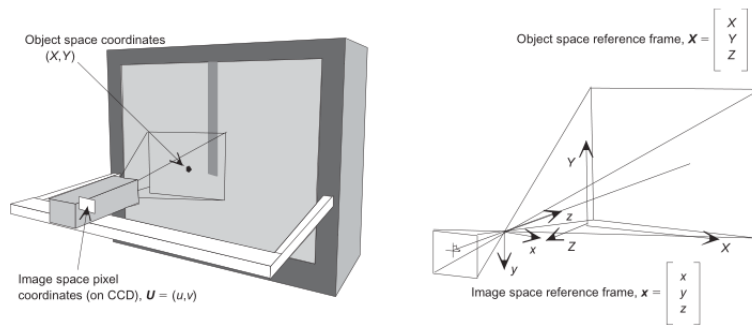


Figure 2.72: Object-space and image-space coordinate system (White et al., 2003)

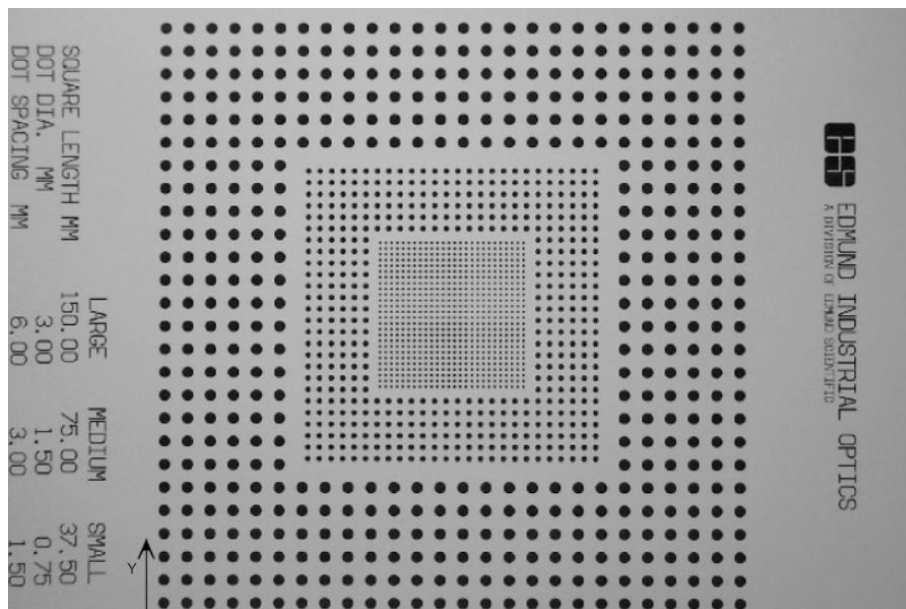


Figure 2.73: Photogrammetric target (White et al., 2003)

2.4.2 Application of PIV

Previous laboratory tests have been performed by several researches to prove PIV successful applications.

White, Take and Bolton (2003) simulated the installation of a displacement pile in sand. Figure 2.74(a) displays the viewing window of a plane-strain chamber with 14 reference targets for photogrammetric transformation parameters optimization. After 1.5 mm of pile movement, PIV analysis of the two images resulted

in the displacement vector field shown in Figure 2.74(b). To demonstrate the zone of deformation, Figure 2.74(c) shows the contours of displacement vector which reveal a high-velocity gradient in the proximity of the pile tip.

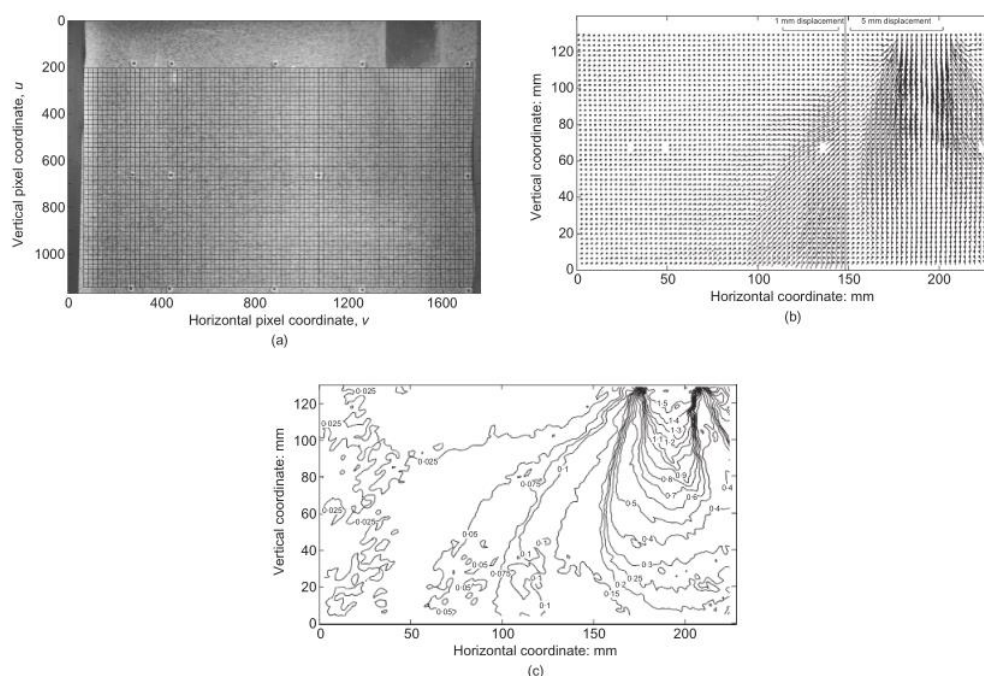


Figure 2.74: Displacement field around plane strain displacement in pile; (a) mesh of PIV patches, (b) displacement vector field, (c) magnitude of displacement vectors (White et al., 2003)

Ni, Hird and Guymer (2010) modelled the movement of clay during pile installation. The clay model was produced by a mixture of amorphous silica and mineral oil which makes the clay almost transparent. By adding reflective particles within the mixture, the research was able to perform PIV analysis on the model to measure displacements during pile installation. Figure 2.75 shows the experimental setup conducted with two separate soil (with and without reflective particle Timiron), LED control points, a prism and a 1-Watt Argon-ion laser to illuminate the soil sample. The model pile was driven 0.35 mm/s downwards while a Canon 350D 8 Megapixel camera show about 300 pictures (0.8 shot per second) with an exposure time of 1/13 to 1/15 s.

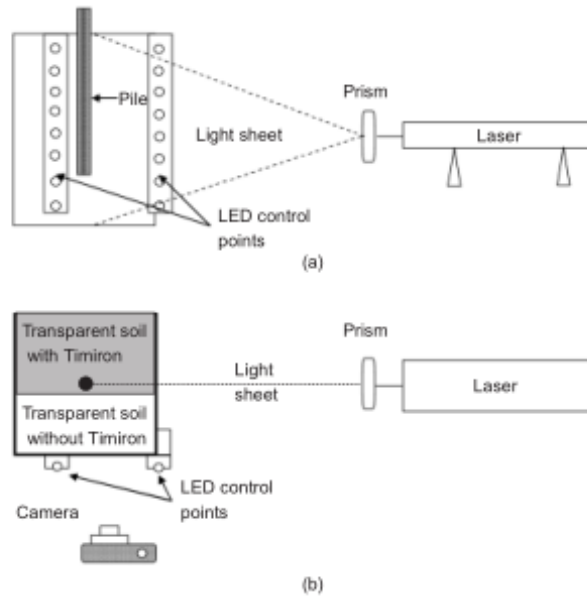


Figure 2.75: Experimental setup; (a) elevated view, (b) plan view (Ni et al., 2010)

Calibrations test was performed to correct lens distortions and refraction of the Perspex viewing window used in the model. Red-marked target markers with predetermined 10 mm width centre-to-centre holes were used as an object-space centroidal converter. Ni et al. (2010) then proceeded to reduce the noise levels by reducing images used in the PIV analysis to a sequence of less than 30 images. This resulted in the noise level reduced to 0.23% and 1.00% for the displacement and strain respectively.

Figure 2.76 shows the displacement vector resulted from Ni's research in the form of the vector quiver plots. Ni et al. (2010) concluded the observed displacements are in agreement with the theoretical predictions of the Shallow Strain Path Method (SSPM) by Sagasetta et al. (1997) and could be used to assess ground disturbance during pile penetration in clay.

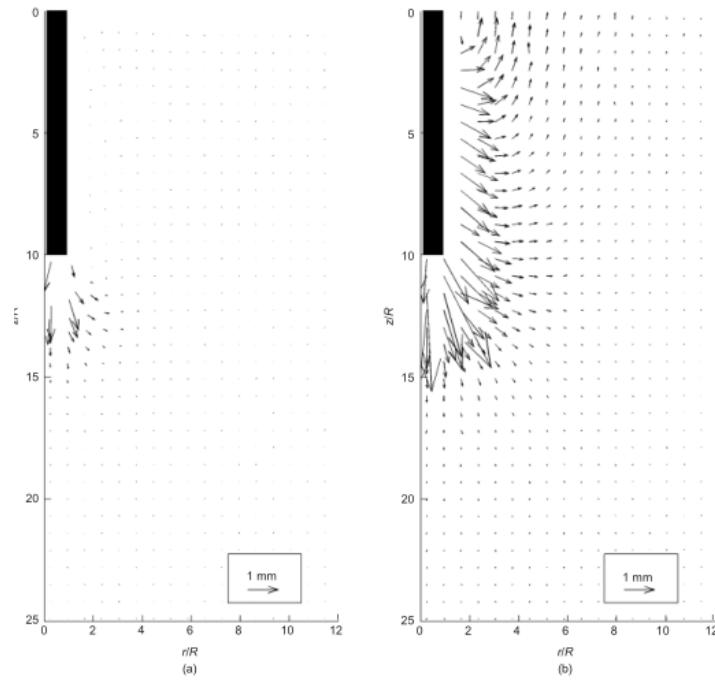


Figure 2.76: Displacement vectors: (a) incremental from $L = 9.5R$ to $L = 10R$; (b) accumulated, from $L = 0R$ to $L = 10R$ (Ni et al., 2010)

Boldyrev et al. (2012) produced a study of Particle Image Velocimetry (PIV) of sand deformations under a test plate in plate strain. Two groups of tests were deployed; with and without reinforcements (8 X 8 mm long and 1.5 mm thick geogrids) at different heights. Figure 2.77 shows the setup of the test that consists of a 720 X 450 X 155 mm box with transparent plexiglass windows. The load was applied to a 50 mm X 155 mm test plate by pneumatic loading. A Canon EOS 400D with 10 Megapixel (MP) sensors having 3888 X 2592 resolution placed 2.5 m from the box was used as the digital image acquirer. Due to spherical image errors, a 1 mm diameter reference marker was used for calibration purposes. Clean quartz sand was used for adding texture and the sand was compacted in the chamber by 10 mm layers to a density of $\rho = 1.59 \text{ g/cm}^3$, porosity, $e = 0.502$ and shear resistance angle, $\phi = 37^\circ$.



Figure 2.77: Automated foundation test set-up: 1- camera, 2- PC, 3- signal transmission unit, 4- pneumatic loading unit, 5- support beam, 6- load test plate with rod, 7- plexiglass wall with stiffener, 8- pressure control unit (Boldyrev et al., 2012)

Graphical results from the unreinforced sand model were presented in the following figures. Figure 2.78 shows the vertical displacement at 8 mm settlement showing 2 zones which are compaction (-) and uplift (+). Note the compacted zone deepens asymmetrical to the plate. Figure 2.79 then indicate the volume strain zone depth of up to $2b$. The compacted zone under the plate formed wedges due to sand compaction. Maximum shear strains continued to develop downwards resulting in the decrease of the plastic zone and forming a wedge such as a Figure 2.80. Figure 2.80 was produced by PIV analysis showing the ultimate strain in excess up to 17.5-fold.

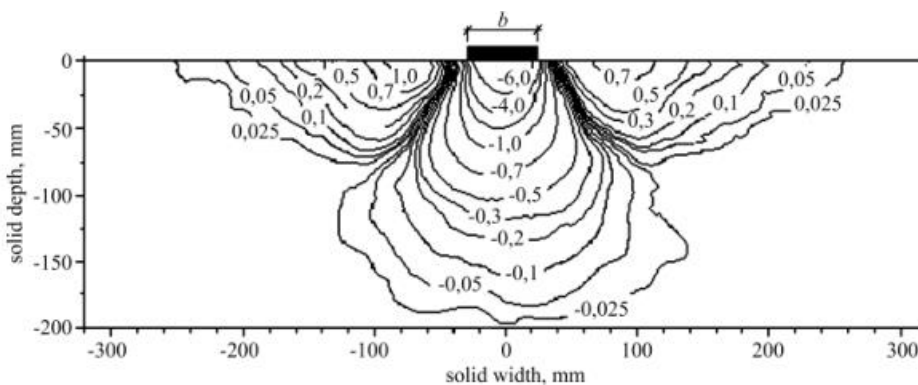


Figure 2.78: Vertical displacement isolines at 8 mm plate settlement: 1- compaction; 2- uplift (Boldyrev et al., 2012)

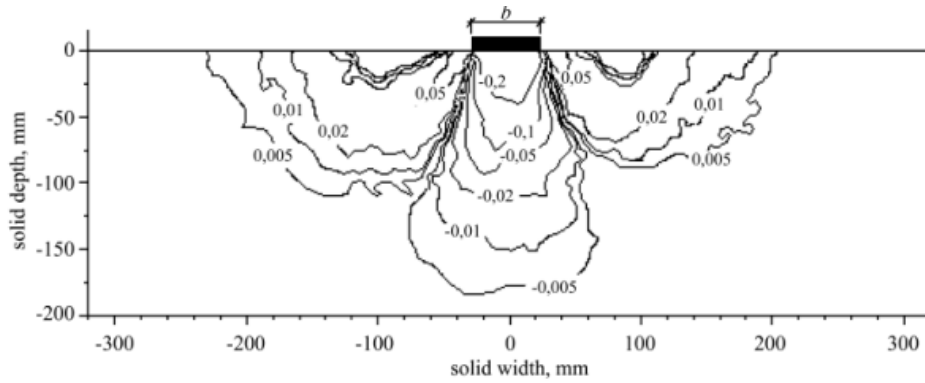


Figure 2.79: Volume strain isolines at 8 mm plate settlement (Boldyrev et al., 2012)

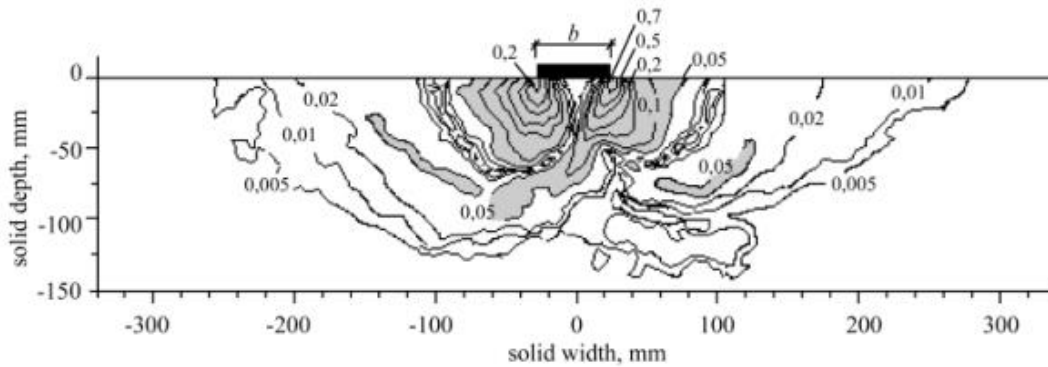


Figure 2.80: Shear strain isolines at 16 mm plate settlement (Boldyrev et al., 2012)

For the reinforced cases, Figure 2.81 provided the geographical representation of the shear strain for the ultimate loading for 1 layer of reinforcement. Figure 2.82 shows the shear strain for a three-layered reinforcement close to the ultimate load. Based on the PIV analysis done on all cases, Boldyrev et al. (2012) presented the changes in pressure-settlement behaviour due to unreinforced and reinforced settlement versus load in Figure 2.83. Boldyrev et al. (2012) concluded the settlement and shear strain zone decrease if sand base stiffness increases (due to the addition of reinforcements). In addition, it was also agreed that the PIV technique is an effective imaging technique to measure strains in the sand as photogrammetry.

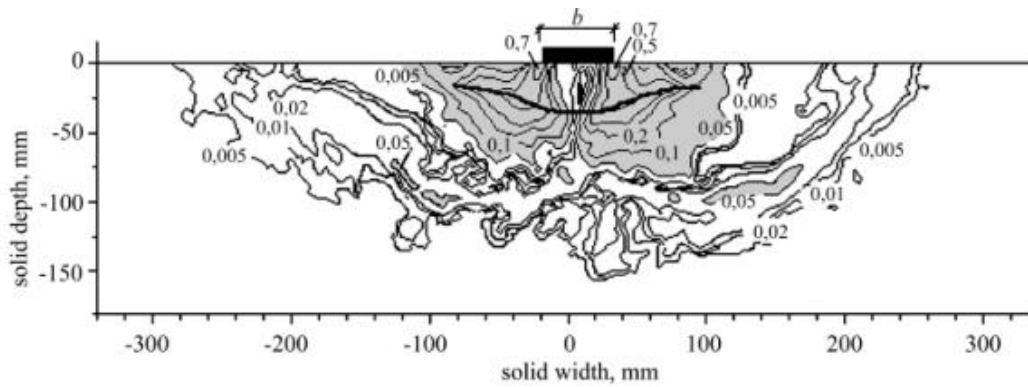


Figure 2.81: 16 mm plate loading. Shear strain isolines for one layer of reinforcements (Boldyrev et al., 2012)

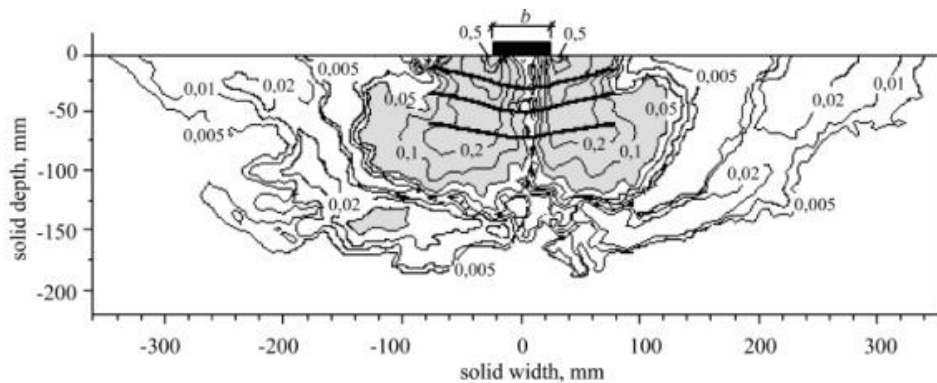


Figure 2.82: 16 mm plate loading. Shear strain isolines for three layers of reinforcements (Boldyrev et al., 2012)

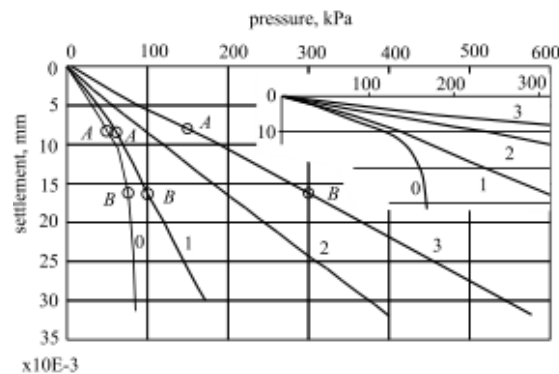


Figure 2.83: Plate settlement versus loads plot; 1- unreinforced; 2,3,4- 1,2,3 layers of reinforcements; A and B -PIV measurement points (Boldyrev et al., 2012)

Khatami et al. (2019) presented on the investigation of arching effect in soils using the Digital Image Correlation (DIC) technique. A trapdoor apparatus fitted with dyed and natural coarse-graded sand were fitted with multiple sensors in this study such as shown in Figure 2.84.

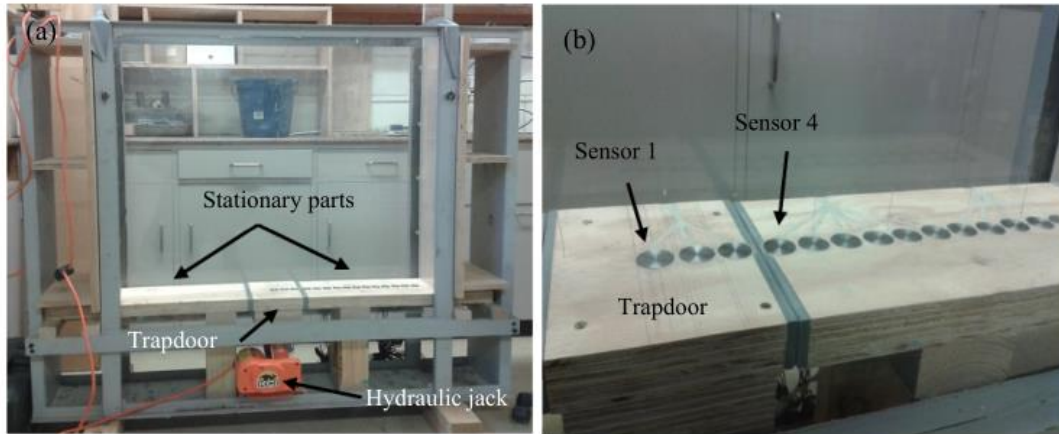


Figure 2.84: The trapdoor apparatus; (a) overview, (b) stress sensor arrangements (Khatami et al., 2019)

This trapdoor apparatus is a slightly modified version of Terzaghi's trapdoor apparatus used to study the arching effect in soils way back from 1936. The principle is that a rectangular prism of soil on a bed has a movable component on the middle; the so-called 'trapdoor'. This trapdoor is movable such as it can move away or push into the soil. Khatami et al. (2019) used two computer programs, which are VicSnap for image acquisition and VIC-2D for the DIC strain analysis developed in the USA. Image acquisition was procured through a monochrome 2.8 MP camera with 1928 X 1448 pixels maximum resolution and a 75 mm Fujinon lens (1/22 – 1/2.8 aperture). 26 frames per second (fps) of image acquisition were used in the study.

A mixture of dyed sand and coarse-grained sand was compacted 10 mm at a time to a height of 200 mm with an approximate area of 1 m X 1 m for the test. DIC analysis begins with an acquisition of a target marker image of a large dot grid patterns with predetermined spacing for reference such as shown in Figure 2.85(a). Figure 2.85(b) shows the typical image of the general specimen used in the study. Moreover, Figure 2.85(c) indicates a close-up of the speckle texture. After the image acquisition, the VIC-2D would then determine the subset size, step and filter sizes needed for the purpose of the DIC analyses of the trapdoor apparatus by considering noise reduction, patterns degradation, analysis time, output precision and smoothness of the acquisition area. A typical subset and area of interest are shown in Figure 2.85(d).

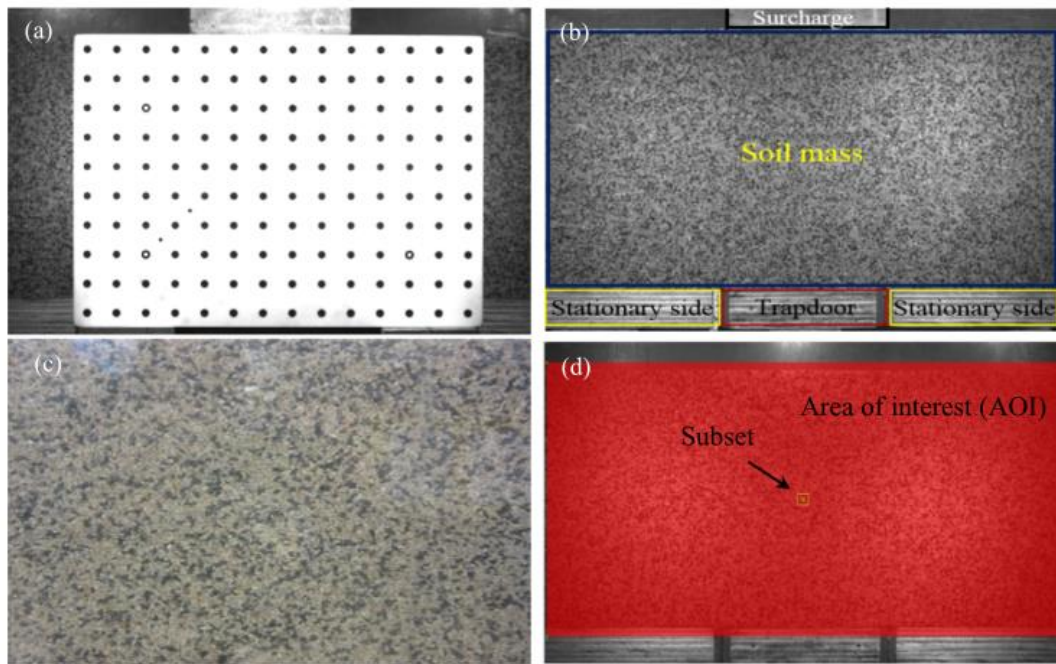


Figure 2.85: Elements in DIC; (a) target marker with 28 mm spacing, (b) typical image of the general specimen, (c) close-up of speckle pattern of the soil and (d) typical subset and Area of Interest (AOI) for the DIC analysis (Khatami et al., 2019)

Horizontal and vertical displacements captured in the trapdoor apparatus to test arching effect without surcharge for 1 mm and 3 mm yield was presented in Figure 2.86 and Figure 2.87 respectively. Moreover, Figure 2.88 and Figure 2.89 showed the horizontal and vertical displacements of the trap door apparatus with the addition of a 5 kPa surcharge from a block of concrete the size of the trapdoor. Note that a triangular area can be observed in both cases. These triangular areas are observed to roughly have the same amount of displacements as the trapdoor. This proves previously researched mathematical modelling of the curved arc evolution from a triangular-curved arc, triangle and finally a rectangle as the trapdoor yields.

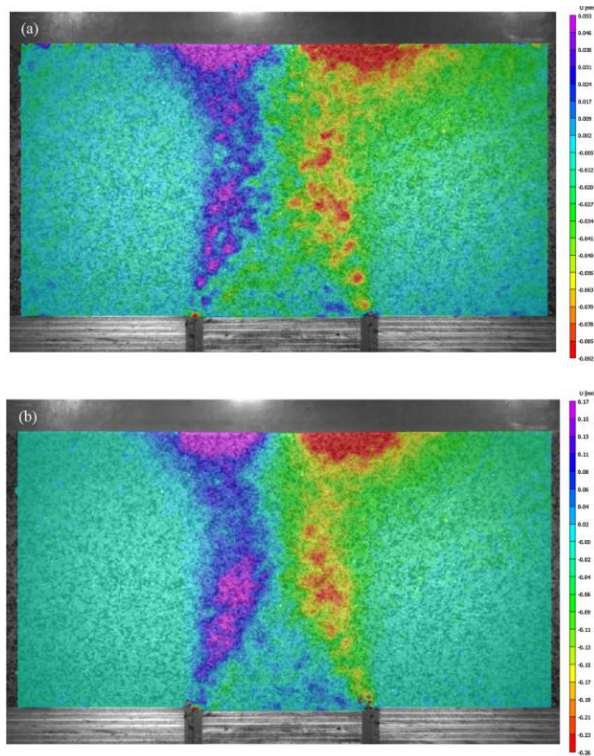


Figure 2.86: Horizontal displacement in a trapdoor apparatus with no surcharge; (a) 1 mm and (b) 3 mm yielding (Khatami et al., 2019)

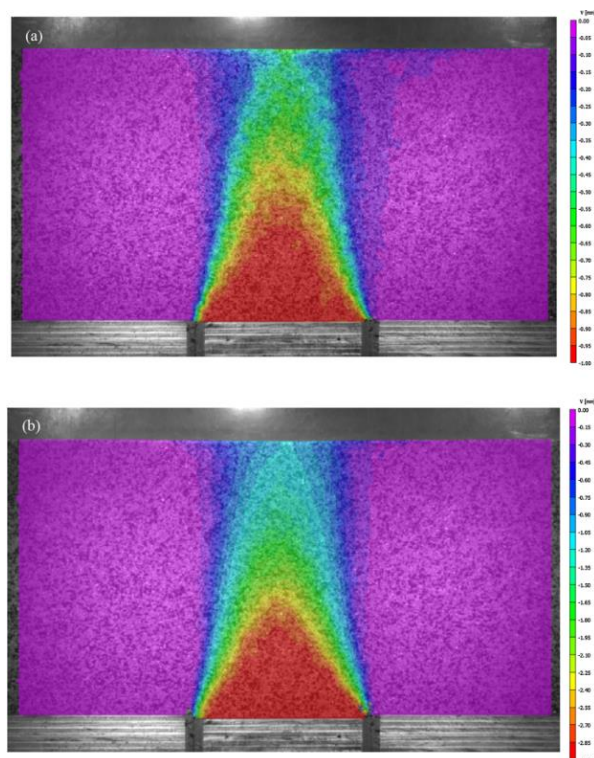


Figure 2.87: Vertical displacement in a trapdoor apparatus with no surcharge; (a) 1 mm and (b) 3 mm yielding (Khatami et al., 2019)

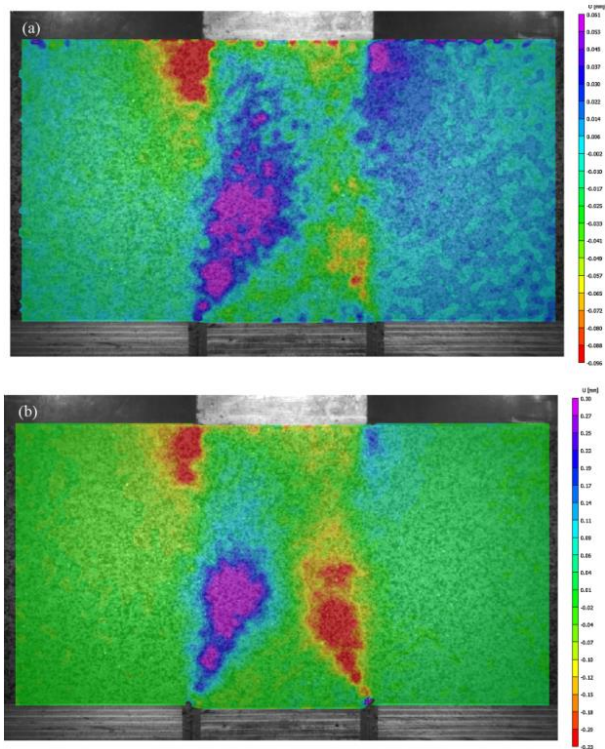


Figure 2.88: Horizontal displacement in a trapdoor apparatus with surcharge; (a) 1 mm and (b) 3 mm yielding (Khatami et al., 2019)

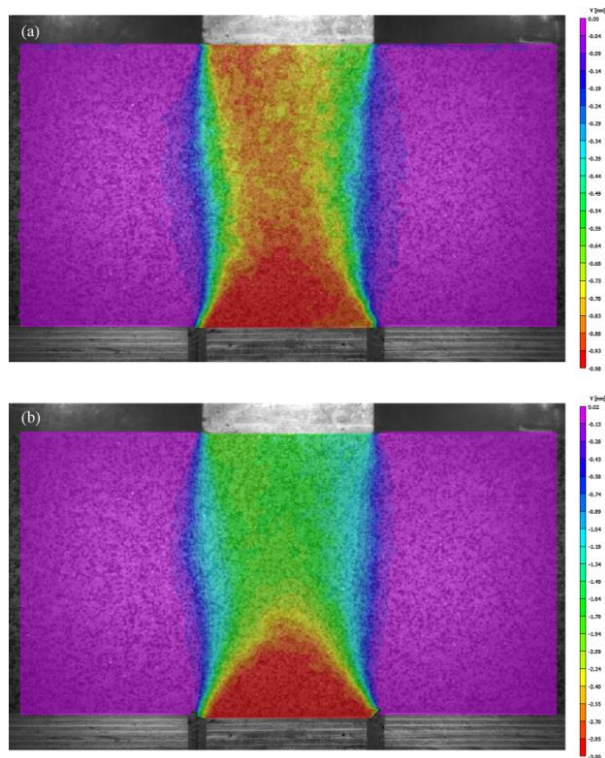


Figure 2.89: Vertical displacement in a trapdoor apparatus with surcharge; (a) 1 mm and (b) 3 mm yielding (Khatami et al., 2019)

After completion of the strain analysis, the vertical strains in the trapdoor with and without surcharge were presented in Figure 2.90 and Figure 2.91 respectively. Note that a triangular area developed as well above the trapdoor as it yielded. Khatami et al. (2019) reported that within this triangle, the soil experienced small vertical strains, but no shear strains. The research concluded the representation of tensions within the vertical strains with and without surcharge in Figure 2.92. Khatami et al. (2019) also concluded that the DIC technique was able to capture effective displacement and strain development during soil arching, thus helping future research better understand the arching phenomenon due to relative displacement in soil. Several precautions were also noted from the research such as systematic and careful sample preparation steps, optical lens distortion calibration, soil texturing and also adequate imaging frame rate of future DIC analysis.

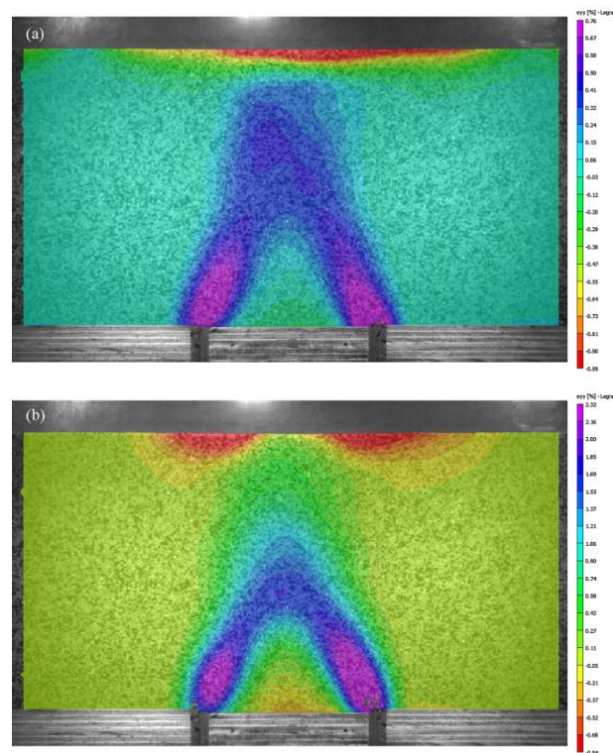


Figure 2.90: Vertical strains in a trapdoor apparatus with no surcharge for (a) 1 mm and (b) 3 mm yield of the trapdoor (Khatami et al., 2019)

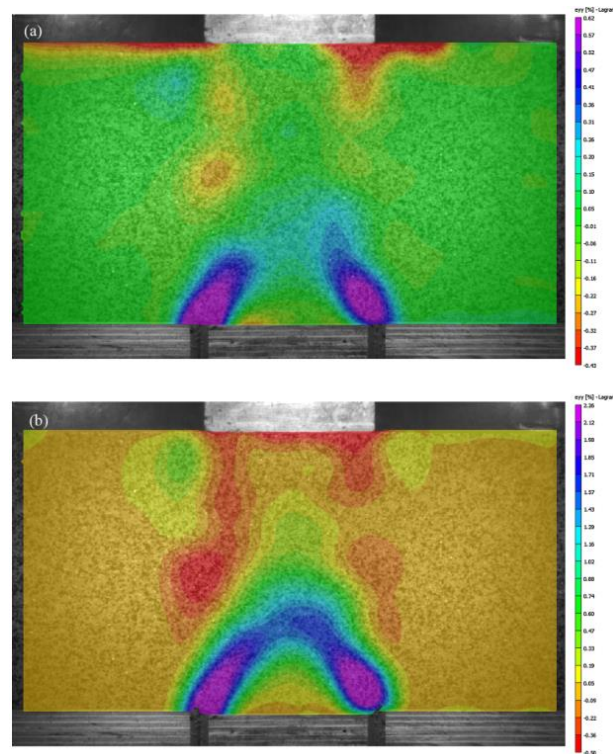


Figure 2.91: Vertical strains in a trapdoor apparatus with 5 kPa surcharge for (a) 1 mm and (b) 3 mm yield of the trapdoor (Khatami et al., 2019)

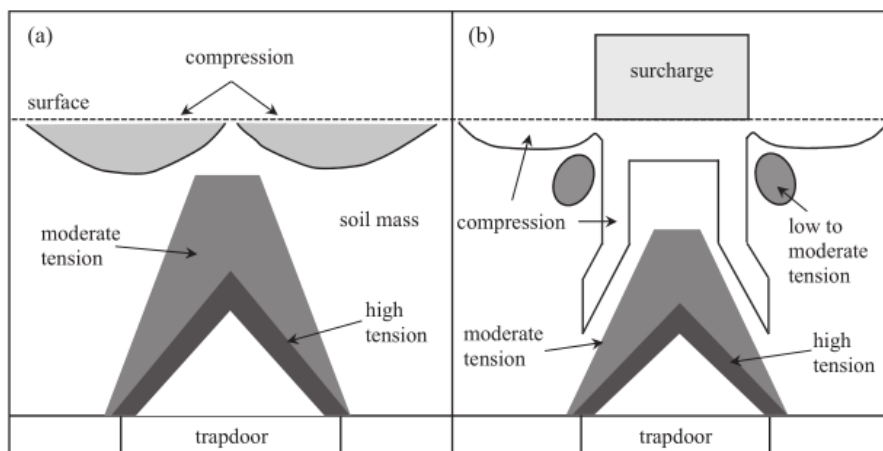


Figure 2.92: Idealised vertical strain of the arching effect illustration (Khatami et al., 2019)

2.5 Numerical Modelling of Slope Failure using GeoStudio

In the past few decades, seepage analysis using numerical modelling has been successfully applied throughout the geotechnical community in line with the swift development of geotechnical software and heightened computer processing power.

Through literature studies, a number of applications and aspects of numerical modelling are presented in this sub-section.

2.5.1 Application of Geostudio on Slope Failure Simulation

Rahardjo et al. (2001) published a study on the effect of antecedent rainfall on slope stability for Singapore. A huge storm in February 1995 caused more than twenty landslides on the Nanyang Technology University Campus. To better understand the effects of antecedent rainfall Rahardjo et al. (2001) used commercialized software known as SEEP/W from GeoStudios, simulating hydrostatic conditions to be used in several analyses for the research.

To simulate the initial condition of pore water pressure identical to the in-situ condition was always known to be very hard. Through trial and error of applying low unit flux to the slope surface for long durations, Rahardjo et al. (2001) fruitfully establish an initial pore-water pressure profile by utilizing a transient state analysis. Rahardjo et al. (2001) also used SEEP/W to simulate changes in pore water pressure due to a number of rainfall patterns. This change of pore water pressure was determined by applying a constant head to the right and left boundaries while zero flux boundary was established above the groundwater table.

Similarly to Rahardjo et al. (2001), SEEP/W was also used by Tsaparas et al. (2002) to perform seepage analysis to establish an unsaturated soil slope that was later used to determine its factor of safety (FOS) by using SLOPE/W. Figure 2.93 shows the two initial depth of groundwater levels (h_w) and the geometry of the homogenous slope used in the numerical analysis while Figure 2.94 indicates the soil parameters used in the study.

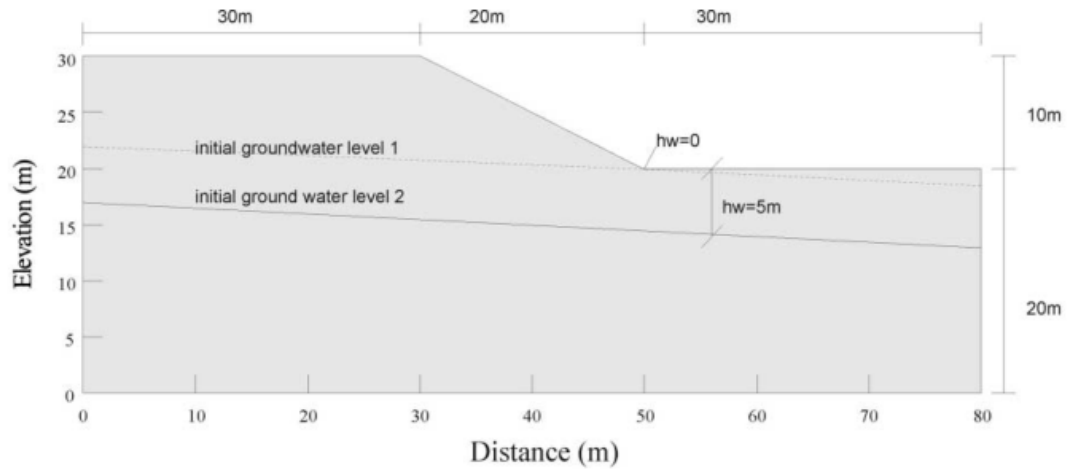


Figure 2.93: Geometry of the homogenous slope used (Tsaparas et al., 2002)

Effective cohesion c' (kPa)	Effective angle of friction ϕ'	ϕ^b angle	Saturated unit weight (kN/m^3)	Unsaturated unit weight (kN/m^3)
1.0	25.0°	24.0°	20.0	19.0

Figure 2.94: Summary of soil parameters used in the study (Tsaparas et al., 2002)

High rainfall was instilled onto the slope resulting in only shallow wetting front due to most of the rainwater becomes run-off. This was done by establishing the surface pore water pressure to be 0 kPa which in turn simulated a no surface water ponding condition on the model surface. Tsaparas et al. (2002) reported that after comparing the pore-water pressure profile of the same distribution of the 240 mm of total rainfall, the depth of wetting front increases as the value of the saturated coefficient of permeability with respect to water (k_{sat}) such as shown in Figure 2.95.

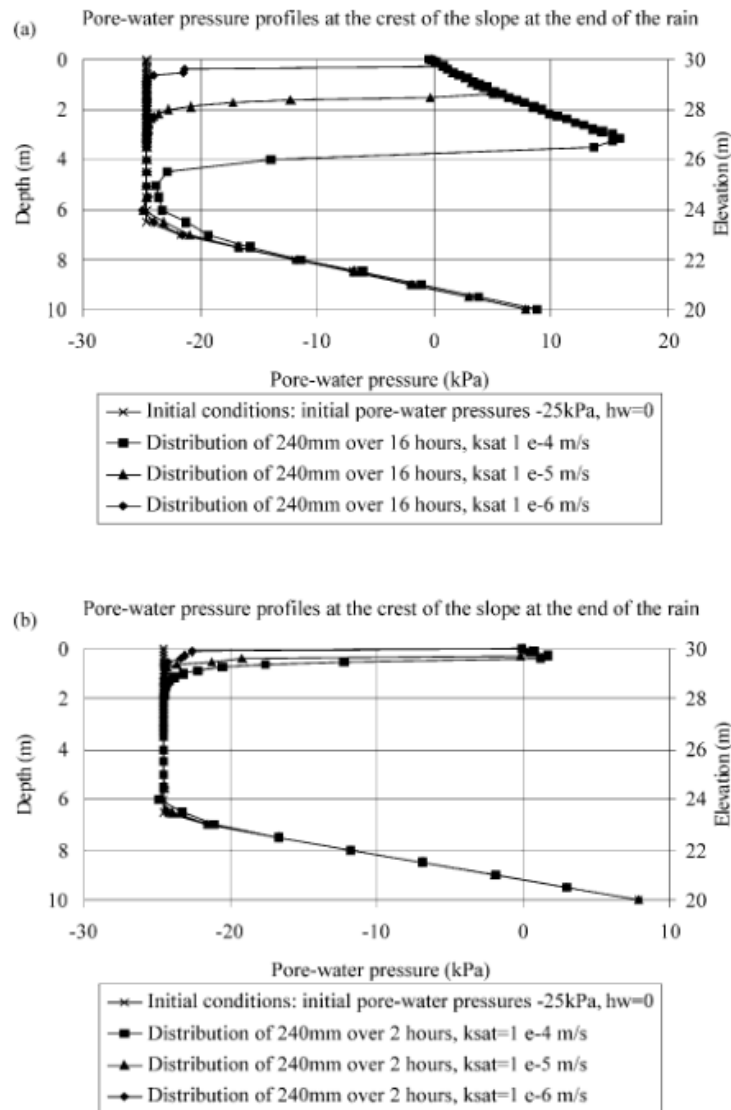


Figure 2.95: Comparison of pore-water pressure profiles at the crest of the slope by the end of rainfall; (a) rainfall over 16 h (intensity 15 mm/h) and (b) rainfall over 2 h (intensity 120 mm/h) (Tsaparas et al., 2002)

Tsaparas et al. (2002) continued the analysis by analysing different distributions of major rainfall (by scenarios) contributing to the FOS of the slope. The research points out that the longer the period of which the rainfall is distributed, the lower will be the FOS of the slope. Evidently, Figure 2.96 shows the FOS versus time of different scenarios throughout the study. From observations, the longest period namely scenario 3 which the rainfall distributed over a 5-day period resulted in the lowest FOS (below 1.0).

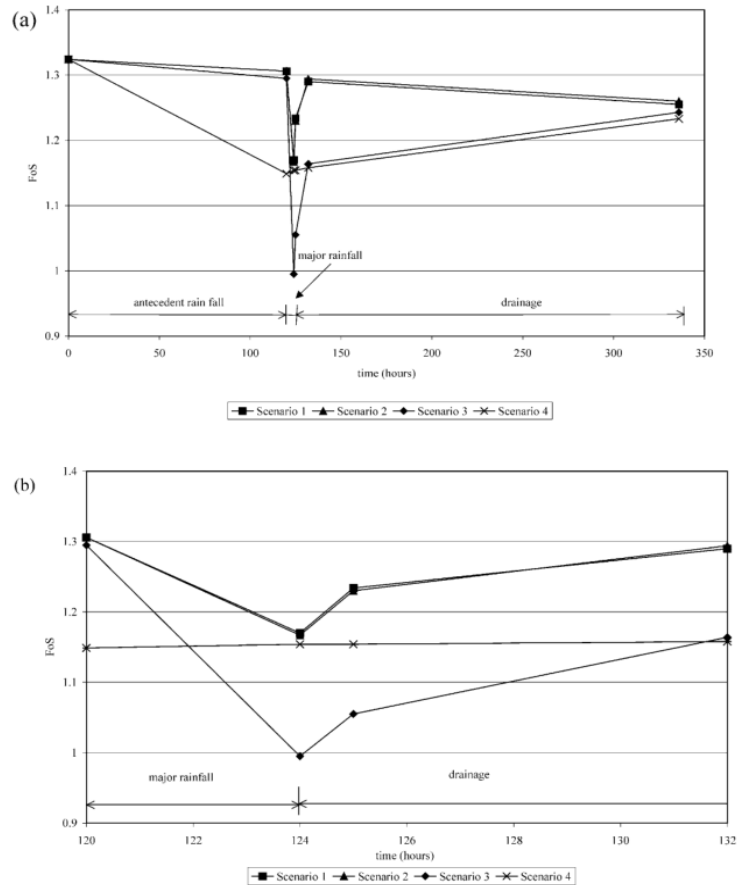


Figure 2.96: Development of the factor of safety (FOS) with time for different distributions of antecedent rainfall for the case of $k_{sat} = 10^{-5}$ m/s, initial pore-water pressure -25 kPa and initial groundwater table at the toe of the slope; (a) the whole simulation and (b) during major rainfall event (Tsaparas et al., 2002)

Tsaparas et al. (2002) concluded that numerical modelling was successfully used in investigating several hydrological parameters on the seepage condition on a typical residual soil slope. Moreover, an antecedent rainfall over a 5-day period prior to major rainfall event can affect the seepage condition even if the amount is very small in comparison to the major rainfall. Throughout the research, the worst case occurred while antecedent rainfall was distributed evenly over the 5-days such as shown in Figure 2.96.

Lee et al. (2009) researched on a simple model used for preliminary evaluation of rainfall-induced slope instability. By first identifying basic hydraulic properties of typical types of soil found in Malaysia and rainfall intensities, the research simulated the suction and factor of safety (FOS) using numerical simulation tools, which are

SEEP/W and SLOPE/W. Figure 2.97 shows the mesh and boundary condition used for simulating transient seepage analysis for SEEP/W used by Lee et al. (2009).

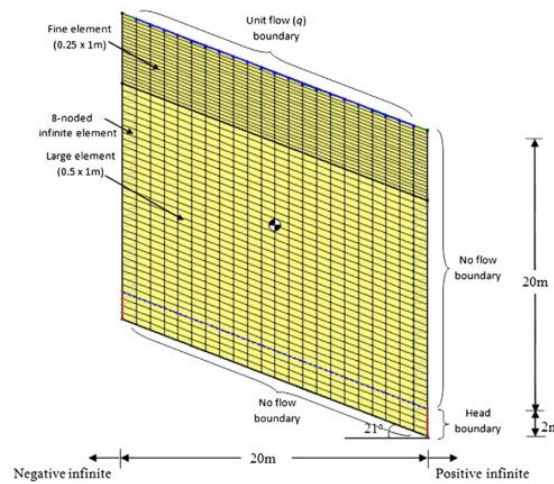


Figure 2.97: Geometry of analysis listing element meshes and boundary condition of the model (Lee et al., 2009)

A 40 m total length of the model, no flow boundaries ($Q = 0$), pressure head equal to water table elevation and a unit flux (q) of varying intensities with no ponding option established for the simulation. After hydrostatic initial condition was established at the beginning of the analysis, a limiting negative pore water pressure was imposed as the limiting values for initial suction. Figure 2.98 shows the suction distributions successfully modelled using SEEP/W by Lee et al. (2009).

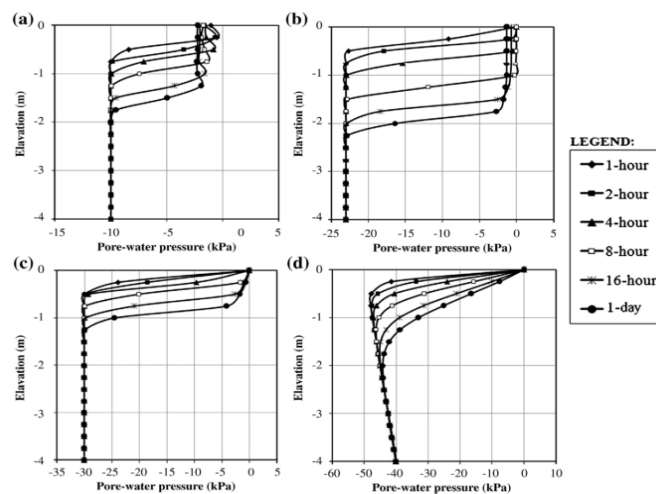


Figure 2.98: Suction distribution from several durations of major rainfall; (a) sand-gravel, (b) silty gravel, (c) sandy silt and (d) silt (kaolin) (Lee et al., 2009)

A model named PERISI was developed based on the relationship of extreme rainfall characteristics (IDF curve), permeability function and soil-water characteristics curve (SWCC) as a tool for early assessment of slope instability due to rainfall. Lee et al. (2009) reported the PERISI model was able to efficiently estimate critical depths of wetting front and the minimum suction value to compute slope instability.

Kristo et al. (2017) studied on the anticipated effects of rainfall intensity for slope stability analysis in Singapore from 2010 to the year 2010. SEEP/W and SLOPE/W was used as seepage and slope stability analysis with data from the Sletar weather station. Kristo et al. (2017) projected a rain intensity of 8 mm/h (year of 2003), 31 mm/h (year 2050) and 57 mm/h (year of 2100) used to mode three sets of slope stability and seepage analysis for 10 h.

Figure 2.99 shows the slope model used for the seepage and slope stability analysis. The slope angle of 27°, with no flow ($Q = 0$) boundary set above the water table and respective total head in accordance with height was implemented. In the research, Kristo et al. (2017) opted for a 20 h analysis divided into 40-time steps (0.5 h each step). Typical SWCC and permeability function for Old Alluvium was analysed using Bishop’s simplified method such as; a cohesion (c') of 8 kPa, friction angle (ϕ') = 35 and angle indicating the rate of change in shear strength relative to suction (ϕ^b) = 20°.

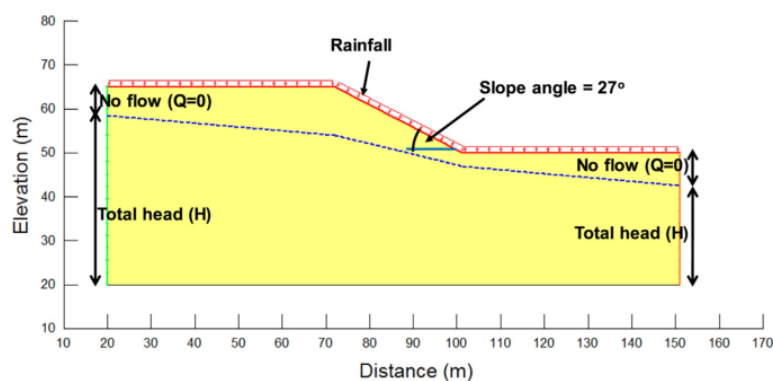


Figure 2.99: Slope model for seepage and slope stability analysis parametric studies (slope height = 15 m and slope angle = 27°) (Kristo et al., 2017)

Kristo et al. (2017) reported the estimated projected variations of safety factor for the year 2003, 2050 and 2100 were increasing steadily suggesting climate change phenomenon would happen and that increase may have unfavourable effects on the slope of Singapore (Figure 2.100).

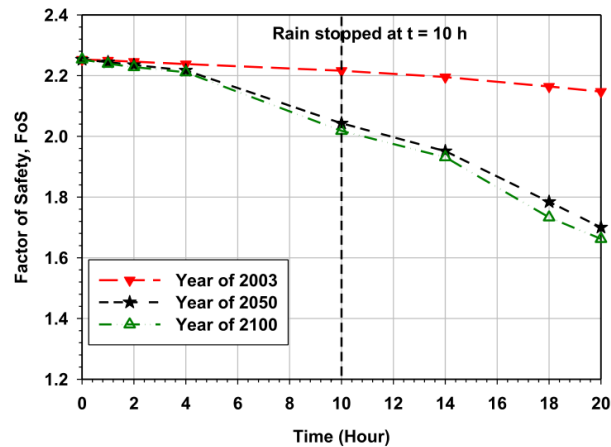


Figure 2.100: Variations of the factor of safety (FOS) during and after rainfall for years 2003, 2050 and 2100 (Kristo et al., 2017)

Kassim (2001) reported that in general, the modelling concept of heterogeneous soil can be divided into two methods, namely porous medium equivalent (continuum method) and discrete fracture method. Continuum method assumed the flow of a volumetrically average basis at microscopic scale to be equivalent to an idea porous medium while discrete fracture method considers each fracture that is characterized by a location orientation, size and transmissivity (Eaton, 2006).

Simply put, the continuum method divided the heterogeneous soils into multiple zones whereby the hydraulic properties of each zone are constant throughout. While discrete fracture method maintains that the subsurface flow has continuously varied properties whereby the distribution of the properties is unclear. Long et al. (1985) clarified the discrete method to be computationally intensive. It can be concluded that while the discrete fracture method gave better extrapolation of a subsurface flow characterization (while including comprehensive statistical analysis and computational power), the continuum method would deliver satisfactory results for a microscopic scale problem and thus offer a better and simpler alternative method.

2.6 Concluding Remarks

Over the past two decades, slope monitoring techniques have evolved rapidly in line with the advancements in the geotechnical monitoring system. The disadvantages of conventional techniques are taken into consideration when developing new and improved slope monitoring system, as they are constantly being innovated and manifested onto new measuring systems as listed in Table 2.1.

For example, by gaining a large area of monitoring, limitations of low precision, big gaps in data and cost factor impede the overall progress of the intended monitoring apparatus. Meanwhile, cheaper slope monitoring systems are susceptible to being vulnerable, susceptible to obstacles in the site and having low precisions. The optimization of combined devices being able to minimize such limiting factors of an effective monitoring system is obliged for future researches in disaster management. The geotechnical community are in need of innovative systems to assess geotechnical hazards and effectively classify the risk of which the threat of slope failure apposes.

A review of the existing slope monitoring systems and devices in this section revealed the advantages and disadvantages of such techniques. Several issues that arose when employing certain techniques are being mitigated throughout the years making sure future generations are well equipped to employ such techniques or instrumentation.

In conclusion, despite the efforts were taken in this field of geotechnical engineering, an integrated system of more simplified, user-friendly, cost-effective, and fast-response monitoring devices would be developed to provide a better insight onto slope instability monitoring. Such a monitoring system would grasp the trust of decision-makers in the mining industry, road and transportation department, and construction industry to invest in a reliable system and aid from lowering of the slope instability hazards.

Table 2.1: The strength and limitations of slope monitoring devices

Strength	Methods	Limitations	References
Low cost, prolong monitoring	Theodolite and Prism	Geomorphology limitations, climate-dependent, not used in active sites, a large gap of monitoring data, equipment protection	Angeli et al. (2000) Rizzo et al. (2002) Little (2005) Herrera et al. (2009) Khan et al. (2010) Fastellini et al. (2011)
Large area of monitoring, fast and easy data transfer, uninterrupted by on-going site works and having a 3-dimensional determination	Laser Monitoring LIDAR	High cost, weak to strong obstacles, having a large gap in monitoring data, range and precision dependent on laser power and susceptible to surrounding noise	Blair et al. (1997) Blair and Lohr (1999) Wehr and Lohr (1999) Little (2005) Jamaluddin and Hussein (2006) NOAA (2018) Taylor-Smith (2019)
A large area of monitoring, user-friendly, low cost per area of monitoring	Global Positioning System (GPS)	Satellite dependent, physical obstruction, low precision, equipment protection and correlation noise from surrounding area or atmosphere	Gili et al. (2000) Malet et al. (2002) Rizzo et al. (2002) Bertacchini et al. (2009) Herrera et al. (2009) Fastellini et al. (2011) Blume (2014)
A large area of monitoring, high precision and unhindered by physical obstruction	Synthetic Aperture Radar (SAR)	Satellite dependent, high cost, timing consuming and a large gap in monitoring data	Bamler and Hartl (1998) Rosen (1998) Berardino et al. (2003) Crosetto et al. (2013) Calo et al. (2014) Jebur et al. (2014)
Operational inactive sites, small gap in monitoring data, remote and unmanned monitoring, operated in any weather conditions, prolong monitoring and precise monitoring	GroundBased Synthetic Interferometric Aperture Radar (GBInSAR)	Limited monitoring range, long duration of data acquisition and weak to strong obstacles	Bozzano et al. (2009) Tarchi et al. (2003) Pierraccini et al. (2001,2003) Herrera et al. (2009)
Self-sufficient, prolong monitoring, real-time data, a large area of monitoring	Automated Robotic Station	Equipment protection Physical obstructions	Bertacchini et al. (2009)
Low cost, high precision, operable in any weather conditions, real-time monitoring, prolonged monitoring and simple monitoring setup	Extensometer	Physical obstruction (snapped wire), equipment protection, high cost, a large gap of monitoring data and temperature affecting accuracy	Blair et al. (1997) Ding et al. (2000) Angeli et al. (2000)
Prolong monitoring and precise monitoring	Inclinometer / Tiltmeter	High cost, equipment protection,	Ding et al. (2000) Herrera et al. (2009) Fastellini et al. (2011) Calo et al. (2014)
Monitoring pressure and groundwater level	Piezometer	Limited range of pressure monitoring	Ding et al. (2000) Little (2005)
Self-sufficient, prolong monitoring, weather dependent, minimal human interaction, real-time monitoring and combined data monitoring for various sensors	Intelligent System	Equipment protection, costly maintenance	Ding et al. (2000) Intrieri et al. (2012) Lacasse and Nadim (2009)
Self-sufficient, real-time monitoring, prolong monitoring, minimal human interaction, user friendly and operates in any weather conditions	Acoustic Emission (AE) Sensor	Noise	Dixon et al. (2014)

CHAPTER 3

PHYSICAL MODELLING OF SLOPE MONITORING DEVICE SIMULATIONS

3.1 Introduction

Through this chapter, materials and equipment used to prepare the physical modelling and numerical analysis are described. Procedures related to the model preparation, loading and present analyses were also discussed. Details of supplementary laboratory tests that accompany the main experiments are also included.

3.2 Research Plan

The aim of this study is to develop a fully Automatic Wireless Accelerometer Monitoring System (AWAM) used for slope monitoring. Figure 3.1 shows the flow chart methodology for this study. Firstly, the soil samples collected were identified. Then a full AWAM was developed to be tested on a physical modelling test on a laboratory scale. The physical model was equipped with a rainfall system to simulate our tropical climate in Malaysia. In addition, a numerical modelling test such as PIV and GeoStudios was conducted and the result and analysis were verified to complete the research flow. Simultaneously, field slope monitoring of an installed slope monitoring system will also be discussed. The following sections will discuss the detailed methodology for this research.

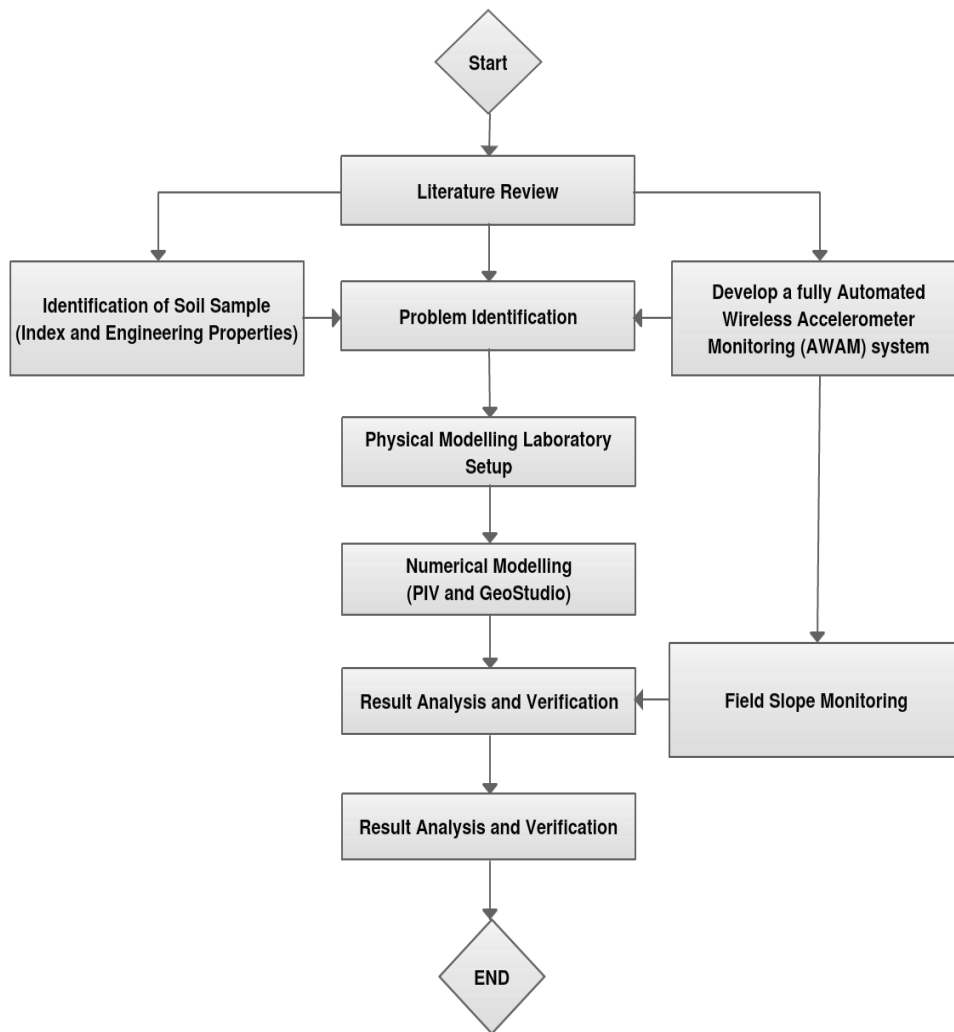


Figure 3.1: Flow chart of the research

3.3 Materials for Testing

3.3.1 Site Selection

The simulated study area is modelled after the Balai Cerapan, Universiti Teknologi Malaysia in Johor (Figure 3.2). The Balai Cerapan is located at $1^{\circ}34'11''$ N and $103^{\circ}38'40''$ E in the South of Johor. The slope of the Balai Cerapan is classified as a cut slope with uniform slope geometry. The slope angles are approximately 21° and have a span of 47 m with 17 m in height.

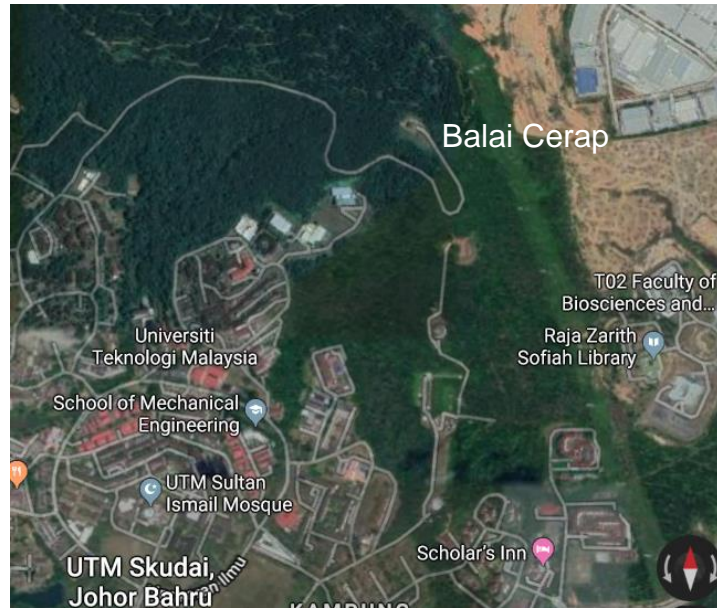


Figure 3.2: Location of the sample site; Balai Cerap, Universiti Teknologi Malaysia (UTM), Malaysia.

3.3.2 Soil Properties

The soil properties were an important input to present analysis procedures therefore it is crucial to define the properties of the collected soil samples. Prior to the initiation of physical modelling tests, the soil materials were placed in several trays and air-dried under laboratory conditions before thoroughly tested such as shown in Figure 3.3.



Figure 3.3: Air drying soil sample in the laboratory

All index and engineering properties works were done according to the British Standard BS1377: Part 1–9: 1990 and the American Society of Testing Method, ASTM: D2325-68: 2000 at the Geotechnical Engineering Laboratory, Universiti Teknologi Malaysia (UTM). The index property test was done according to BS1377 Part 2: 1990 which involves particle size distribution determination, Atterberg Limits and specific gravity (G_s).

Moreover, the determinations of the engineering properties of the soil sample were acquired through compaction and shear strength test. Compaction was done to measure maximum dry density (MDD) and optimum moisture content (OMC) of the soil sample. The tests were executed with guidelines procedures from BS1377 Part 4: 1990 to acquire the relationship between dry density and moisture contents. For the shearing test, consolidated isotropic undrained (CIU) triaxial compression test (Figure 3.4) was implemented to acquire the effective shear strength of the soil due to most of the natural slope in Malaysia are in consolidated and undrained conditions (Kassim, 2011). BS1377 Part 8: 1990 was used as the procedures for the present shear strength test.



Figure 3.4: Triaxial compression test

3.3.3 Determination of Soil Water Characteristic Curve (SWCC)

Soil water characteristic curve was determined experimentally using axis translation whereby air pressure (u_a) inside the laboratory equipment was increased while the pressure of the water phases (u_w) remained at atmospheric level (Simms and Yanful, 2004). The pressure plate extractor test was done at Geotechnical Engineering Laboratory, Universiti Teknologi Malaysia (UTM). ASTM D2325-68 (ASTM, 2000) was used as a guideline for the test procedure. The laboratory equipment of the pressure plate extractor test includes a chamber to withstand high pressure and a burette to measure extracted water as shown in Figure 3.5.

The test initiates with the sample preparations of weights determination (soil and sample rings) and filling the retainer rings with soil. The soil sample is positioned below a saturated (submerged in water for 24 hours) ceramic plate and sealed in the pressure plate moisture extractor apparatus. Pressure ranging from 1 to 15 kPa was induced into the soil sample and left overnight. Upon completion, the dry mass of each specimen and the water content for all the samples were measured. Volumetric water content (θ) of the soil sample can be computed from the equation:

$$\theta = \frac{wG_s}{1+e} \quad (3.1)$$

Thus, the SWCC can be configured from the relationship of volumetric water contents and matric suctions.



Figure 3.5: Pressure plate extractor setup in UTM

3.4 Equipment for Testing

3.4.1 Loading Frame

Series of loading on the model ground will be applied throughout the research. These loadings would have to be specifically tailored accordingly to simulate specific intended loading points. Additionally, a safe and repeatable environment is crucial for the execution of the loading. With this in mind; a rigid loading frame 2500 mm in length, 2000 mm in height and 1500 mm width steel frame was employed in this study such as shown in Figure 3.6.

The steel frame was designed to withstand a reversal of load (compression and tension) of 50 kN at every 100 mm spacing in both directions. In order to sustain the high loading executed during the loading stages, the loading frame was bolted and reinforced structurally to the floor of the laboratory. Throughout the study, it was concluded that the loading frame was sufficient to carry all the designated loads from

the loading stage and deemed to be rigid as the predicted deflection was less than 0.2% of the frame length.



Figure 3.6: Loading frame housing a testing chamber in physical modelling tests

3.4.2 Testing Chamber

A model of the soft ground was prepared in a rigid box with a dimension of 1000 mm in length, 800 mm height and 300 mm width as shown in Figure 3.7. Sidewalls of the chamber were made out of acrylic sheets (allowing visualization) and enclosed by a bolted steel frame for structural support. The base of the testing chamber was made dotted with small openings large enough to only let water drain out of the chamber during modelling (infiltration model).

One side of the model chamber was modified (holes added at designated coordinates) to allow for tensiometer apparatus installation such as shown in Figure 3.8. Holes for surface water run-off were also added to the side of the testing chamber to simulate a no-ponding upper boundary condition for the ground model during

experimentations. The model test preparation is discussed in detail on the following subsections.

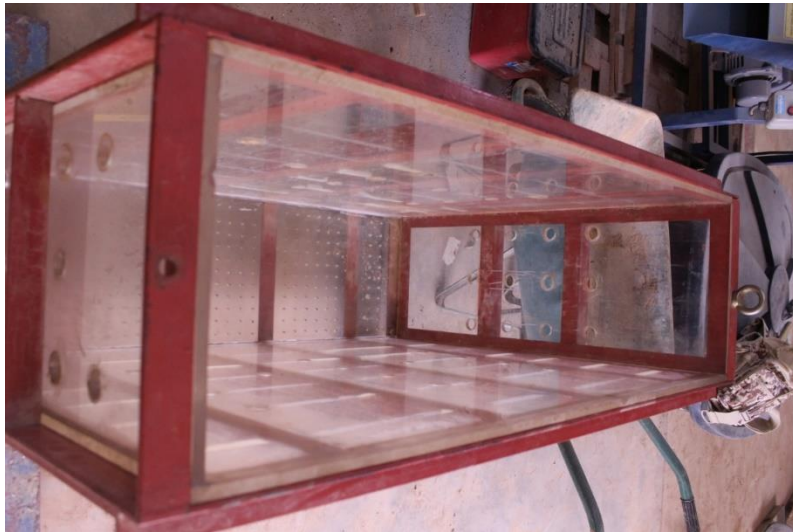


Figure 3.7: Testing chamber used to mould the model ground for physical testing (without soil)

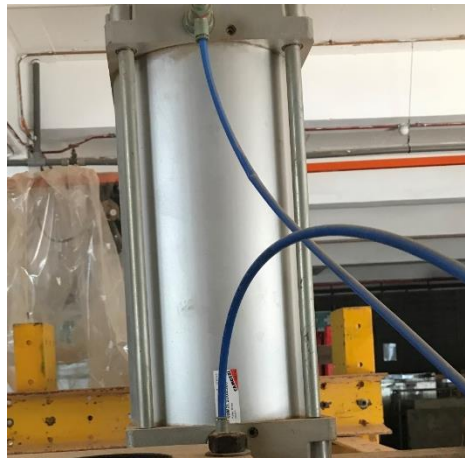


Figure 3.8: Tensiometer holes on the other side of the testing chamber

3.4.3 Pneumatic Cylinder

The model ground was applied with incremental pressure by a pneumatic cylinder as shown in Figure 3.9 (a) was manufactured by Camozzi Malaysia Sdn. Bhd. The maximum pressure to be exerted by the pneumatic cylinder was 8 kN equivalent to 10 bar at the pressure gauge. This pneumatic cylinder was supplied with constant

air pressure by an air compressor system that is controlled by a pressure reducing control valve. The pneumatic cylinder was bolted to the loading frame and attached with a loading shaft that rests upon a load cell and through it imposed pressure to the loading plate thus applying force to the soil surface (Figure 3.9(b)) in the loading stages if the physical modelling.



(a)



(b)

Figure 3.9: Pneumatic cylinder; (a) cylinder body and (b) pneumatic cylinder connected to a loading shaft and applying pressure to the model ground

3.4.4 Rigid Footing

A rigid footing was made from stainless steel with 150 mm width, 300 mm length and 20 mm thick in dimensions. The rigid footing was used as a load distributor

for the pressure from the pneumatic cylinder covering a 0.045 m² area to simulate loadings to the ground model. The rigid footing will be forced into the ground model until loading stages finishes such as shown in Figure 3.10. The rigidity of the loading plate was confirmed when predicted deflection of the footing was less than 0.2% of the footing length.

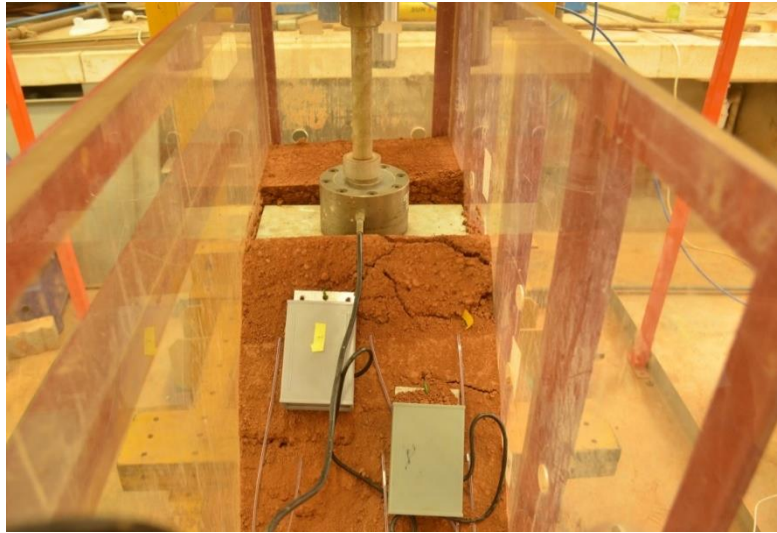


Figure 3.10: Loading plate pushed into the ground model to distribute loading

3.4.5 Rain Simulator

The rain simulator is a water flow system that includes a water storage tank, a water pump, polyvinyl chloride (PVC) piping system and a flow regulator to control rain intensity during rain simulations. An overall side view of the rainfall simulator apparatus is shown in Figure 3.11.

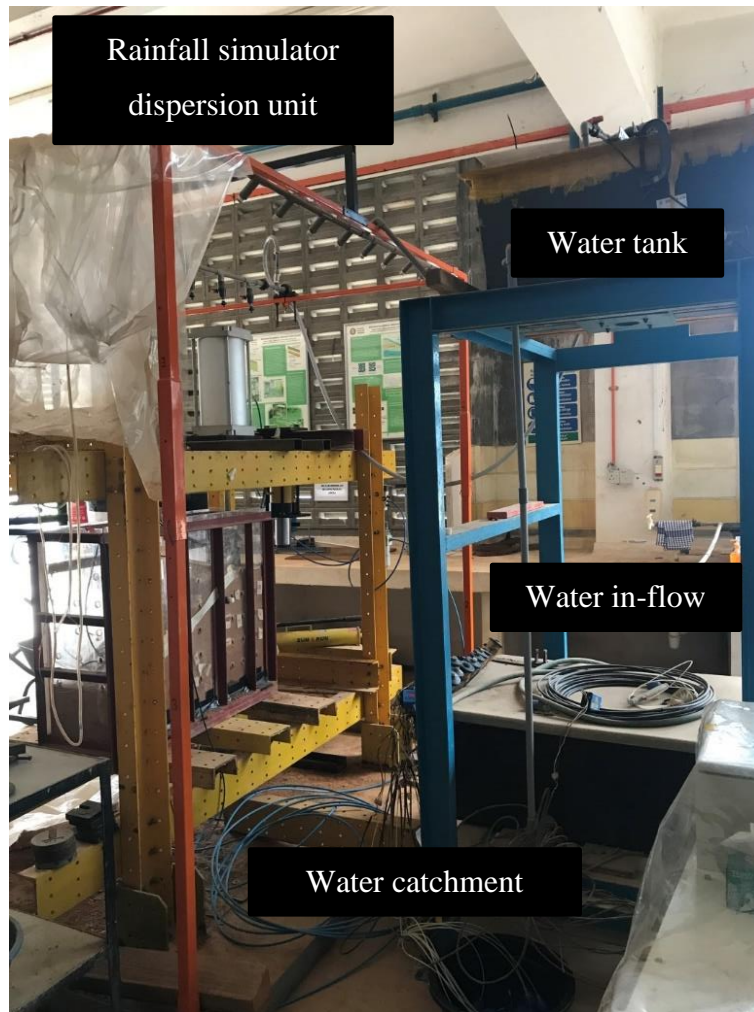


Figure 3.11: Rainfall simulator in the Geotechnical Laboratory Universiti Teknologi Malaysia (UTM)

The water storage tank was placed on top of a platform 2.8 m from the ground surface with a capacity to store 216 L of water at any given time. To maintain a steady-state flow of water into the rain simulator, a high-pressured water pump placed inside the water tank was used to supply a steady 8 L/min water flow into the system. Tap water was regulated throughout the rain simulator apparatus using 12.5 mm diameter PVC pipe and its flow can be controlled using several flow regulators installed at different parts of the simulator.

The rainfall simulator dispersion unit consists of a sprayer arm, sprayer nozzle and flow regulators. Rainfall was generated by using 8 sprayer nozzles each with its own regulator distributed 100 mm apart such as shown in Figure 3.12. Water was spread laterally from the sprayer through a pin-size-hole nozzle. To prevent excessive

force that may erode the ground model surface, the rainfall simulator was placed 1 m on top of the ground model supported by a steel frame. In addition, a steel catchment area of excessive rainfall was constructed in the bottom part of the simulator to prevent laboratory flooding incident. Through this setup, rainfall simulations were deemed to be delivered in a uniform pattern throughout the physical modelling.



Figure 3.12: Rainfall flow nozzles each with its regulators

3.4.6 Alignment Box

A target marker was used as a part of a calibration procedure when executing the PIV analysis. The target marker was constructed on a 5 mm thick Perspex with an area of 150 mm X 150 mm with the Perspex displaying multiple dotted grid-like textures with 20 mm spacing such as shown in Figure 3.13. The white dots overlaid by a black background were designed to ease detection for PIV analysis. Details of the target marker use are further discussed in the PIV subsection.



Figure 3.13: Target marker displayed in front of a ground model

3.5 Measurement Method

3.5.1 Data Logging and Acquisition

The research uses three separate sets of data logging and acquisition system which are for the loading stage data acquisition, tensiometer soil suction measurement and data logging by the AWAM system developed by the research. Three separate subchapters are used so that an enhanced description of the loggings is presented.

3.5.1.1 Loading Stage Physical Modeling

For the loading data acquisitions, LVDT and load cell apparatus were connected to a TML Data Logger and logged through a personal computer. A 100 mm stroke length Linear Variable Displacement Transducer (LVDT) type CDP-100 produced by Tokyo Sokki Kenkyujo Co. Ltd was utilized for measuring displacements during loading stages of the physical modelling. The LVDT used in the study was shown in Figure 3.14 attached to the loading frame using a magnet coupler to make sure the LVDT stays in place during the loading stages.

Figure 3.15 shows the 222 kN load cell model VLC-B120 produced by VMC California, USA used in the study to measure force. Both the LVDT and the load cell were connected to the 8 channel 16-bit Portable TML Data Logger (Figure 3.16) model number TDS-303 produced by Tokyo Sokki Kenkyujo Co. Ltd. and the readings are logged to a personal computer by a computer interface RS-232C using a USB2.0 cable.

To validate the results from the data acquisition from the loadings, the LVDT and load cell were each calibrated. A digital micrometre was used by pushing the LVDT slider in and out over a range of 0 to 100 mm in an incremental 2.5 mm intervals. In addition, Figure 3.17 indicates the setup that was used to calibrate the load cell. The load cell was mounted on top of another calibrated load cell and placed inside a load induce frame as shown. An incremental load of 200 N was induced into both load cells until 2 kN. Subsequently, the plot of voltage output and displacement of both the load cell and LVDT calibrations showed a great relationship with the calculated coefficient R^2 is equal to 1. The calibrations used in the research are included in Appendix A.



Figure 3.14: LVDT used to measure displacement units equipped with a magnet coupler



Figure 3.15: Load cell transducer made by VMC California USA used in the study



Figure 3.16: Portable data logger TML TDS-303 for loading stage data acquisition



Figure 3.17: Calibration of load cell commencing in the UTM laboratory

3.5.1.2 Tensiometer Soil Suction Measurement

In the same way, the LVDT and load cells are connected to a logging system, the tensiometers have a similar setup however coupled with a different kind of logging device. The CR800 model data logger by Campbell Scientific Inc. was used to log tensiometers data output as illustrated in Figure 3.18. The tensiometer logging system was connected to a personal computer in the same way as the logging system in the loading stage subsection mentioned previously. The CR800 data logger was installed with a 32 single-ended multiplexer (MUX AM416) to enable 12 tensiometer readings to be registered in a personal computer as revealed in Figure 3.19. A simple program was written to set up a means of connection between the logger and tensiometer devices by the logging software Loggernet 4.0.

Since the required power management for the tensiometer transducer system was 24 V and quite different instead of the power supply for CR800 data logger of 12 V, an AC/DC transformer was connected to the tensiometer transducer. This arrangement is likewise to the laboratory system setup by Kassim (2011) only but the

absence of a solid-state relay due to the short period of time used to log tensiometers data.



Figure 3.18: The data logger by Campbell Scientific model CR800 used by tensiometers data logging with protruding labelled wires connected to all the tensiometers used in the study

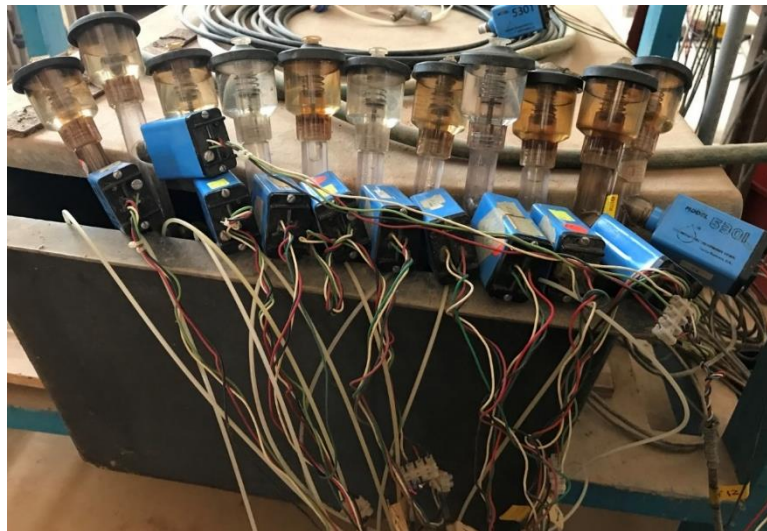


Figure 3.19: 12 units of tensiometers with wires connecting to the data logging system

The tensiometer transducer was calibrated by the supplier of the tensiometer apparatus on-site for data acquisition validation. A vacuum hand pump and an

Ammeter was used as the calibration apparatus such as shown in Figure 3.20. Vacuum conditions were applied in the increment of 25 centibars (cbs) up until 100 cbs and readings of the Ammeter are recorded. The relationship between the centibars (cbs) and milliamp (mA) was consequently calculated to be in good relationship with the R^2 equals to 1.

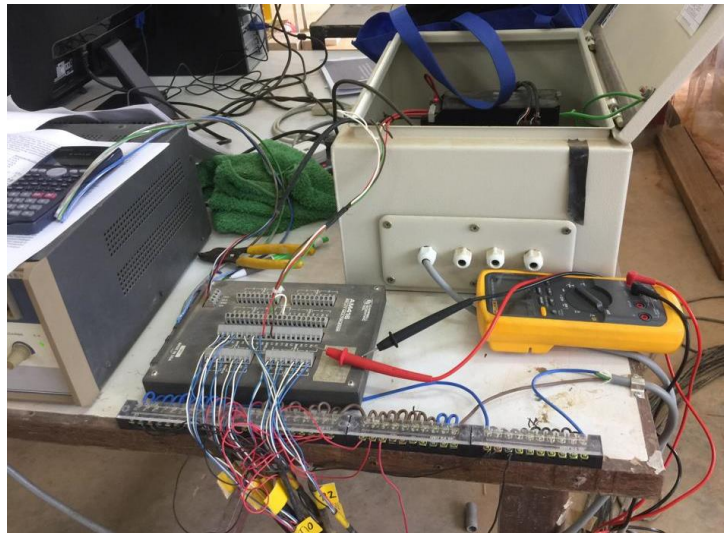


Figure 3.20: Calibration of tensiometer readings are being carried out with an Ammeter milliamp (mA) reading of tensiometer on the multiplexor used in the study

3.5.1.3 AWAM Device

In the case of the slope failure, predictive data logging by the newly developed lab scaled Automated Wireless Accelererometer Monitoring (AWAM) system, data logging was done wirelessly through the system's wireless Bluetooth receiver connected to a personal computer. Two AWAM devices powered by portable 10000 mili Ampere-hour (mAh) Power Banks that was placed on top of the ground model was employed as the data acquisition apparatus to detect slope movement in this study as illustrated in Figure 3.21.

The AWAM device data measurement was recorded into a personal computer using a windows interface by the name of AG GPS Reader that was also developed by the research such as shown in Figure 3.22. Validation of both the device's data acquiring capabilities is further discussed in the following chapter.



Figure 3.21: The two AWAM devices on top of a ground model being powered by a Power Bank clamped to the testing chamber during loading stages

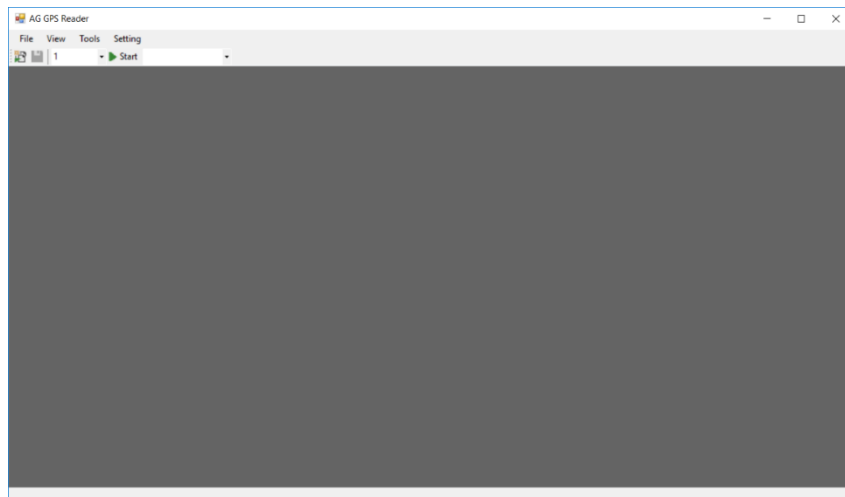


Figure 3.22: AG GPS Reader program used to monitor readings from the AWAM device installed onto a personal computer

3.5.2 Digital Camera

It goes without saying that a still digital photography camera has a more qualitative resolution and image quality as compared to a video camera. This quality is essential as an input for numerical simulations in this research. Thus, a Canon model D5100 digital camera with 16.2 MP (4928 x 3264) was chosen as the charge-couple device (CCD) to capture a series of still photos of soil deformation through the Perspex window of the testing chamber.

The Nikon D5100 camera was mounted on a Manfrotto model Mk394-H aluminium tripod (Figure 3.23) and placed on a designated marker just 720 mm in front of the testing chamber. A balancing bubble attached to the tripod was utilized to make sure the camera setup was propped upright during photo acquisitions.



Figure 3.23: Canon D5100 on an aluminium tripod used in the research

Table 3.1 shows the specifications of Nikon D5100 used in the study. The camera was fitted with an 18-55 mm Nikon lens model AF-S DX Nikkor. The camera lens was set to capture still photos manually, using a remote shutter switch to avoid unnecessary movement of the camera that may affect the quality of the photos during photo acquisitions. A dark backdrop was propped behind the camera to minimize the reflective properties of the Perspex glass. The ISO was set to a constant value of 400 during the entire photo attainments. Continuous shoot mode was set to the camera and images were taken on an average rate of 0.8 frames per second. Photos from the camera were transferred to a personal computer via memory card transfer and used in the analysis.

Table 3.1: Nikon D5100 digital camera specifications

Parts	Specifications
Main body	Type: Single-lens reflex digital camera Dimensions: 128 x 87 x 79 mm Weight: 560g Effective pixels: 16.2 million Image sensor :23.6 x 15.6 mm CMOS sensor
Storage	Image size (pixels): 4,928 x 3,264 (L) File format: JPEG (JPEG-Baseline compliant with fine (1:4), normal (1:8) or basic (1:16) compression)
Shutter	Type: Electronically-controlled vertical-travel focal-plane shutter Speed: 1/4000 to 30 s in steps of 1/3 or 1/2 EV
Exposure	ISO sensitivity: ISO 100 to 6400 in steps of 1/3 EV
Focus	Autofocus: Nikon Multi-CAM 1000 autofocus sensor module with TTL phase detection, 11 focus points (including one cross-type sensor) and AF-assist illuminator Lens servo: Manual focus (MF); Electronic rangefinder can be used
White balance	Auto, incandescent, fluorescent (7 types), direct sunlight, flash, cloudy, shade, preset manual, all except preset manual with fine-tuning

3.6 Model Preparation

The following subchapters would portray the model preparation stage prior to the loading stage. Basic procedures for mixing, consolidation and model trimming are portrayed lengthily.

3.6.1 Laterite Mixing

The ground model soil was prepared in an industrial size mixer by combining a total of 286.5 kg of laterite soil from the site with 31 kg of distilled water in five separate batches. The soil was air-dried for at least 48 hours and sieved passing 2 mm for the test to gain homogeneity conditions. The soil used was placed into the mixer while distilled water was poured slowly onto it, all while the mixer slowly turns such as shown in Figure 3.24.



Figure 3.24: Slowly pouring distilled water into the mixer

Personal protection equipment such as mask, gloves and glasses were worn during the mixing process as the soil debris would be dispersed nonchalantly during the whole mixing process. The whole mixing process was done in between three to four intervals with each session lasting up to 15 minutes. During each intersession, lumps of soil mass were broken up using hand tools. A final 30 minutes of mixing was executed to ensure a proper mix was done.

3.6.2 Slope Construction

Slope construction was performed in two main stages, the first stage being filling and compacting while the next procedure is to trim the ground model to its desired geometry.

3.6.2.1 Testing Chamber Preparations, Filling and Compaction

The first step to prepare the ground model was to fill and compact the soil into the testing chamber as described in subchapter 3.4.2. The testing chamber gaps were first secured using a multi-purpose silicone rubber filler meant to keep the soil from leaking out such as shown in Figure 3.25.



Figure 3.25: Filling the gaps between the testing chamber acrylic sides with silicone rubber

In order to maintain the intended moisture content, density, and homogeneity of the soil, soil compaction was performed in 5 layers. After filling up the testing chamber with the ground model soil, soil compaction was done by manual stamping of the ground model using hand tools with a constant 30 blows per layer such as shown in Figure 3.26.



Figure 3.26: Manual compaction of the ground model using a hand tool

The first layer was designed to a thickness of 100 mm; which was comprised of a 50 mm height layer of coarse gravel meant for drainage layered by a 50 mm height of the ground model soil while the remaining layers were constructed at 100 mm in

height respectively. The top layers are modelled into its intended geometry with the assistance of several pieces of wood (formwork) as illustrated in Figure 3.27.



Figure 3.27: The compaction of the ground model being modelled into 5 layers and shaped with formwork whilst the first layer being layered with 50 mm gravel.

The top surface of each layer was scratched before constructing the next layer, to keep the layers interconnected and to avoid inhomogeneity in the model. The ground model was left for a few hours while preparations for the trimming procedure were done.

3.6.2.2 Model Trimming

After compaction of all the layers in the designated frame, the designed gradient of the slope was created by carefully removing the extra volume of the soil from the model. Hand tools such as scraper and measuring tape were used to trim the ground model into its intended design model such as shown in Figure 3.28. The proposed gradient of the model varied from a ratio of 1:2 and 1.15 vertical to horizontal ratio. The final ground model after trimming was done is illustrated in Figure 3.29.



Figure 3.28: Reshaping the ground model onto its intended shape with hand tools



Figure 3.29: Finished ground model setup ready for testing

3.7 Model Soil Test

This subsection describes the test notation and model test procedure for the ground model including the procedure for the loading stage, tensiometer and PIV data acquisition.

3.7.1 Test Notation

The schemes for the testing are shown in Table 3.2. The tests are divided into two heights to width ratio and different intensities of simulated rainfall.

Table 3.2: Test scheme for experiments

Test	Test Notation	Height (mm)	Width depth ratio	Rain Intensity (mm/h)	Area of Load (m ²)	Rain Duration (hrs)
1	Case A	500	1:2	1.7196×10^{-5}	0.15	1 hour
2	Case B	500	1:2	1.7694×10^{-6}	0.15	24 hours
3	Case C	500	1:2	0	0.15	0
4	Case D	500	1:1	1.7196×10^{-5}	0.15	1 hour
5	Case E	500	1:1	1.7694×10^{-6}	0.15	24 hours
6	Case F	500	1:1	0	0.15	0

3.7.2 Model Test Procedure

After the completion of the ground model as described in subsection 3.6, the ground model was relocated to the test area inside the loading frame. Then, the arrangement for the tensiometer installations commences. 12 units of pre-calibrated tensiometers were installed into the ground model. Each tensiometer's ceramic tip was inserted into designated holes of the testing chamber accordingly as illustrated in Figure 3.30.



Figure 3.30: 12 units of tensiometer installation into the ground model

The ground model was subjected to rainfall simulation as mentioned in subsection 3.4.5 for the varied duration of 1 to 24 hours of rainfall according to the intended rainfall duration in the test scheme. About 70% rainfall will be applied to the model according to the actual data record in field data while the remaining 30% will be assumed to be surface runoff (Rahardjo et al., 2013).

After rainfall simulations ended, the pneumatic cylinder was installed on top of the ground model by attaching it to the loading frame. A loading plate was placed in its designated location just below the pneumatic cylinder on top of the ground model. Following that, LVDTs were installed on the frame and attached to the pneumatic cylinder to record the vertical displacement of the soil. The load cell for the loading stage was placed on top of the loading plate and the pneumatic cylinder was descended promptly on top of the load cell. The data acquisition system of the loading and vertical displacement as mentioned in subsection 3.5.1.1 was then arranged accordingly.

Simultaneously, AWAM devices will be set up on top of slope surface; one device on top of the slope surface (AWAM1) and the second one will be in the middle of the slope surface (AWAM2) as illustrated in Figure 3.31. The AWAM devices were embedded into the soil model using a stainless-steel anchorage system to make sure the device can provide proper rotation readings as the y-axis is fixed. The depth of the anchorage system was made to pass the expected slip circle failure to provide reliable data. Further discussions on the rotation readings of the AWAM device will be made in the following chapter. Data for the AWAM device was recorded wirelessly via Bluetooth in 1s interval as mentioned in subchapter 3.5.1.3.

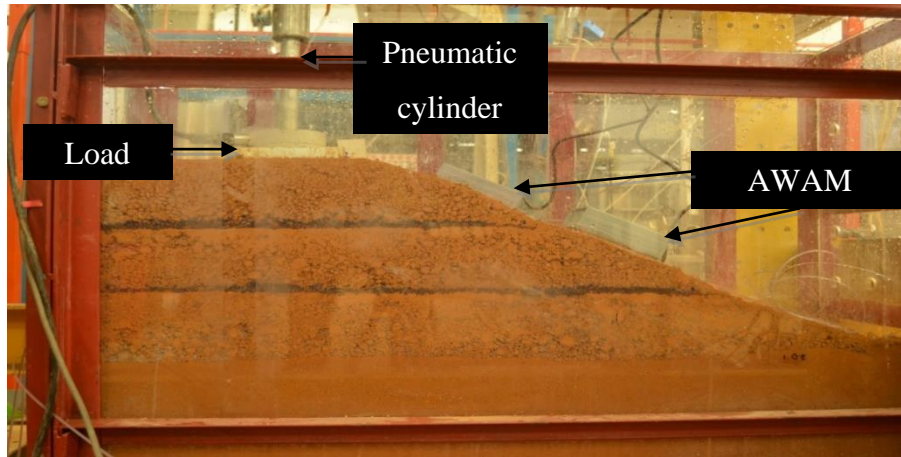


Figure 3.31: AWAM device location on the model ground

After completing the procedures for the loading data acquisition and AWAM installations, the digital camera as mentioned in subsection 3.5.2 was placed in front of the testing chamber and prepared accordingly as shown in Figure 3.32.



Figure 3.32: Camera Setup for PIV data acquisition

After all, preparations are complete, the loading test commences with the initiation of the pneumatic cylinder with an eight-bar force acting on the ground model. All data acquisition units including the data for the vertical displacement, loading, AWAM device and camera still shots are prompted and recorded simultaneously for the whole duration of the load-bearing until significant failure to the ground model was observed.

3.8 Particle Image Velocimetry (PIV)

3.8.1 Introduction

This subchapter describes the steps of post-processing of images captured during the loading stages. In addition, it also describes the details on the PIV analysis for it to observe soil displacement patterns during loading until failure. The process description would be divided into three categories which are pre-analysis, PIV analysis and post-processing.

3.8.2 Pre-PIV Analysis

After the images from the loading stage are transferred from the camera to a computer, a series of steps are required to prepare the images for PIV analysis. The steps are described as the following:

1. Firstly, the images are carefully selected to be in the range of 50 total images. Blurry or incoherent series of pictures (inconsistent sequence of pictures due to surrounding interferences) are taken out of the analysis. Bear in mind that the series of images also would cover the whole duration of the loading stages from the start test until the test finally stops due to meeting failure condition.
2. Next up are the renaming procedure of each selected images. Each selected images are required to be numerically identified, having sequential order i.e. DSC_XXXX followed by DSC_XXXY where XXXX and XXXY are the nth number of a sequence followed by a (n+1) th sequence of the image names.
3. Following that, two folders are created and named 'TestX' and 'Targetmarker' where X is the number designated for a specified test. Bear in mind the name of the folders would require for it to not have spaces in them as the MATLAB program would not register names with spaces in

them. TestX would contain all the selected images while Targetmarker would house an identically numbered series of images of the first picture that is copied 50 times over.

4. In addition, all the files of codes and subroutines from the PIV analysis are copied into both folders. Figure 3.33 shows the Pre-PIV analysis stage that has finished its preparations.

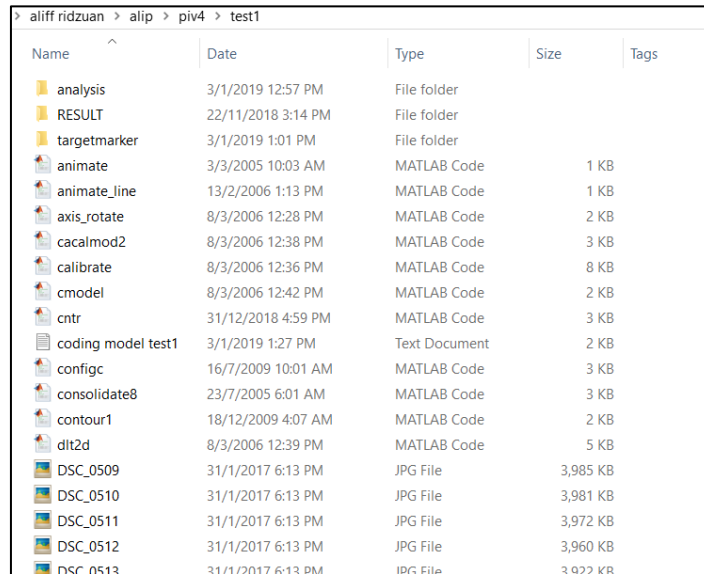


Figure 3.33: Screenshot of a proper finished preparation folder, ready for PIV analysis that contains folders for a result, target marker and subroutines from the GeoPIV8 module

5. In addition, a text file named 'XYCoordinate' with the coordinates of each target marker point such as illustrated in Figure 3.34 was created and added into the Targetmarker folder.

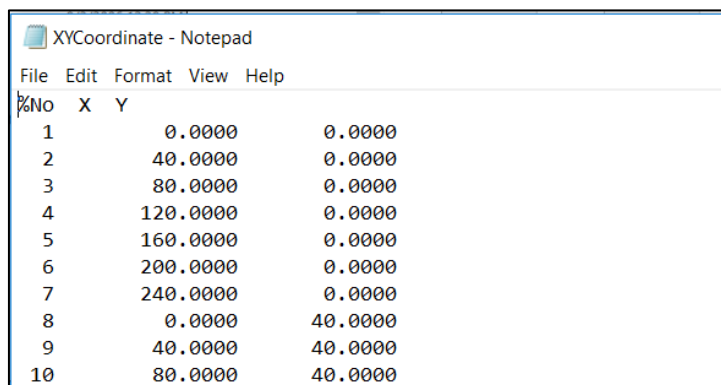


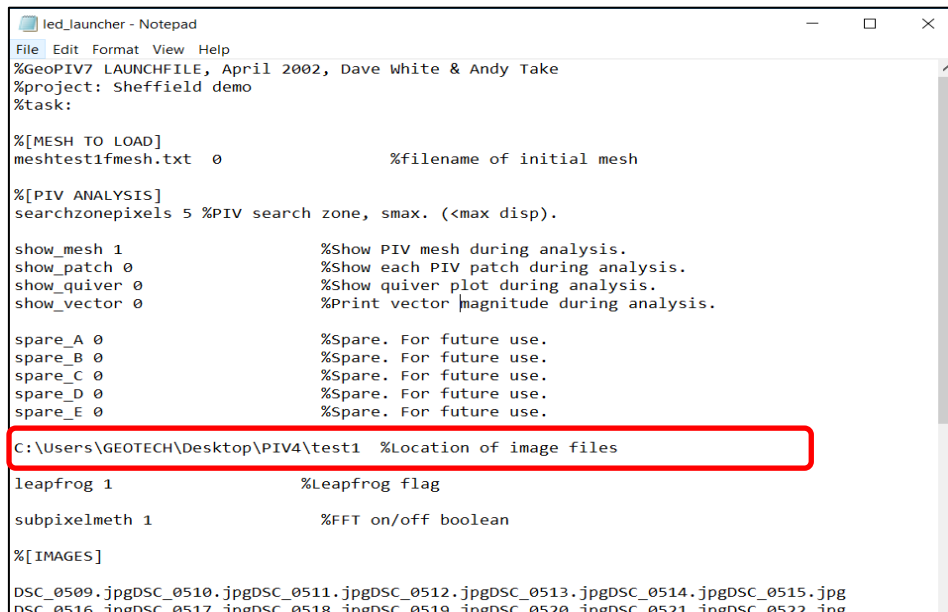
Figure 3.34: XYCoordinate file example placed in the Targetmarker folder

3.8.3 Running Procedures of the PIV Analysis

To run the PIV analysis, the research utilizes a MATLAB based PIV module by the name of GeoPIV8. Steps on executing the PIV analysis are portrayed extensively in the following subchapters.

3.8.3.1 Inspection of Subroutines

After preparation stages have been finalized, there would be codes and subroutines that are required to be modified to suit the need for the analysis. First of all, we have to make sure that all the subroutines and codes are present and in accordance to the GeoPIV8 module. Highlighted are the subroutines that are in need of some modification which is the 'led_launcher.txt'. These subroutines must be adjusted to be according to the current ongoing test. Figure 3.35 illustrates the modified led_launcher file that suits the current analysis.



```
led_launcher - Notepad
File Edit Format View Help
%GeoPIV7 LAUNCHFILE, April 2002, Dave White & Andy Take
%project: Sheffield demo
%task:

%[MESH TO LOAD]
meshtest1fmesh.txt 0 %filename of initial mesh

%[PIV ANALYSIS]
searchzonepixels 5 %PIV search zone, smax. (<max disp).

show_mesh 1 %Show PIV mesh during analysis.
show_patch 0 %Show each PIV patch during analysis.
show_quiver 0 %Show quiver plot during analysis.
show_vector 0 %Print vector magnitude during analysis.

spare_A 0 %Spare. For future use.
spare_B 0 %Spare. For future use.
spare_C 0 %Spare. For future use.
spare_D 0 %Spare. For future use.
spare_E 0 %Spare. For future use.

C:\Users\GEOTECH\Desktop\PIV4\test1 %Location of image files

leapfrog 1 %Leapfrog flag

subpixelmeth 1 %FFT on/off boolean

%[IMAGES]
DSC_0509.jpgDSC_0510.jpgDSC_0511.jpgDSC_0512.jpgDSC_0513.jpgDSC_0514.jpgDSC_0515.jpg
DSC_0516.jpgDSC_0517.jpgDSC_0518.jpgDSC_0519.jpgDSC_0520.jpgDSC_0521.jpgDSC_0522.jpg
```

Figure 3.35: led_launcher file adjusted to suit the location of image files

3.8.3.2 Running regimlistgen

Enter the command `regimlistgen` into the MATLAB program and entering values of image start (first image number i.e. XXXX), image end (last image number) and `'step=1'`. The command `regimlistgen` will update the list in `'registered_propics_list.txt'` and its updated contents are copied onto the `[% [IMAGES]'` part in the `led_launcher` file. The file is then saved for further processing. Figure 3.36 illustrates the contents of `'registered_propics_list.txt'` file after running the `regimlistgen` command.

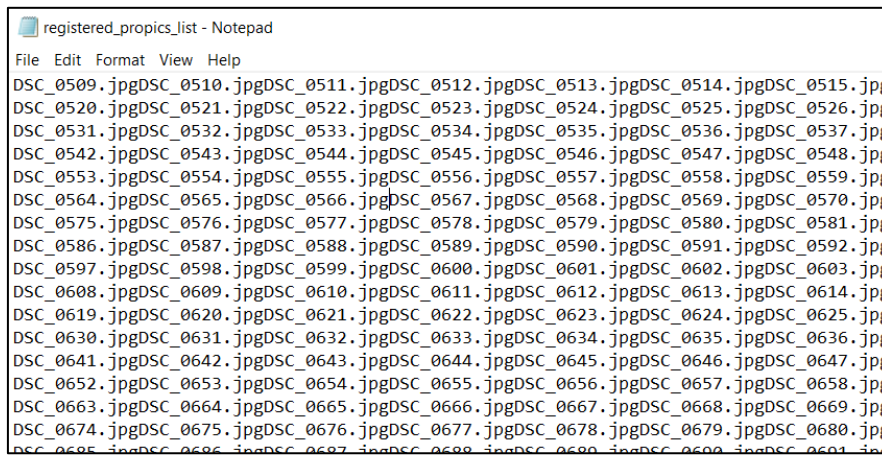


Figure 3.36: `registered_propics_list` file generated after running `regimlistgen` command

3.8.3.3 Running fmeshing

After reinserting the image list generated, next up is the command for meshing the images in the analysis by entering the command `"fmeshing('DSC_XXXX','testX',50)"`. XXXX is the number of the first image, testX is the string name of the current analysis and the value 50 is the patch size. A window to select the mesh area will be prompt. Close the window after the selection has been done. Figure 3.37 shows the window of selection for the fmeshing area of the intended first image on the current test.



Figure 3.37: Meshing of the target image

3.8.3.4 Running GeoPIV8

Next, the command “GeoPIV8” would be entered and the analysis proceeds after the selection of the ‘led_launcher’ file as the subroutine when prompt. In the analysis folder, several files named ‘PIV_DSC_XXXX_DSC_XXXY’ would be generated. XXXX and XXXY are the nth and (n+1)th images in the analysis. Figure 3.38 depicts the several files generated by entering the GeoPIV8 command.

Name	Date	Type	Size
mousemeshrandom	21/1/2003 10:40 PM	MATLAB Code	3 KB
out.prn	23/9/2018 3:36 PM	PRN File	42 KB
patchshow8	23/7/2005 6:04 AM	MATLAB Code	6 KB
PIV_DSC_0509_DSC_0510	2/1/2019 1:25 PM	Text Document	241 KB
PIV_DSC_0510_DSC_0511	2/1/2019 1:25 PM	Text Document	241 KB
PIV_DSC_0511_DSC_0512	2/1/2019 1:25 PM	Text Document	241 KB
PIV_DSC_0512_DSC_0513	2/1/2019 1:25 PM	Text Document	241 KB
PIV_DSC_0513_DSC_0514	2/1/2019 1:25 PM	Text Document	241 KB
PIV_DSC_0514_DSC_0515	2/1/2019 1:25 PM	Text Document	241 KB
PIV_DSC_0515_DSC_0516	2/1/2019 1:26 PM	Text Document	241 KB
PIV_DSC_0516_DSC_0517	2/1/2019 1:26 PM	Text Document	241 KB
PIV_DSC_0517_DSC_0518	2/1/2019 1:26 PM	Text Document	241 KB
PIV_DSC_0518_DSC_0519	2/1/2019 1:26 PM	Text Document	241 KB
PIV_DSC_0519_DSC_0520	2/1/2019 1:26 PM	Text Document	241 KB
PIV_DSC_0520_DSC_0521	2/1/2019 1:27 PM	Text Document	241 KB
PIV_DSC_0521_DSC_0522	2/1/2019 1:27 PM	Text Document	241 KB

Figure 3.38: Several files named ‘PIV_DSC_XXXX_DSC_XXXY’ that is generated by entering the GeoPIV8 command

3.8.3.5 led_launcher Processing and Running regimlistgen Command for targetmarker Folder

Tracking back to the ‘targetmarker’ folder, steps from subchapter 3.8.3.1 and 3.8.3.2 (led_launcher setup and regimlistgen) are repeated and adjusted according to the targetmarker analysis.

3.8.3.6 Running geoCENTROID8

In the command window, the command ‘geoCENTROID8(‘testX.txt’,300,32,0,350)’ was entered. geoCENTROID8 is the subroutine, testX is the string name for the current test, 300 is the size of selection for the target market dot, 32x32 is the mesh size and the value 0 and 350 is the centroid search threshold. After the command geoCENTROID8 was entered, it would prompt a selection of images from the targetmarker folder. Selecting the first image would prompt a window showing the first image. The centre of each black dot on the physical target marker was selected, prompting a red square box centring on the selection point such as illustrated in Figure 3.39. Finishing the remaining selection on the target marker point would trigger the analysis to search for the centroidal points of each target marker dot such as shown in Figure 3.40. Upon completion, a MATLAB window to manually select the lower and upper threshold would be prompt. The geoCENTROID8 subroutine would end after selecting the range of lower and upper threshold with the most linear value. A centroiding result would be created in the ‘targetmarker’ folder containing two files with the name CENTROID_testX.txt and CONTROL_testX.

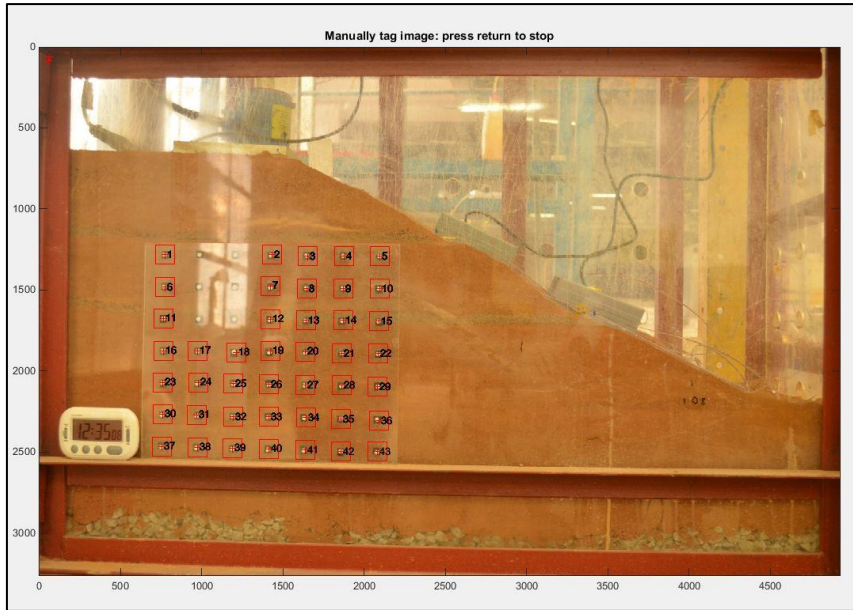


Figure 3.39: Tagging physical target marker prompting red squares and numbering on the centre of the black dots of the target image

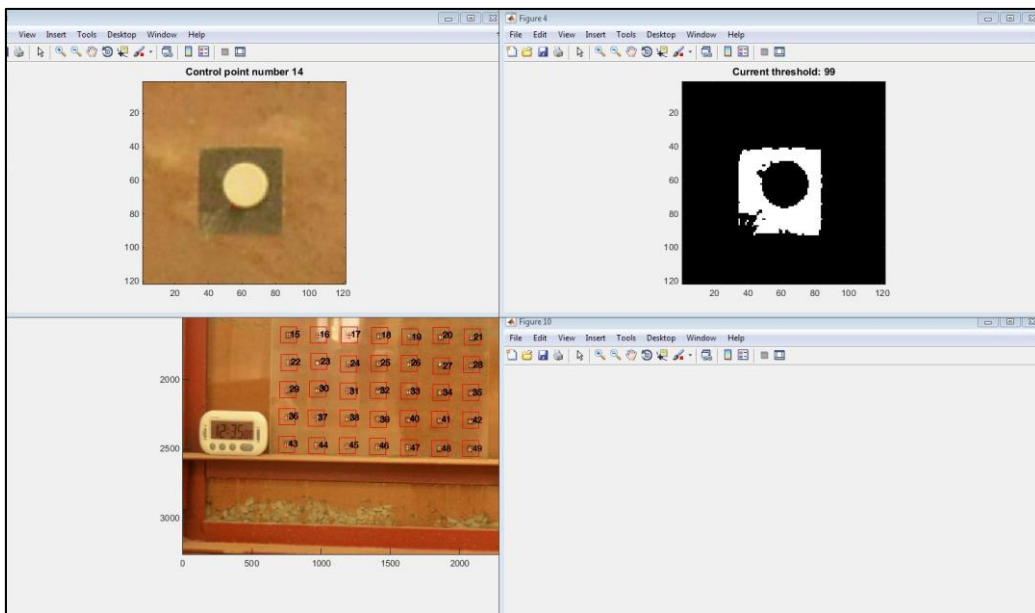


Figure 3.40: The subroutine geoCENTROID8 running to find the centroid of each dot on the target marker

3.8.3.7 Running fmeshing and GeoPIV8 on the targetmarker Folder

Steps in subchapters 3.8.3.3 and 3.8.3.4 were repeated for the targetmarker folder. The proper led_launcher file in the target marker folder was selected. As per the 3.8.3.4 step, similar resulting files would be generated.

3.8.3.8 Running consolidate8

Tracking back to the main folder testX in the MATLAB program directory, the command 'uvdata=consolidate8' was entered. When prompted, the 'led_launcher' file from the main testX folder was selected. This step is to consolidate the data written by the analysis.

3.8.3.9 Running geoCALIBRATE8(uvdata) (Calibration with the targetmarker)

The ninth step is to input the command '[XYdata]=geoCALIBRATE8(uvdata)' while selecting the led_launcher file from the target marker folder, followed selecting the file 'XYCoordinate' such as shown in Figure 3.41. These steps are taken to calibrate the coordinates from the target marker folder, thus transitioning the points calculated in the MATLAB program from space vector to actual empirical (mm) readings.

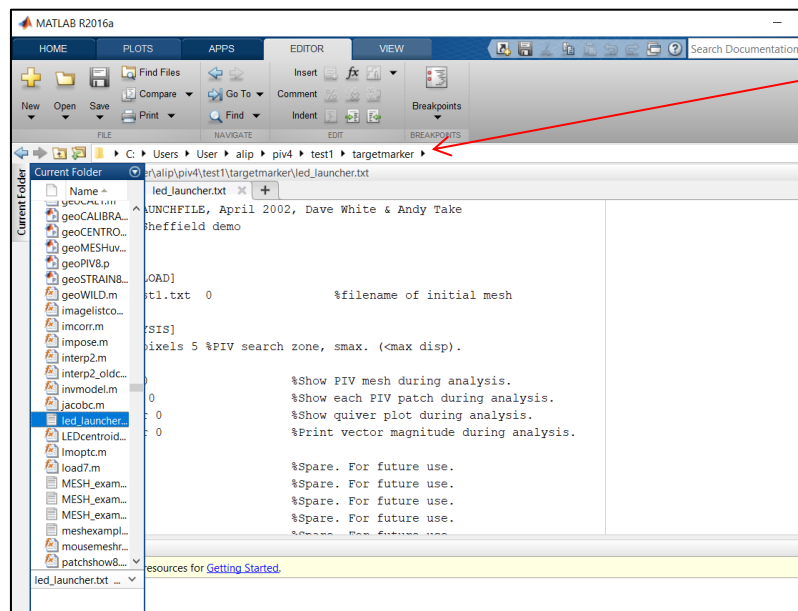


Figure 3.41: The highlighted file of led_launcher to be selected during geoCALIBRATE8 step that is in the target marker folder

3.8.3.10 Running qq.m (Vector Result)

The vector result for the PIV analysis would be plotted by entering the command 'qq(XYdata,1,50,1)'. The number 1 and 50 represents the first and the 50th image respectively while the 1 at the end denotes the scale of the result. Figure 3.42 illustrates the 'qq.m' subroutine result for the vector of the current test. Note that several customizations were done to the 'qq.m' subroutine for an intended result on the configuration of the result.

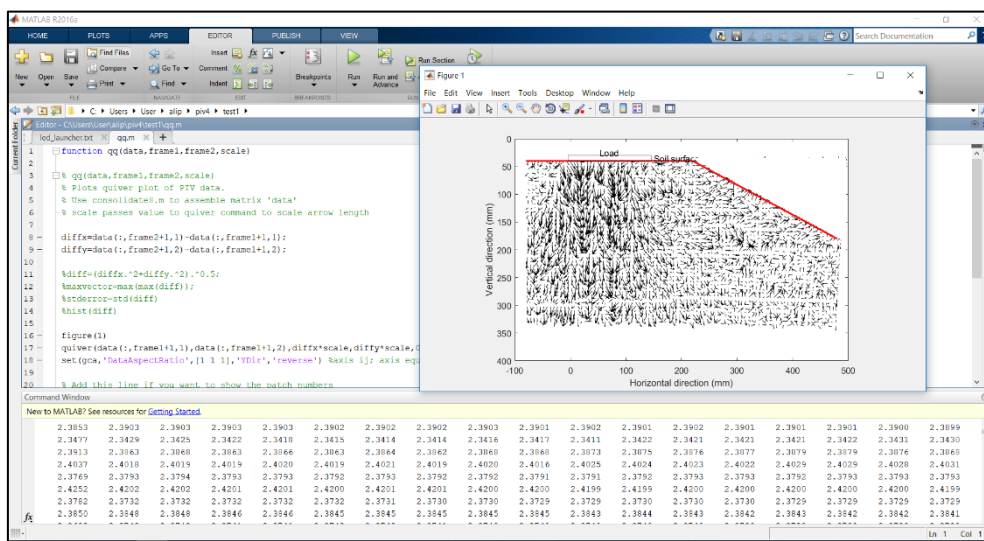


Figure 3.42: Vector for testX simulated after qq.m command

3.8.3.11 Running cntr (Contour Mapping)

The following procedures are optional to further enhance the output of the PIV analysis. By entering the command 'cntr(XYdata,1,50,8)', the program would prompt the cumulative contours of displacement for the current analysis. The number 1 represents the number of the first image while 50 is the 50th image from the total image used in the analysis. The 8 is the scale of the intended contour result. Similar to the vector case, several customizations were done to the 'cntr.m' the subroutine which is the configurations for the intended output of the plot. An example of the proper customization such as the label, colour, contour range of value, lines of the ground model geometry and the labelling in the PIV analysis is illustrated in Figure 3.43.

```

40 - end
41 - end
42 - %im=imread(strcat(filename1,'.JPG'));
43 - %im=imread('sf10_001.JPG');
44 - %imagesc(im); colormap(gray);axis image
45 - %hold on
46 - v = ([-10,-8,-6,-4,-2,2,4,6,8]);
47 - [G,h] = contour(xa,ya,va,v);
48 - set(h,'ShowText','on','TextStep',get(h,'LevelStep')*1)
49 - xlabel('Horizontal direction (mm)')
50 - ylabel('Vertical direction (mm)')
51 - colormap cool
52 -
53 - axis ([-100 800 -200 250])
54 - axis ij
55 - line ([-100 200],[-125 -125],'Color','r','LineWidth',2);
56 - line ([200 800],[-125 175],'Color','r','LineWidth',2);
57 - %line ([900 1000],[175 250],'Color','r','LineWidth',2);
58 - rectangle ('position',[-25,-135,150,10]);
59 - text (130,-135,'Soil surface')
60 - text (50,-145,'Load','horizontalAlignment','center');

```

Figure 3.43: The code customized for the subroutine ‘cntr.m’ used in the PIV analysis

3.8.3.12 Plotting Shear Strain

In order to plot the shear strain of the model for the PIV analysis, there are two commands to be entered into the MATLAB program; the first one being ‘[strains]=geoSTRAIN8(XYdata)’. Following that, a window prompting a file selection would appear and by selecting the ‘ELE_testX’ file from the main folder analysis, the analysis would proceed with the analysis. To plot the current test outcome of the shear strain of the analysis, the command ‘plotstrains(strains,50,1)’ would be entered. 50 is the number of images that are intended for the total strain plotted. For the plotting of the whole test, 50 images were used as an input. The number 1 represents the value of total maximum shear strain. This value can be changed to 2 for the output of total volumetric strain and the number 3 which is the incremental maximum shear strain such as illustrated by the green coloured command in Figure 3.44. The strain value would be displayed in the % value.

It was noted that similarly to the vector and contour analysis described in subchapter 3.8.3.10 and 3.8.3.11, several adjustments and customization according to

the current analysis are required before the intended values such as the scale, area of plot, coarseness and values of the plot are correctly plotted.

```

function plotstrains(strains, frame, quantity)

% Plotting of strain data produced by geoSTRAIN8
% strains: output from geoSTRAIN8
% frame: final frame of interest (total strains plotted between start and this frame)
% quantity: 1- total maximum shear strain, 2- total volumetric strain, 3- incremental maximum shear strain
% strains displayed in %.
% NOTE: YOU WILL NEED TO EDIT LINES 25 & 26 TO SET THE COARSENESS OF THE PLOT
% DJW 27/2/05

ele_x=strains(:,frame,2); % X coordinate
ele_y=strains(:,frame,3); % Y coordinate

ele_exx=strains(:,frame,4+1)*100; % total XX strain
ele_eyy=strains(:,frame,5+1)*100; % total YY strain
if quantity==1
    ele_strain=strains(:,frame,9+1)*100; %
elseif quantity==2
    ele_strain=strains(:,frame,11+1)*100;
elseif quantity==3
    ele_strain=strains(:,frame,22+1)*100;
end

% SET COARSENESS OF PLOT
xxi=-50:10:4000;
  
```

Figure 3.44: The ‘plotstrain.m’ the subroutine that plots the strain for the PIV analysis

3.8.4 Repetition of Steps for Subsequent Set of Analysis

The process mentioned in subsections 3.8.2 and 3.8.3 was repeated for each set of images captured during the whole research. The algorithms used in the research are included in Appendix B.

3.9 Concluding Remarks

This chapter initiates by describing the methodology employed in this research through a flow chart explaining the overview of the research plan. Furthermore, the chapter discussed the materials and equipment used in the testing. Determination processes of the site selection, soil properties and Soil Water Characteristic Curve (SWCC) are explained in detail. In addition, all the equipment for the testing stages are all listed out and explained in detail in each of its subchapters.

Measurement methods of different sets of data acquisitions are compiled and presented such as for the loading stages, Tensiometer data acquisitions and Particle Image Velocimetry (PIV) data acquisitions. Worth to note that the three sets of data acquisitions are simultaneously running in each set of testing, thus highlighting the importance of pre-testing checks and calibrations to ensure a smooth and orderly experimentation setup. Each of the subchapters was laden with images and sketches of applied apparatus and specifications for future researches reference.

The model preparation setup, slope construction and test procedures were also explained in detail in the chapter. Step by step process and procedures are strengthened by the addition of images to simplify explanations. Measurement apparatus placement and preparations were detailed from the initiation of the test until the final step of testing.

The chapter was finalized by fully describing the preparations and procedures for the Particle Image Velocimetry (PIV) analysis from the pre-processing stage until the final analysis steps to produce a vector, contour and shear strain results.

CHAPTER 4

CALIBRATION OF SLOPE MONITORING DEVICE

4.1 Introduction

Calibrations were required to properly ascertain the accuracy of output for the slope monitoring device developed by the research. The procedures for the calibrations were modifications to procedures suggested by Carver and Looney (2008), Fisher (2010), Evans et al. (2014), Baranilingesan and Rajesh (2018), Bravo-Haro and Elghazouli (2019). Carver and Looney (2008) studied the values of the calibration of accelerometers for industrial applications in terms of the performance impact of the accelerometers towards industrialization. Fisher (2010) prepared an application note on the determination of inclination of an accelerometer. Baranilingesan and Rajesh (2018) further demonstrate the application notes done by Fisher (2010) by applying the inclination calculation onto a programmable inclination sensing using accelerometers. Meanwhile, Evans et al., (2014) researched about the performance of several low-cost accelerometers and suggested several accelerometer tests including Box-flip test, Transfer-function tests and Clip and Linearity tests to study the response of all the accelerometers models. These testing were then refined in Bravo-Haro and Elghazouli (2019) research to assemble low-cost seismic sensing. Figure 4.1 demonstrates the raw value of the Box-Flip accelerometer data output for the calibration purposes of Evans et al. (2014) calibrations. Evans et al. (2014) reported on the readings changes of an accelerometer attached to a box when subjected to a 360° flipping. The phase changes of the accelerometer were well documented until finally, it reached its initial state of 0 m/s².

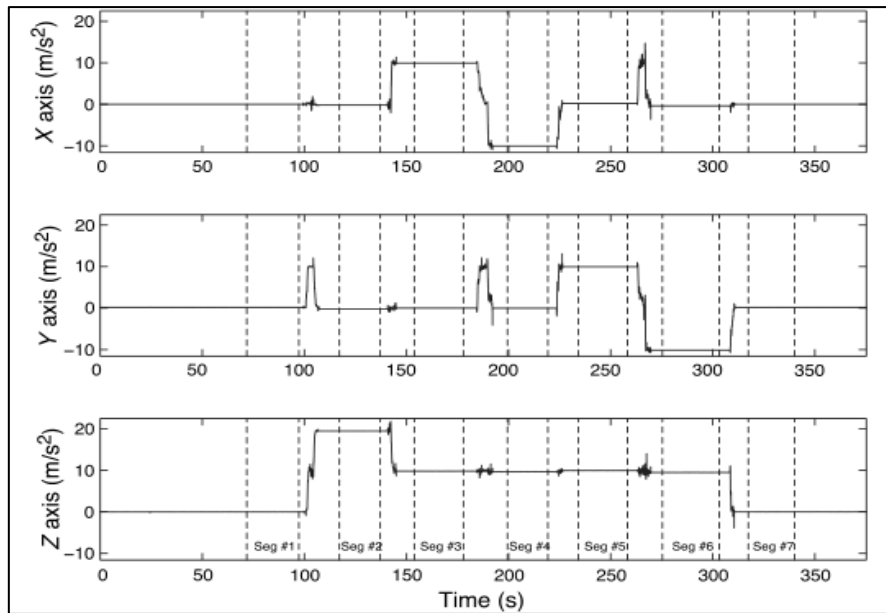


Figure 4.1: Example of the Box-Flip raw data output (Evans et al., 2014)

In this chapter, the calibration of the Automated Wireless Accelerometer Monitoring (AWAM) system was discussed. Three sets of calibrations were needed to obtain the real calibration value of the Automated Wireless Accelerometer Monitoring (AWAM) system output. Firstly, the AWAM device was submitted to a movement on a singular axis to measure its reaction to a singular plane movement. Then, a modified version of the initial calibration setup was proposed that constricts the device on one of its axes and tilts the device to a specified range of angular variations. Finally, the research developed a simpler calibration procedure for future device calibrations purposes.

All the calibrations were performed in a controlled laboratory environment to minimize external interference such as temperature, pressure and humidity (Hutt et al., 2009). In this chapter, the values of calibrations were calculated and presented. These values were required to determine the output of the AWAM device and to set the threshold failure value of the monitoring system.

4.2 Calibration Equipment

4.2.1 Automated Wireless Accelerometer Monitoring (AWAM) device

Both AWAM devices such as mentioned on subchapter 3.5.1.3 were used in the calibration procedures. The AWAM device was powered by a portable 10000 milli Ampere-hour (mAh) Power Bank model BST-011Q manufactured by Besiter Qualcomm, that supplied 5.0 Volts of direct current (DC) to the AWAM device's data acquisition. Data acquisition was performed through monitoring the device's readings on a personal computer using the Windows interface program developed by the research named AG GPS Reader developed in the research as shown in Figure 4.2.

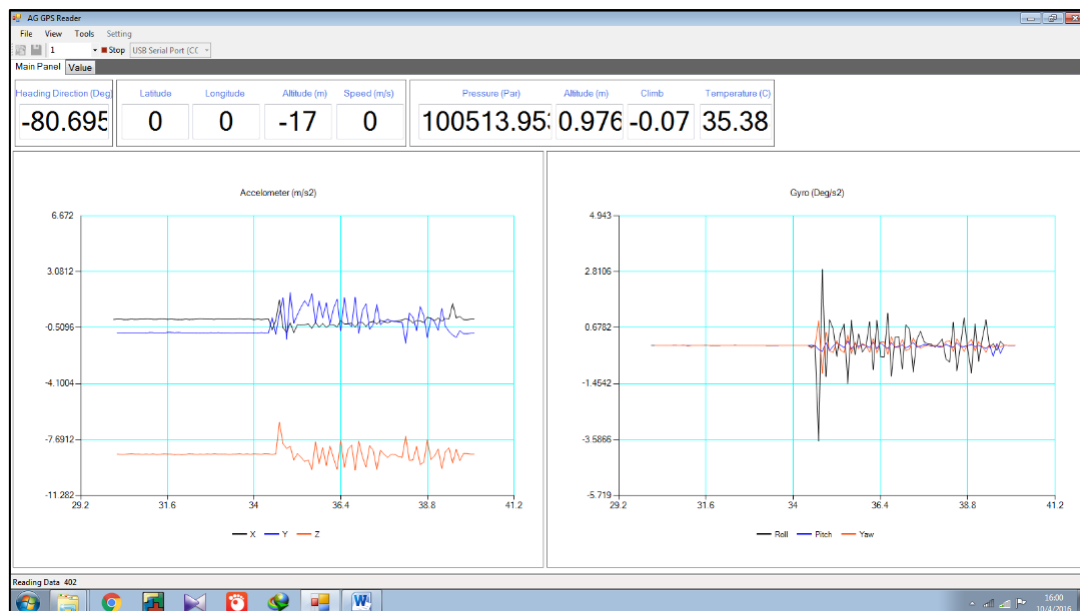


Figure 4.2: AG GPS reader program developed by the research to interpret AWAM device readings on a personal computer

The data was projected on the AG GPS reader program by displaying two sets of output which are Accelerometer (m/s²) and Gyro (Deg/s²) vs time data sets. Accelerometers indicate the linear acceleration while Gyro indicates the angular movement of the AWAM device. Several other outputs were displayed as supplementary data including the Heading direction (Deg), Latitude, Longitude, Altitude, Climb and Temperature of the device.

4.2.2 Linear Variable Displacement Transducer (LVDT)

Such as discussed in subchapter 3.5.1.1, the same 100 mm stroke length LVDT was used as a displacement measuring apparatus for the calibration purposes. The LVDT was connected to the identical 8 channel 16-bit Portable TML Data Logger model number TDS-303 and monitored through a computer.

4.2.3 DXL360 Digital Protractor Inclinometer Level Box

The calibration procedures involve around calibrating flat and angled surface of various values. The digital protractor level box would ensure that the flat and angular variations of the calibration procedures are accurate and reliable. Figure 4.3 illustrates the DXL360 digital protractor used in the research including its make and model that was checked for reliability using a level bubble. The digital protractor model offers high accuracy of up to $\pm 0.05^\circ$ deviation read, high resolution of up to 0.02° , singular and dual-axis measurements, wireless setup and a magnetic base to ease calibration setup.



Figure 4.3: Dual axis digital protractor model DXL360 manufactured by Shenzhen Capital Electronics Co., Ltd. checked for flat surface readings using a bubble level

4.3 Calibration Procedures

4.3.1 Initial Calibration

The purpose of calibration is to rectify the actual value of any movement changes that can affect the result of Automated Wireless Accelerometer Monitoring (AWAM) system by a singular axis movement, by means of moving the device in a single x, y and z-axis direction per movement. This calibration result may be used to provide the data from any movements in the slope body by measuring the changes of the sensor readings in the AWAM device that is in motion in a single axis. The test set up is shown in Figure 4.4.

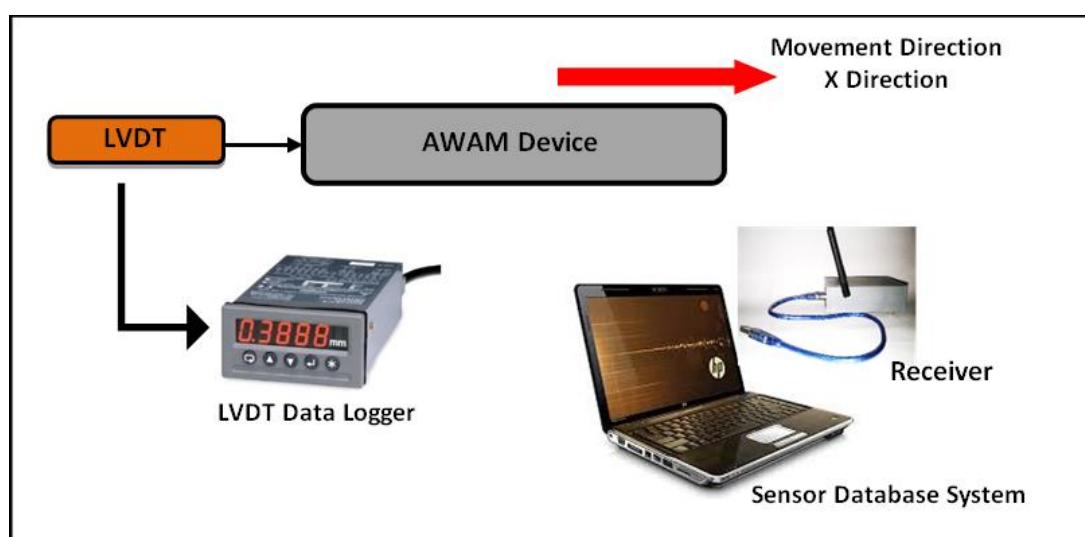


Figure 4.4: Initial calibration setup

The AWAM device was moved slowly and the data from both Linear Variable Differential Transducer (LVDT) and Sensor Database System were taken and recorded. Calibration test was done by conducting four tests in different directions to determine the correlation between acquired data from LVDT and the AWAM System. All of the tests were done in the x-direction (Tests 1 to 3) and the readings were taken before and after movements of the sensor as shown in Figure 4.5 to Figure 4.7.

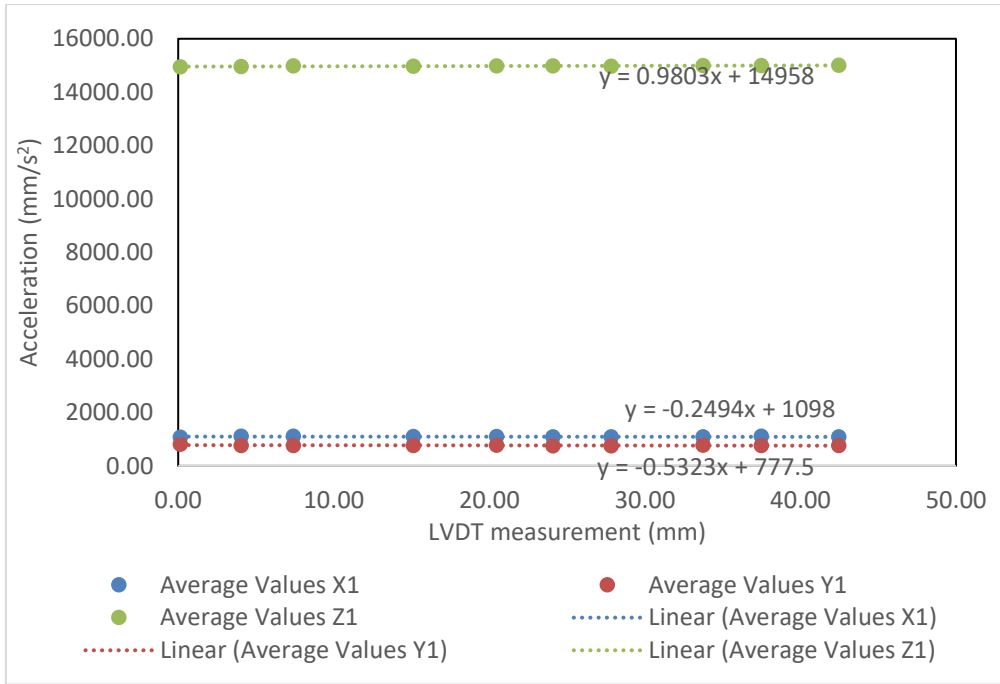


Figure 4.5: AWAM reading vs LVDT measurement Test 1

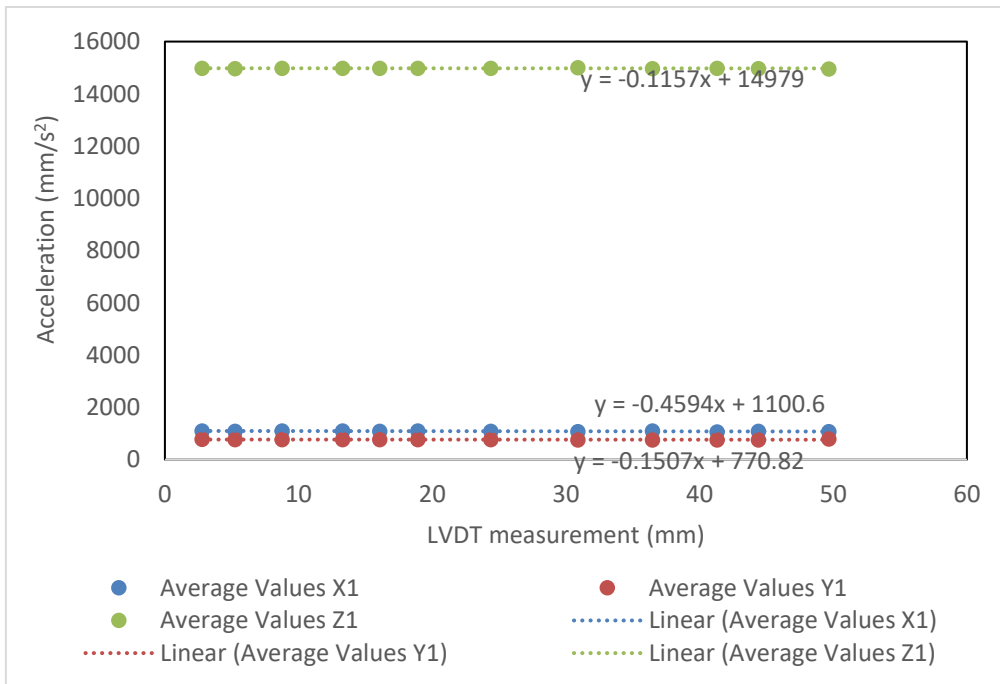


Figure 4.6: AWAM reading vs LVDT measurement Test 2

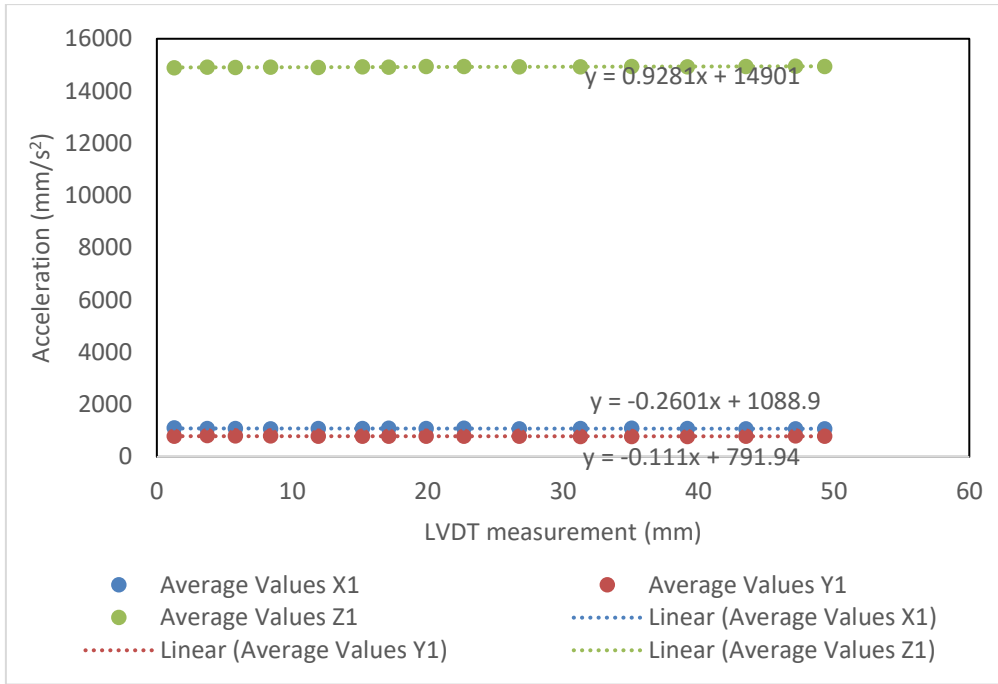


Figure 4.7: AWAM reading vs LVDT measurement Test 3

Based on the result of the calibration tests, Table 4.1 tabulates the summary of results including the goodness-of-fit measure for linear regression models (R^2). Afterwards, Figure 4.8 illustrates the combined x-axis measurement of the AWAM device in correlation with the LVDT movement.

Table 4.1: Summary result of calibration setup

Axis	Slope Gradient (m value from the graph)					
	Test 1	Test 1 R^2	Test 2	Test 2 R^2	Test 3	Test 3 R^2
X	-0.249	0.0964	-0.4594	0.3595	-0.260	0.1798
Y	-0.532	0.2287	-0.1507	0.0547	-0.111	0.0361
Z	0.980	0.7650	-0.1157	0.0309	0.928	0.7233

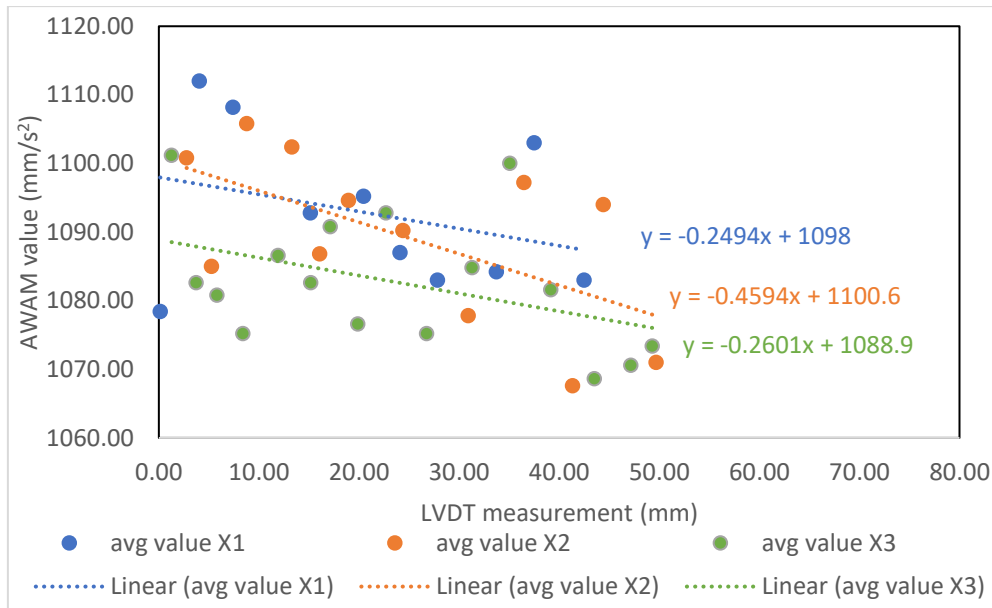


Figure 4.8: Analysis of AWAM value against LVDT movement for all test in the x-axis

Based on the combination of results from the readings of the AWAM device in the x-axis, it was evidently clear that there was no correlation between the data obtained from sensors and movement measured by the LVDT. The slope gradient of the graph (m value) is not consistent throughout all the test measurements. The research did not proceed with the analysis from the other two axes y and z since the analysis of the x-axis produced insignificant trend of calibrations.

From these results, it can be concluded that the device was not able to provide any reading on position changes in the same plane. Therefore, modifications were applied to adequately perform the calibrations needed for the accelerometers and are discussed in the following subchapters.

4.3.2 Primary Calibration Procedure

Based on the initial calibration setup that was explained in subchapter 4.3.1, the AWAM device was unable to produce satisfactory readings to be used in slope monitoring. This is due to the fact the device was not able to give out readings when it moved three-dimensionally as previously discussed. The primary calibration

procedure was modified according to previous research done by Fisher (2010) and Baranilingesan and Rajesh (2018) that reported the tilting (angular displacement) movement would produce a more accurate solution to capturing measurements such as shown in Figure 4.9.

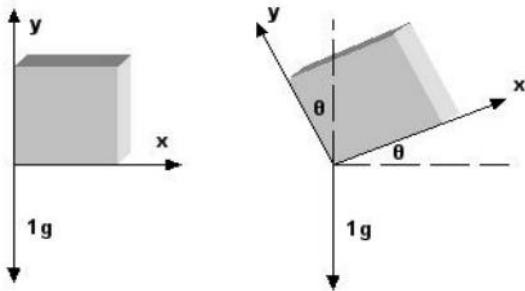


Figure 4.9: Dual-axis accelerometer with one axis of tilt (Baranilingesan and Rajesh, 2018)

According to Baranilingesan and Rajesh (2018), a fixed single axis condition of the AWAM device parallel to gravity would produce x-axis acceleration detection proportional to the sine of the angle of inclination. Due to the fact, the calibrations were modified by raising the device to calculated height, while one axis is being held in place using pieces of formwork and a retort stand. The angular measurement was subsequently checked using a calibrated digital protractor such as illustrated in Figure 4.10.

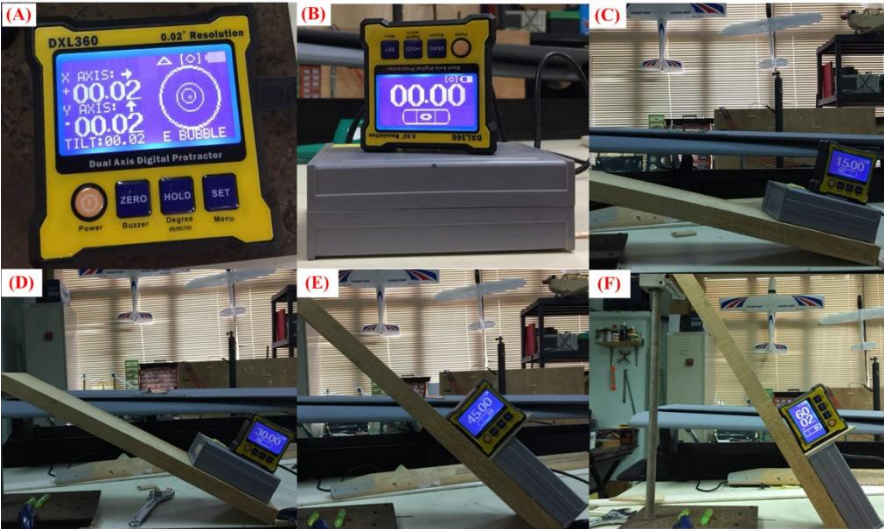


Figure 4.10: Calibration AWAM device setup

Firstly, the surface of the testing area was cleaned and setup to be a level surface for testing (Figure 4.10(A)). Calibration of the device proceeds with data acquisition of the AWAM device for 60 seconds on five different angles; firstly, on a flat surface (0°), followed by a 15° , 30° , 45° and 60° inclinations such as shown in Figure 4.10(B) until Figure 4.10(F) respectively. Note that in the case of slope stability calibrations measurement, the range of inclinations measurement needed was limited to the slope inclination. Thus, the narrow range of inclination calibrations was researched to be adequate for the slope stability measurement cases as the findings from Fisher (2010) shown in Figure 4.11(a) indicate the ranges of the x-axis are linear between -200° until 200° . Figure 4.11(b) further elaborates the linear approximation to be used in place of the inverse sine function when a narrow range of inclinations are required.

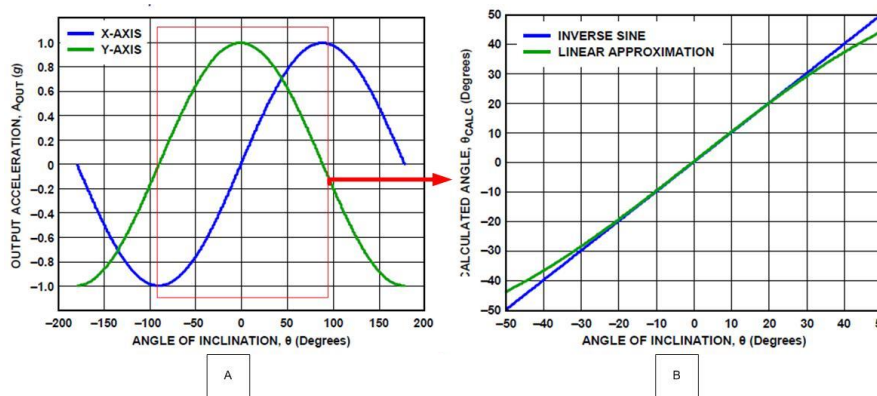


Figure 4.11: Output acceleration vs angle of inclination for dual axis sensing; a) overall angle, b) angle of -50° until 50° for the x-axis showing linear approximation (Fisher, 2010).

The data result from the primary device calibrations was tabulated in Table 4.2.

Table 4.2: Summary Result of Calibration Test with Different Angles

Analysis	0°	15°	30°	45°	60°
AWAM1 (x-axis)	-0.3845	2.5262	4.2507	6.4381	8.3063
AWAM2 (x-axis)	-0.5364	2.3393	4.3734	6.5364	8.1796
AWAM1 (z-axis)	-8.6162	-8.2972	-7.6572	-6.2288	-4.0772
AWAM2 (z-axis)	-9.3432	-9.0941	-8.3537	-6.8829	-4.9823

Based on the result of Table 4.2, the device is able to measure the tilting effect during ground movements. The calibration values of both the x-axis and z-axis were

discussed. The y-axis calibrations were not needed in the current research due to the fact that the y-axis of the AWAM device would be fixed. This was relevant in agreement with the results produced by Fisher (2010), stating only the values for two out of the three axes.

Due to that, the angle of tilting can be calibrated with the linear equation of each of the AWAM devices as illustrated in Figure 4.12. The linear equation of the x-axis calibration test was mentioned with the following relationship:

$$\text{AWAM1 x: } y = 0.0014x^2 - 0.0105x - 8.5684 \quad (4.1)$$

$$\text{AWAM2 x: } y = 0.0013x^2 - 0.0039x - 9.3416 \quad (4.2)$$

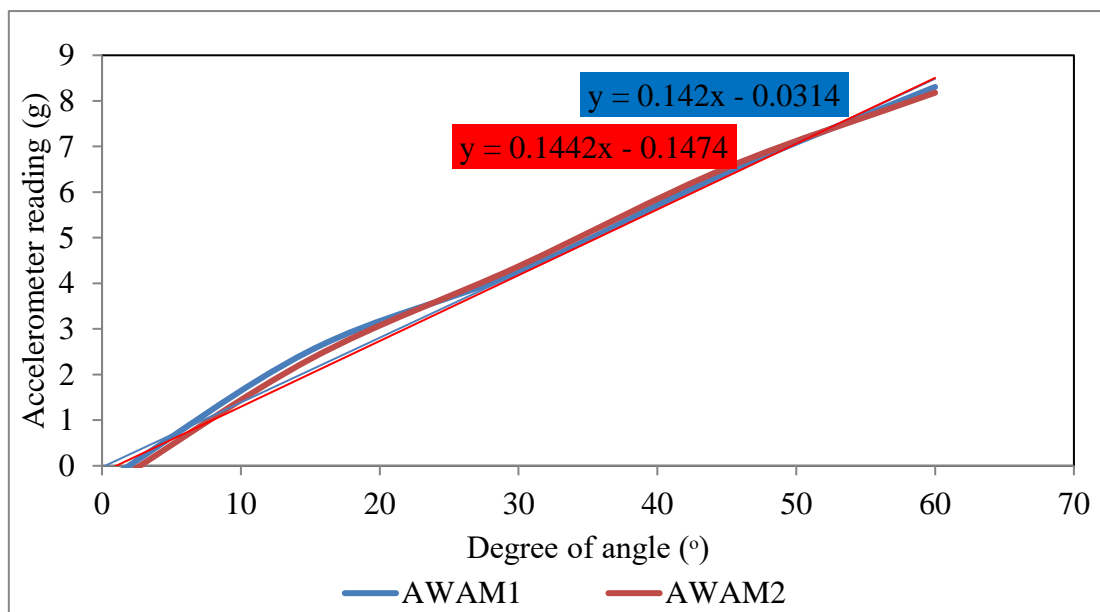


Figure 4.12: Calibration result of the AWAM devices on the x-axis

Figure 4.13 illustrates the calibration values of the AWAM device on the aforementioned z-axis. It can be observed from the figure, the curve of result behaves polynomially by the order of 2 through a fitting of trendline onto the calibration readings. Previous researchers produced a ratio of both the values x and y-axis through a calibration range of -200 to 200 degree which resulted in the sine and cosine relationship, while the current research approach is through each axis separately

calibrated with a specific range of angle (0-70 degree) hence the polynomial relationship.

Z-axis calibration values for the devices are shown in the following for devices AWAM1 and AWAM2, respectively:

$$\text{AWAM1 z: } y = 0.0014x^2 - 0.0105x - 8.5684 \quad (4.3)$$

$$\text{AWAM2 z: } y = 0.0013x^2 - 0.0039x - 9.3416 \quad (4.4)$$

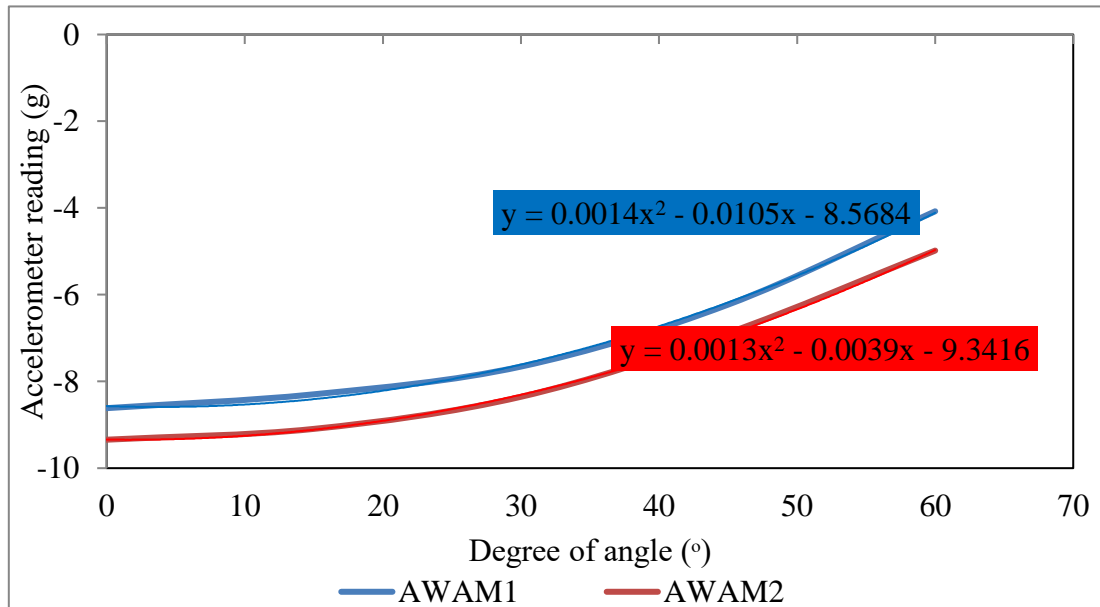


Figure 4.13: Calibration result of the AWAM devices on the z-axis

Figure 4.14 was the resulting combination of the calibration value for the x and z-axis. To properly compare the resulting calibrations done by the current research to the previous research done by Fisher (2010) and Baranilingesan and Rajesh (2018), an interpretation of the result was properly executed. Figure 4.15(A) depicts the orientation of axis opted by the current research and was determined to be inversely different than the orientation carried out by previous researchers such as shown in Figure 4.15(B). Hence, the value of z-axis from the current research would need to be converted to accentuate previous researcher findings. Figure 4.16 illustrates the inverse value of z-axis from the current research in combination with the x-axis calibration result. This resulting output of acceleration value from the current research to be

comparable to the orientation of axes from previous research was determined to be closely similar as the findings from the Fisher (2010) and Baranilingesan and Rajesh (2018) as previously shown in Figure 4.11.

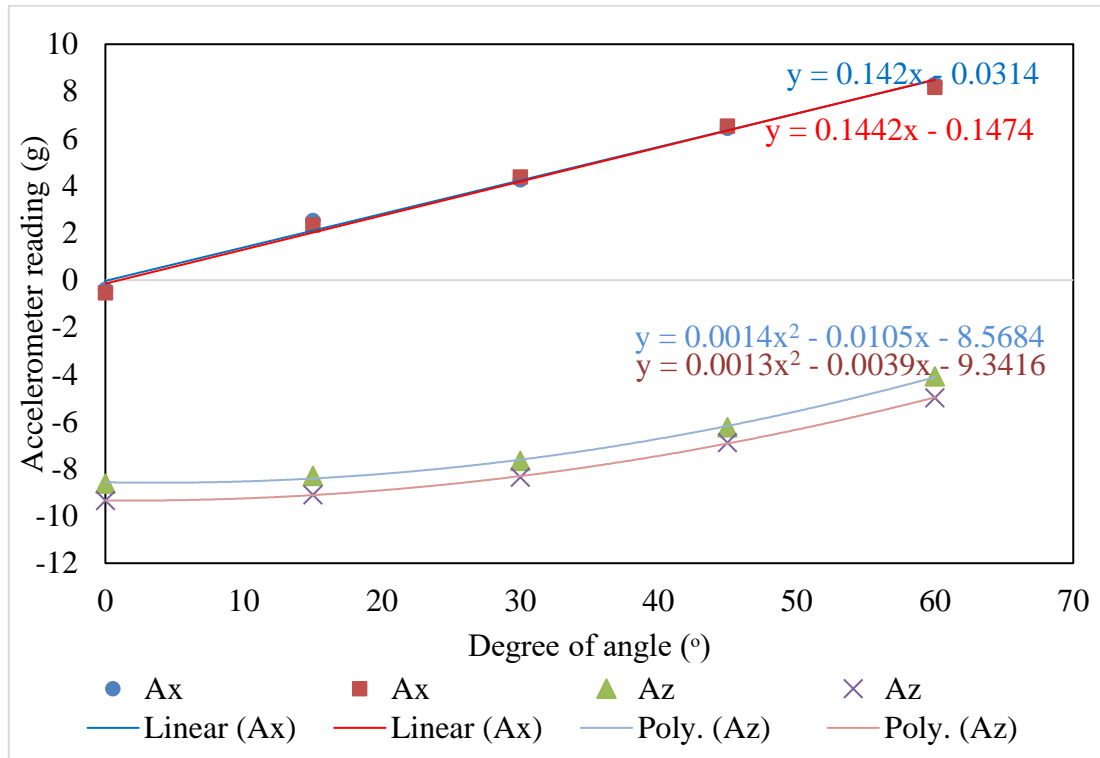


Figure 4.14: Output acceleration vs degree of angle

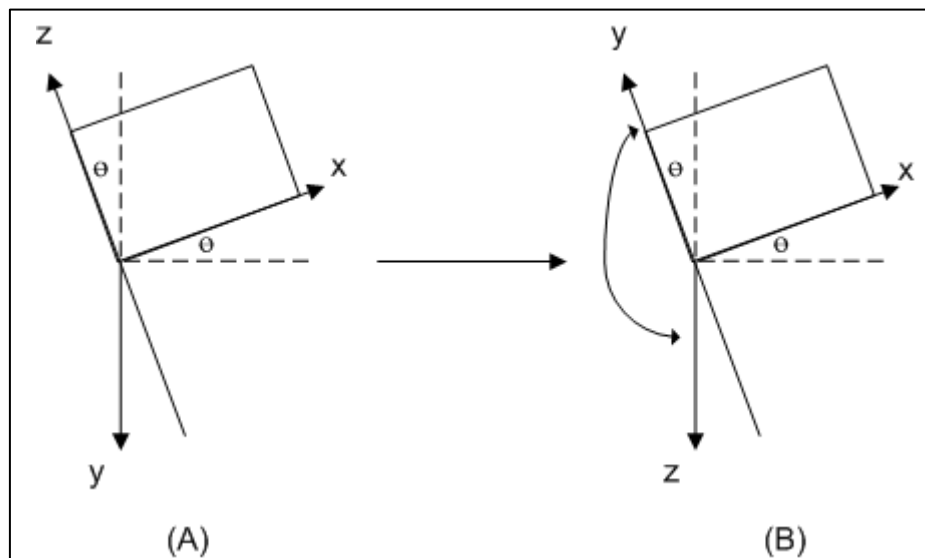


Figure 4.15: Orientation of axes; (A) from the AWAM device orientation, (B) previous researcher axes orientation

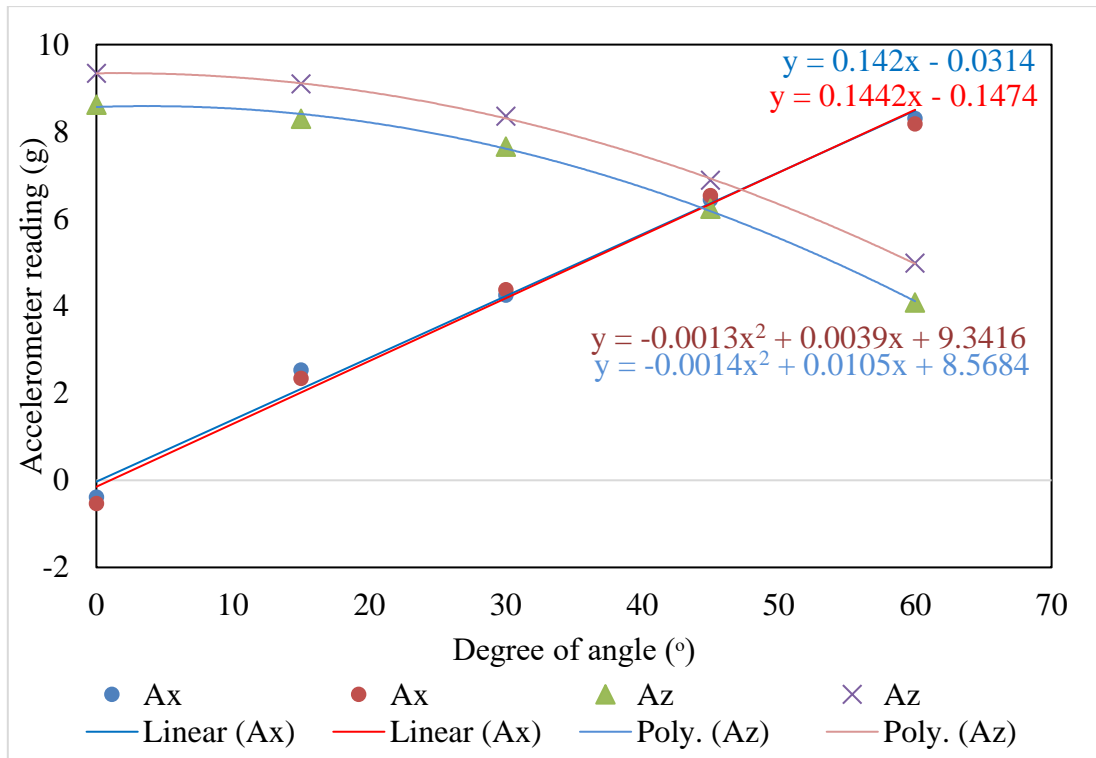


Figure 4.16: Modified accelerometer readings vs degree of angle for AWAM device

Therefore, it was evidently clear that the calibration value of both the AWAM device was in coherence with previous research. The research proceeds with the calibration value as stated in Equation 1.1 to Equation 1.4 in interpreting the outcome of the AWAM devices.

4.3.3 Additional Calibrations (Flip Test)

Following the procedures from subchapter 4.3.2, the calibration procedure was tweaked for a simpler calibration method to calibrate prospective AWAM devices. The calibration method was named ‘flip test’ and its procedures are illustrated in Figure 4.17.

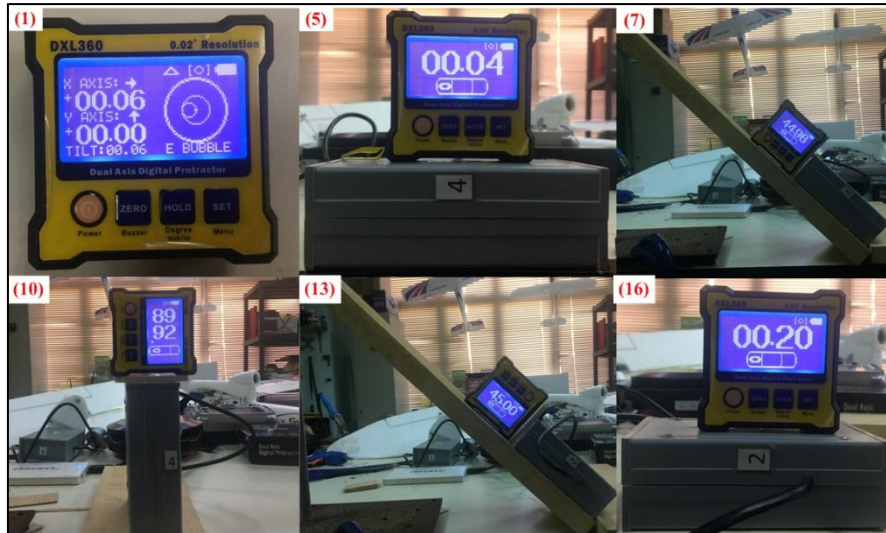


Figure 4.17: Flip test calibration procedures

A step-by-step Standard of Procedure (SOP) for the AWAM device calibrations were developed. The flip test calibration procedures are listed as follow:

1. Ensure that the mounting surface meets the flat surface requirement by having the surface cleaned and checked using a digital protractor calibrated using water level to determine the degree of flatness.
2. Place the accelerometer device on the flat surface; connect the power cables to power on the device and the transmitter to the monitoring system
3. Record trial data with a minimum of 10 seconds of data measurement while checking the data measurement to ensure the accelerometer was connected appropriately to the monitoring system
4. Stop the measurement and disconnect the power cables
5. Connect the power cables and start monitoring for about 60 seconds on the even surface. The digital protractor was placed on top to ensure 0 degree was obtained.
6. Stop the measurement, save the measurement as 0.xlsx and disconnect the power cables
7. Set the accelerometer device to tilt at a 45 degrees.

8. Connect the power cables and start monitoring for about 60 seconds.
9. Stop the measurement, save the measurement as 45.xlsx and disconnect the power cables again
10. Set the accelerometer device to 90 degrees.
11. Connect the power cables and start monitoring for about 60 seconds.
12. Stop the measurement, save the measurement as 90.xlsx and disconnect the power cables again
13. Set the accelerometer device to 135 degrees.
14. Connect the power cables and start monitoring for about 60 seconds.
15. Stop the measurement, save the measurement as 135.xlsx and disconnect the power cables again
16. Lastly, turn the accelerometer device 180 degrees.
17. Connect the power cables and start monitoring for about 60 seconds
18. Stop all measurements save the last data as 180.
19. Combine all 0-180 data and construct a graph to analyze data.

After finishing the calibration procedures listed, the AWAM device readings were analyzed in the Microsoft Excel. The average reading from 0 degrees flipped over to 180 degrees would be similar or near to the value of the acceleration of gravity (g) which is 9.8 m/s^2 . This finding is quite similar to the findings from Evans et al. (2014) that suggest the accelerometer data from the research reverts back to 0 m/s^2 after undergoing 360 degrees of the flip test. Table 4.3 and Table 4.4 shows the average value per axis of a cumulative 3,277 points of data entry for accelerometer readings with respect to the degree changes from an initial flat angle until it was turned upside down. In addition, values of standard deviation for each of the readings are included in the respective tables.

Table 4.3: Accelerometer readings respective to the degree change and standard deviation value for AWAM1

Degree (°)	Average value (g)		Standard deviation
0	avg value Az =	-8.81	0.02
	avg value Ay =	0.25	0.01
	avg value Ax =	-0.31	0.01
45	avg value Az=	-5.64	0.03
	avg value Ay=	0.19	0.02
	avg value Ax=	0.19	0.02
90	avg value Az=	1.47	0.02
	avg value Ay=	0.07	0.01
	avg value Ax=	-9.70	0.01
135	avg value Az=	8.27	0.02
	avg value Ay=	0.10	0.02
	avg value Ax=	-6.48	0.02
180	avg value Az=	10.82	0.02
	avg value Ay=	-0.19	0.03
	avg value Ax=	0.58	0.02

Table 4.4: Accelerometer readings respective to the degree change and standard deviation value for AWAM2

Degree (°)	Average value (g)		Standard deviation
0	avg value Az =	-9.36	0.02
	avg value Ay =	0.10	0.01
	avg value Ax =	-0.60	0.01
45	avg value Az=	-6.00	0.02
	avg value Ay=	0.14	0.01
	avg value Ax=	-7.27	0.01
90	avg value Az=	1.09	0.02
	avg value Ay=	0.16	0.01
	avg value Ax=	-9.60	0.01
135	avg value Az=	7.75	0.02
	avg value Ay=	0.39	0.01
	avg value Ax=	-6.28	0.01
180	avg value Az=	10.17	0.01
	avg value Ay=	0.27	0.01
	avg value Ax=	0.84	0.01

Figure 4.18 and Figure 4.19 illustrates the value of readings from the data acquisition system captured through a computer for both AWAM1 and AWAM2. The values of initial and final readings are highlighted in both figures. The sum values of

both the initial and final readings should be approximate to the value of gravity (9.8 m/s²).

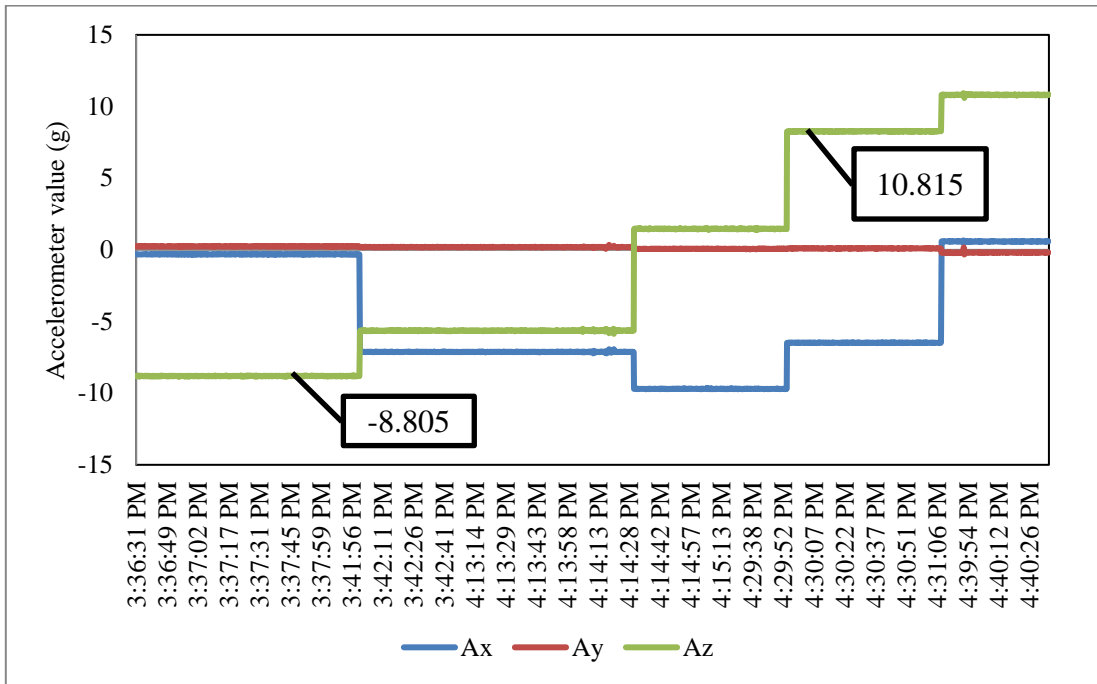


Figure 4.18: Accelerometer calibration value vs time AWAM1

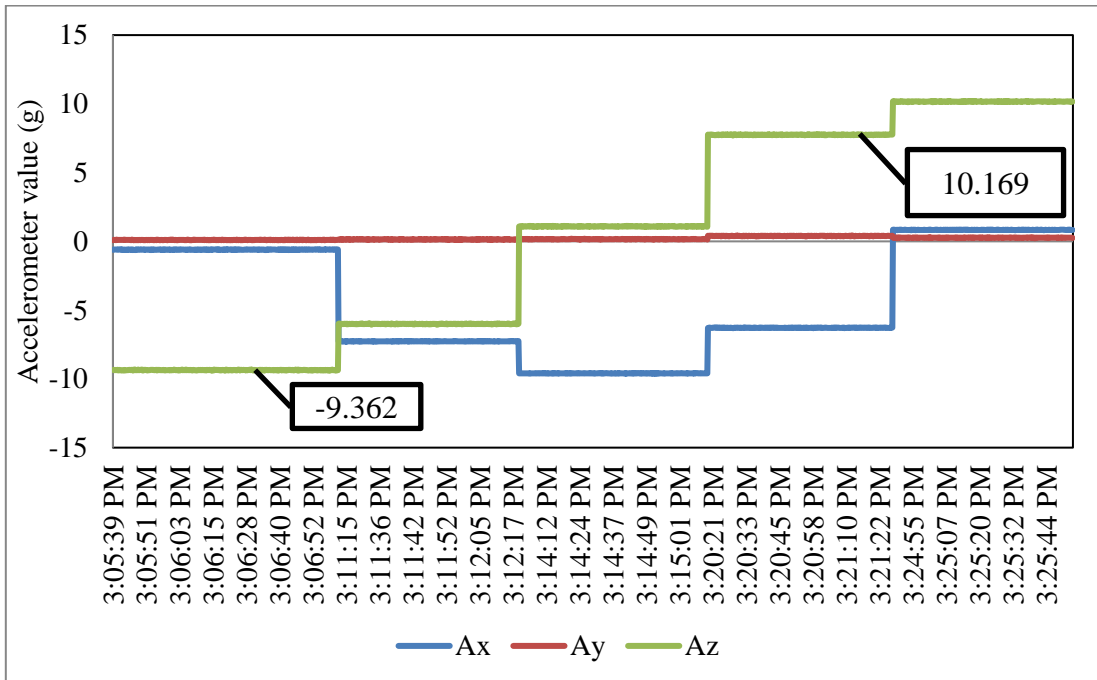


Figure 4.19: Accelerometer calibration value vs time AWAM2

In a nutshell, the flip calibration value equals to the average value of initial reading subtracted by the final reading. The flip test value from the aforementioned

figures are $(-8.805 - 10.815) / 2$ and $(-9.36 - 10.17) / 2$; both equals to -9.8 which is quite similar to the value of 1g.

4.4 Concluding Remarks

This chapter revolves around the calibration setup and process of the Automatic Wireless Accelerometer Monitoring (AWAM) System devices. All the equipment and apparatus used in the calibration setup was described extensively for its function on the calibration of the AWAM device. In addition, a clear image of the digital protractor used in determining the angle of inclination was also portrayed.

Several calibration procedures were highlighted in this chapter including the initial calibrations, primary calibration and also the additional but standardized procedure of calibration for the current and prospective AWAM devices. Findings from primary calibrations were also justified by comparing to previous researches output. The numbered step by step procedure aided by illustrations was meticulously developed for future replications of the calibration procedures. The interpretation of the AWAM data acquisition result would be highly dependent on the outcome of this calibration such as the value of the threshold for the alarm system. The tilting of the device can be concluded in Figure 4.20. The combination of the increase of x° value coupled with the decrease of the z° value would mean the device is tilting clockwise and vice-versa.

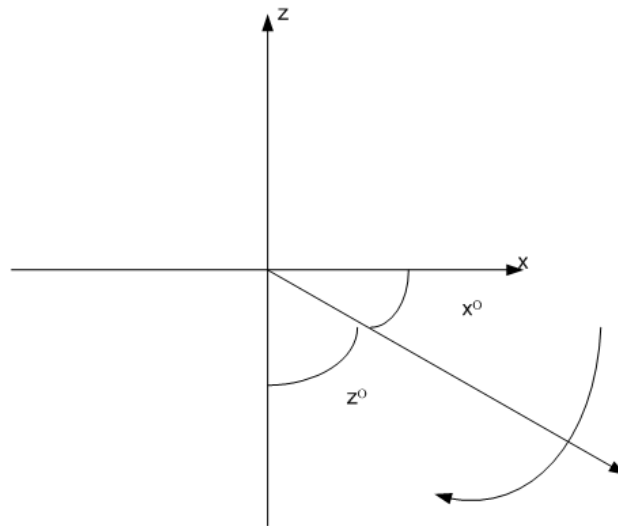


Figure 4.20: Tilting device interpretation using difference of angle from x and z-axis

The chapter was finalized after describing the value of both calibrations with the added explanation for the calculations used in the calibration.

CHAPTER 5

EXPERIMENTAL RESULT

5.1 Introduction

The current chapter will focus on delivering the results from the physical modelling performed on the slope model. The chapter has been divided into two parts which are the materials and the physical model result. The materials part would report on the ground model soil description and properties, Soil Water Characteristic Curve (SWCC), Hydraulic Conductivity Function and rainfall patterns. The physical model results from the part present the findings from the tensiometer result, loading stages results, slope deformation, Automated Wireless Accelerometer Monitoring (AWAM) device readings and Particle Image Velocimetry (PIV) analysis. Subchapter 5.4 provides a summary of the whole chapter in detail.

5.2 Materials

A series of index property tests was conducted on the soil model used in this study. The main physical index property of the soil was classified dependent on its Atterberg limits, specific gravity and particle size distribution. The equipment used in this study was also discussed in the following sections.

5.2.1 Materials Description and Properties

The soil was excavated from a site in Balai Cerapan, UTM. Figure 5.1 shows the particle size distributions of residual soil for Grade VI of the Balai Cerapan. The reddish-brown soil of the excavated layer was later classified according to the British

Soil Classification System (BSCS) as sandy silt (MHS) with smooth-textured soil particles. The Grade VI was determined to have fine content of about 67% and was highly plastic.

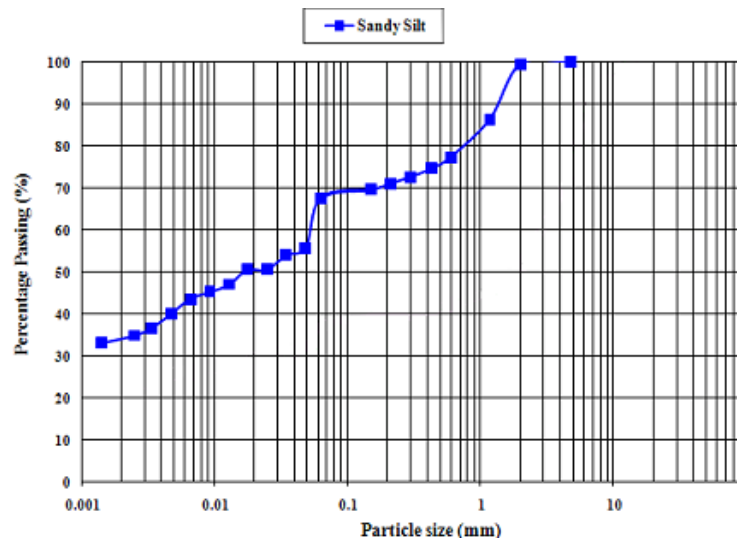


Figure 5.1: Particle size distribution of the model soil

From Table 5.1, the liquid limit of residual soil from Balai Cerapan showed to be valued at 59.3% while the plastic limit is 35.5%. These values are attributed to having a high percentage of fines content and highly plastic. In addition, the plasticity index of the soil was plotted below the A-line which is the range of silty materials (Craig, 2004). The specific gravity of the soil is 2.65 suggest a relatively high amount of high specific gravity minerals in the soil and indicates a more weathered soil.

Compaction test regarding the Grade VI soils at the site revealed the maximum dry density (ρ_{dmax}) to be 1415 kg/m³ while its optimum moisture content (w_{opt}) was determined to be 31.0%. The constant head permeability testing of soil produced the result of permeability values of the soil to be 5.0 x 10⁻⁷ m/s. Also shown in the table, several tests were performed on undisturbed soil samples from the site particularly using Consolidated Isotropic Undrained (CIU) triaxial test to determine the effective friction angle (ϕ') and effective cohesion (c') resulting in the value of 32.1° and 7.6 kPa respectively.

Table 5.1: Summary of soil properties of the Grade VI of Balai Cerapan

	Grade VI (Sandy Silt)
Composition	
Gravel (%)	0
Sand (%)	33
Silt (%)	34
Clay (%)	33
LL (%)	59.3
PL (%)	31.9
PI	27.4
Soil Classification BSCS	MHS
w_n (%)	32
G_s	2.65
MDD (kg/m^3)	1415
OMC (%)	31.0
k_{sat} (m/s)	5.00×10^{-7}
CIU Test	
c' (kPa)	7.6
ϕ' ($^\circ$)	32.1

5.2.2 Soil Water Characteristic Curve (SWCC)

The soil-water characteristic curve (SWCC) of the ground model from Balai Cerapan is shown in Figure 5.2.

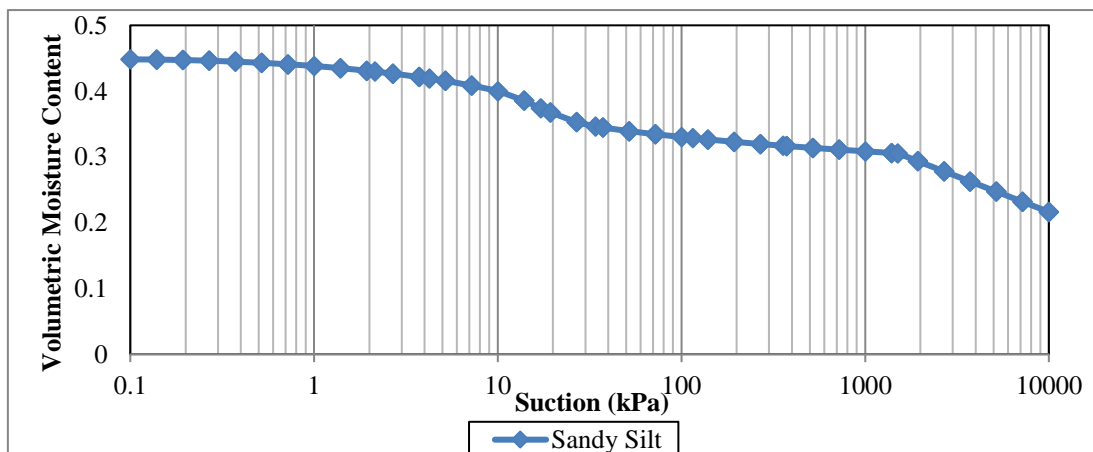


Figure 5.2: The soil-water characteristic curves (SWCC) of the ground model

Based on the SWCC, parameters such as saturated volumetric water content (θ_s), air entry value A_{ev} and residual volumetric water content (θ_r) of the soil were able to be identified and tabulated in Table 5.2.

Table 5.2: SWCC parameters of the ground model

Soil Type	Grade VI Sandy Silt
Saturated Volumetric Water Content, θ_s	0.45
Air Entry Value (kPa)	7
Residual Water Content, θ_r	0.34
Minimum Suction at Residual Water Content, ψ_{min} (kPa)	32

5.2.3 Hydraulic Conductivity Function

Figure 5.3 shows Genutchten’s predictive method to produce hydraulic conductivity. In addition, it showed the coefficient of hydraulic conductivity in Grade VI to decrease beyond 10 kPa or matric suction. From observation, the hydraulic conductivity and SWCC graph can be explained by the particle size distribution and the structure of the soil. The ability of soil to maintain saturation is dependent on the grain size and inter-particle pore size of the soil (Kassim, 2011). Higher grain size and inter-particle pores resulted in higher saturated permeability. Hence, the sandy silt used in the study which consisted of more fine particles has a higher ability to retain water under high suction resulting in higher Air entry value, A_{ev} (i.e 7 kPa for sandy silt).

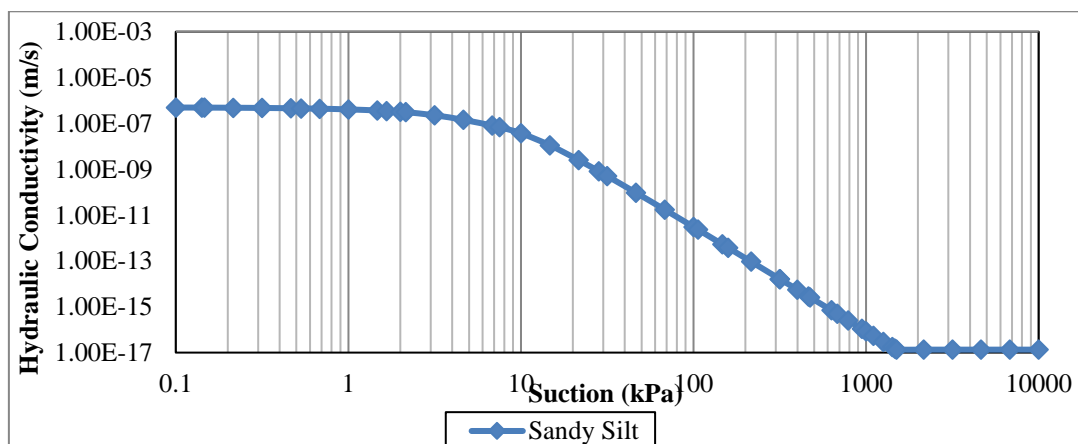


Figure 5.3: Hydraulic conductivity of residual soil using Genutchten’s method (1980)

5.2.4 Rainfall Patterns

The 1 hour and 24 hours rainfall of this study was based on the Intensity-Duration-Frequency curve (Figure 5.4) to differentiate the effects of rainfall on the suction distribution of the ground model against a model without rainfall.

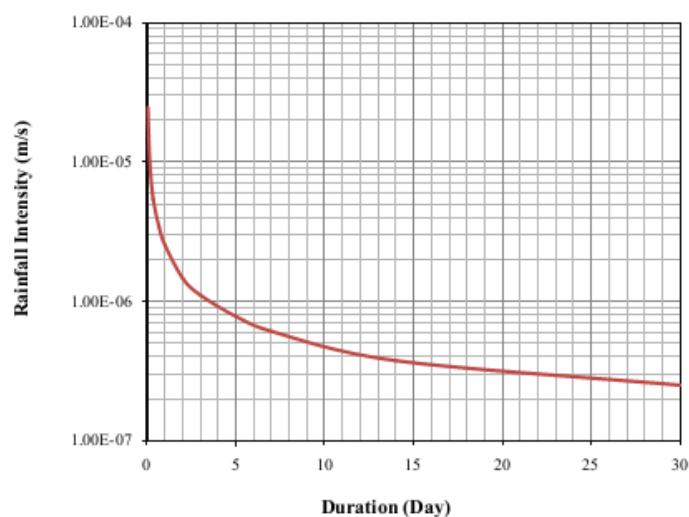


Figure 5.4: Intensity-Duration-Frequency (IDF) curve of Johor Bahru, Malaysia (Kassim, 2011)

Nevertheless, these values are shrunk to about 70% as effective rainfall in the infiltration due to some losses occurs as a result of surface runoff. Table 5.3 shows the value of the rainfall intensity used in modelling the physical modelling tests from the IDF curve in Figure 5.4.

Table 5.3: Modelling rainfall patterns

Rainfall Pattern	Intensity (m/s)	Duration
1	1.7196×10^{-5}	1 hour
2	1.7694×10^{-6}	24 hours

5.3 Laboratory Model Result

Physical laboratory tests were carried out as described in section 3.6.2 for all six of the model tests illustrated in sub-section 3.6.1. The aforementioned subchapters

will discuss on the results of the physical model in 5 stages: i) pore water pressure (Pre-loading), ii) stress-strain relationship (Loading stage) and three post-loading analysis which are: iii) deformation analysis, iv) AWAM readings and v) PIV analysis.

5.3.1 Laboratory Infiltration Test on the Homogenous Soil Layer

This section focuses on the analysis result of the infiltration model test with 27° and 45° inclination models with varied rainfall patterns (1-hour and 24-hour rainfall). It is worthwhile to note that the results projected on the homogenous soils layer are only for the suction measurements observed at the face of the slope at 0.6 m (27° slope angle cases) and 0.45 m (45° slope angle cases) from the left edge of the ground model because the suctions observed at the crest (0.3 m) and toe (0.9 m) was found to be almost identical to each other. This is similar to the findings by Kassim (2011) in the homogenous residual soil layer result analysis for suction measurements.

T11_cb was the tensiometer sensor that was situated on the upper part of the face of the slope, followed by T10_cb and T9_cb as shown in Figure 5.5 and 5.6 for both degrees of slope angle cases respectively.

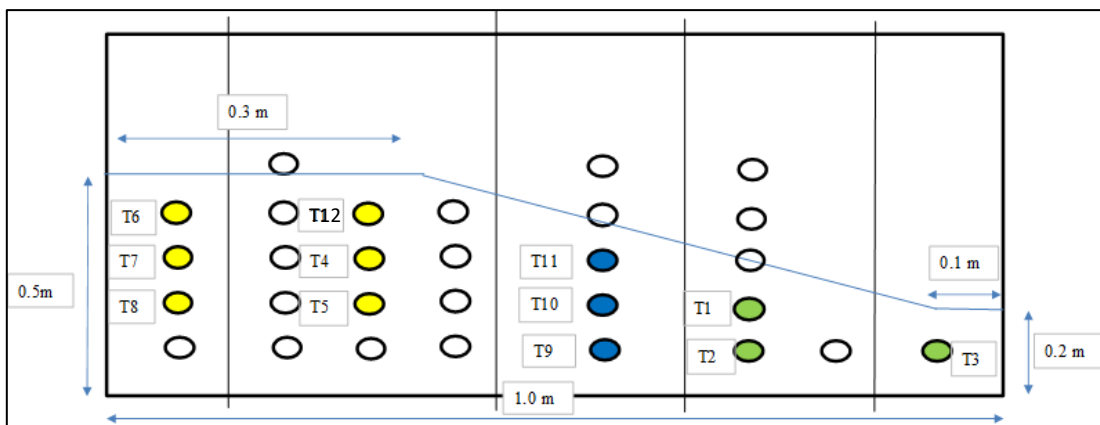


Figure 5.5: Tensiometer sensor locations for 27° slope angle cases (Cases A and D)

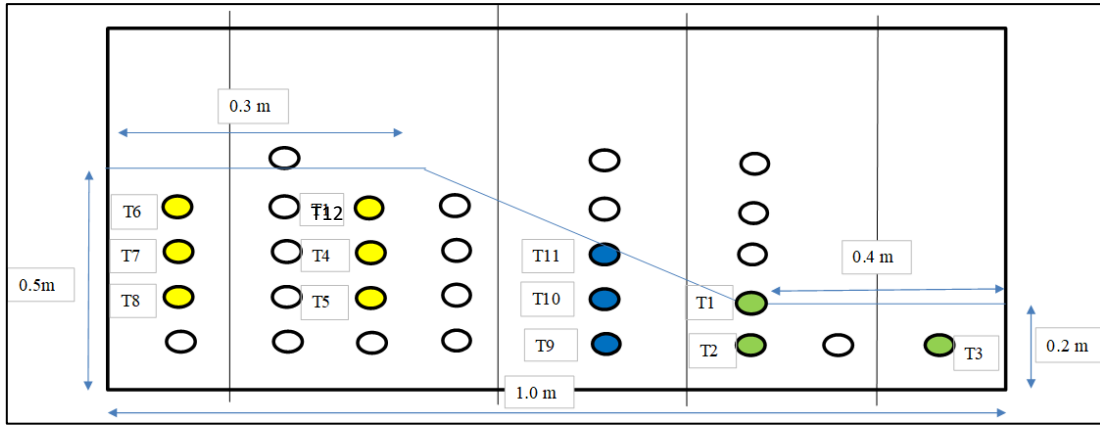


Figure 5.6: Tensiometer sensor locations for 45° slope angle cases (Cases B and E)

Figure 5.7 to Figure 5.10 show the pore water pressure vs. time for the model tests with the pressure from the crest singled-out. The figures depict that the pore pressure increased with time in reaction to the rainfall introduced to the ground model. The time duration for each of the rainfall durations is detailed out on every figure.

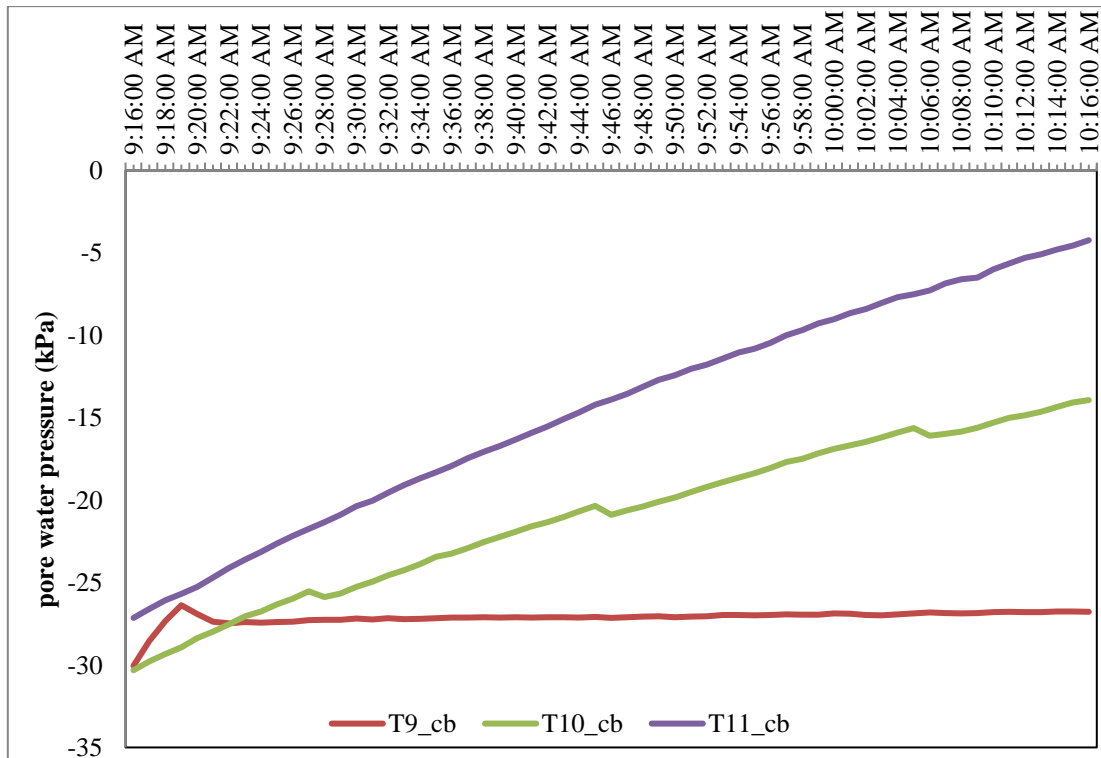


Figure 5.7: Pore water pressure vs. time for Case A (27° slope angle and 1-Hour rain)

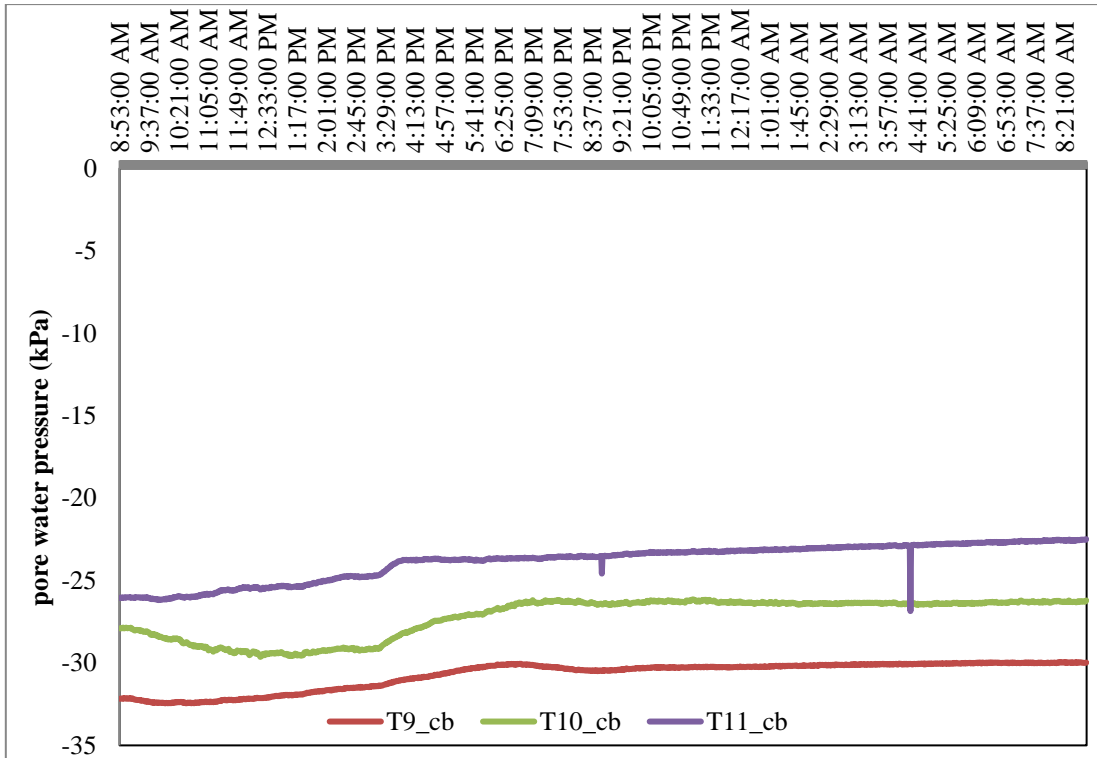


Figure 5.8: Pore water pressure vs. time for Case B (27° slope angle and 24-Hour rain)

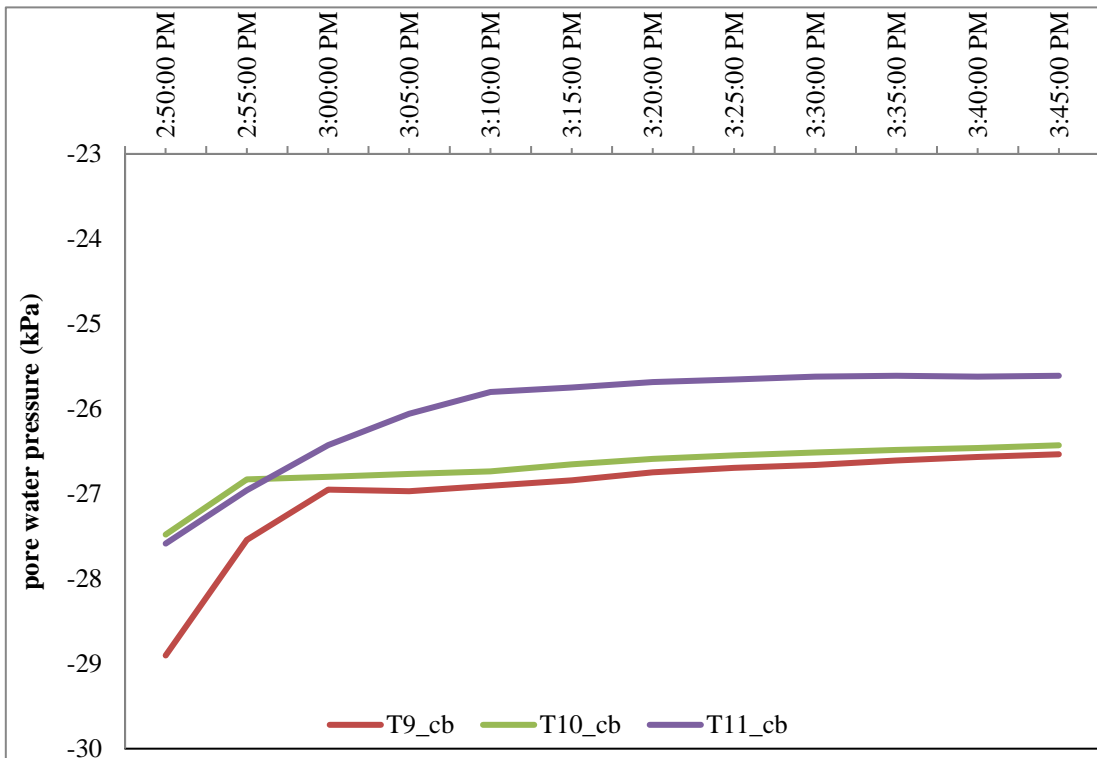


Figure 5.9: Pore water pressure vs. time for Case D (45° slope angle and 1-Hour rain)

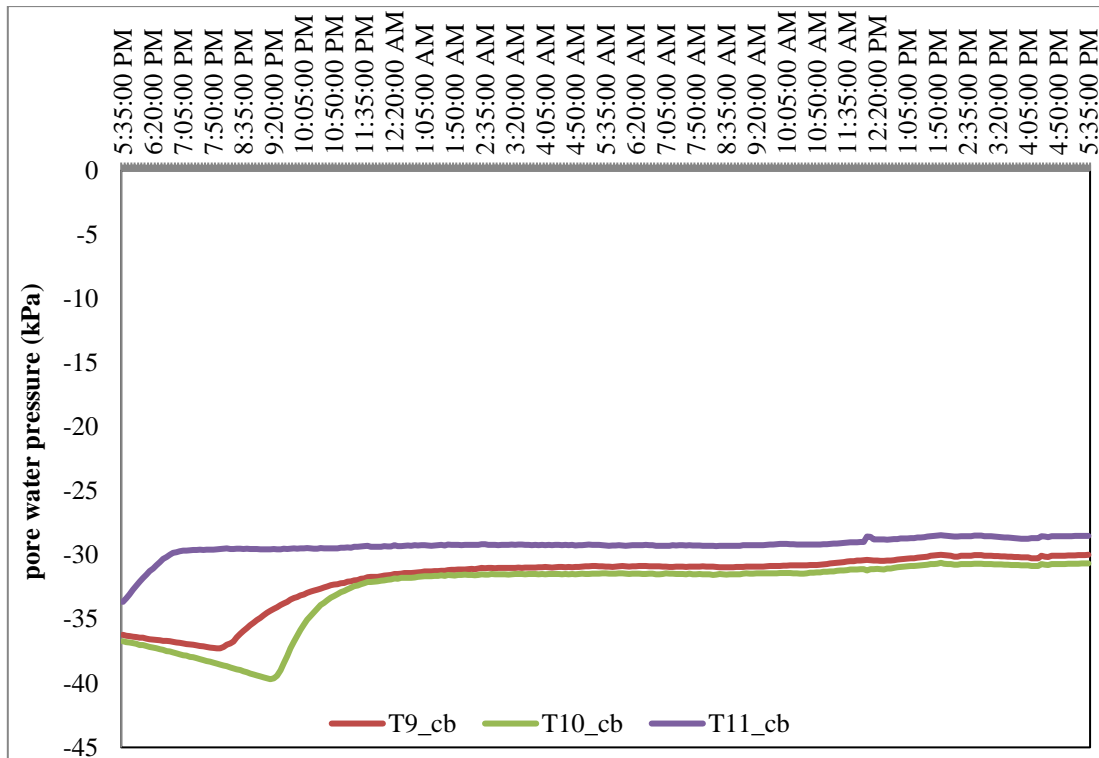


Figure 5.10: Pore water pressure vs. time for Case E (45° slope angle and 24-Hour rain)

From the trend of the suction variation over time shown on the previous figures, it was observed that the pore water pressure recorded on the slope model during rainfall simulations were generally consistent and following an upward trend from start to finish. The pore water pressure vs. time for all the cases was then analyzed to illustrate the suction vs. depth for further analysis. Figure 5.11 shows the decrease of suction with respect to time at all depths of 0.1 m, 0.15m, 0.2 m, 0.25m and 0.3 m which describes a uniform downward progression of the infiltration as anticipated in the homogenous soil system for rainfall intensity.

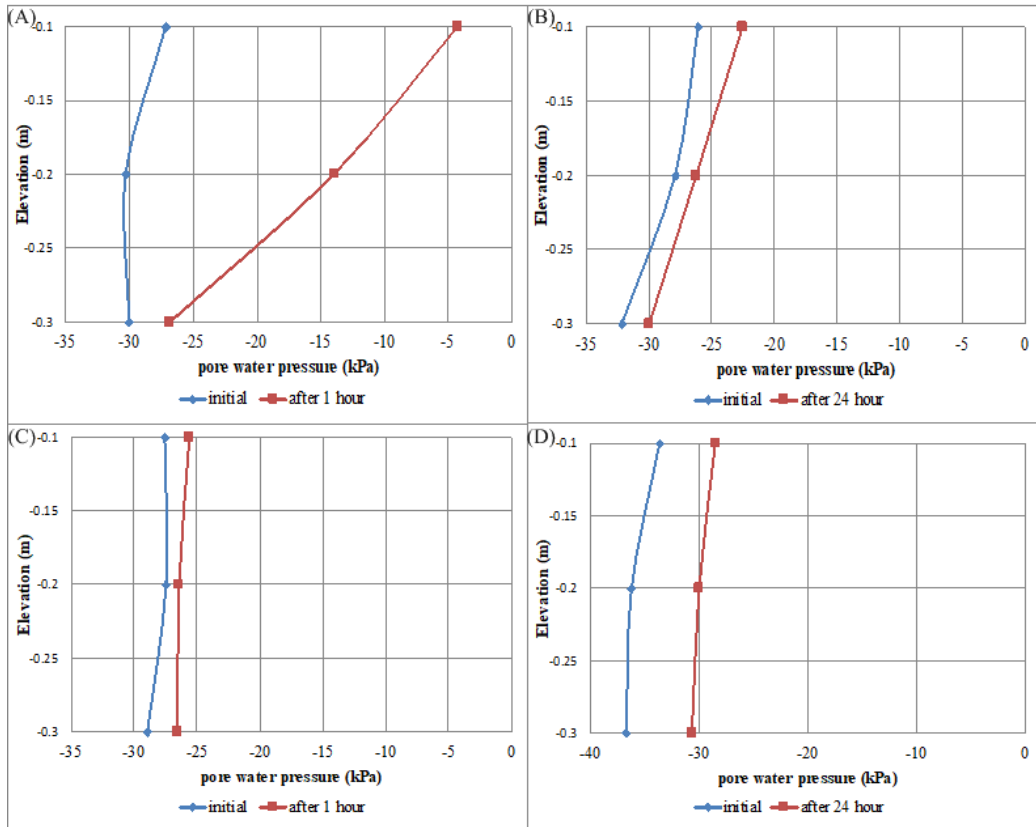


Figure 5.11: Pore water pressure vs. Elevation for model tests; (A) 27° slope angle and 1-Hour rain, (B) 27° slope angle and 24-Hour rain, (C) 45° slope angle and 1-Hour rain and (D) 45° slope angle and 24-Hour rain

It can be concluded from Figure 5.11(A) that the infiltration resulted from the high intensity and short duration (1-hour rainfall) is limited at shallower depths illustrated by the minimum suction of 4.8 kPa that was observed at the depth of 0.1 m. While the following depths of 0.2 m and 0.3 m registering the minimum suction of 14 kPa and 27 kPa respectively indicating that the rainfall simulation minimally affects the suction as the depth increases. This result was in total agreement in comparison to the suction vs elevation result for 1-hour rainfall on 2-D infiltration model done by Kassim (2011). In contrast with the analysis result from Figure 5.11(B) with the same slope angle, the pore water pressure distribution decreases uniformly on overall depth for the low intensity and long duration (24-hours of rainfall) up until a constant value. A slightly lower suction was observed on the shallower depths compared to the lower depths of the slope model as compared to the initial conditions. A constant lower value of suction in overall depths suggest the rainfall infiltration reached lower depths uniformly over the span of the 24 hours of rainfall.

Figure 5.11(C) and Figure 5.11(D) illustrates the pore water pressure vs elevation for the steeper angle of slope (45° slope). In contrast to its gentler slope angle counterpart illustrated in Figure 5.11(A), the suction distribution of high intensity and short duration rainfall (1-hour rainfall) for a steeper angle of slope shown in Figure 5.11(C) measured a slightly lower suction of 26 kPa after 1 hour of induced rainfall compared to the initial condition. This rather opposite behaviour for high intensity and short duration rainfall was due to the difference of slope inclinations limiting the infiltration of rainfall on the slope model thus resulting in higher suction. Previous findings by Kassim (1998) and Huat et al. (2005) were in agreement with the resulting suction of higher slope angle value having higher suctions. Finally, for Figure 5.11(D) the suction trend behaved in agreement to its counterpart Figure 5.11(B) as the longer duration of rainfall showed decreasing trends of suction up until a constant value was reached.

5.3.2 Loading Test

The result obtained from LVDT and data logger was used to record the displacement of soil in distance (mm) and the Load Cell was used to measure the applied load. Figure 5.12 shows the relationship between the load/stress on a soil material and the corresponding strain/deformation record by LVDT obtained from all 6 of the physical laboratory model tests.

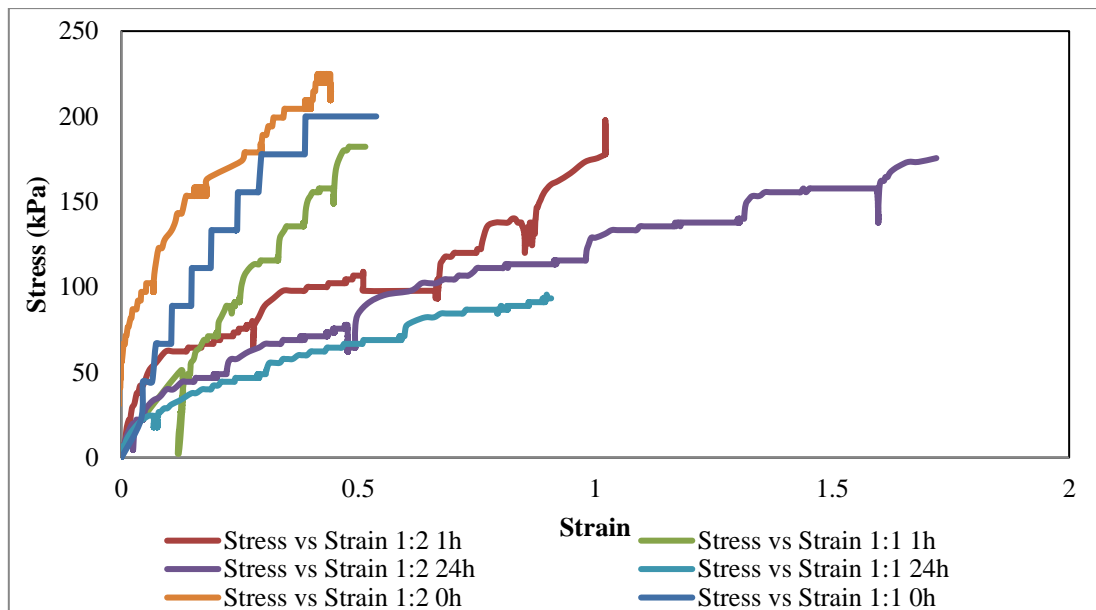


Figure 5.12: Stress vs. strain for the model tests

The graph shows the normal curve of applied vertical load versus vertical displacement as obtained from the data logger. It shows that the plotted graph is similar to the stress versus strain graph of soil behaviour obtained by Kalatehjari et al. (2015). The stress was increased gradually until it reached its maximum loading of 8 kN.

Table 5.4 shows the maximum stress achieved for each physical modelling test as derived from Figure 5.12. The model tests were stopped after reaching maximum stress to allow for further deformation analysis. A thorough explanation for each result based on different degree values of slope (27° and 45°) and rainfall intensity (0, 1 and 24 hours) of the laboratory model is presented in the following sub-sections.

Table 5.4: The maximum stress load on the model tests

No.	Test Notation	Test Details	Maximum Stress (kPa)
1	Case A	Test 1:2 slope with 1 Hour rain	177.8 kPa
2	Case B	Test 1:2 slope with 24 Hour rain	173.3 kPa
3	Case C	Test 1:2 slope without rain	224.9 kPa
4	Case D	Test 1:1 slope with 1 Hour rain	182.2 kPa
5	Case E	Test 1:1 slope with 24 Hour rain	91.1 kPa
6	Case F	Test 1:1 slope without rain	200.0 kPa

5.3.3 Slope Deformation Result

After the pre-loading and loading stages of the tests, the post-loading analysis of the research firstly illustrates the deformation result of the model slope. Figure 5.13 to Figure 5.18 portrays the slope failure mechanism of all six tests from Case A until Case F of the research. As previously mentioned in subchapter 3.7.2, a digital camera captured still shots of the slope model throughout the entirety of the loading stages providing the research with a step by step movement tracker of the slope model. The slope deformation result was divided into three parts which are the initial state, the ground model state after a significant movement was detected on the AWAM device and the final state after maximum loading was applied on the ground model.

A straight line was drawn on the base of the AWAM1 device as a baseline to observe the movement of the device from the initial state to the final stages of the slope failure. In addition, a curved arrow illustrates the rough estimation of the ground movement on the slope face after sequences of loading was exerted on the ground model. A comprehensive ground movement analysis was continued on the following subchapters.



Figure 5.13: Slope deformation of the ground model for Case A; (A) initial state (B) significant AWAM device reading and (C) final condition after maximum loading



Figure 5.14: Slope deformation of the ground model for Case B; (A) initial state (B) significant AWAM device reading and (C) final condition after maximum loading

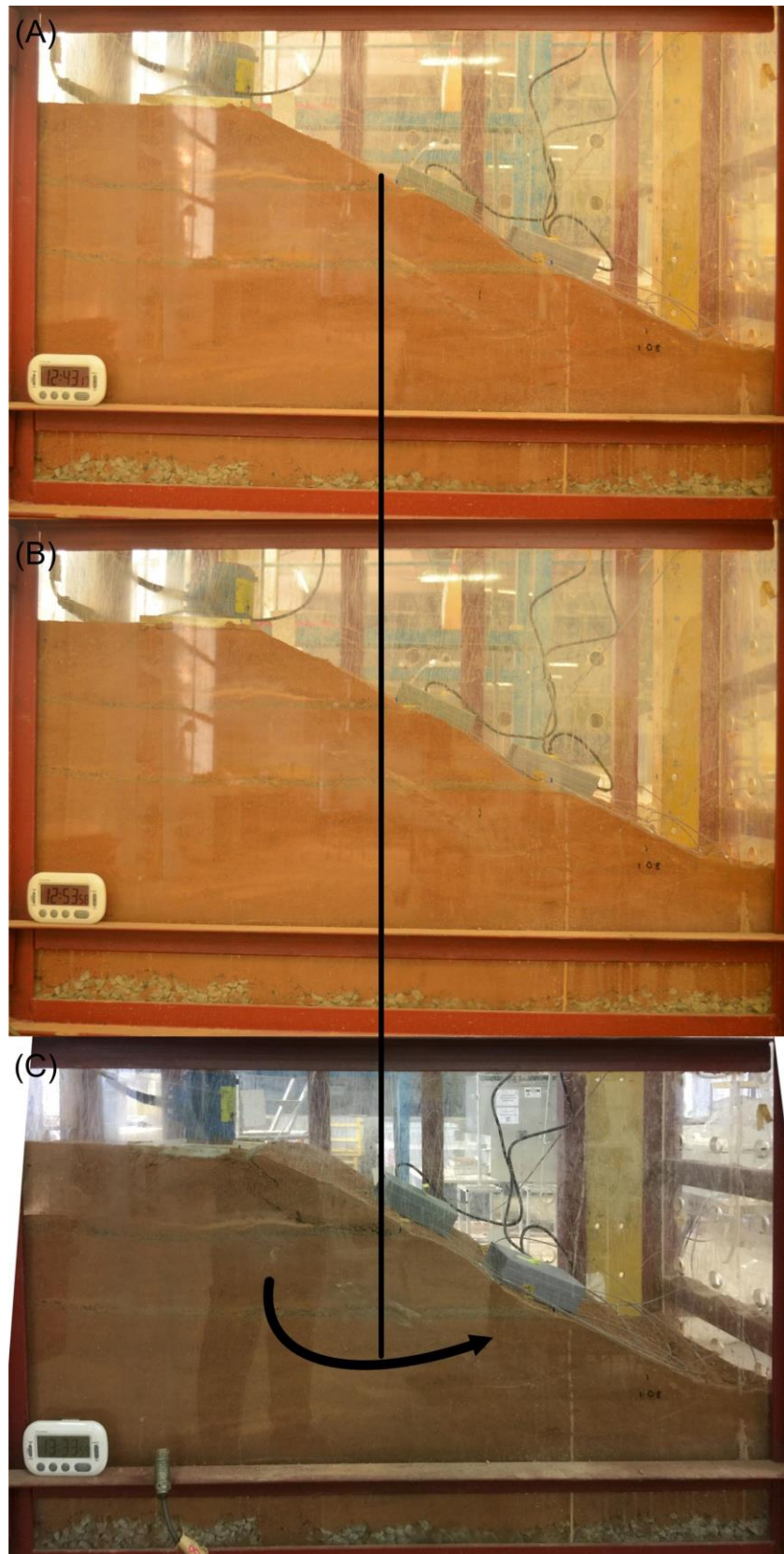


Figure 5.15: Slope deformation of the ground model for Case C; (A) initial state (B) significant AWAM device reading and (C) final condition after maximum loading

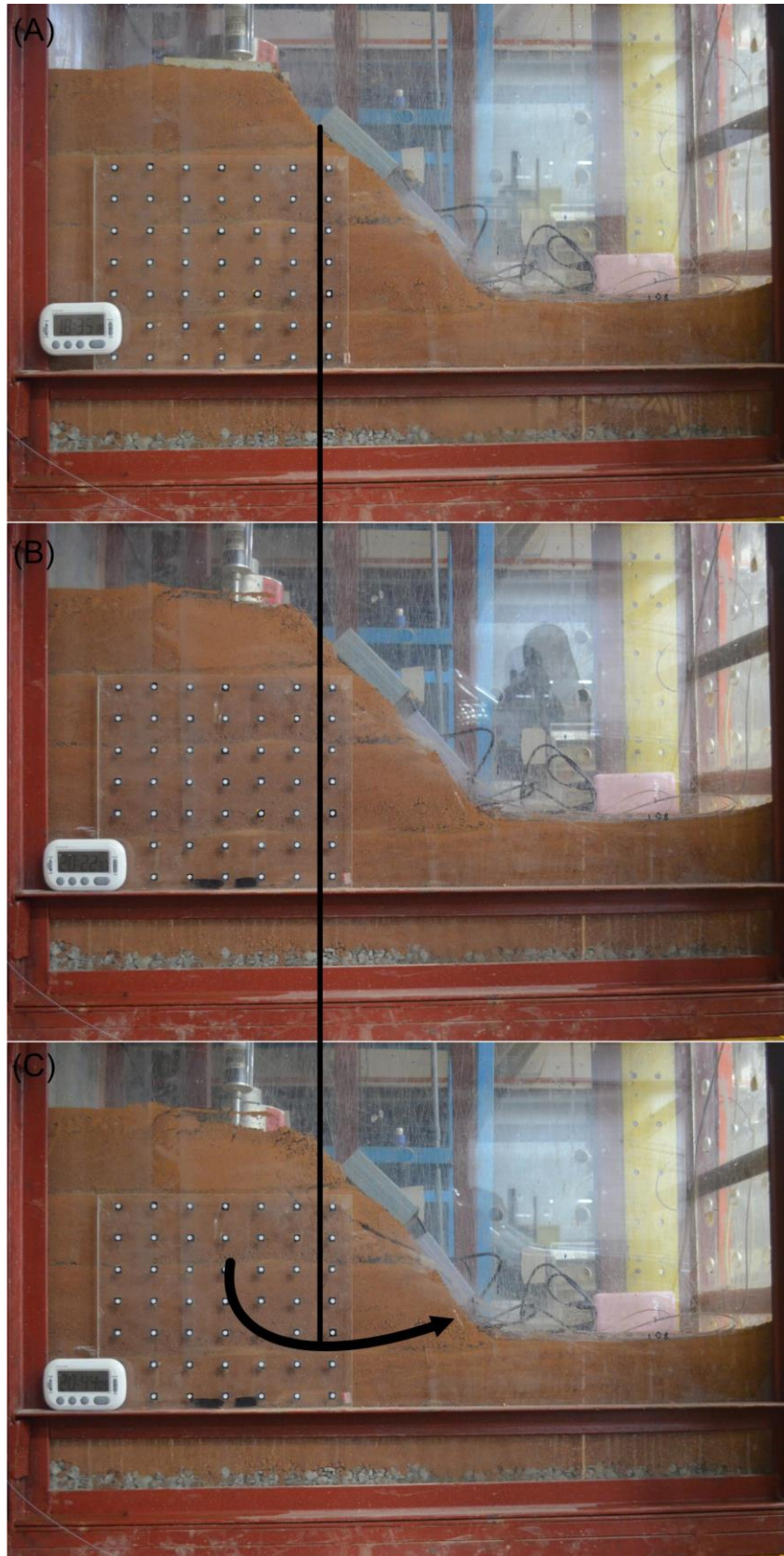


Figure 5.16: Slope deformation of the ground model for Case D; (A) initial state (B) significant AWAM device reading and (C) final condition after maximum loading



Figure 5.17: Slope deformation of the ground model for Case E; (A) initial state (B) significant AWAM device reading and (C) final condition after maximum loading

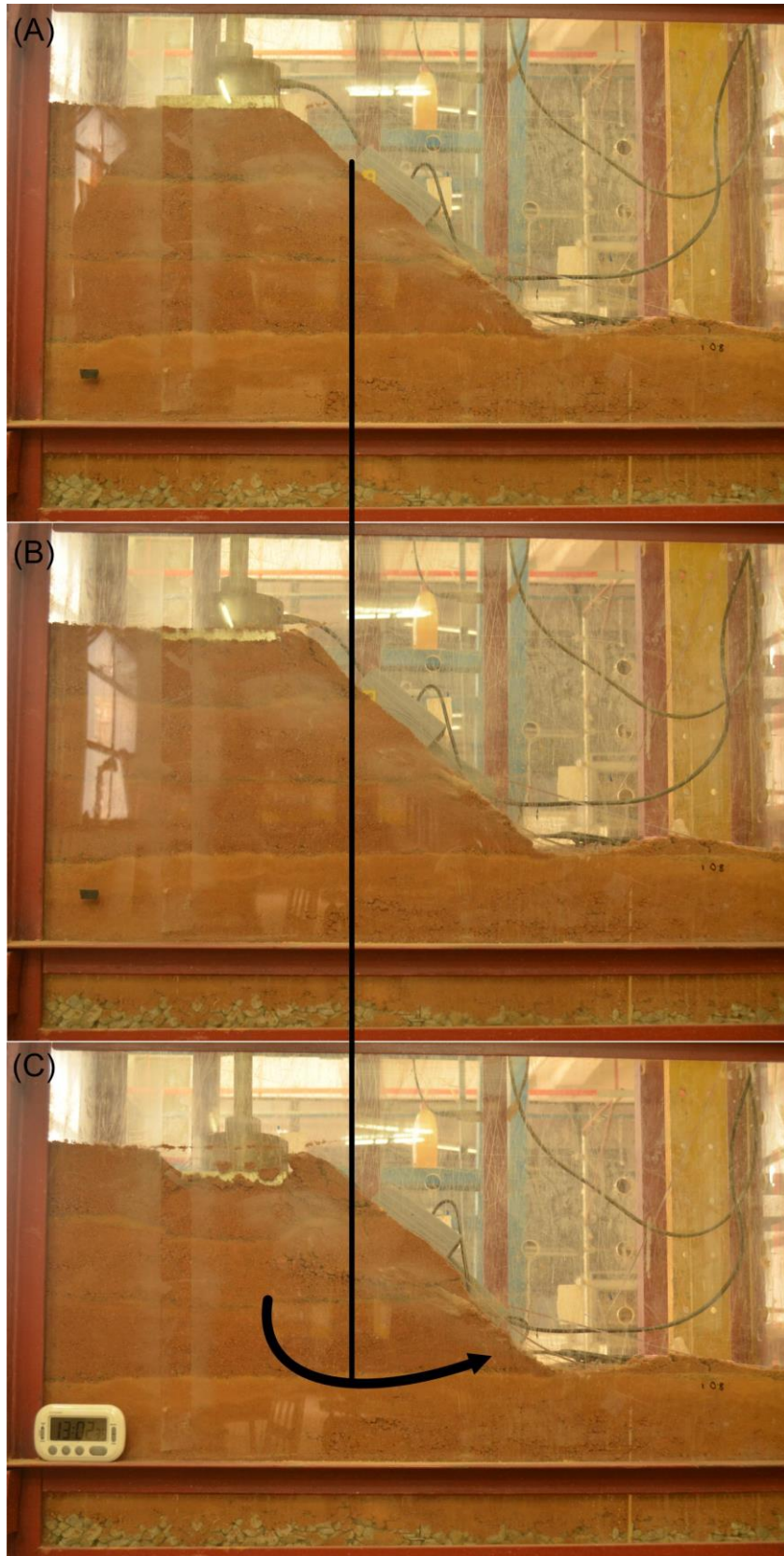


Figure 5.18: Slope deformation of the ground model for Case F; (A) initial state (B) significant AWAM device reading and (C) final condition after maximum loading

From the subsequent figures of the slope deformation result, it can be observed quite clearly the AWAM device apparently moved by a significant amount in cases B, E and F while the rest of the cases was observed to illustrate more subtle movements. Cases B and E clearly point out the fact evidently a longer exposure to rainfall significantly affect the robustness of the slope model. Furthermore, case F was noticeably deformed compared to case C due to the fact the slope model of case F was constructed with a greater slope angle. All of the cases exhibit the expected slope movement prior to failure while also displaying a visible slip circle failure on the face of the slope. The research progressed to quantify the magnitude of the slope movement by using results from the AWAM readings and Particle Image Velocimetry (PIV).

5.3.4 AWAM Readings

The results of the physical model testing were analysed in order to interpret the output signal from the AWAM devices. Each of the cases contains readings of two independently powered AWAM devices placed on different locations on the face of the ground model as explained in subchapter 3.5.1.3. The output of the accelerometers was translated to slope degree in accordance with the calibrations done on subchapter 4.3.2. After that, both the readings from the AWAM1 and AWAM2 devices were then broken down on to two sets of slope degree difference per minute. Slope degree differences per minute analysis were opted to analyse the magnitude of the precursor slope movement before slope failure. In addition, the slope movement per minute analysis were chosen due to the fact that the refresh rate capabilities of the AWAM system data logging to trigger the failure notifications were exactly 60 seconds. For each of the corresponding cases, the precursor slope degree change before failure and the maximum degree change representing slope failure were identified and discussed in the following subchapters. A thorough explanation and conclusion were drawn up for all the cases in subchapter 5.3.4.7.

5.3.4.1 Test 1:2 Slope with 1 Hour Rain (Case A)

For the first case which is the Test 1:2 slope with 1 Hour rain (Case A), Figure 5.19 represents the combined accelerometer readings from both AWAM1 and AWAM2 readings translated into a degree over time representation.

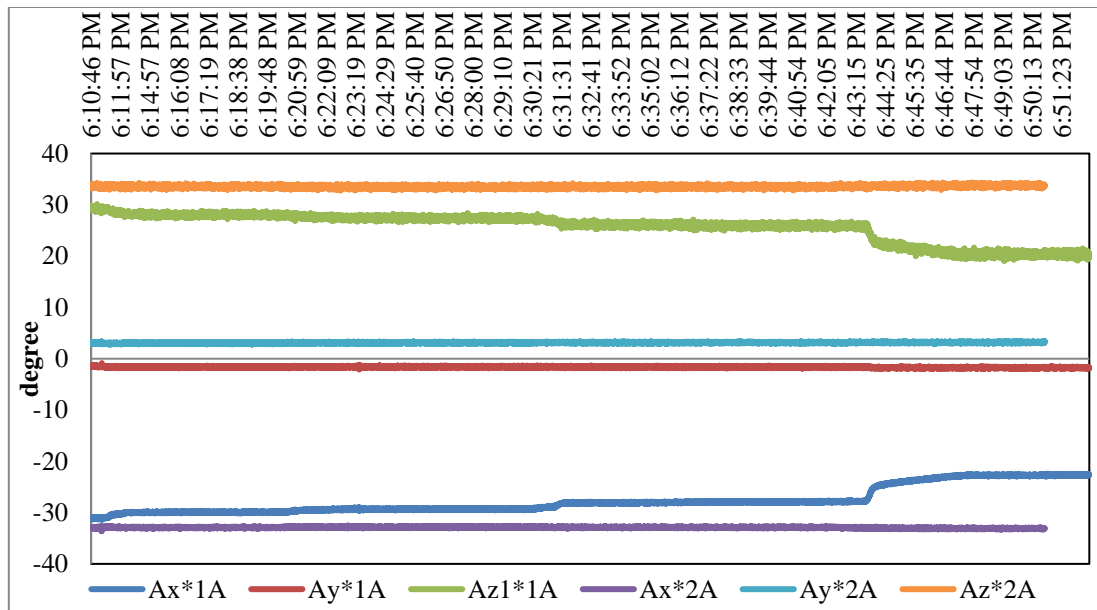


Figure 5.19: AWAM1 (1A) & AWAM2 (2A) result of degree change overtime data for Case A

The test commences at 6:10:46 PM. The initial degree recorded for the AWAM1 was -28.6° for the x-axis and 33.2° for the z-axis while the AWAM2 device recorded -32.7° and 33.2° readings for the x-axis and z-axis respectively. The testing progresses with incremental load until maximum loading failure was applied and slope failure was observed. The AWAM devices continue to log readings of the slope degree until the test stops at 6:51:20 PM after slope failure was observed.

To quantify the magnitude of slope degree movement and to measure the failure trigger threshold for the alarm notifications from the AWAM readings, a slope degree movement per minute were then formulated and analysed. The slope degree differences per minute analysis for Case A was represented in Figure 5.20 and Figure 5.21 for the AWAM1 and AWAM2 respectively.

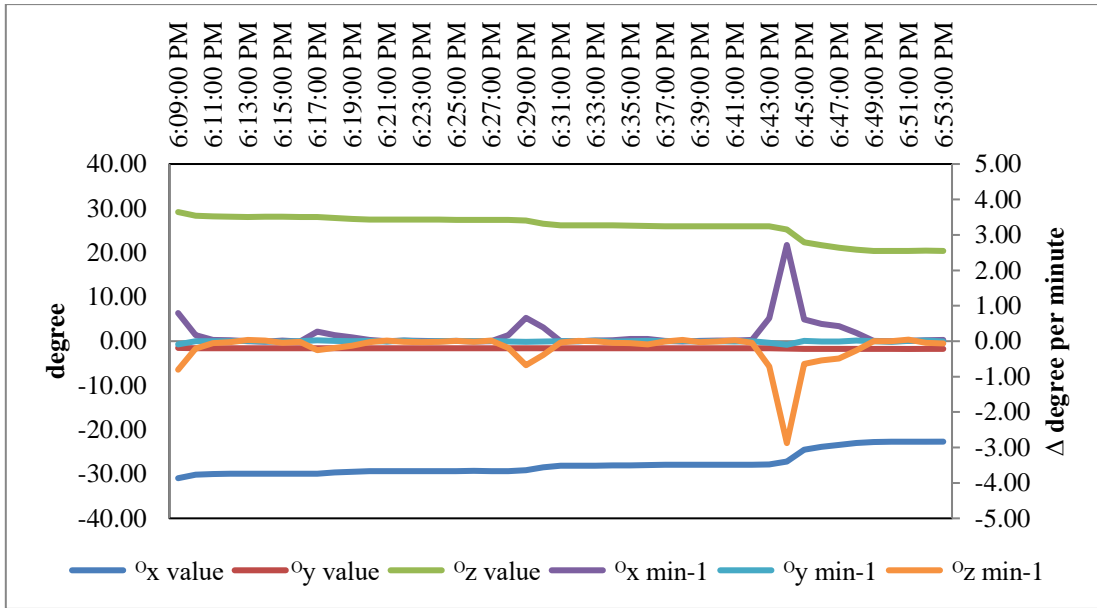


Figure 5.20: Degree of slope change over a minute for AWAM1 case A

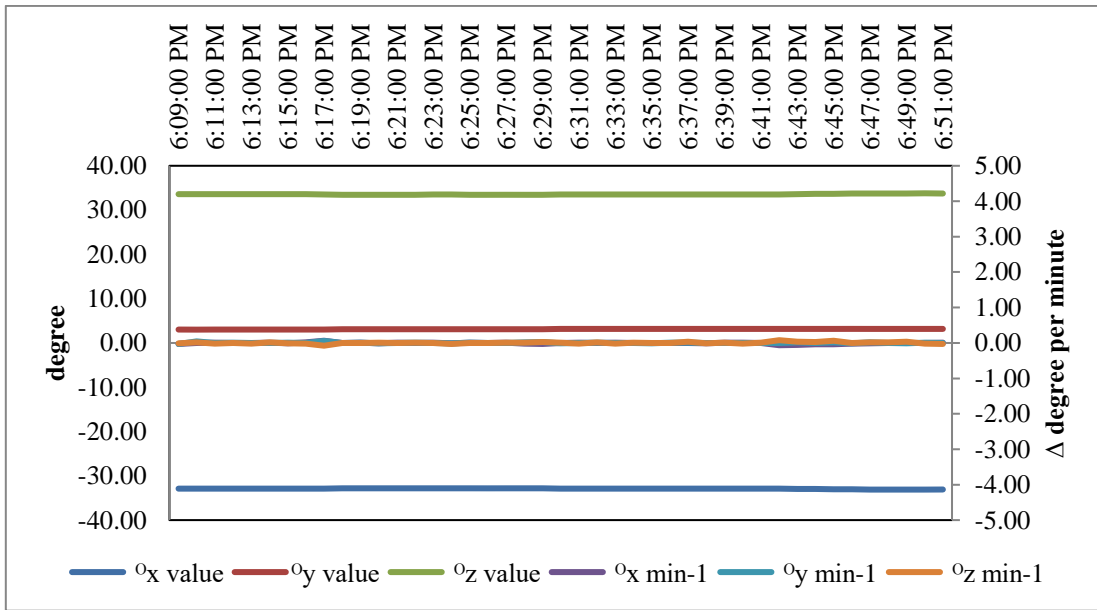


Figure 5.21: Degree of slope change over a minute for AWAM2 case A

Based on the previous figures, it can be observed that the AWAM1 device detected a solid movement per minute right from the start. This was dismissed as the movement from when the test initializes as the initial loading rests upon the ground model. Around 6:29:00 PM, the AWAM system logs an enormous spike of movement from both the x and z-axis of the slope on the AWAM1 device. The upward spike of the x-axis for the AWAM1 device lasted for the duration of three minutes with the added overall slope degree change of 0.17° , 0.66° and 0.39° occurring from 6:28:00

PM to 6:30:00 PM, with a total slope degree change of 1.22° . For the z-axis a slightly higher spike of -0.19° , -0.68° and -0.39° was identified on the same three minutes of the x-axis spike, bringing the total slope movement to -1.26° . The final spike representing the final failure load was observed to have a magnitude of 2.72° for the x-axis and -2.88° for the z-axis at 6:44:00 PM.

After tracing the time of the spike, it was found out that the spikes durations were identified to happen at the $2/3$ of the design load for the test which was 118.5 kPa. After the final failure spike of slope movement, the test concluded at 6:51:00 PM. For the three axes of AWAM2, the AWAM device was analysed to have no readings. The research concluded the fact that the device registers zero slope difference was due to the fact that the AWAM2 device is outside the range of the slip circle failure.

5.3.4.2 Test 1:2 Slope with 1 Hour Rain (Case B)

Figure 5.22 represents the combined accelerometer readings from both AWAM1 and AWAM2 readings translated into a degree over time representation for the Case B which is the Test 1:2 slope with 24 Hours rain.

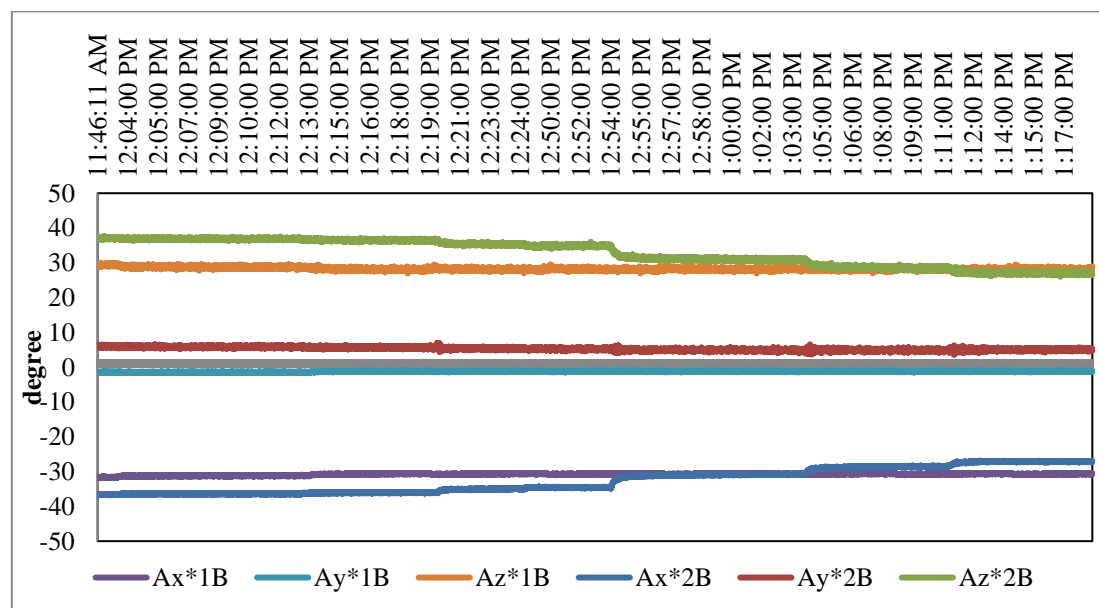


Figure 5.22: AWAM1 (1B) & AWAM2 (2B) result of degree change overtime data for Case B

The test commences at 11:46:11 PM. The initial degree recorded for the AWAM1 was -31.7° for the x-axis and 29.0° for the z-axis. While the AWAM2 device recorded x and z-axis was -36.7° and 36.6° respectively. The testing progresses with incremental load until maximum loading failure was applied and slope failure was observed. The AWAM devices continue to log readings of the slope degree until the test stops at 1:17:00 PM after slope failure was observed. The slope degree difference per minute analysis for Case B were then analysed and represented in Figure 5.23 and Figure 5.24 for the AWAM1 and AWAM2 respectively.

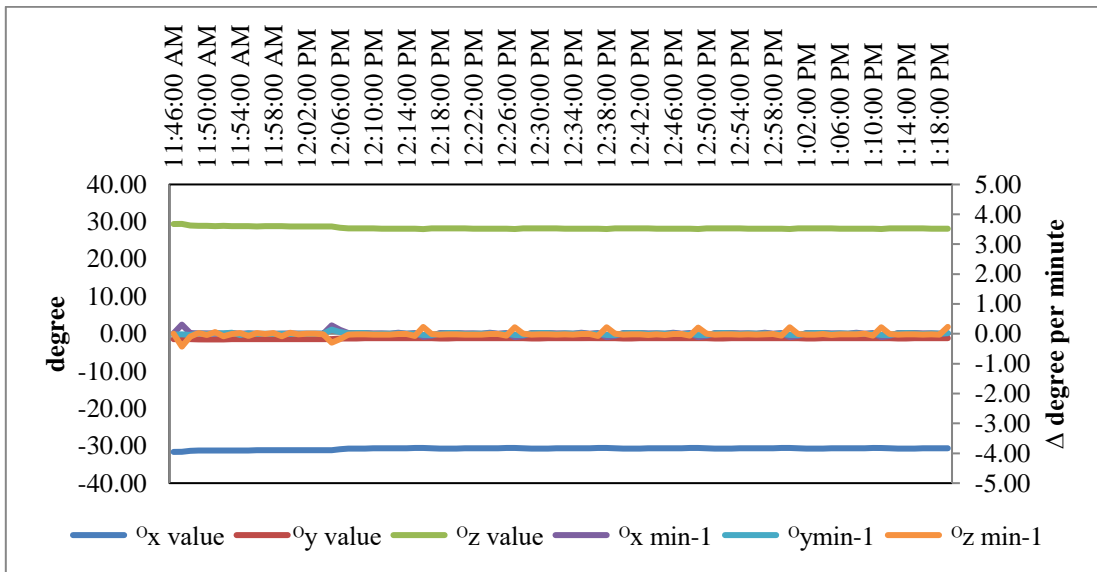


Figure 5.23: Degree of slope change over a minute for AWAM1 case B

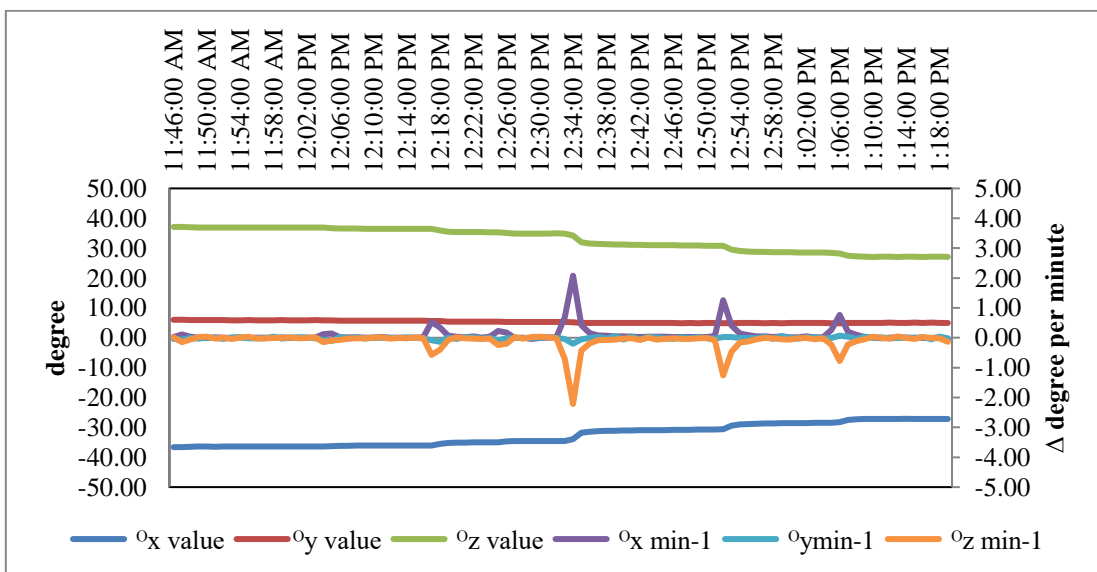


Figure 5.24: Degree of slope change over a minute for AWAM2 case B

Based on the previous figures, the AWAM1 device was analysed to had no significant readings. The research concluded the fact that the device registers zero slope difference was due to the fact that the AWAM1 device is outside the range of the slip circle failure.

Meanwhile, it can be observed that the AWAM2 device did detect a solid movement per minute. Around 12:34:00 PM, the AWAM system logs an enormous spike of movement from both the x and z-axis of the slope on the AWAM2 device. The upward spike of the x-axis for the AWAM2 device lasted for four minutes with the added overall slope degree change of 0.67° , 2.08° , 0.42° and 0.16° occurring from 12:33:00 PM to 12:35:00 PM with a total slope degree change of 3.33° . For the z-axis a slightly higher spike of -0.70° , -2.22° , -0.42° , -0.19° and -0.08° collectively was identified starting from 12:34:00 PM, bringing the total slope movement to -3.61° . The final spike representing the final failure load was observed to have a magnitude of 1.25° for the x-axis and -1.26° for the z-axis at 6:44:00 PM.

After tracing the time of the spike, it was found out that the spikes durations were identified to happen at the 1/2 of the design load for the test which was 78.9 kPa. After the final failure spike of slope movement, the test concluded at 1:18:00 PM.

5.3.4.3 Test 1:2 Slope without Rain (Case C)

Figure 5.25 represents the combined accelerometer readings from both AWAM1 and AWAM2 readings translated into a degree over time representation for the Case C which is the Test 1:2 slope without rain.

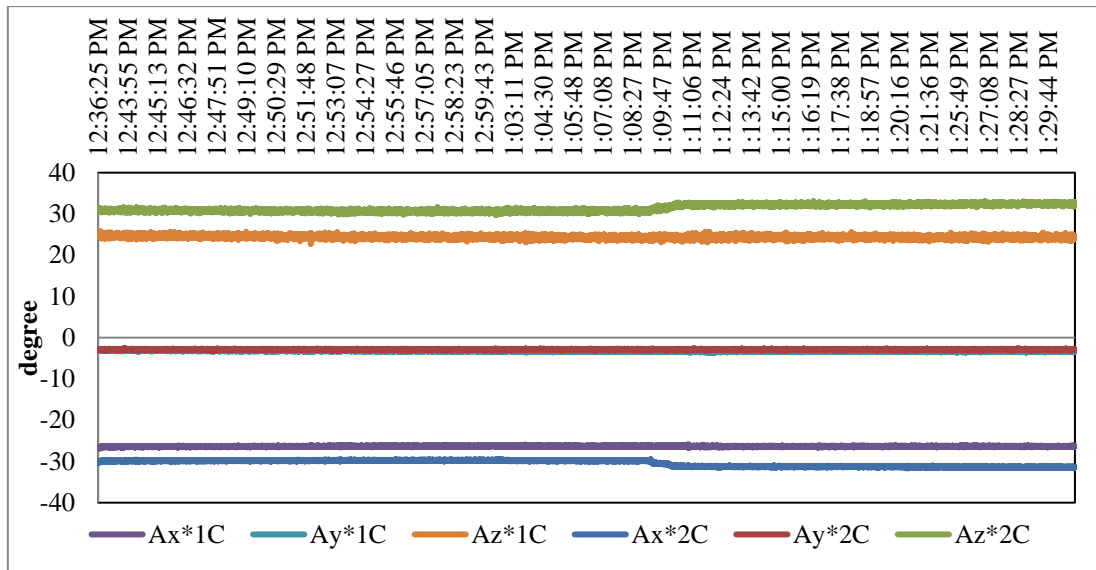


Figure 5.25: AWAM1 (1C) & AWAM2 (2C) result of degree change overtime data for Case C

The test commences at 12:36:25 PM. The initial degree recorded for the AWAM1 was -26.5° for the x-axis and 24.9° for the z-axis. While the AWAM2 device recorded x and z-axis was -30.0° and 30.9° respectively. The testing progresses with incremental load until maximum loading failure was applied and slope failure was observed. The AWAM devices continue to log readings of the slope degree until the test stops at 1:29:44 PM after slope failure was observed. The slope degree difference per minute analysis for Case C was then analysed and represented in Figure 5.26 and Figure 5.27 for the AWAM1 and AWAM2 respectively.

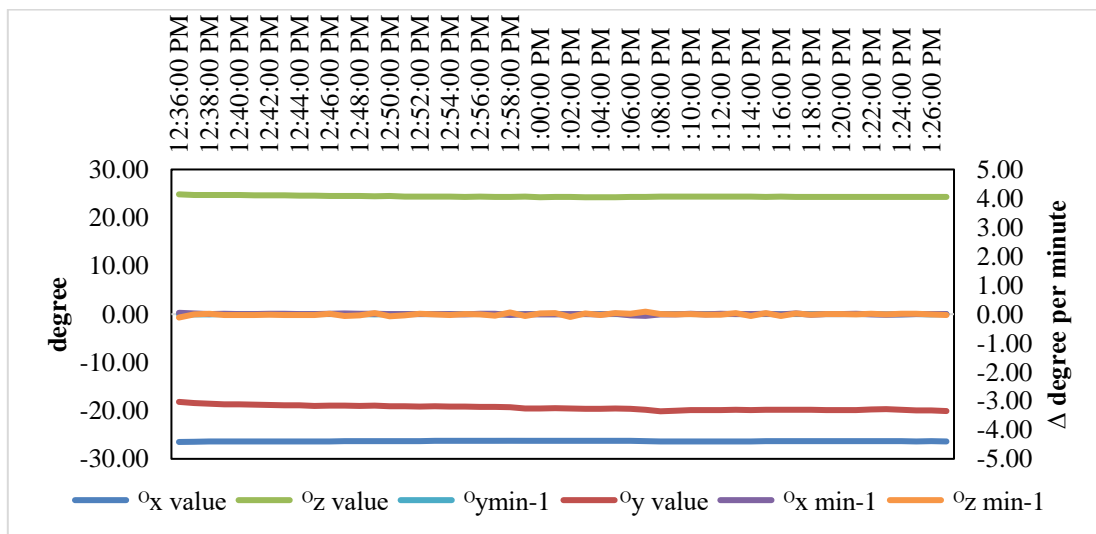


Figure 5.26: Degree of slope change over a minute for AWAM1 case C

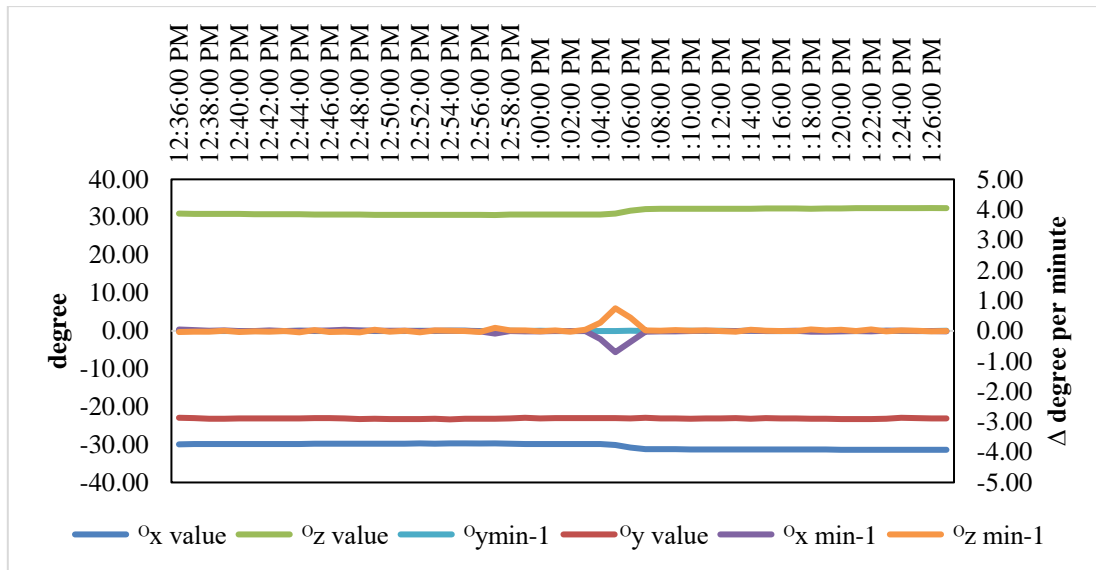


Figure 5.27: Degree of slope change over a minute for AWAM2 case C

Based on the previous figures, the AWAM1 device was analysed to have no significant readings. The research concluded the fact that the device registers zero slope difference was due to the fact that the AWAM1 device is outside the range of the slip circle failure.

Meanwhile, it can be observed that the AWAM2 device did detect a solid movement per minute. Around 1:05:00 PM, the AWAM system logs a solid spike of movement from both the x and z-axis of the slope on the AWAM2 device. The downward spike of the x-axis for the AWAM2 device lasted for the duration of three minutes with the added overall slope degree change of 0.27° , 0.70° , and 0.37° occurring from 1:04:00 PM to 1:06:00 PM with a total slope degree change of -1.37° . For the z-axis, a slightly higher spike of 0.27° , 0.75° and 0.44° per minute collectively was identified starting from 1:04:00 PM, bringing the total slope movement to 1.46° . The slope degree change per minute remains linear until the test ended at 1:26:00 PM.

After tracing the time of the spike, it was found out that the spikes durations were identified to happen at the $2/3$ of the design load for the test which was 143.0 kPa.

5.3.4.4 Test 1:1 Slope with 1 Hour Rain (Case D)

Figure 5.28 represents the combined accelerometer readings from both AWAM1 and AWAM2 readings translated into a degree over time representation for the Case D which is the Test 1:2 slope with 1 Hour rain.

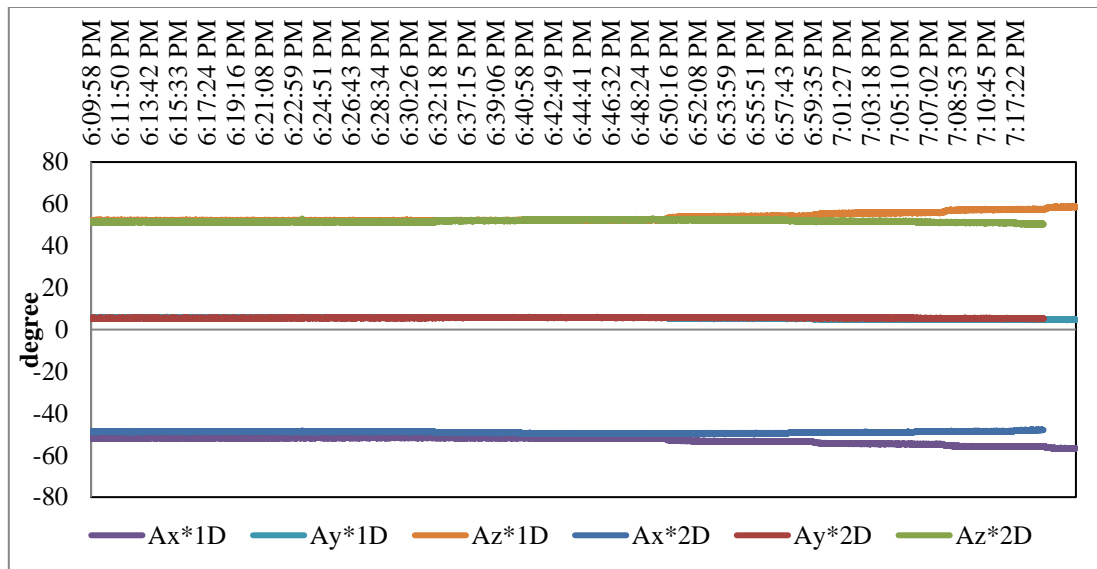


Figure 5.28: AWAM1 (1D) & AWAM2 (2D) result of degree change overtime data for Case D

The test commences at 6:09:58 PM. The initial degree recorded for the AWAM1 was -51.8° for the x-axis and 52.2° for the z-axis. While the AWAM2 device recorded x and z-axis was -48.8° and 51.4° respectively. The testing progresses with incremental load until maximum loading failure was applied and slope failure was observed. The AWAM devices continue to log readings of the slope degree until the test stops at 7:17:22 PM after slope failure was observed. The slope degree difference per minute analysis for Case D were then analysed and represented in Figure 5.29 and Figure 5.30 for the AWAM1 and AWAM2 respectively.

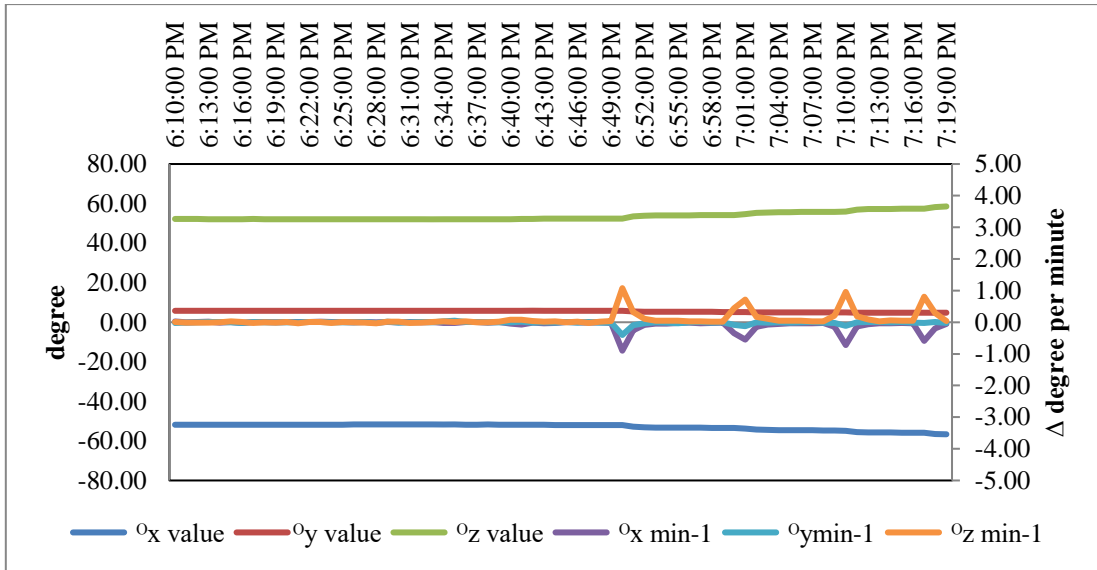


Figure 5.29: Degree of slope change over a minute for AWAM1 case D

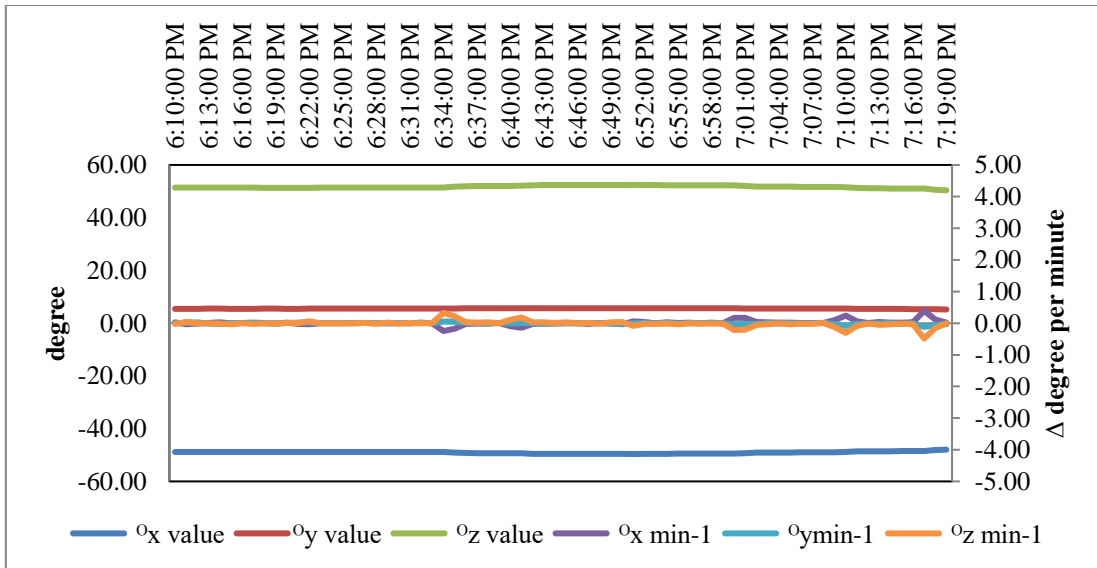


Figure 5.30: Degree of slope change over a minute for AWAM2 case D

Based on the previous figures at around 6:50:00 PM, the AWAM system logs an enormous spike of movement from both the x and z-axis of the slope on the AWAM1 device. The downward spike of the x-axis for the AWAM1 device lasted for two minutes with the added overall slope degree change of -0.90° and -0.26° , occurring from 6:50:00 PM to 6:51:00 PM with a total slope degree change of -1.16° . For the z-axis, a slightly higher spike of 1.08° , 0.32° and 0.11° was identified from 6:50:00 PM to 6:52:00 PM, bringing the total slope movement to 1.51° . The final spike representing the final failure load was observed to have a magnitude of -0.59° for the x-axis and 0.81° for the z-axis at 6:44:00 PM. For the three axes of AWAM2, the

AWAM2 device was analysed to have several spikes of slope change per minute but was regarded to have no significant value for an alarm trigger.

After tracing the time of the spike, it was found out that the spikes durations were identified to happen at the 2/3 of the design load for the test which was 120.0 kPa. After the final failure spike of slope movement, the test concluded at 7:19:00 PM. The research concluded the fact that the device registers zero slope difference was due to the fact that the AWAM2 device is outside the range of the slip circle failure.

5.3.4.5 Test 1:1 Slope with 24 Hour Rain (Case E)

Figure 5.31 represents the combined accelerometer readings from both AWAM1 and AWAM2 readings translated into a degree over time representation for the Case E which is the Test 1:2 slope with 24 Hours of rain.

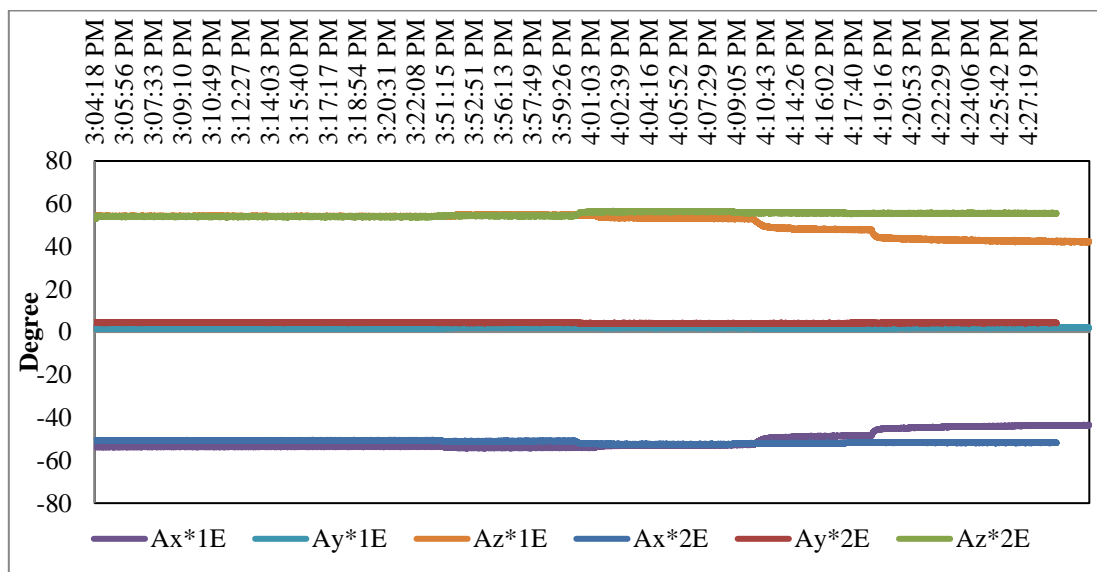


Figure 5.31: AWAM1 (1E) & AWAM2 (2E) result of degree change overtime data for Case E

The test commences at 3:04:18 PM. The initial degree recorded for the AWAM1 was -53.7° for the x-axis and 54.2° for the z-axis. While the AWAM2 device recorded x and z-axis was -50.8° and 54.1° respectively. The testing progresses with incremental load until maximum loading failure was applied and slope failure was

observed. The AWAM devices continue to log readings of the slope degree until the test stops at 4:27:19 PM after slope failure was observed. The slope degree difference per minute analysis for Case E were then analysed and represented in Figure 5.32 and Figure 5.33 for the AWAM1 and AWAM2 respectively.

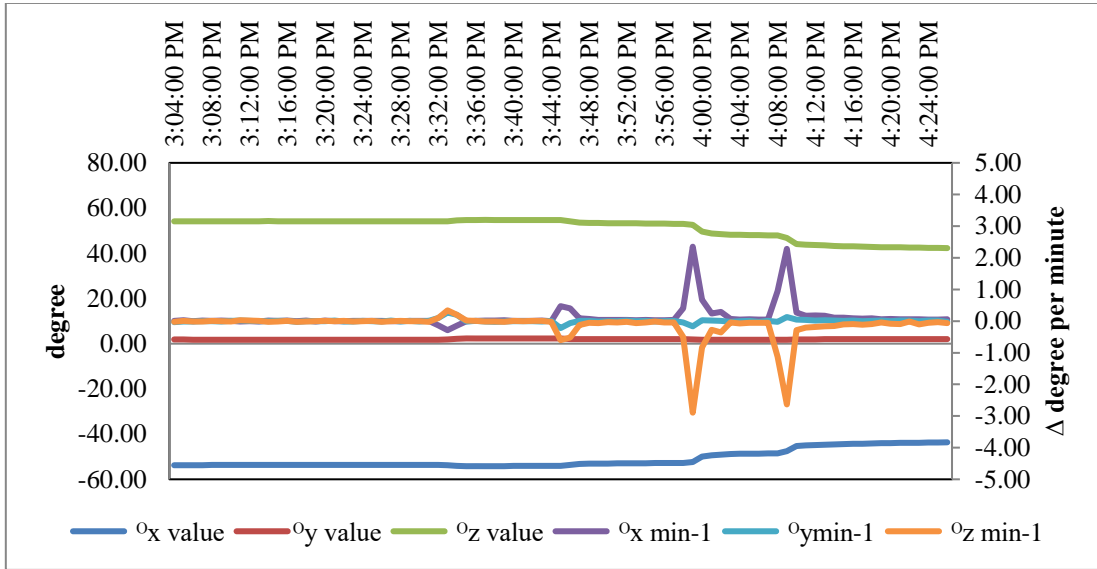


Figure 5.32: Degree of slope change over a minute for AWAM1 case E

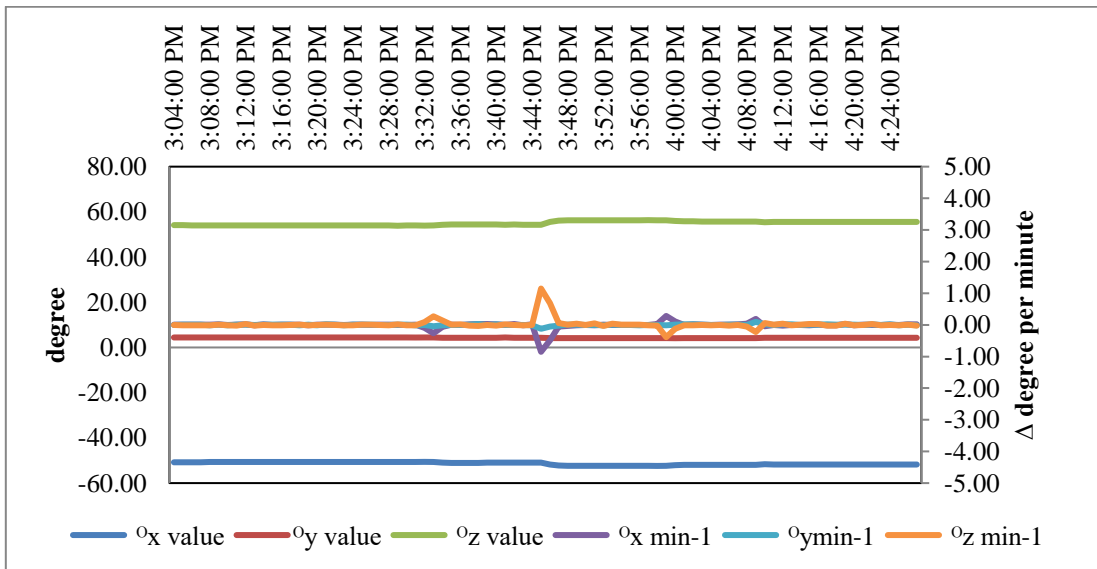


Figure 5.33: Degree of slope change over a minute for AWAM2 case E

The degree of slope change per minute analyses revealed that both of the AWAM devices register spikes of slope change per minute. Based on the previous

figures; at around 3:45:00 PM the AWAM system logs a moderate spike of movement from the AWAM1 device, whilst a huge spike was detected on the AWAM2 device.

The upward spike of the x-axis for the AWAM1 device lasted for three minutes with the added overall slope degree change of 0.47° , 0.40° and 0.08° , occurring from 3:45:00 PM to 3:47:00 PM with a total slope degree change of 0.95° . For the z-axis, a slightly higher spike of -0.60° , -0.52° and -0.12° was identified from 3:45:00 PM to 3:47:00 PM bringing the total slope movement to -1.24° . The next big spike occurred at 3:59:00 PM, registering an upward spike of 2.35° on the x-axis while -2.89° spike on the z-axis. The final spike representing the final failure load was observed to have a magnitude of 2.28° for the x-axis and -2.64° for the z-axis at 4:09:00 PM.

The downward spike of the x-axis for the AWAM2 device lasted for two minutes with the added overall slope degree change of -0.85° and -0.49° , occurring from 3:45:00 PM to 3:46:00 PM with a total slope degree change of -1.34° . For the z-axis, a slightly higher spike of 1.15° and 0.68° was identified from 3:45:00 PM to 3:46:00 PM bringing the total slope movement to 1.83° . The rest of the readings were thought to be linear with two insignificant readings of spikes until the test concluded at 4:24:00 PM.

After tracing the time of the spike, it was found out that the spikes durations for the AWAM1 device were identified to happen at first at the $1/2$ of the design load for the test which was 45.0 kPa occurring at 3:45:00 PM. After that, a higher spike of slope movement per minute was registered at $2/3$ of the designed load which was 60 kPa occurring at 3:59:00 PM. For the AWAM2 device readings, the only spike registered was at the $1/2$ of the designed load occurring at 3:45:00 PM. After the final failure spike of slope movement, the test concluded at 4:24:00 PM.

5.3.4.6 Test 1:1 Slope without Rain (Case F)

Figure 5.34 represents the combined accelerometer readings from both AWAM1 and AWAM2 readings translated into a degree over time representation for the Case F which is the Test 1:1 slope without rain.

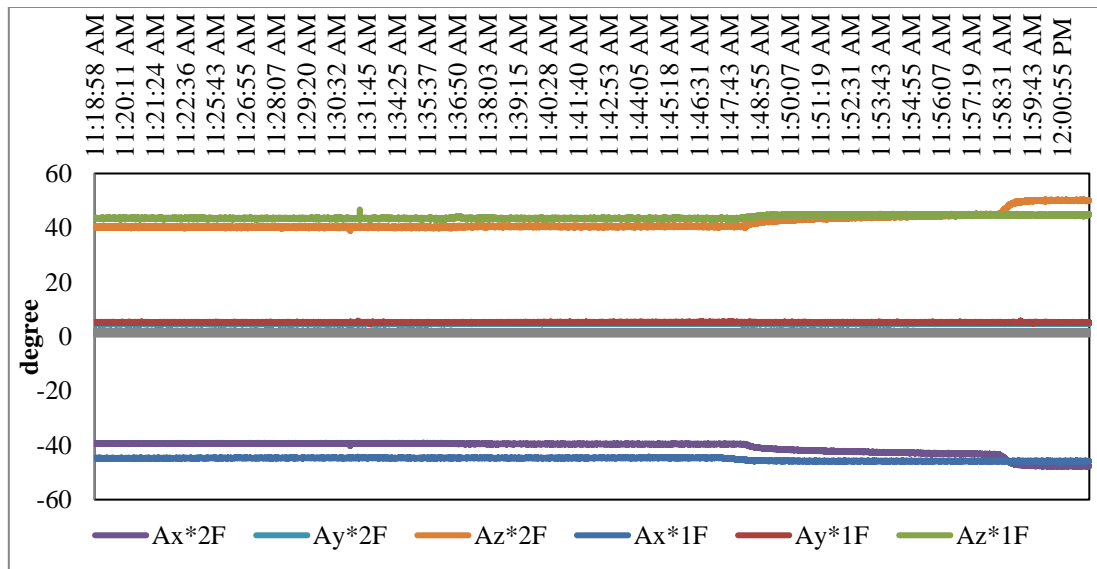


Figure 5.34: AWAM1 (1F) & AWAM2 (2F) result of degree change overtime data for Case F

The test commences at 11:18:58 AM. The initial degree recorded for the AWAM1 was -44.7° for the x-axis and 43.5° for the z-axis while the AWAM2 device recorded x and z-axis was -39.4° and 40.3° respectively. The testing progresses with incremental load until maximum loading failure was applied and slope failure was observed. The AWAM devices continue to log readings of the slope degree until the test stops at 12:00:55 PM after slope failure was observed. The slope degree difference per minute analysis for Case F were then analysed and represented in Figure 5.35 and Figure 5.36 for the AWAM1 and AWAM2 respectively.

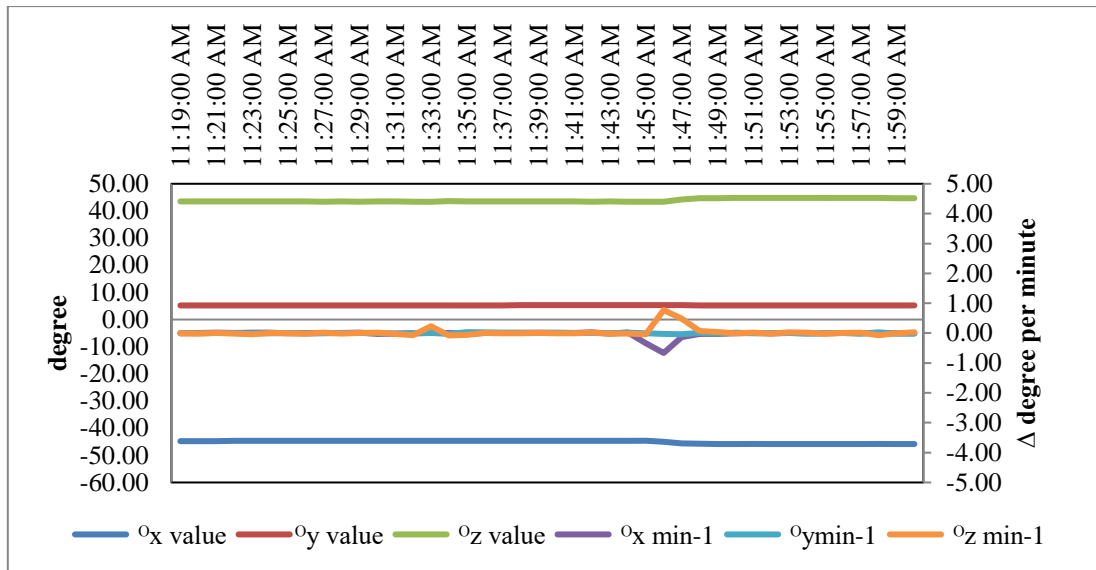


Figure 5.35: Degree of slope change over a minute for AWAM1 case F

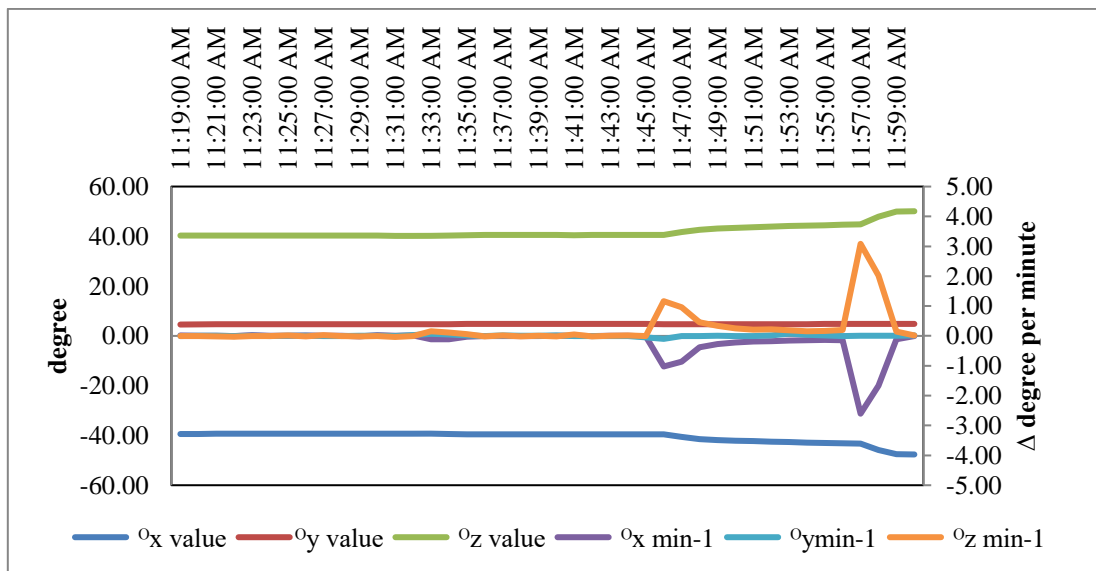


Figure 5.36: Degree of slope change over a minute for AWAM2 case F

The degree of slope change per minute analyses revealed that both of the AWAM devices register spikes of slope change per minute. Based on the previous figures; at around 11:46:00 AM the AWAM system logs a moderate spike of movement from the AWAM1 device, whilst a huge spike was detected on the AWAM2 device.

The downward spike of the x-axis for the AWAM1 device lasted for three minutes with the added overall slope degree change of -0.34° , -0.66° and -0.13° , occurring from 11:45:00 AM to 11:47:00 AM with a total slope degree change of -1.13° . For the z-axis, a slightly higher spike of 0.77° , 0.48° and 0.07° were identified from 11:45:00 AM to 11:47:00 AM bringing the total slope movement to 1.32° . The final spike representing the final failure load was observed to have a magnitude of 2.28° for the x-axis and -2.64° for the z-axis at 4:09:00 PM. The rest of the readings were thought to be linear with no insignificant readings of spikes until the test concluded at 11:59:00 AM

The downward spike of the x-axis for the AWAM2 device lasted for the duration of three minutes with the added overall slope degree change of -1.02° , -0.86° and -0.38° , occurring from 11:46:00 AM to 11:48:00 AM with a total slope degree change of -2.26° . For the z-axis, a slightly higher spike of 1.16° , 0.96° and 0.45° was identified from 3:46:00 PM to 3:48:00 PM bringing the total slope movement to 3.57° . The AWAM1 device registered no final spike reading of the final failure load induced on the slope model.

After tracing the time of the spike, it was found out that the spikes durations for the AWAM1 device were identified to happen at first at the $2/3$ of the design load for the test which was 133.3 kPa occurring at 11:46:00 AM. Similar spikes were registered on AWAM2 device readings, logging at the similar $2/3$ of the designed load point at 11:46:00 AM. The final spike representing the final failure load was observed to have a magnitude of -2.60° for the x-axis and 3.08° for the z-axis at 11:57:00 AM. After the final failure spike of slope movement, the test concluded at 11:59:00 AM.

5.3.4.7 Concluding Notes

Though the initial slope degree value was intended to be approximate to the constructed slope of 27° and 45° , due to the uneven surface of the face of the slope after being exposed to the rain model a marginal slope difference was deemed

acceptable. This was apparent as the value from the Cases C and F which was not susceptible to rainfall simulations were approximately nearer to the constructed slope.

The degree of slope change per minute was constructed to determine the threshold or trigger value for the alarm system that was essential in the system. These values over a range of 27° to 45° slope angle gave the approximate readings to be considered when designing an alarm trigger for a slope monitoring system. Each behaviour of the AWAM device also provided insights on the slope failure mechanism of a constructed slope.

The positive movement of the x-axis combined with the negative movement of the z-axis suggest the AWAM device tilted clockwise from the initial placements of the device such as described in subchapter 4.4 and such as shown in Figure 5.37. While inversely, a decrease of x-axis angle paired with an increase of z-axis angle suggest a counter-clockwise tilt of the devices.

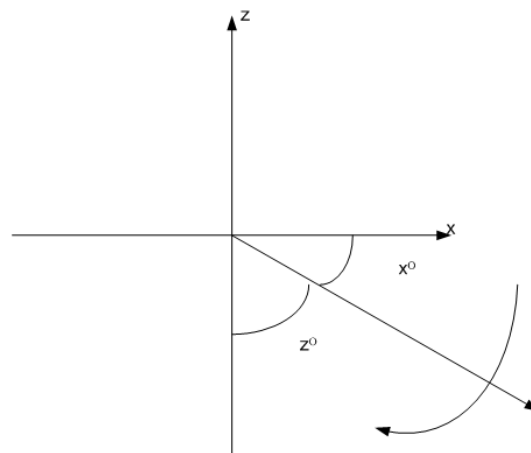


Figure 5.37: Downward movement as x^0 increases and z^0 decreases

After tracing the time of the spike, it was found out that the spikes durations were identified to happen at the $2/3$ of the design load for the Cases A, C, D and F while Cases B and E registered spikes of data at $1/2$ of the design load. This was observed to be contributed by the fact that Cases B and E had a longer duration of rainfall simulations. While also lowering their stress-strain relationships, these cases were fast-forwarding its failure precursor movement significantly until only half of the

design load ahead of the rest of the cases which registered precursor spike at 2/3 of the designed load.

For some of the tests, the AWAM device was analysed to have no readings. This was thought to have resulted from the slip circle failure being outside of the ranges of the AWAM sensors. Whilst the AWAM1 which was placed slightly higher on the slope face apart from the AWAM2, all of the cases managed to register a precursor failure slope movement either on one of the devices or registering on both. Having wider extensions of AWAM sensors to cover an entirety of a slope face was determined to be essential in order to have proper monitoring of a designated slope. Table 5.5 lists out the summary of the initial device angle and precursor spikes on all of the cases.

Using this pre-cursor slight movement of soil prior to complete failure of the slope, the device can successfully predict the bound to happen slope failure.

Table 5.5: AWAM device results summary

Device	Initial device angle (°)				Highest Precursor Spike device angle (°)				Total Precursor Spike device angle (°)				Final Spike device angle (°)			
	A1		A2		A1		A2		A1		A2		A1		A2	
Axis	x-axis	z-axis	x-axis	z-axis	x-axis	z-axis	x-axis	z-axis	x-axis	z-axis	x-axis	z-axis	x-axis	z-axis	x-axis	z-axis
Case A	-28.60	33.20	-32.70	33.20	0.67	-0.68	-	-	1.22	-1.26	-	-	2.72	2.88	-	-
Case B	-31.60	29.40	-36.60	37.10	-	-	2.08	-2.22	-	-	3.33	-3.61	-	-	1.25	-1.26
Case C	-26.50	24.90	-30.00	30.93	-	-	-0.70	0.75	-	-	-1.37	1.46	-	-	-0.59	0.81
Case D	-51.83	52.17	-48.80	51.40	-0.60	1.08	-	-	-1.16	1.51	-	-	-0.59	0.81	-	-
Case E	-53.70	54.20	-50.80	54.10	0.47	-0.60	-0.85	1.15	0.95	-1.24	-1.34	1.83	2.28	-2.64	-	-
Case F	-44.70	43.53	-39.40	40.31	-0.66	0.77	-1.02	1.16	-1.13	1.32	-2.26	3.57	-	-	-2.60	3.08

* (-) value represent insignificantly small data

5.3.5 PIV Result

The PIV analysis was done after the post-processing of the images from the tests as described in subchapter 3.8. To show the soil movements of the ground model, the PIV analysis was terminated at the vector plot stage to show the displacements of the soils at vertical direction beneath the loading plate. The slip circle failure directed towards the slope face and soil movement beneath the loading plate was illustrated successfully by the PIV analysis.

Figure 5.38 to Figure 5.43 shows the soil displacements for all the model tests respectively. The slope model and loading plate were plotted on the PIV vector result for a better representation of the soil movements. It can be clearly observed that some wild vectors were present outside the field of interest highlighted and can be removed from the analysis by using the subroutine 'GEOWILD' if deemed necessary, though were remained in place as it does not affect the interpretations of the result in any way.

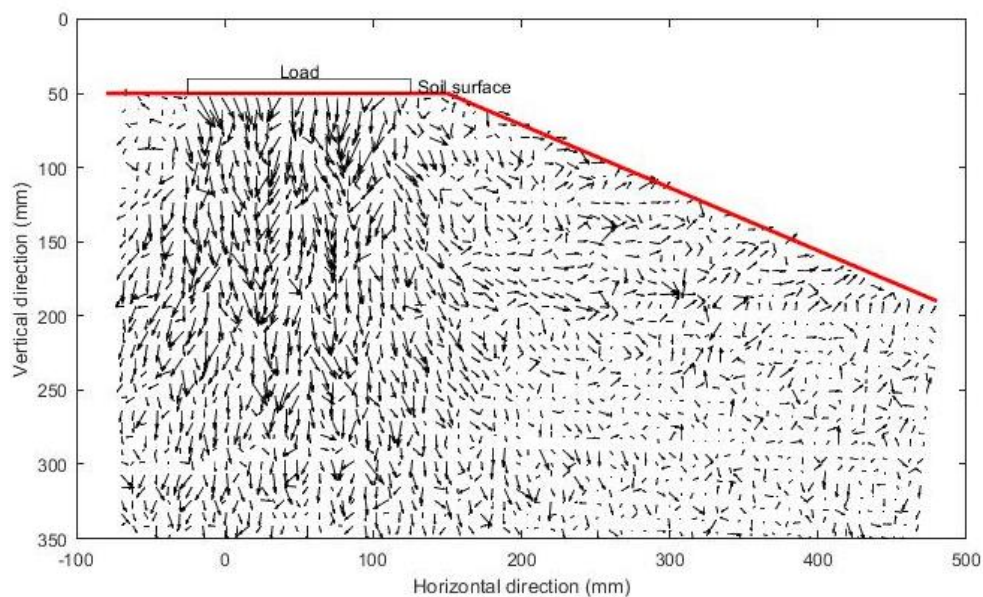


Figure 5.38: Slope displacements for Case A (27° Degree and 1-Hour rain)

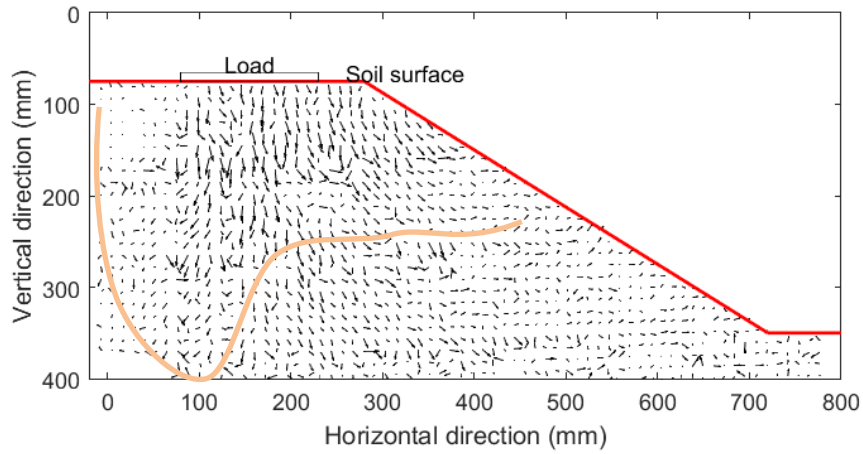


Figure 5.39: Slope displacements for Case B (27° Degree and 24-Hour rain)

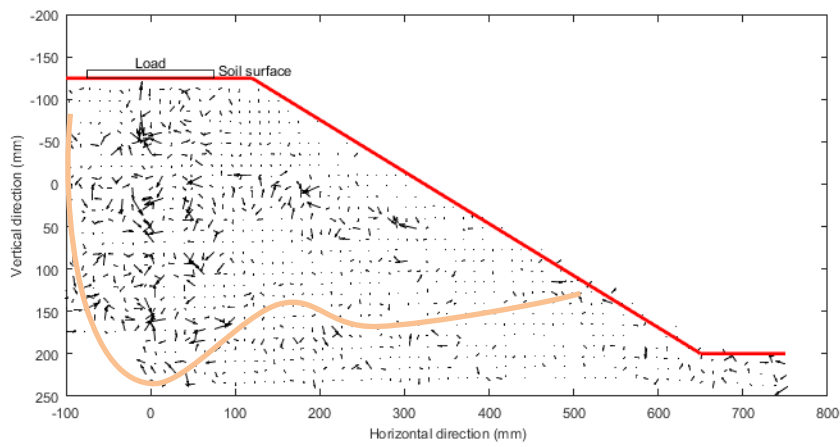


Figure 5.40: Slope displacements for Case C (27° Degree and 0-Hour rain)

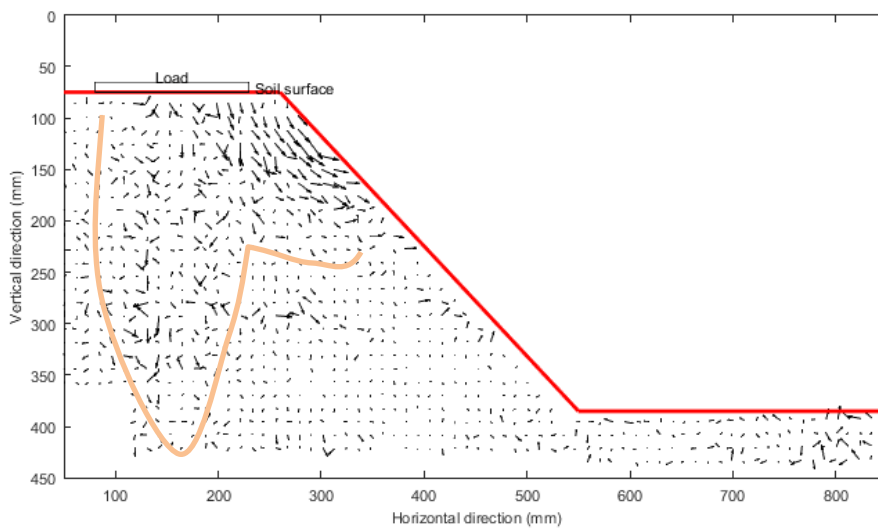


Figure 5.41: Slope displacements for Case D (45° Degree and 1-Hour rain)

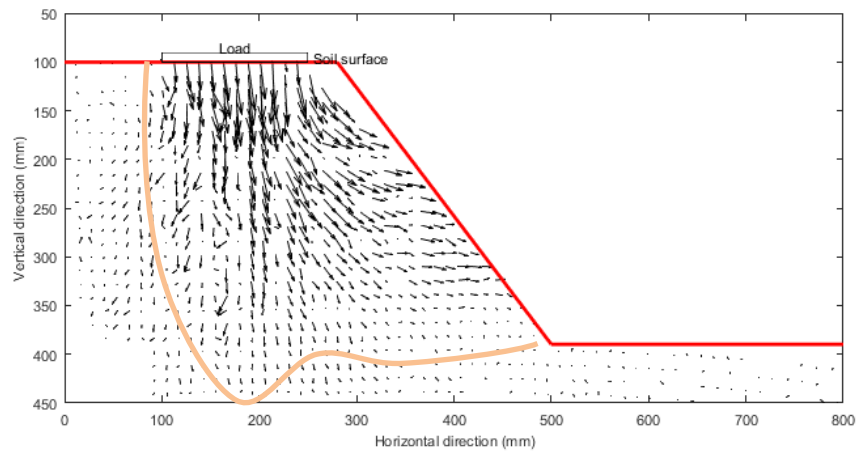


Figure 5.42: Slope displacements for Case A (45° Degree and 24-Hour rain)

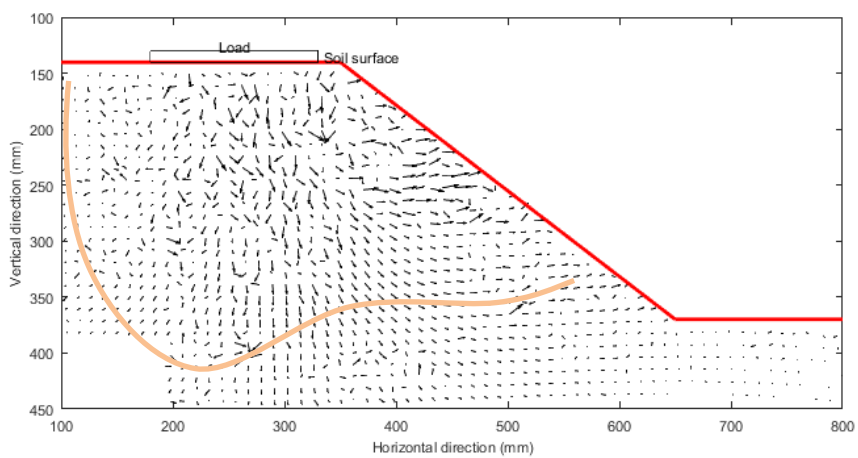


Figure 5.43: Slope displacements for Case A (45° Degree and 0-Hour rain)

From the following figures, it was observed that the displacement of the soil beneath the loading plate align perfectly with the result from subsection 5.3.3. Results from subchapter 5.3.4 can be corroborated by the results from the PIV vector simulations since only the soil movement within a particular slip circle would be detected by specific AWAM device placements. For case A, only the higher placement of the AWAM sensors which was AWAM1 detected slope movements. That was also true for cases B and C when only AWAM2 which was the lower sensor picked up spikes of movement. Case D in particular only registered slope movement in AWAM1 much similar the results from Case A. While finally Cases E and F demonstrate both AWAM device registered movements of slope since the slip circle failure was widespread enough to enable both AWAM devices detection.

Hence, it was concluded that the PIV vector simulation successfully produced the illustrations of a typical slip circle failure that corresponds well with the results obtained from the placements of the AWAM sensors.

The research proceeds after the vector plot stage with the contour mapping and shear strain plotting as mentioned in subchapter 3.8. This would further illustrate the magnitude of deformation and also shear strain that was occurring in the slope model during the physical modelling stage of the research. The following figures were composed by displaying two sets of vertical and horizontal movements within the slope model followed by the shear strain for each of the cases.

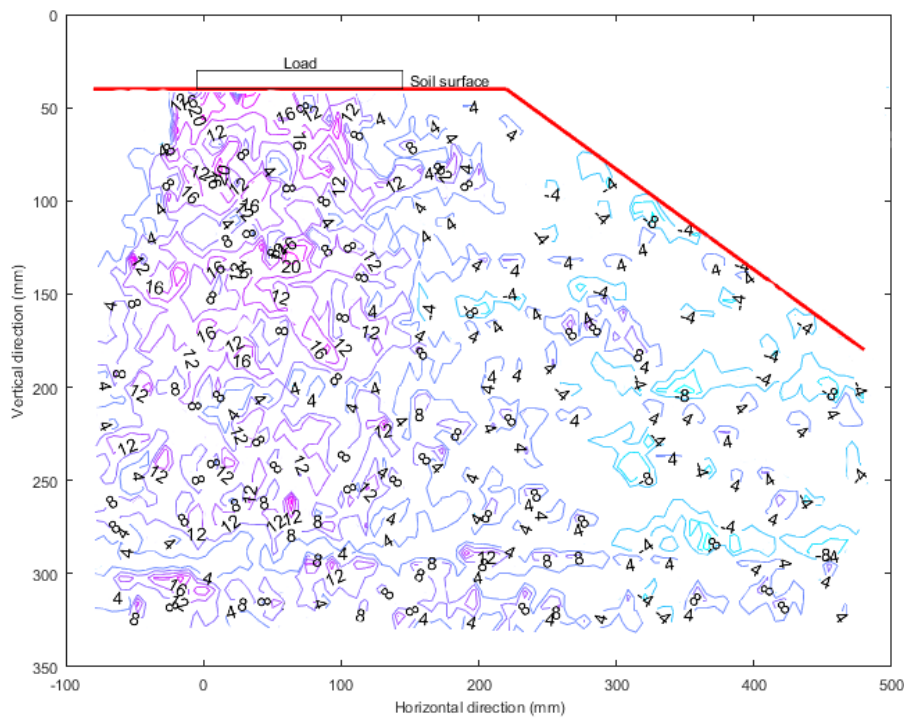


Figure 5.44: Contours of cumulative vertical displacement for Case A (27° Degree and 1-Hour rain)

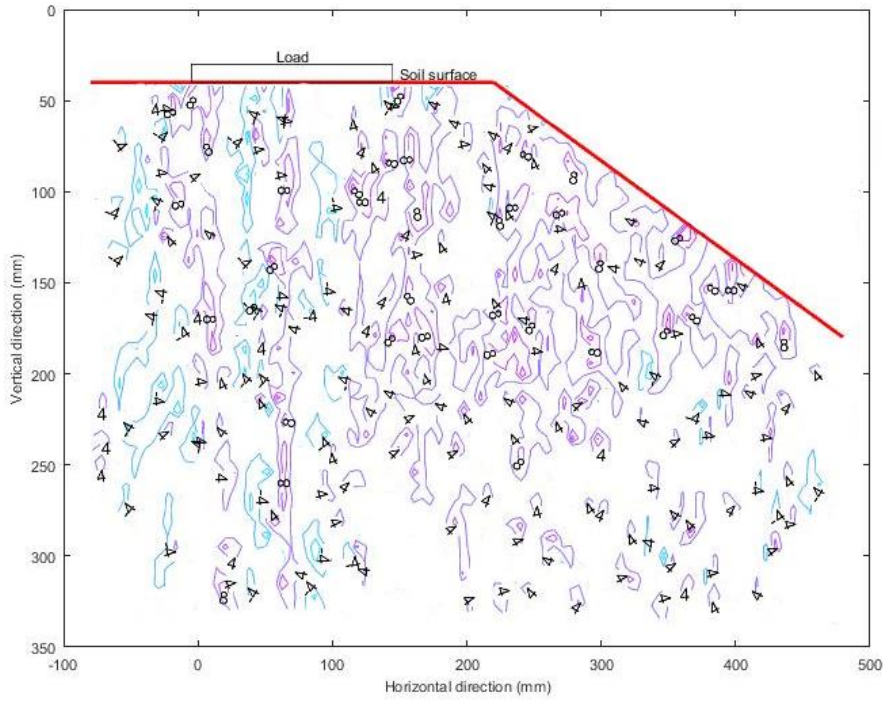


Figure 5.45: Contours of cumulative horizontal displacement for Case A (27° Degree and 1-Hour rain)

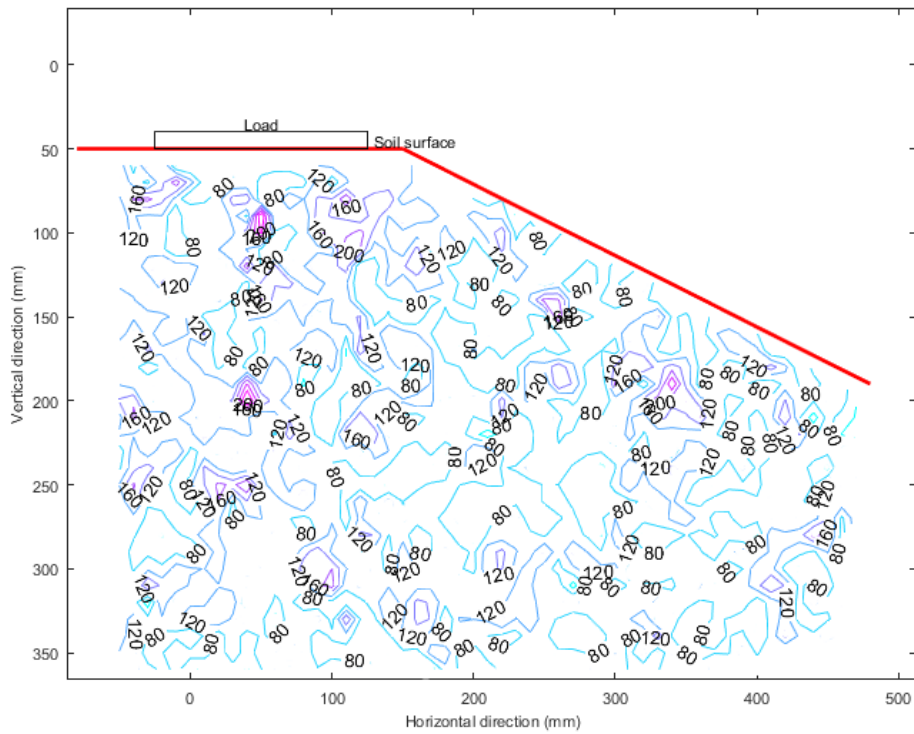


Figure 5.46: Contours of shear strain for Case A (27° Degree and 1-Hour rain)

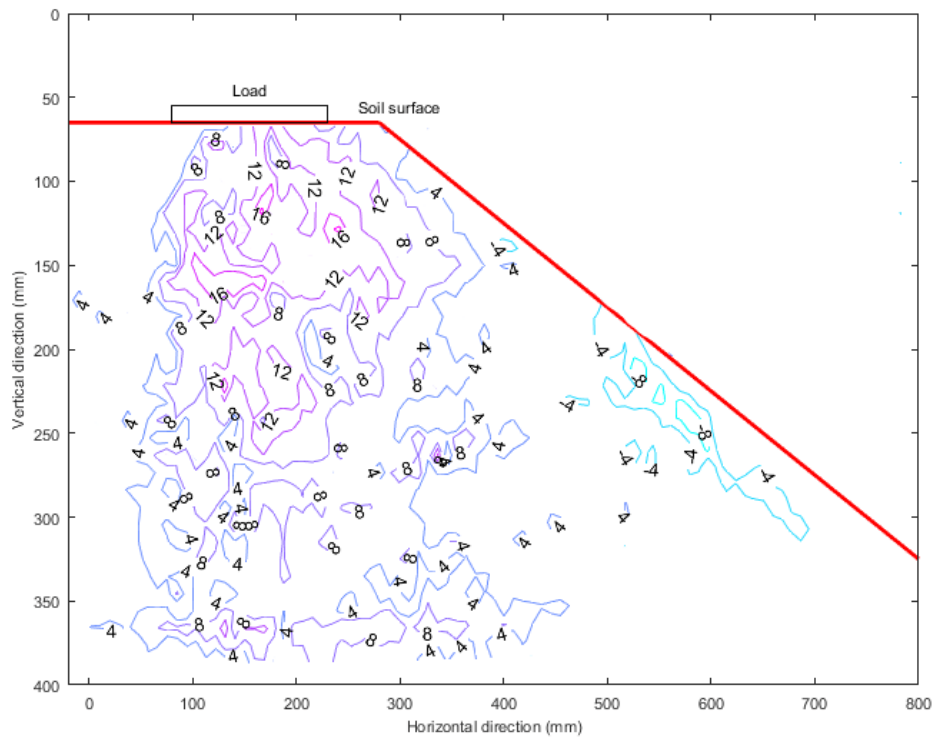


Figure 5.47: Contours of cumulative vertical displacement for Case B (27° Degree and 24-Hour rain)

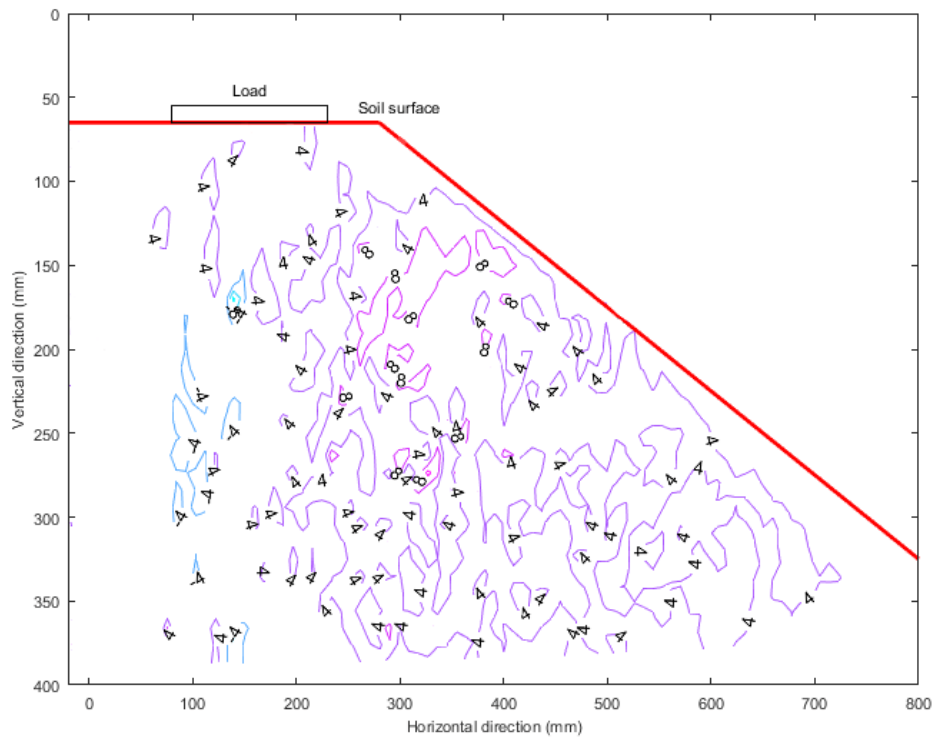


Figure 5.48: Contours of cumulative horizontal displacement for Case B (27° Degree and 24-Hour rain)

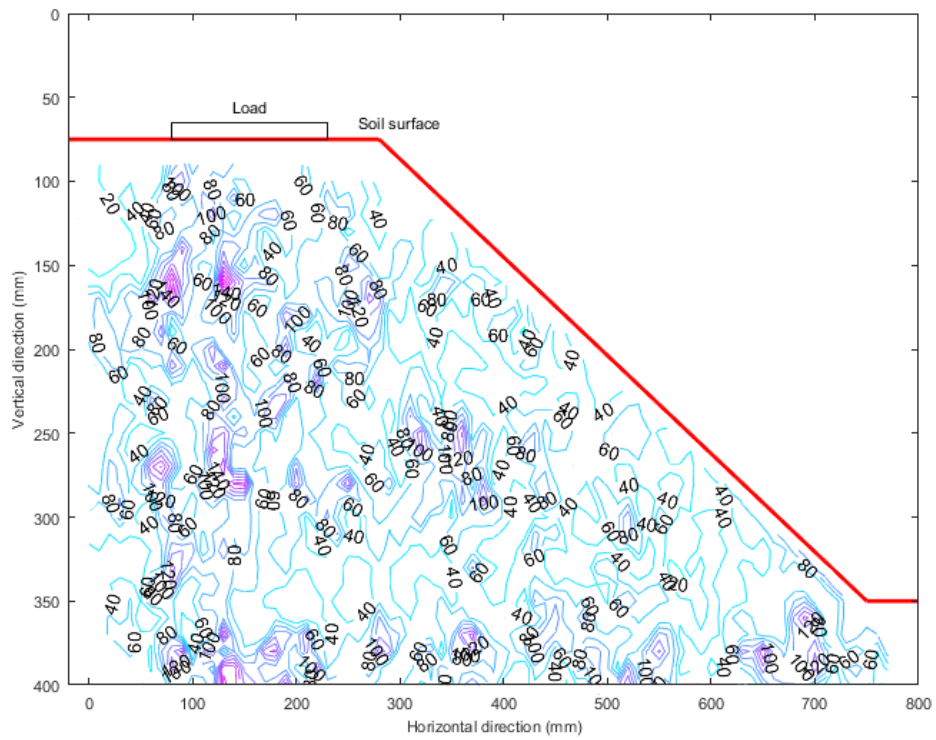


Figure 5.49: Contours of shear strain for Case B (27° Degree and 24-Hour rain)

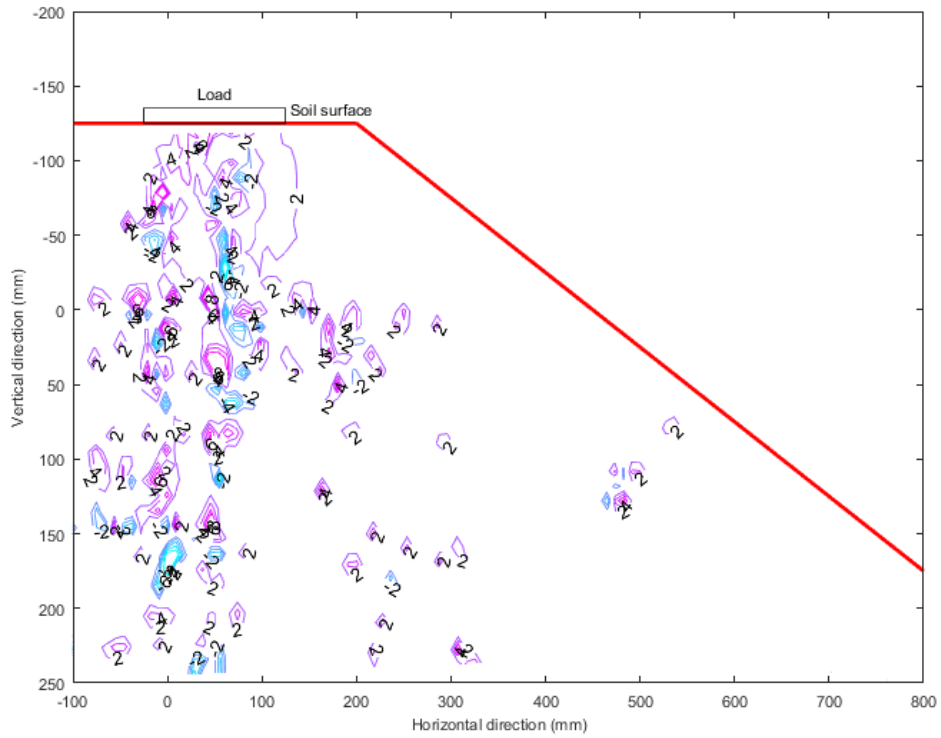


Figure 5.50: Contours of cumulative vertical displacement for Case C (27° Degree and 0-Hour rain)

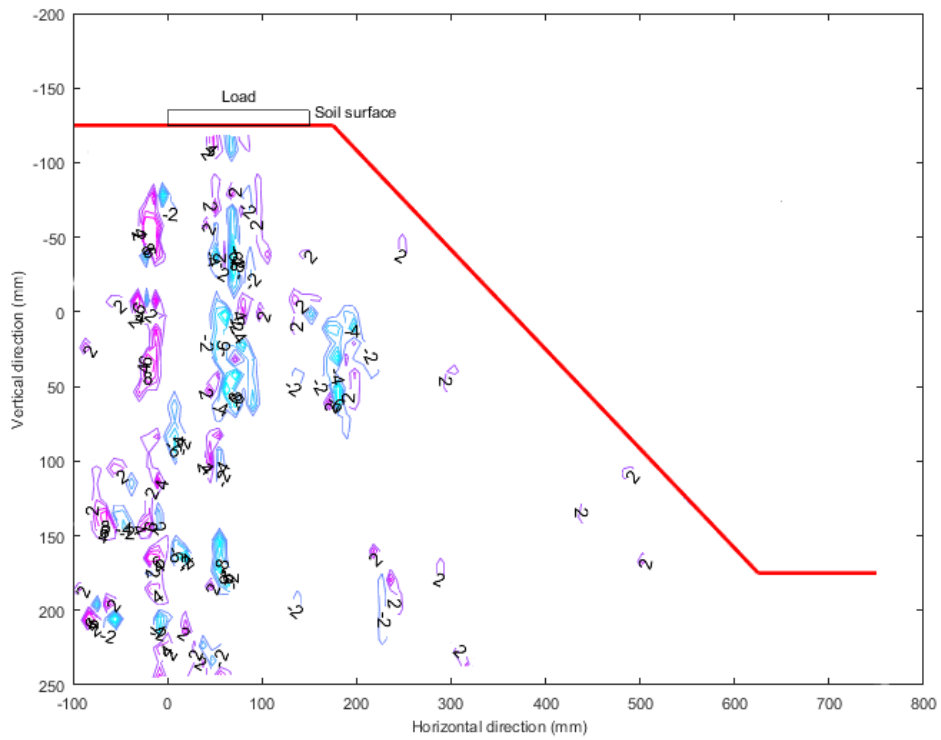


Figure 5.51: Contours of cumulative horizontal displacement for Case C (27° Degree and 0-Hour rain)

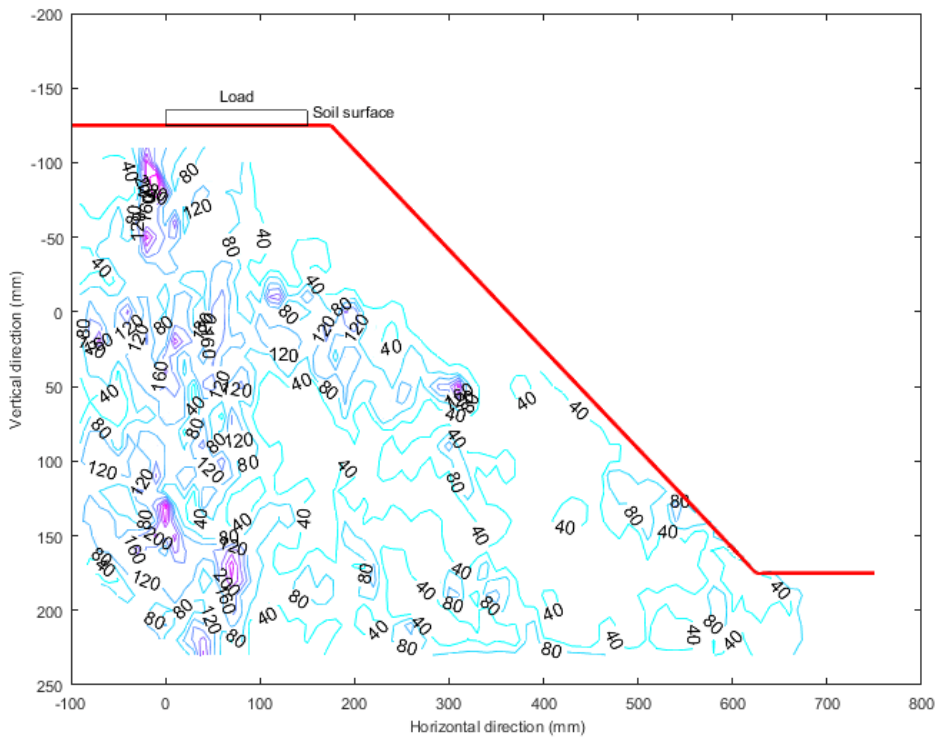


Figure 5.52: Contours of shear strain for Case C (27° Degree and 0-Hour rain)

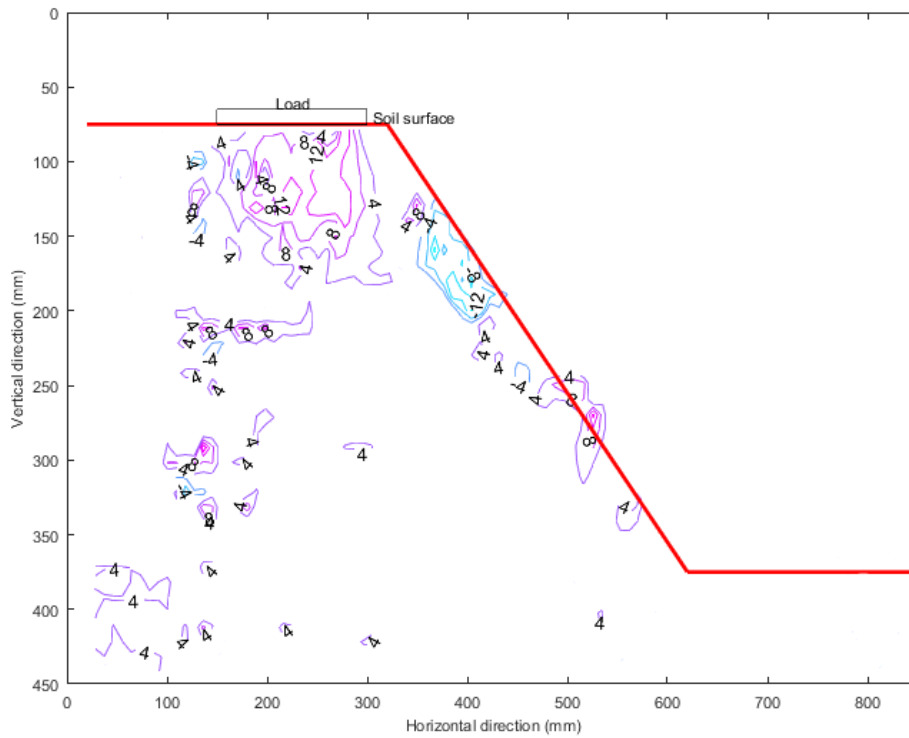


Figure 5.53: Contours of cumulative vertical displacement for Case D (45° Degree and 1-Hour rain)

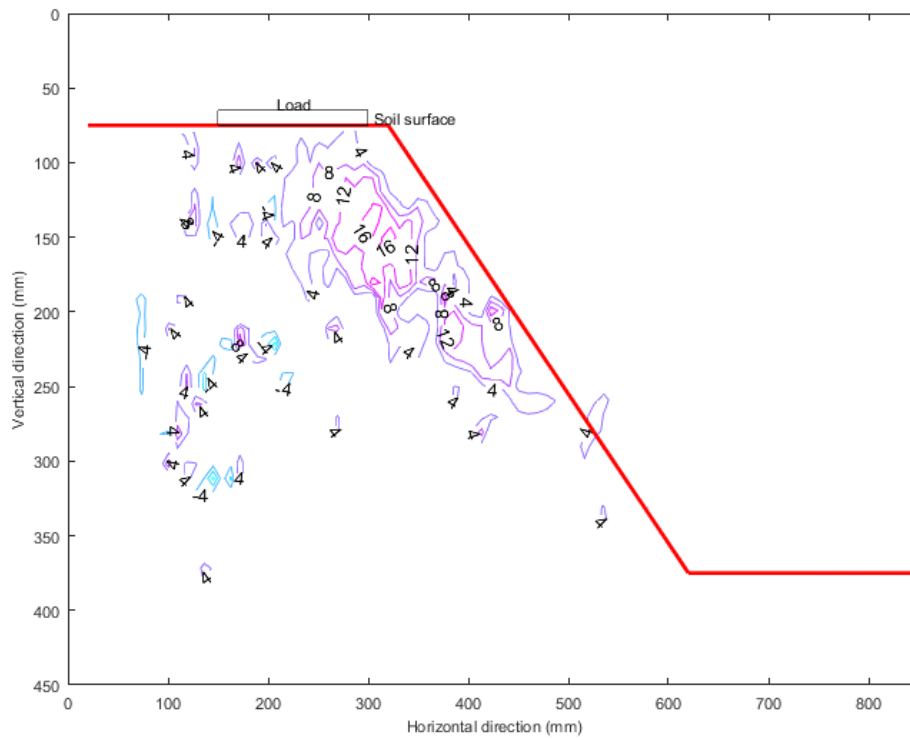


Figure 5.54: Contours of cumulative horizontal displacement for Case D (45° Degree and 1-Hour rain)

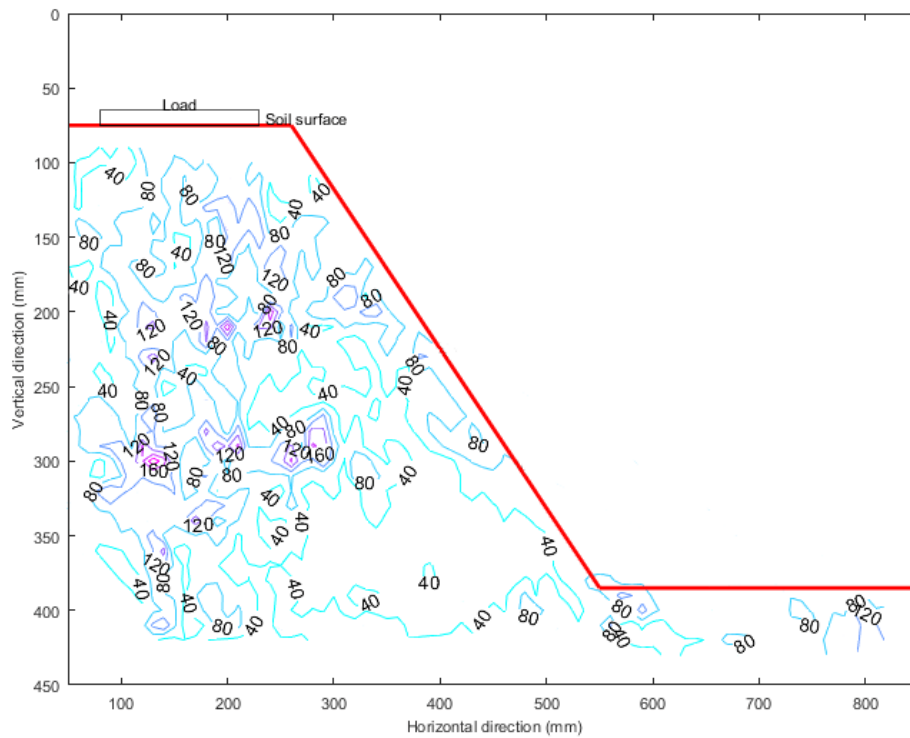


Figure 5.55: Contours of shear strain for Case D (45° Degree and 1-Hour rain)

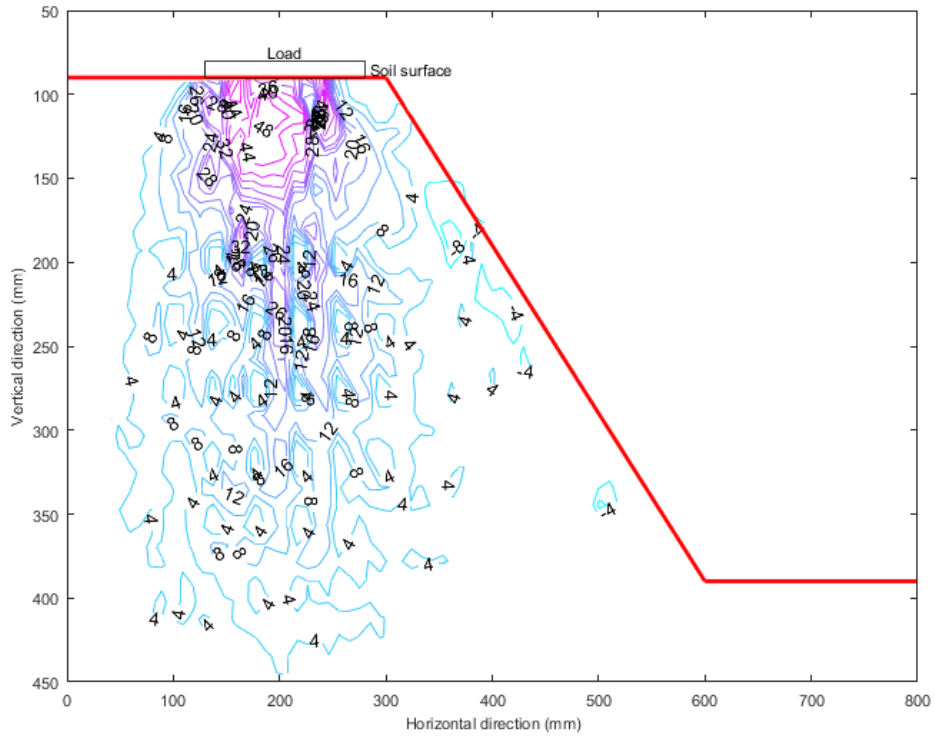


Figure 5.56: Contours of cumulative vertical displacement for Case E (45° Degree and 24-Hour rain)

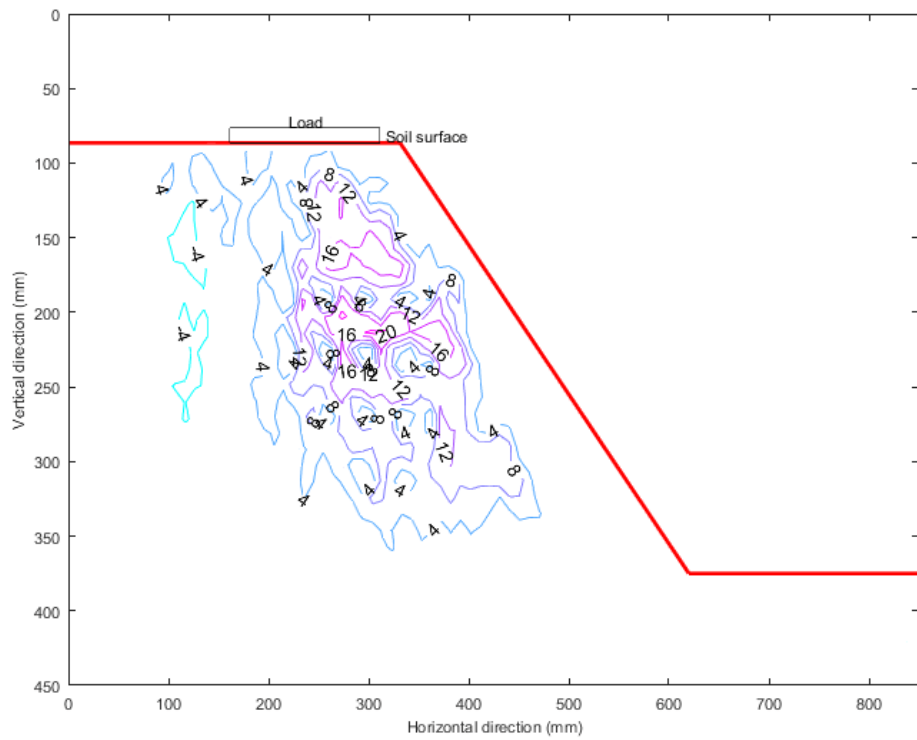


Figure 5.57: Contours of cumulative horizontal displacement for Case E (45° Degree and 24-Hour rain)

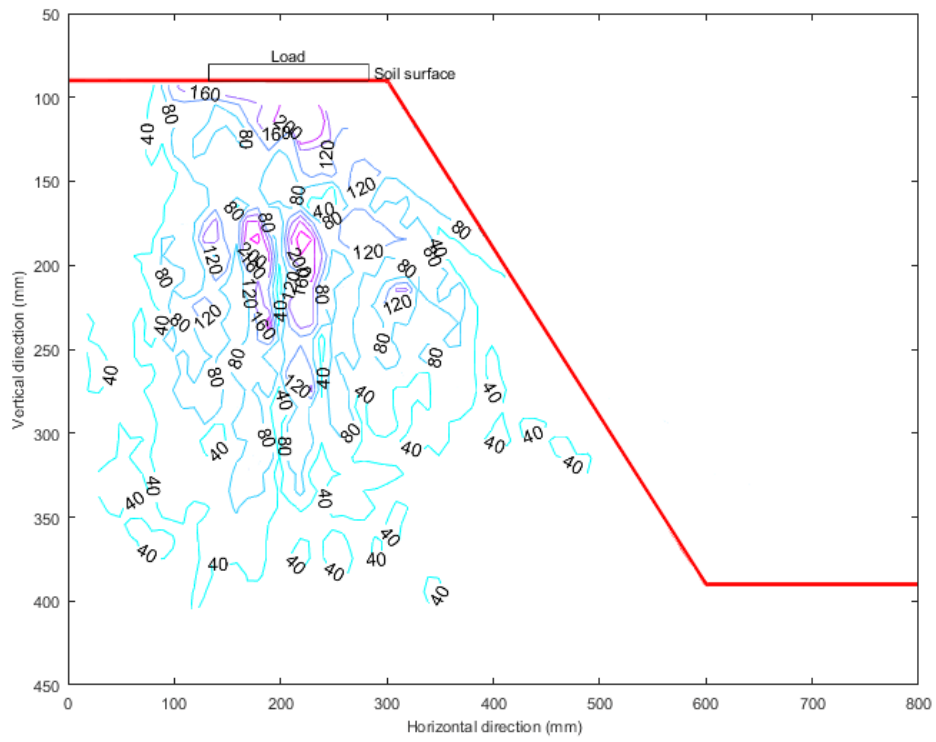


Figure 5.58: Contours of shear strain for Case E (45° Degree and 24-Hour rain)

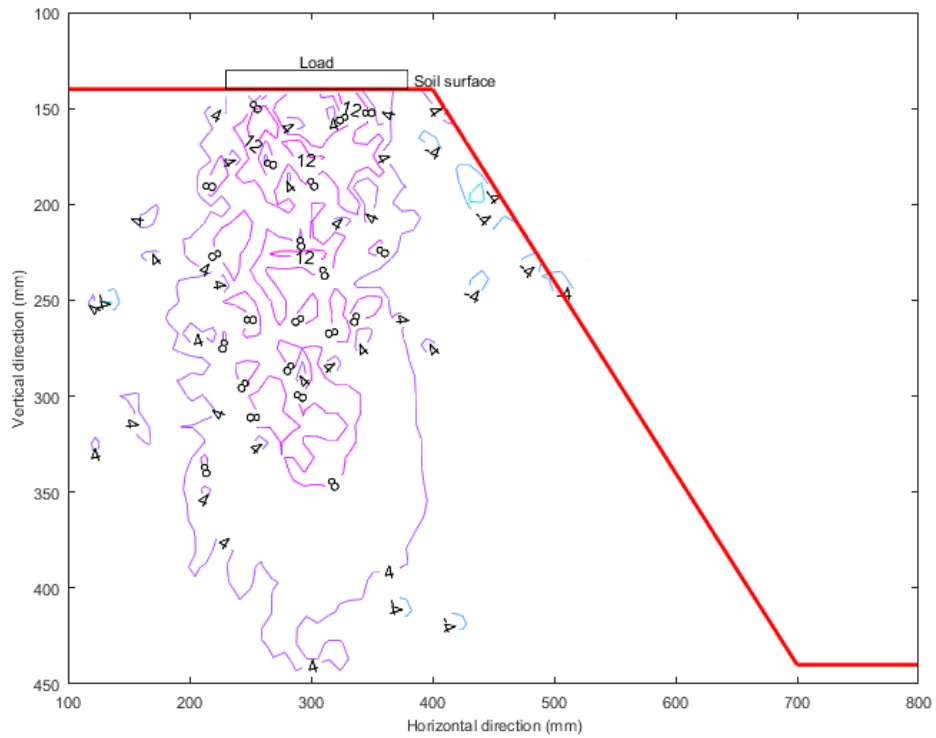


Figure 5.59: Contours of cumulative vertical displacement for Case F (27° Degree and 0-Hour rain)

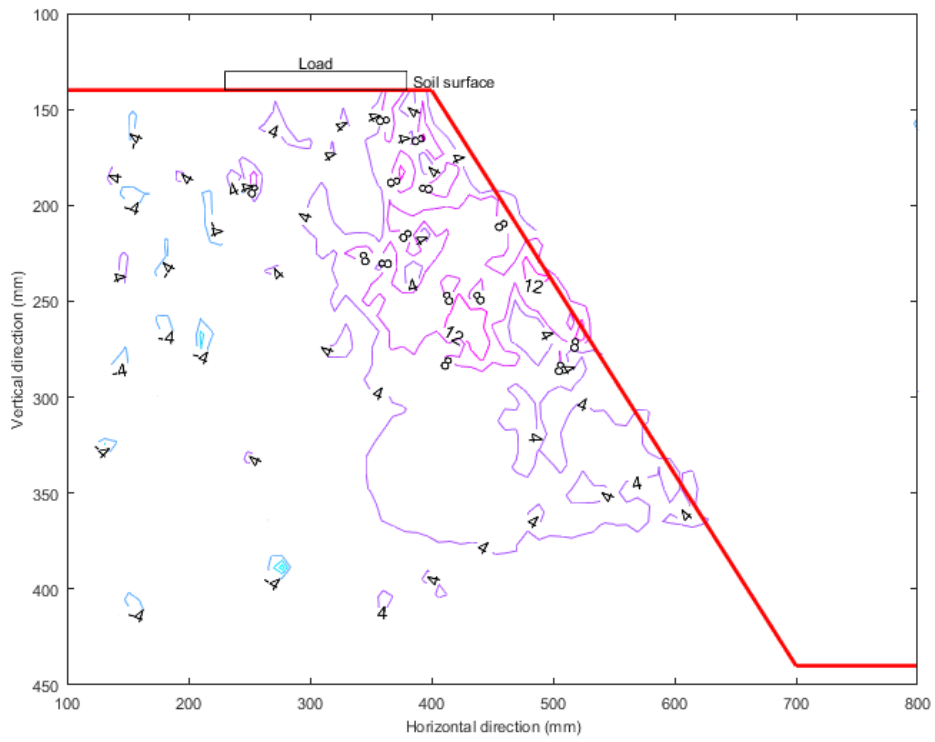


Figure 5.60: Contours of cumulative horizontal displacement for Case F (45° Degree and 0-Hour rain)

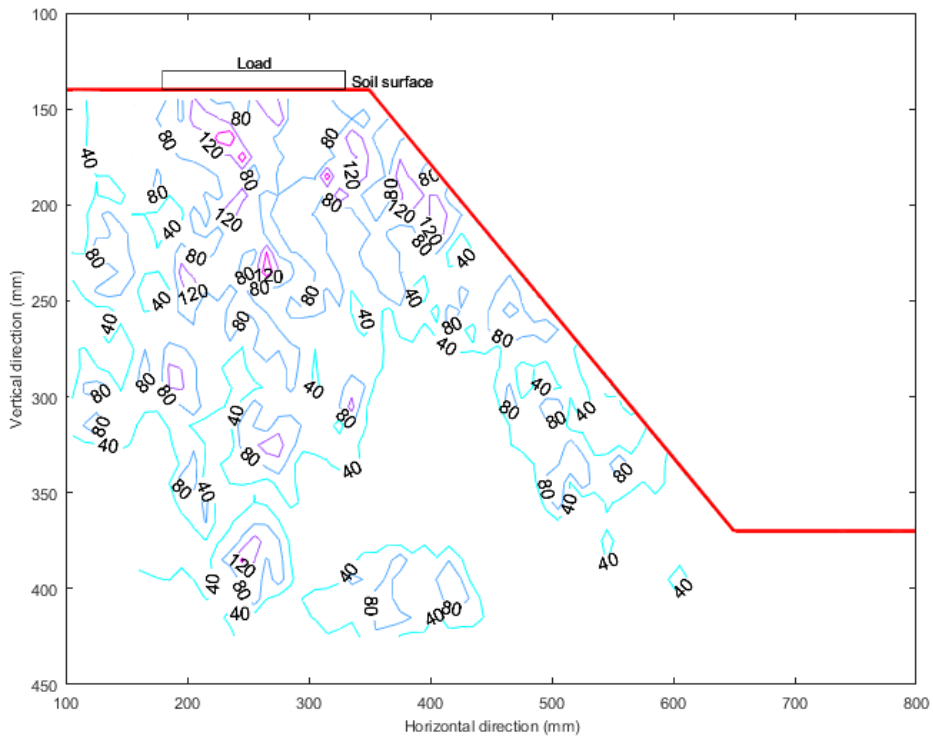


Figure 5.61: Contours of shear strain for Case F (45° Degree and 0-Hour rain)

Figure 5.44 to Figure 5.61 illustrate the magnitude for both vertical and horizontal movement of soil accompanied by the shear strain for each of the cases. The numbers shown in the vertical and horizontal movement figures are the representational value of the soil movements in millimetres relative to the percentage of the loading plate width.

Figure 5.44, Figure 5.47, Figure 5.50, Figure 5.53, Figure 5.56 and Figure 5.59 show the cumulative vertical displacement for cases A, B, C, D, E and F respectively. Most of the vertical displacements from all the cases exhibit a higher magnitude of value directly under the loading plate compared to the other parts in the slope model. These movements were also traced to be directed towards the slope face suggesting a heave of soil movements quite similar to the slip circle failure mechanism observed in subchapter 5.3.3. Quite noticeably in Cases D, E and F whereby the negative vertical soil movements occur close to the slope face while also propagating outside of the slope face boundary. These high movements from a bigger slope angle comparative to the other cases support the idea of slope angle magnitude having an immense factor in the deformational behaviour of a slope.

For the horizontal displacements, Figure 5.45, Figure 5.48, Figure 5.51, Figure 5.54, Figure 5.57 and Figure 5.60 displayed a similar trend of soil movements whereby the soil underneath the loading plate moved towards the slope face of the slope model. Negative traces of the horizontal soil movement were also observed to the left of the loading plate. Cases D and F showed a significant difference from the whole cases whereby the soil movements were analysed to spread outside of the slope face boundary.

Shear strain analysis of all the cases was presented in Figure 5.46, Figure 5.49, Figure 5.52, Figure 5.55, Figure 5.58 and Figure 5.61. The shear strain analysis of the slope model entirely follows the comparable trend of shear strain manifesting beneath the loading plate near the edge and propagating towards the slope face. This was evidently clear in clarifying that higher shear strain occurred at the base of the slip circle failure mechanism.

5.4 Concluding Remarks

The chapter earlier discussed on the result of the physical property tests on the soil used to construct the slope model and classifies the soil according to the BSCS. Several key values of the soil model were highlighted for the application of analysis throughout the research. In addition, SWCC and hydraulic conductivity function of the slope model were determined to be utilized in further analysis. The rainfall intensity for the rainfall simulations was also discussed.

The research proceeds to provide a comprehensive display of results obtained from the tensiometer analysis. A pore water pressure versus elevation model was constructed for all rainfall related cases and its behaviour was extensively discussed. Following that, the loading stages results were illustrated by the stress versus strain figure from initial loading until final failure load. Furthermore, the deformation result was presented in three stages which are the initial condition followed by the precursor movement prior to failure mode and finally the state whereby the slope model entirely fails. Visible slip circle failure was noted on the deformation results presented. The research then proceeds to display the results from the AWAM device for each of the cases. The precursor movement prior to failure moments was established after analyzing the degree of slope change over one minute for all of the cases. Spikes of data was displayed successfully indicating the prevalence of quantifying the precursor movement prior to failure, to be used as a means of the trigger warning for the AWAM system in slope monitoring. The clockwise and counter-clockwise movement mechanics of the AWAM device was also discussed. Finally, the importance of the placements of the AWAM device and the time of detecting precursor movement prior to slope failure were highlighted.

Post-processing of the still images acquired during the loading stages revealed that the PIV technique was able to efficiently quantify the soil movement and strain development during slope failure. Applying this technique to corroborate readings from the AWAM device to measure slope failure tendencies was deemed adequate and sufficient while also portraying the failure mechanism of the slope model. Regions in the slope model to undergo vertical and horizontal movement were also determined.

Understanding the failure mechanism in a certain slope condition would enable an enhanced basis on the probable location of the AWAM device to efficiently monitor slope movements.

The results presented in the chapter successfully achieved two of the research objectives set upon this research. The AWAM device was determined to be able to function as the slope monitoring device as intended. The threshold value to be set upon the AWAM system failure signal was also obtained for the range of scope of the research.

CHAPTER 6

NUMERICAL MODELLING OF SLOPE FAILURE SIMULATION

6.1 Introduction

In the current chapter, a cross-referencing method of laboratory-scale versus numerical modelling was prepared to complement each of the experimental findings. Scale-up of the laboratory model of the slope stability were modelled using GeoStudio 2012, a modelling software that integrates multiple modelling analysis components which includes; ground deformation, hydraulic flow and properties which in turn completes a slope stability analysis (Yeh et al., 2015; Sinarta et al., 2017)

Suction distribution profile in residual soil simulated through computer modelling by taking into consideration numerous modelling approaches that best compliment the physical modelling simulation of slope stability studies. A relationship between water movement, soil suction and failure loading were explored to justify the results of the physical modelling. Continuum method was chosen as the modelling concept of the numerical analysis for its simplicity in analysis to provide borderline and estimation of results for a full-scale design problem.

The next subchapters primarily in 6.2 would discuss on the model characteristics and material summary obtained from the physical modelling while subsection 6.3 would progressively entail the complete methodology and analysis flow of the numerical models used in this research. An extensive display of the slope modelling result would be discussed in subchapter 6.4. The next part would discuss the comparison between the results of then physical modelling and numerical modelling that was demonstrated by each analysis. Subchapters 6.5 wraps up the whole chapter with a technical remark on the whole numerical analysis in the research.

6.2 Modelling of Materials

To study the effect of the model slope stability subjected to rainfall and loading, several properties of the numerical model was depicted from the physical modelling of the research. The physical properties of the model were previously mentioned in subchapter 5.2.1 while soil-water characteristic curve (SWCC) and permeability function of the soil was previously stated in subchapter 5.2.2 and 5.2.3 respectively.

Only one type of residual soil was employed in this study as described in subchapter 5.2.1 which is sandy silt, MHS (Grade VI). Preceding the rainfall simulations, an initial condition was applied to the soil based on a few criteria which are; to represent the dry condition of the soil and for it to be realistic and practicable in real site condition. The minimum suction at residual water content, ψ_{min} should correspond well to the residual water content, θ_r in the SWCC of the soil (i.e., $\psi_{min} = 32$ kPa at $\theta_r = 0.34$). Thus, the value 32 kPa was chosen as the limiting values of the initial condition for sandy silt in this study. This conclusion is backed by previous studies (Yang et al, 2004; Gofar et al., 2008; Lee et al., 2009) that established the suction at the dry condition of most types of soil can be approximated to the suction corresponding to residual water content in soil characteristic curve. Table 6.1 summarizes the soil parameters used in the numerical analysis of the study.

Table 6.1: Summary of soil properties

	Grade VI (Sandy Silt)
Soil Classification BSCS	MHS
Saturated Permeability, k_{sat} (m/s)	5.00×10^{-7}
Minimum Suction at Residual Water Content, ψ_{min} (kPa)	32
Residual Water Content, θ_r	0.34

6.3 Modelling Geometry and Simulation Methods

The modelling of slope failure initiates by listing details of the modelling schemes applied in the study to accommodate the varied slope stability range of

parameter testing done on the physical modelling stage. Table 6.2 presents the details of the modelling scheme conducted in the research.

Table 6.2: Modelling scheme for numerical modelling

Modelling scheme	Rain Intensity (m/s)	Slope angle ratio (height: length)	Maximum loading on the slope (kPa)
A	1.7196×10^{-5}	1:2	177.8 kPa
B	1.7694×10^{-6}	1:2	173.3 kPa
C	0	1:2	224.9 kPa
D	1.7196×10^{-5}	1:1	182.2 kPa
E	1.7694×10^{-6}	1:1	91.1 kPa
F	0	1:1	200 kPa

As mentioned beforehand, the Geostudio 2012 was utilized to assess the slope stability results. Two products of the Geostudio was used in the numerical analysis namely SEEP/W and SLOPE/W. SEEP/W was first used to model the slope's seepage simulation where rain intensity was introduced to the model while simulating real site condition suction measurements. The then obtained pore-water pressures were transferred to the slope stability analysis, SLOPE/W, to calculate the factor of safety, FOS, of the slope throughout the whole duration from initial conditions until failure through loading.

6.3.1 General Setting

The model was established based on the physical modelling slope geometry conducted by the research. The slope geometry and boundary conditions that were simulated by the study was shown in Figure 6.1 and Figure 6.2 respectively. The slope angle was selected to be 27° (1:2 slope) and 45° (1:1 slope), whilst slope height was upscaled to be 3 m and the slope length was set to be 10 m. These setting were upscaled to be 10 times from the values used for physical modelling. As an added measure to limit boundary effect on the model, a 4.0 m distance was added to both the left and right side of the model. As per the figure's illustration, the groundwater table was assumed to be at a considerable depth below the slope surface (from 1.0 m AF

boundary to 0.9 m at the vertical boundary DE). Above the groundwater table line; AG and DH, there was no flux ($Q = 0$). Below the groundwater table; GF and HE respectively, a constant head boundary condition was assumed. The bottom boundary FE was assumed to have no-flow boundary.

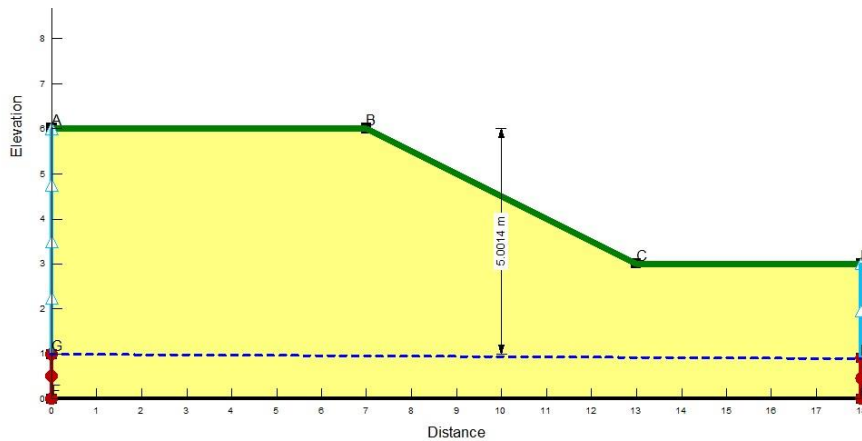


Figure 6.1: Modelling scheme for slope 1:2 ratio (27° slope)

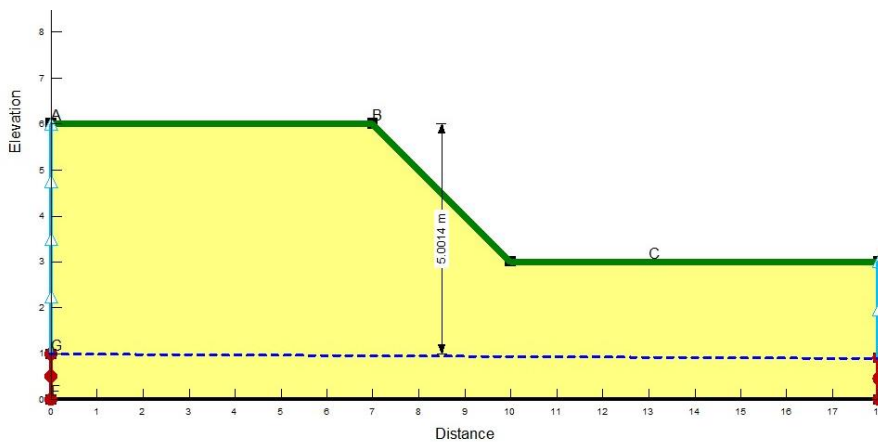


Figure 6.2: Modelling scheme for slope 1:1 ratio (45° slope)

6.3.2 Initial Condition SEEP/W

An initial condition was established at the beginning of the transient seepage analysis by applying “Initial Head/PWP Conditions” from the tried and tested water table height; for a sufficient duration of 24 hours to simulate pore-water pressure identical to the actual site condition. Cell size was set to 0.2 x 1 m resulting in 2226 Nodes and 2120 Elements meshed in the analysis.

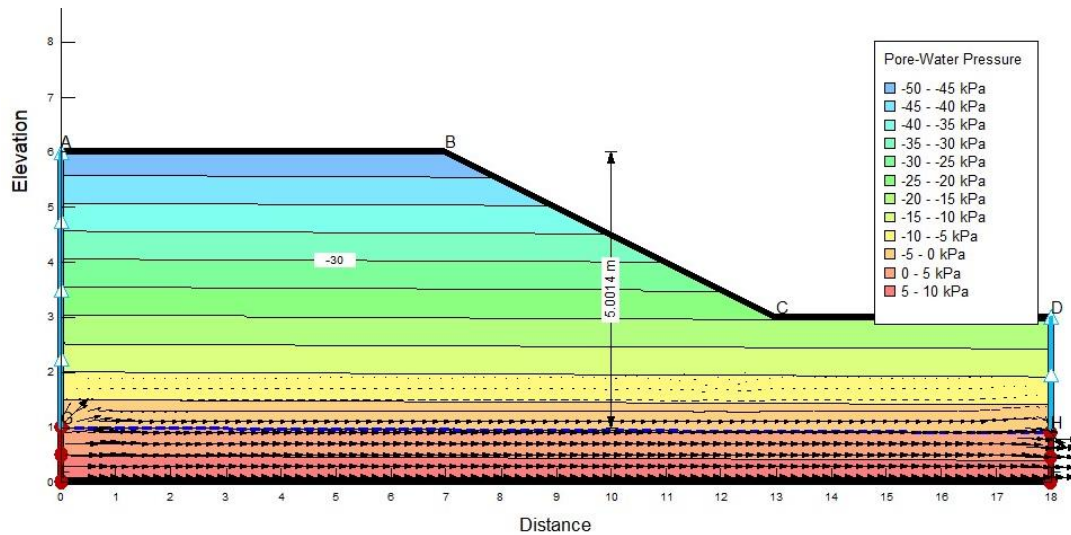


Figure 6.3: SEEP/W initial condition after 84,600 seconds of simulation

Figure 6.3 portrays the result of the SEEP/W simulations of the initial conditions for the following analysis. Worth to note the value of -30 kPa from the midpoint of B and C was intentionally setup to simulate the initial conditions of the pore water pressure on the face part of the model. This, in turn, would obey the limit of 32 kPa setup limit that was set to the sandy silt material of the model. This overview of the pore water simulations was in agreement with the simulations done by previous studies of SEEP/W simulations (Yeh et al., 2015; Sinarta et al., 2017).

6.3.3 Transient Seepage of Rainfall Simulations

After reaching the desired initial conditions, rainfall flux was applied to the slope surface from HB, BC to CD with the rain intensity being 1.7196×10^{-5} m/sec for 1-hour rain duration and 1.7694×10^{-6} m/sec for the 24 rain duration intensity whilst a no rain condition was intentionally left blank.

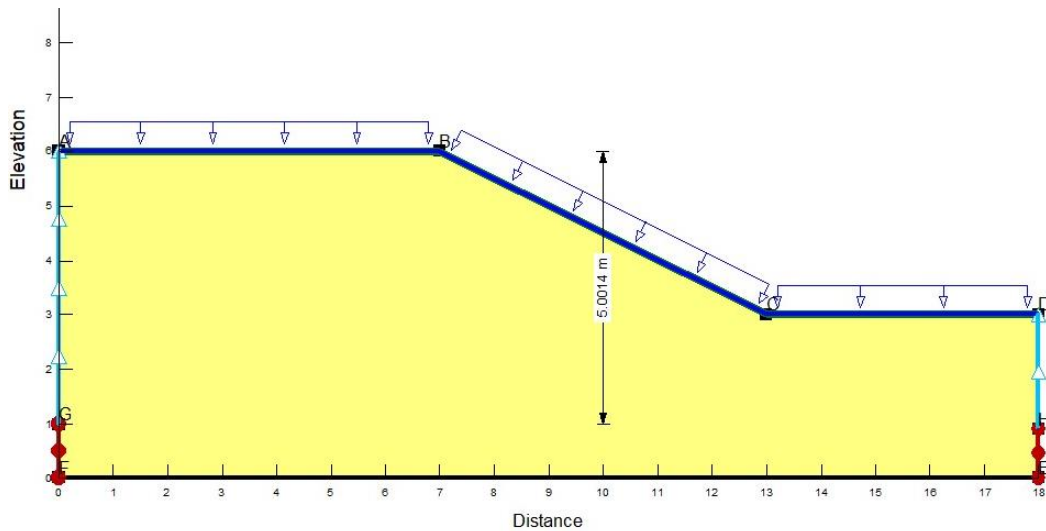


Figure 6.4: Rainfall intensity (blue arrow) was added to the model via boundary condition setup

Figure 6.4 depicts the rainfall intensity addition to the simulated model in the SEEP/W interface. The entire surface slopes parts including the crest, face and toe of the slope were drawn to include the rainfall intensity boundary condition and simulated accordingly based on the time intended of the rainfall to befall the ground surface. In the time sub-option of the analysis setup, the durations for an hour of rainfall was represented to be 7,200 seconds whilst 86,400 seconds was the value entered for a whole day of rainfall simulation.

6.3.4 Slope Stability with Load Simulations using SLOPE/W

The model slope after transient seepage rainfall simulation was solved was then analysed using SLOPE/W to simulate the slope stability. The Morgenstern-Price method was chosen to be the analysis type for the overall simulations while slip surface determinations were displayed using the entry and exit option with the total number of slope surfaces to store being set to 5. All the other options then remained to default.

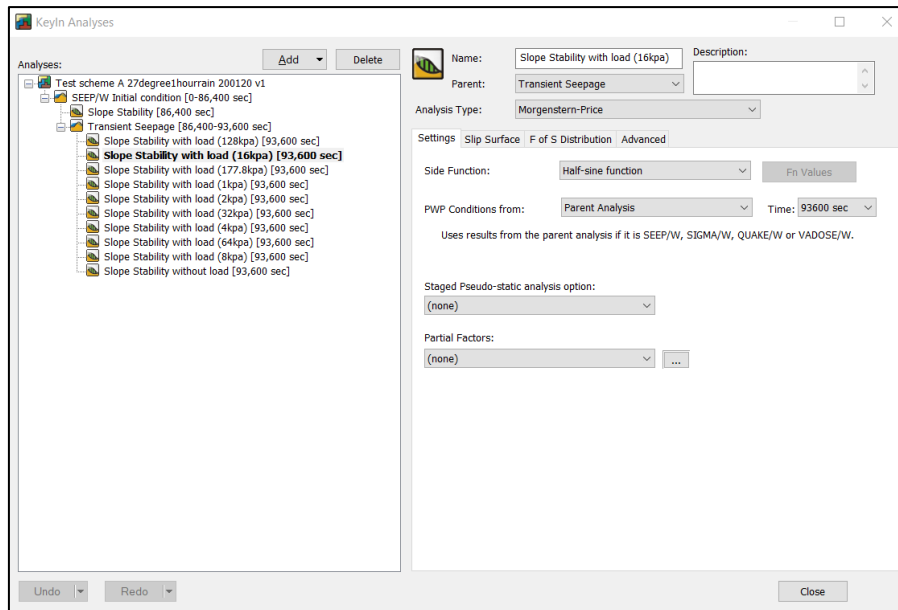


Figure 6.5: ‘KeyIn Analysis’ tab of the Geostudio depicting the overall analysis done throughout the simulations

Figure 6.5 illustrates the ‘KeyIn’ analysis tab in which the slope stability with load analysis was simulated using incremental load from 1 kPa until intended maximum loading was achieved which in turn simulates the failure conditions of the ground model in the physical model stage of the research. Each slope stability analysis was ensured to utilize the pore water pressure conditions from its parent analysis which is the transient seepage (rainfall simulated analysis). In addition, the time was set to be ‘(last)’ according to the duration model of the rainfall simulations.

A 1.0 m height of surcharge load was drawn on the slope crest exactly 0.5 m from the slope for a length of 1.5 m to model a similar setup of loading until failure used in the physical model such as shown in Figure 6.6. In addition, the red lines on the figure illustrate the entry and exit boundary for slip surface determinations for a typical SLOPE/W analysis. Each and every one of the factors of safety (FOS) value simulated by the SLOPE/W was recorded and tabulated in order for it to be graphically represented and shown in the following subchapters.

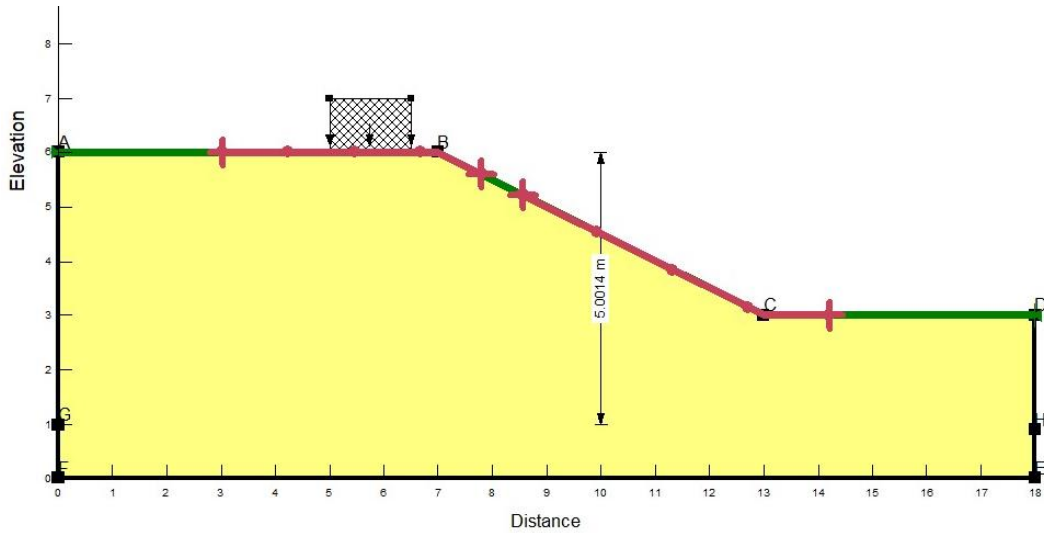


Figure 6.6: Checkered box drawn to simulate the loading conditions of the SLOPE/W loading condition whilst red line representing entry and exit boundary for slip surface

As shown in Figure 6.7, the green area represents the most critical factor of safety (FOS) for the SLOPE/W analysis outcome. Several possible outcomes will be generated by the analysis but the critical slope will have the lowest value of FOS for the analysis. The green area of the slip circle will only be deemed to be a successful analysis if only the slip circle area is in between the boundary setup of the entry and exit drawn previously.

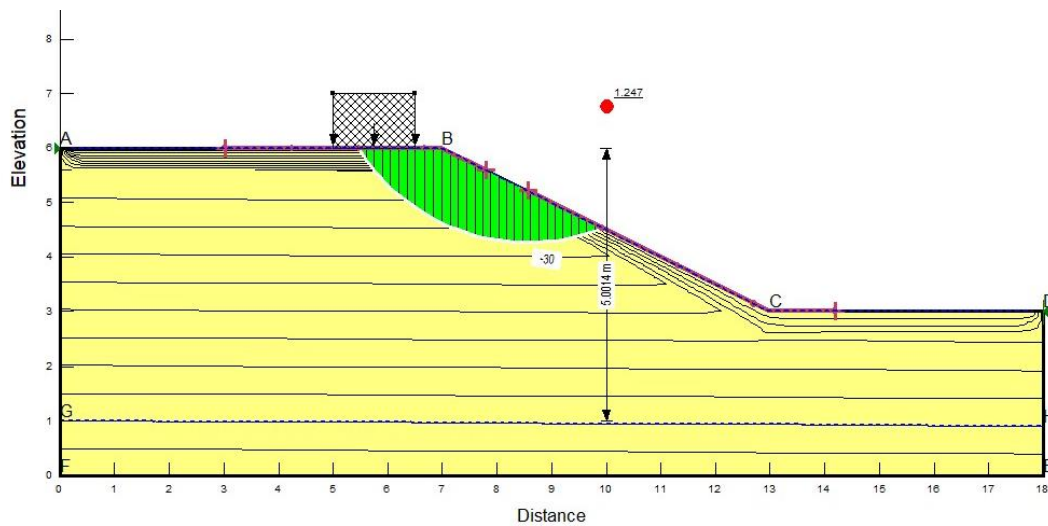


Figure 6.7: Example of a SLOPE/W analysis resulting in a value of FOS

6.4 Result of Slope Modelling

6.4.1 Pore-water Pressure vs. Depth

The readings of rainfall simulations onto a ground model can obtain changes of the pore water pressure in the transient seepage analysis and be graphically represented. The subchapter would display the transient analysis results which are the transient seepage display of pore water pressure while finally resulting in the depth vs. pore-water pressure of each case that contains rainfall analysis.

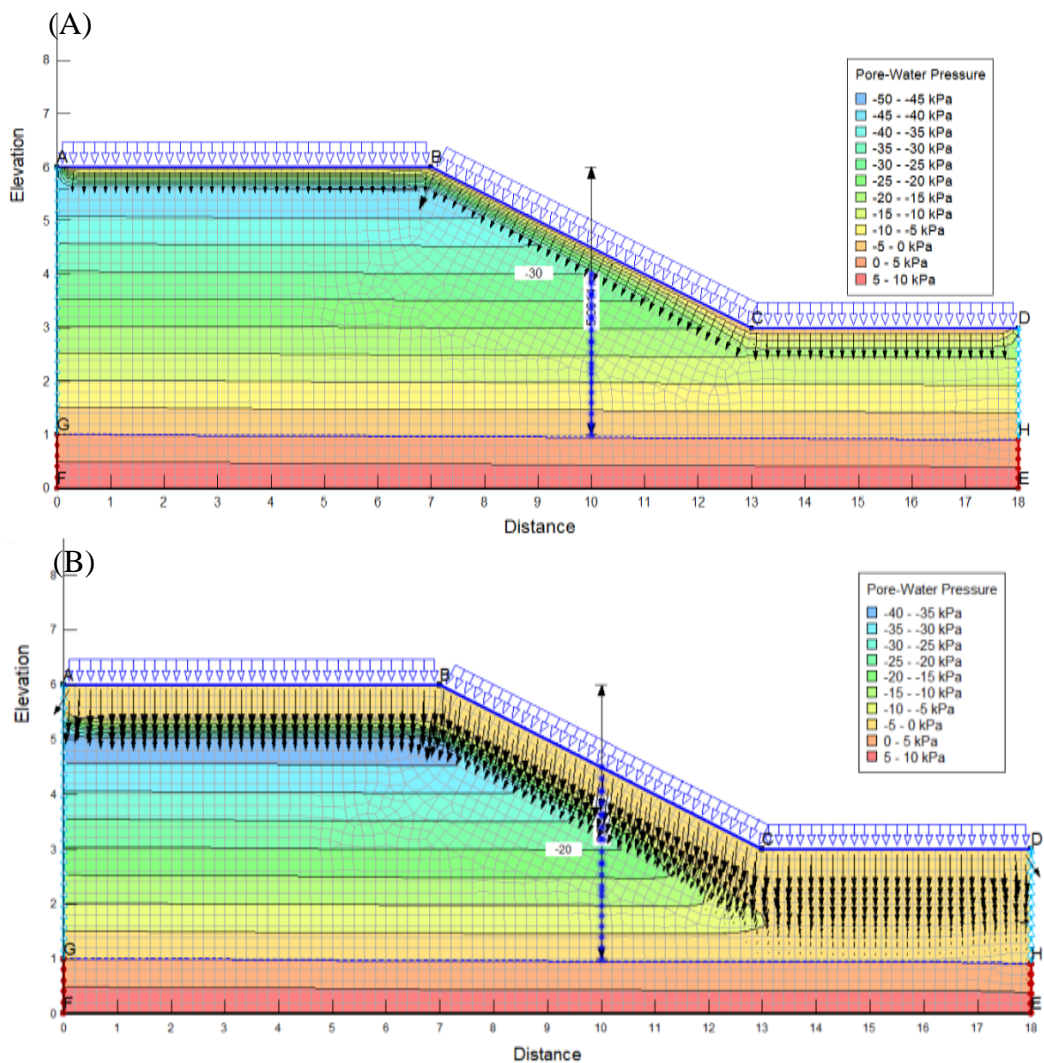


Figure 6.8: Pore water simulations result for SEEP/W; (A) case A and (B) case B

Figure 6.8 illustrates the overview of the pore water simulations resulting from the SEEP/W analysis of Case A (Figure 6.8(A)) and Case B (Figure 6.8(B)). Both of

these cases have an inclination of 27° degree of slope making them a slightly gentle slope than the cases D and E of the transient analysis.

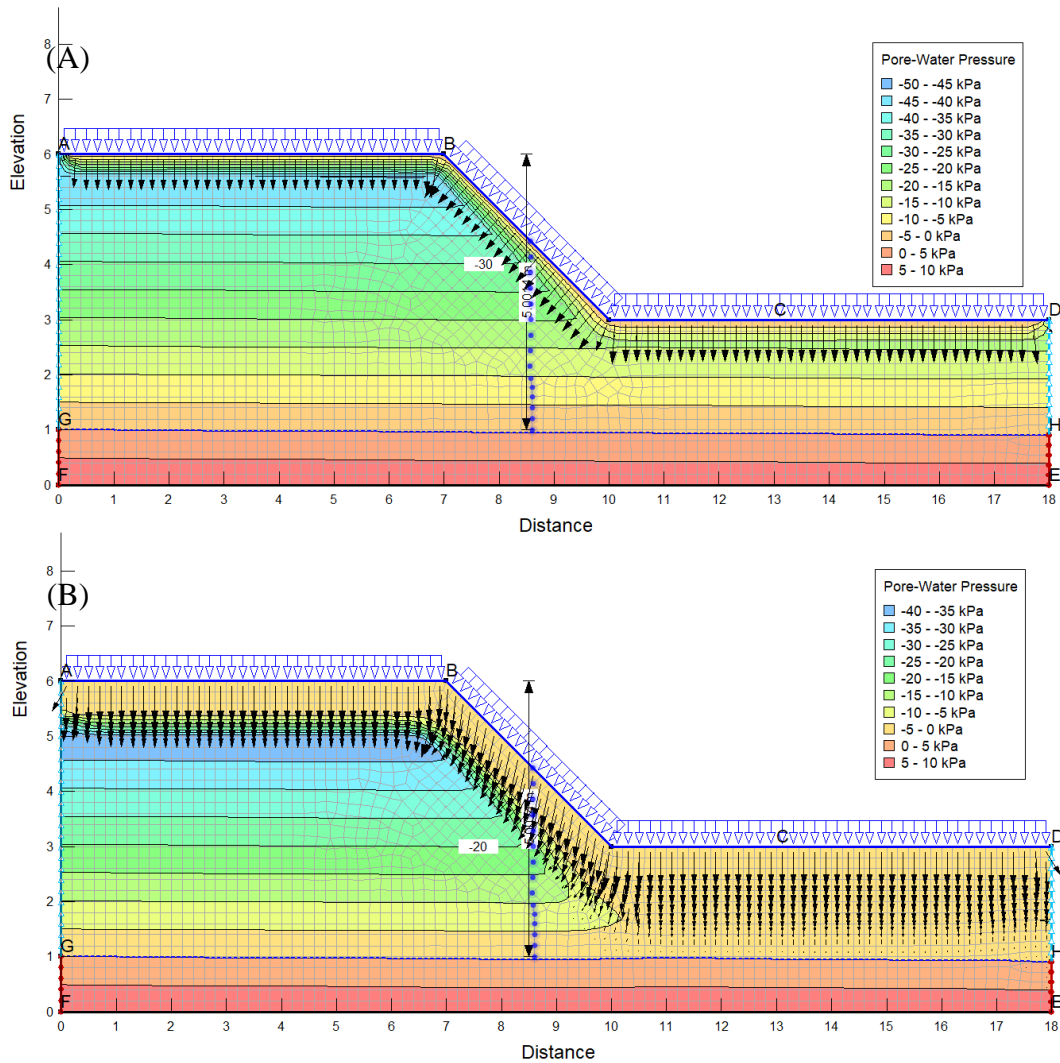


Figure 6.9: Pore water simulations result for SEEP/W for; (A) case D, (B) case E

Meanwhile, Figure 6.9 displays the transient seepage analysis result for the cases D and E which indicates the pore water pressure changes of the 1:2 slopes, also known for the 45° slope configuration.

Upon initial observation, it is worth to note the distinct difference between both of the figures is the volume of rainfall intensity that has been inflicted upon the ground model. The model with the 24-hour inflicted rainfall was illustrated by the SEEP/W analysis to measure a significantly thicker layer of -5 to 0 kPa on the surface of the

model compared to the 1-hour rainfall. This clearly simulates the ground upper layers to be saturated with water dependent on the time of the rainfall simulated.

To further investigate the values of pore-water pressure on the face of the slope, the analysis continued with the selection of points on the ground model. On the ‘Results’ option of the SEEP/W analysis, the sub-option ‘Graph’ was selected from the main menu ‘Draw’ such as shown in Figure 6.10.

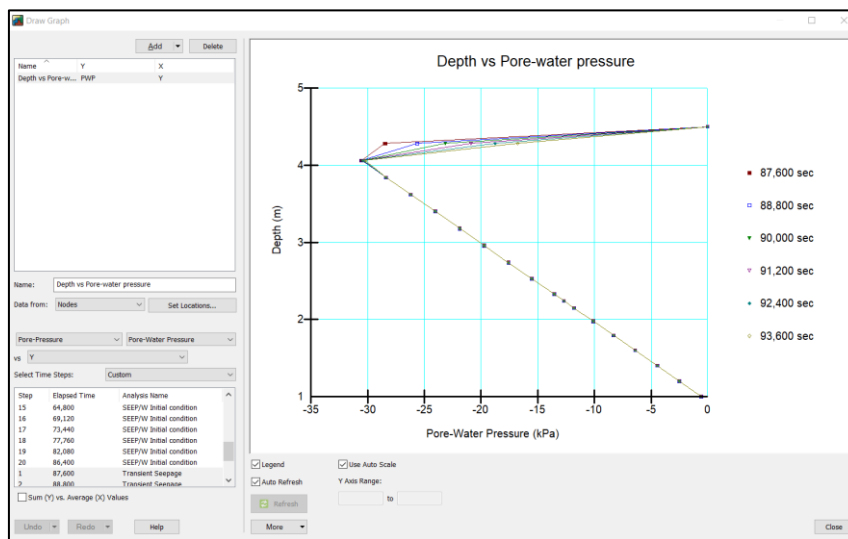


Figure 6.10: Draw graph sub-option to graphically interpret depth vs. pore-water pressure

After selecting pore-water pressure vs. Y on the selection panel, the lines of blue dots from both Figure 6.8 and also Figure 6.9 were then selected manually after opening the ‘Set Locations’ sub-option on the Draw Graph window. Multiple points selection on the ground model halfway between point B and C would then represent the pore water pressure change according to the depth of the face of the slope. A custom selection of the ‘Time Steps’ by selecting Transient Seepage timings was then done to draw the appropriate depth vs. pore-water pressure in regards to each case’s timings. The later drawn graph was further modified through the ‘Options’ tab in the ‘More’ dropdown menu by enabling the 90-degree to rotate option and customizing the labels of each axis to produce the intended interpretation of the depth vs. pore-water pressure in terms of elapsed timings.

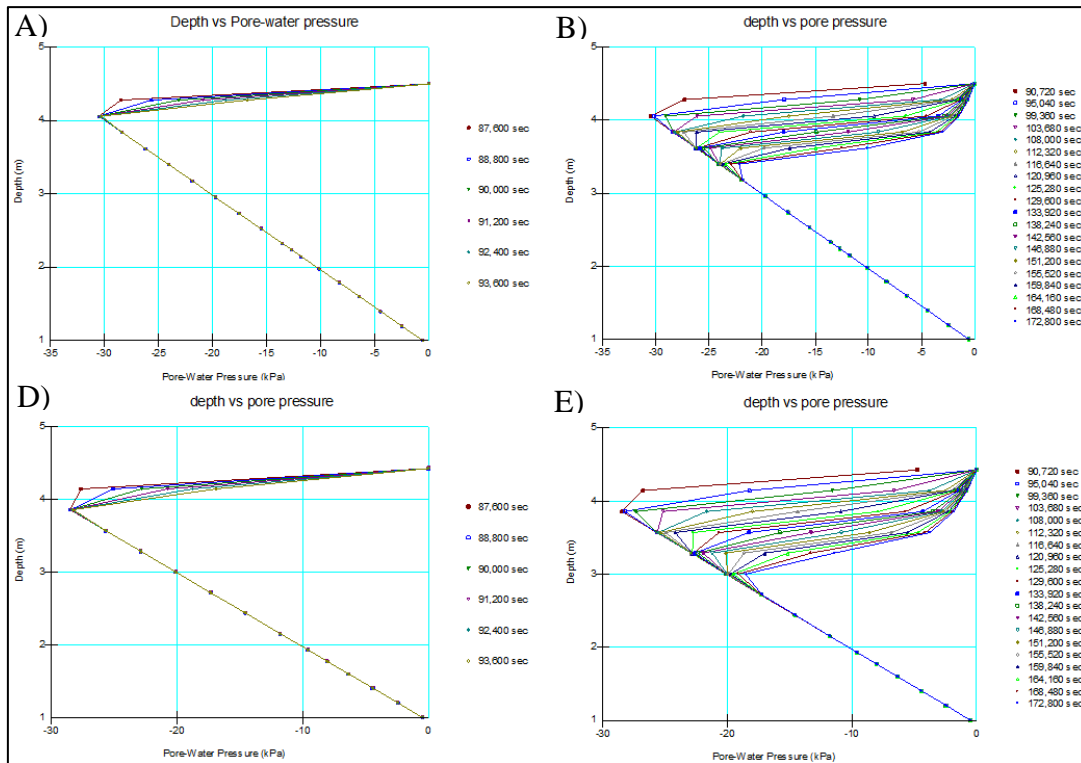


Figure 6.11: Compilation of the Depth vs. PWP for all cases; A) case A, B) case B, D) case D and E) case E

Figure 6.11 compiles the results of the transient seepage depth vs. pore-water pressure on the points selected on the face part of the slope with every time step variations. In general, the pore-water pressure changes at every time steps simulated by the SLOPE/W analysis. Cases A and D display similar time steps due to the identical rainfall intensity which is 1-hour rain and divided through 6-time steps while cases B and E undergo a similar 20 times steps of 24-hour rainfall intensity.

On a general note, the values of the pore-water pressure change from near saturation value which is approaching 0 kPa on the uppermost height to a negative pore-water pressure up until a certain value but then reverts back to approaching 0 kPa as depth increases. This whole scenario occurs due to the infiltration of water to partially saturate the ground model with the rainfall as time and depth increase up to a certain depth. These conditions evidently simulate real ground conditions which limit the infiltration of water due to capillary barrier effect making deeper soil suction to maintain its negative pore-water pressure or in other words soil suction value. Meanwhile as can be seen from the cases B and E; after a significant amount of rainfall has been simulated on the ground model, the pore-water pressure appears to be near to

0 kPa value even on the 1 m depth which indicates the upper levels up until 1 m depth of the ground model to produce conditions nearing saturation. These near saturation conditions would surely affect the slope stability analysis to detect the factor of safety (FOS) of the ground model on the subsequent analysis of the research.

6.4.2 Factor of Safety (FOS) vs. Time

Data processed from the transient seepage analysis was then further analyzed using SLOPE/W to quantify its slope stability analysis. As illustrated in subchapter 6.3.4, the incremental load of 1.0 kPa until designated failure loading value was simulated to graphically interpret the FOS decline until failure of all cases.

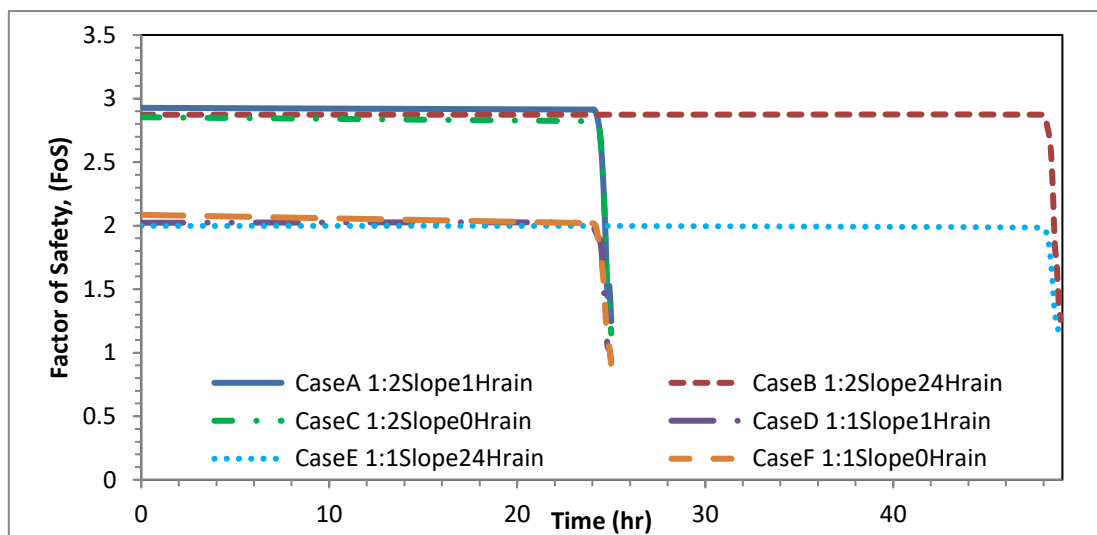


Figure 6.12: Factor of Safety (FOS) of the ground model vs. time for all cases

Figure 6.12 displays the FOS vs. time compilations of all the cases of the slope stability analysis with failure loadings. The FOS values were carefully simulated through each loading of each case inducing a critical slip failure and then compacted onto a single interpretation. As can be seen from the initial observation of the graph, the cases B and E duration was extended to be 49 hours due to extent of the test duration being 24 hours of rainfall-induced preceding a 24-hour initial conditions simulations setup. While the other cases following a nearly similar trend of 26 hours of slope stability analysis following a 24-hour period of initial conditions and 1-hour

rainfall simulations. The initial load of 1.0 kPa until the failure load was modelled to have been subjected to the ground model in a 1-hour duration period quite similarly to the physical modelling timings.

Generally, all the modelled SLOPE/W slope stability FOS was observed to reach its lowest value and nearing the value 1.0 as a sign of failure. In addition, the values rapidly decrease exponentially after loadings exceed 64 kPa. According to the trends of the graph, it was evidently clear that the slope degree of 27° inclination which is represented by cases A, B and C significantly surpass the safety factor values registered by its counterpart which is the 45° slope inclination. A value of 1.247 vs. 0.924 was recorded for cases A and D which share identical rainfall intensity while 1.258 vs. 1.141 values was recorded for cases B vs, case E as the two different slopes induced with a similar 24-hour rainfall. For the cases of zero rainfall which are cases C and F; evidently, a shallower incline of slope proves to have a higher FOS which is 1.152 compared to the 0.899 registered by the steeper slope.

An additional analysis was done to compare the resulting FOS values for the pre-cursor movement prior to failure loading value detected by the AWAM system to the FOS of failure load such as shown in Table 6.3. It was well perceived that the FOS of the pre-cursor movement rests well before the final load FOS indicating a well establish gap from pre-cursor movements until its final failure load. This gap symbolizes the clear potential of an early warning slope failure detection ability to diagnose the risk of slope failure before slope failure stage occurs.

Table 6.3: Pre-cursor movement FOS compared to the final failure load

Test	Pre-cursor movement	Final load
Case A	1.450	1.247
Case B	1.697	1.258
Case C	1.354	1.152
Case D	1.050	0.924
Case E	1.265	1.141
Case F	1.048	0.899

On a different perspective, it can be concluded that a longer duration of rainfall was noted to have a higher FOS compared the case whereby a high intensity of rainfall was induced over a short span onto a ground model. Cases A and B can be compared to have the similar make of ground model properties but the 24-hour rainfall-induced case stood to have a higher FOS which is 1.258 compared to the case of the 1-hour duration of rain which registers the value 1.247. Similar to cases A and B, Cases D and E were comparable in which these cases have similar slope inclination but varied rainfall intensity. As mentioned previously; the value 1.141 registered by Case E surpassed the value of FOS for case D which is 0.924, strengthening the early assessment made in the previous subchapter of the saturated conditions directly affecting the slope stability value of FOS.

6.5 Comparison of Results from Numerical and Physical Modelling

In this subchapter, the numerical modelling result for the pore-water vs. depth on both cases of the 1-hour rain and 24-hour rain simulations were compared.

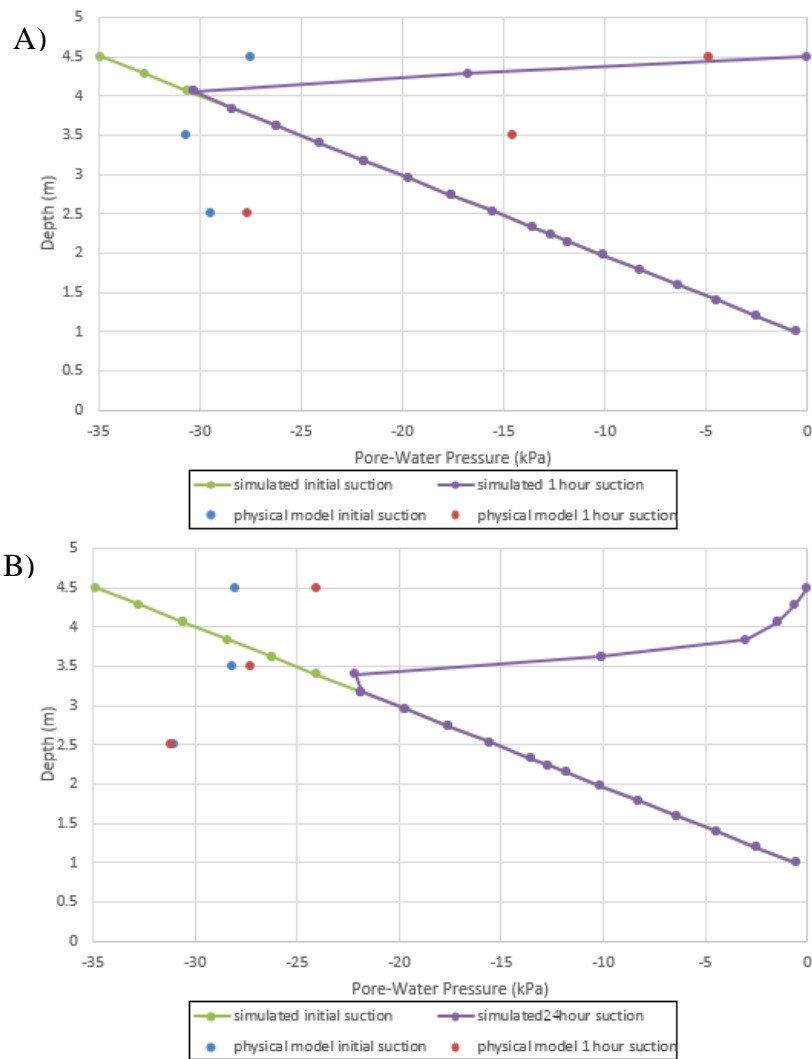


Figure 6.13: Vertical pore-water profile comparison for physical model and simulated readings for both cases; A) 1-hour rain and B) 24-hour rain

Figure 6.13 depicts the combination of results for the suction profile with respect to comparative depths for both physical model and simulation model. All of the comparative results were done on the face part of the slope model. In general, several similar behaviours were noted from the simulations and physical model results from data sets of the results when overlapped on one another. For the 1-hour rainfall pore-water profile simulations, both data sets of the physical model and numerical model were in agreement in the upper layers of the slope model whereby an increase of pore-water pressure was observed after an hour of rainfall was introduced into the ground model. As the depth decreases, pore-water pressure of both the simulated and physical model readings decreases up to a certain depth until the pore-water pressure values are in proximity with one another.

As for the 24-hour rainfall simulations, the pore-water profiles behave similarly with the former situation aside from the physical model exhibit a rather smaller distinction of value for the upper layers of the ground model. Finally, as the depth decreases down to 2.5 m, the pore-water pressure value converges together until similar values of pore-water pressure value were observed on the results.

As observed, the results from the physical model value by comparison to the simulated values showed approximate behaviour evidently supporting the concept that the numerical model provides a rather accurate prediction for the soil profile rainfall simulations. The soil suction profile depicted beforehand plainly proves the effect of the capillary barrier effect to sustain pore-water pressure in deeper layers of the slope model from the water infiltration due to rainfall. These findings were in agreement with the remarks of previous researches that observed deeper depths of tropical residual soil slope to be dry or moist in retrospect to the upper layer of soil slope being exposed to wet and dry conditions (Kassim, 2011).

6.6 Concluding Remarks

The chapter discussed the complete steps of numerical modelling for the physical model using the Geostudio 2012 software. In addition, results of pore-water pressure with respect to depth and factor of safety (FOS) determination for the physical modelling were obtained. The materials, geometry and hydraulic conditions were discussed at length throughout the chapter. 6 physical modelling schemes were successfully simulated with the full description of the numerical analysis gradually portrayed. Initiating with the initial conditions setup by using the SEEP/W component of the Geostudio 2012, transient seepage of the rainfall simulations was then performed to simulate rainfall-induced on the ground model. After that, the output of SEEP/W was carried forward onto the SLOPE/W analysis simulating the slope stability factor of safety determination for the ground model.

Compilations for the pore-water pressure vs. depth and FOS vs. time for all the cases were then compiled for a better understanding of the mechanism for slope

stability predictions. It was ascertained that the slip circle failure simulated in the SLOPE/W was well within the boundary setup in the geometry section as can be seen on subchapter 6.3.4 and in addition, justifies the dimensions of the physical model used in the research. The pre-cursor movement FOS compared to the final loading was also analysed to ascertain the ability of AWAM system as an early warning slope failure detection system. The values of pore-water pressure vs. depth were then compared to the readings from the physical modelling to evidently portrayed the ability of the numerical simulations to predict the soil profile in simulating rainfall conditions. Finally, the simulations were able to prove the capillary barrier effect notion to maintain pore-water pressure in deeper layers of soil slope being induced with varied rainfall conditions.

CHAPTER 7

SITE WORK OF AUTOMATED WIRELESS ACCELEROMETER MONITORING (AWAM) SYSTEM

7.1 Introduction

Throughout this chapter, the development stages on the Automated Wireless Accelerometer Monitoring (AWAM) system were comprehensively discussed. The development was organized by initially setting up the overall work plan of the development for the system. A detailed AWAM system background study was presented, envisioning to the completion of objectives and aims of the system. After careful planning and forecasting, the project continues with the equipment assembly and system trials. After an extensive duration of system trials and bug fixes of the system, site testing was procured by initially conducting several soil investigations procedures to determine the basic properties of soil on the testing grounds.

Following that, the AWAM system monitoring measurements through the system's website were described in detail. A complete walkthrough of the website's function and display were defined to portray the system's capabilities in slope monitoring. Besides that, the procedure for the system's installation on-site was discussed thoroughly. Finally, the system's data logging result for a designated duration was disclosed to indicate the system's capabilities in monitoring slope deformations.

7.2 Site Work Plan

The aim of this study is to develop a fully AWAM system used for slope monitoring. As an initial step towards the AWAM system's development, a flow chart

of the steps in the system's development was established. Figure 7.1 shows the flow chart methodology for this study.

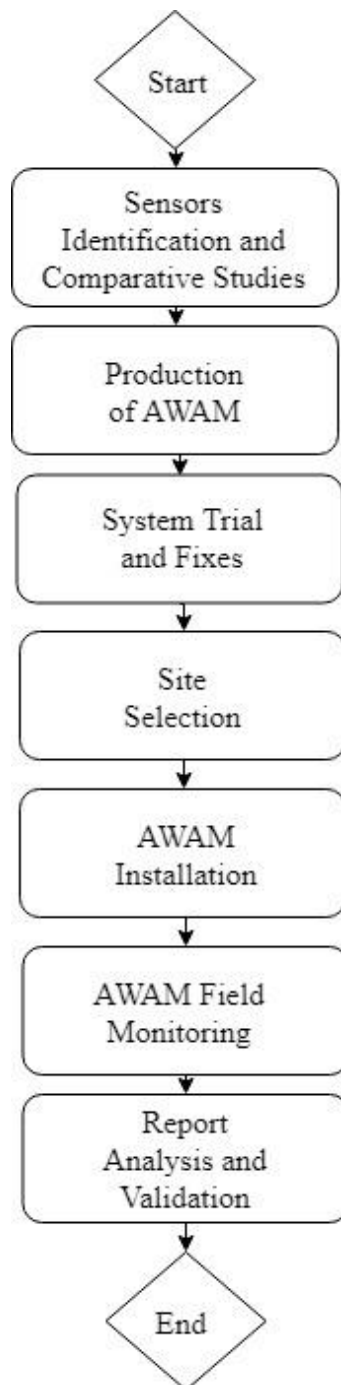


Figure 7.1: Flowchart of AWAM development

7.3 Automatic Wireless Accelerometer Monitoring (AWAM) System Development

7.3.1 Introduction

Automatic Wireless Accelerometer Monitoring System (AWAM) is a new product containing a combination of geotechnical instrumentations, self-sufficient power supply and data transfer via wireless. It was envisioned to be free of human input to automatically monitor deformation of the slope by using a combination of gyroscopes and accelerometer. An extensive literature study was implemented before designing the system comprehensively.

The pinnacle of the sensors implemented in the system includes the utilization of gyroscopes and accelerometers. Gyroscope works by using Earth's gravity to determine rotational orientation while accelerometer is a device to measure non-gravitational accelerations. By combining these sensors, the data collections were able to determine the position and orientation of an object.

It was anticipated that the system was able to operate and gather readings although through obstacles and constant climate changes. Following that, the researcher decided that the data transfer was done via wireless thus extending the range of the area monitoring accordingly. In addition, by powering the sensors of the system through solar panels, the system was able to measure deformation data even in remote sites. The whole innovative system is thought to be a new cost-effective and fast-response/time method in monitoring slopes.

The range of monitoring between the sensors and the receiver of the device is within a few kilometres (depending on wiring lengths) and allows monitoring of each type of movements that affects the slope. Data from the receiver was synchronized with a cloud server and simultaneously would be analysed by using software that has been designed to suit the function of this device. Wireless LAN (WLAN) and mobile communications (GSM / GPRS / UMTS Network) is a communication tool for data streaming between measuring receiver and the data acquisition software. The analysed

data can be monitored directly through means of mobile communication apparatus such as shown in Figure 7.2.



Figure 7.2: Diagram Process of AWAM System

Data acquisition and analysis software are including data management, analysis, and alarm systems. Data interpretations can be accessed directly via mobile devices including personal computer or laptop, and smartphones. These mobile devices are used to receive the required data from the monitoring system through any communication provider and allow the data acquisition and analysis software to work with the mobile device like an alarm system. The software is very important in the monitoring system for acquiring data from an accelerometer, a means of calculating threshold measurements and recording the results. When the threshold value exceeds its limitations, any person subscribed would be entitled to receive the critical signal failure (the limit deformation before failure).

With this system, it is expected that the critical slope monitoring can be operable with the price offered is lower than the existing tools with improved energy efficiency. The transmission and acquisition of more data would also be more accurate

and faster. Figure 7.3 shows the proposed apparatus for the site monitoring setup of the AWAM system.

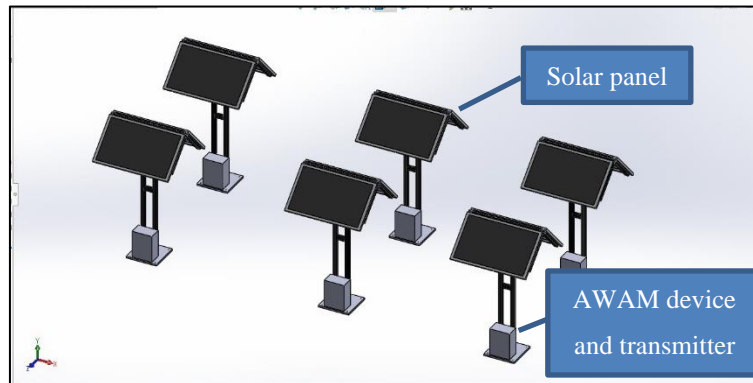


Figure 7.3: Proposed site installation

The site installation would be similar to the standard rainfall monitoring system on site. Figure 7.4 and Figure 7.5 shows the example of the long-term continuous data monitoring that was done in the Atlantic Highlands (Reilly et al, 2017). In the case of vandalism, extra precautions such as hoarding, signage and constant monitoring can be proposed if such measures are needed.



Figure 7.4: United States Geological Survey (USGS) open-canopy rain gauge on-site (Reilly et al, 2017)



Figure 7.5: Typical rain gauge installation including an enclosed datalogger and temperature sensor assembly (Smith et al., 2017)

The production stage of the AWAM system was prepared for a few months before the laboratory testing reached its final stages of testing. Two identical but separated monitoring systems in a cluster of three sets per system were produced to start-up the field-testing stage. Figure 7.6 shows the production stages of the AWAM system.



Figure 7.6: Production stages

Basically, each node of the AWAM system consists of three parts which are the solar panel, body and on the slope surface sensors. To allow for rural installations; the system was designed to be lightweight (approximately 10 kilograms), ease of installation (a few simple steps of setup) and equipped to fit various ranges of the area of monitoring. The following subchapters would entail an in-depth description of the development of the AWAM system.

7.4 Equipment for Site Work

The AWAM system for slope deformation monitoring site devices merely focused on simple designs for ease of installation. The following subchapter describes a detail equipment assembly of the system from the casing of the system until the web host used in the system's development. A basic drawn model of the site equipment assembly is shown in Figure 7.7.

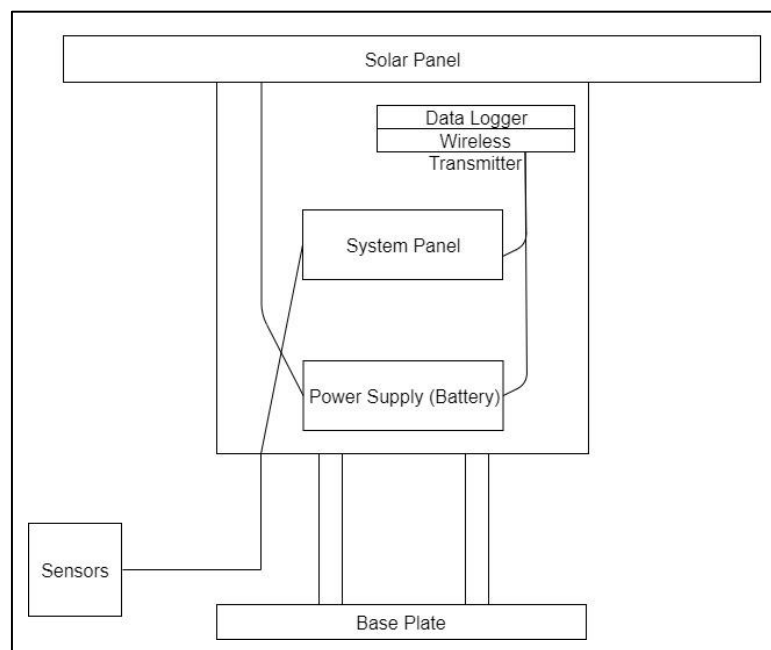


Figure 7.7: Overview of the overall system assembly for the AWAM site device

All the specifications and dimensions for the AWAM system equipment were described in-depth in the following subchapters.

7.4.1 Outdoor Capabilities

A variety of equipment was specially selected to make sure the AWAM device would take proper measurements of the slope deformation in long durations and minimize maintenance operations. The following subchapters describe the enhancements and improvement of equipment for outdoor capabilities for the AWAM system. These enhancements are only possible after a short period of try-and-error stage whereby difficulties such as water infiltration and vapour dissipation affected the electrical boards, which in time caused the system to malfunction in extreme weather conditions.

7.4.1.1 Power Station Casing

A major attribute to the robustness of the AWAM system is that the system would allow for continuous monitoring under harsh climate conditions. As a housing to enclose all the circuitry boards, power supply and wireless transmitter the research opted for a waterproof enclosure box such as shown in Figure 7.8.



Figure 7.8: Power station housing of the AWAM system

Table 7.1 presents the specifications of the housing case for the AWAM system. As shown in the table, the research determined the size of the enclosure to be adequate to house all the remaining components of the system incoherently to ensure

the well-being of the electrical system embedded in the system. The enclosure was made with Acrylonitrile Butadiene Styrene (ABS) Thermoplastic which is a relatively inexpensive polymer. Throughout the comparison studies for the enclosure selection, it was decided that the material would be enough to endure harsh climate conditions for slope monitoring. In addition, its strong resistance to corrosive chemicals and physical impact made it quite the candidate for long-term protection of the AWAM system.

Table 7.1: Power station casing specifications

Name	Waterproof Enclosure Box IP56
Brand	Wireman
Model	EB1296
Dimensions	310 x 230 x 145 mm
Material	Acrylonitrile Butadiene Styrene (ABS) Thermoplastic

Figure 7.9 illustrates the overall enclosure that houses all the components of the power station encasing the power supply, wireless transmitter and supplementary circuitry of the AWAM system.



Figure 7.9: The overview of the waterproof enclosure box of the AWAM system in site conditions

7.4.1.2 Sensor Casing

As can be seen from Figure 7.10, the casings for the sensors embedded on the slope surface of the AWAM system exhibit the same sturdiness of the enclosure for the power station enclosure. These casings were remodelled to fit the sensors enclosed within and to allow for a solar cable (for power supply purposes) to be connected to the power station. The protruding point of the wires was sealed with a silicon rubber resin to ensure a waterproofed housing of the sensors.



Figure 7.10: Enclosure box of the casing for the sensors of the AWAM system

Table 7.2 provides the specifications for the sensor casings. The dimensions are predetermined to be sufficed in housing the current circuitry of the AWAM system. If additional sensors are to be taken into consideration, a larger size casing would not be a hindrance to the overall system's performance. The material for the casing was also selected for its properties to be robust in real site slope conditions.

Table 7.2: Sensor casing specifications

Name	PVC Enclosure Box
Brand	AVIO digital
Model	EB-643
Dimensions	150 x 100 x 75 mm
Material	Polyvinyl chloride (PVC)

7.4.1.3 Power Station Column

Figure 7.11 illustrates the columns supporting the erected power station of the AWAM system. For the purpose of mass production, the Aluminium profile v-slot was selected to be the backbone of the structural integrity of the power station. The material's strength, ease of remodelling and customizable properties as per the AWAM system purposes stands out amongst all in the comparative study stage.

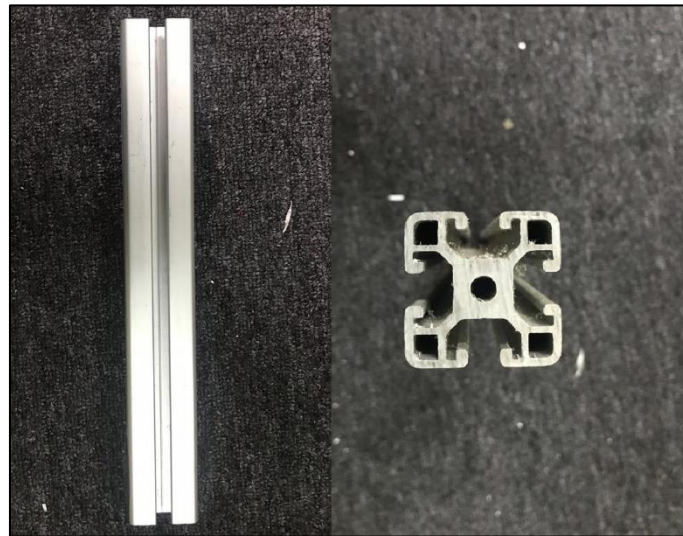


Figure 7.11: Column supporting the power stations enclosure box

Table 7.3 presents the details on the aluminium profile column specifications. Initially, a pre-cut model of the aluminium profile was manufactured with the length being approximately 1 m. It was decided that the length of the aluminium profile suited the AWAM system's power stations specification to ensure that a sturdy model was developed. Moreover, the material used to manufacture the columns was also deemed to be robust.

Table 7.3: Power station column specifications

Name	Aluminium Profile V-Slot Clear Anodized 2040
Brand	KAG MAKER
Model	AP1C2040
Dimensions	1005 mm
Material	Aluminium

7.4.1.4 Base Plate

Figure 7.12 portrays the evident usage of a base plate supporting the power station on fieldwork monitoring devices. It was decided that a steel base plate was the best possible material to support the entire weight and mass of the power station on the fieldwork. Since the specifications of the base plate were simple within the research intended design, it was considered that the base plate would be fabricated in-house. The base model was designed to have pinholes to be fitted with simple designs of foundation installations to increase its stability on the field conditions.



Figure 7.12: Steel base plate supporting the base of the power station

Table 7.4 lists all the specifications used to model the base plate of the power station. The key aspect to take note is the dimensions that were chosen to keep the power station balance in real site conditions. An optimal size was constructed to make sure the base plate provided stability, ease of transport and installations.

Table 7.4: Base plate specifications

Name	Steel base Plate
Brand	Self-Fabricated
Dimensions	300 x 200 x 20 mm
Material	Stainless Steel

7.4.2 Power Supply

As mentioned in the introduction of this chapter, one of the perks of the AWAM system is in its capabilities to measure soil deformation data in prolonged durations with minimal maintenance. It was hypothesized that a battery charged during the day using solar panels and maintaining its current during lights out, powering the whole system would be a simple task. Contrary to expectations, several tests run were needed to finally produce a significantly efficient power supply for the AWAM system. In order to do so, a careful selection of compatible and qualitative equipment in maintaining the power supply was needed.

7.4.2.1 Solar Charge Controller

Figure 7.13 illustrates the solar charge controller of the AWAM system embedded within the secure protection of the power station enclosure box. It is very apparent that the solar power controller needs to be robust, being able to operate in long periods of time and efficiently regulates the charge levels on the battery. The research opted to use the solar charge controller that was made in China. This study made a selection to opt the solar charging controller due to its specifications that rest well within the requirements of maintaining power to the slope monitoring devices.



Figure 7.13: Solar charge controller of the power supply

The control circuit includes a temperature sensor to measure the temperature of the solar battery. Evidently, as the temperature drops, the battery becomes more resistant to charging and vice-versa. Since the battery's chemical reactions are interconnected with the temperature, the on-board circuit regulates the charging stage of the power supply to avoid overcharging and overloading. Charging was designed to be automatic; all the while a discharging protection system was in place to avoid short circuitry. The front panel indicator shows the status and several working modes that were programmable in the system. Two Universal Serial Bus (USB) input slots were available to be connected to a personal computer for system programming. Table 7.5 sums the specifications of the solar panel battery regulator charge controller stating its dimensions, weight, working temperature and model.

Table 7.5: Solar charge controller specifications

Name	12V/24V Solar Panel Battery Regulator Charge Controller Regulator
Brand	PWM
Model	1172
Dimensions	150 x 78 x 35 mm
Battery Voltage	12V/24V auto
USB Output	5V/3A
Working Temperature	-35C to +60C -35C to +60C
Weight	150g
Colour	Blue & Black

7.4.2.2 Solar Panel

Solar panels are made up from many silicon photovoltaic (PV) cells which generate direct current (DC) electricity from sunlight. Worth to note that it is light energy, not heat, that which produces the electricity in photovoltaic cells. Energy convergence relies on the orientation of the solar panels, the efficiency of power converting and energy losses from; shading, dirt and ambient temperature.

Figure 7.14 illustrates the solar panel used in the AWAM system, produced by Solarmo (M) Sdn. Bhd. manufactured in East Malaysia Kota Kinabalu, Sabah.

Procuring local goods ensures the suitability of the solar device making it more reliable in the current climate of the intended monitoring mechanism. In addition to being affordable, the qualitative aspect of the solar panels guarantees the durability and efficient power management for the power station.



Figure 7.14: Solar panel installed on top of the power station on the AWAM device

Table 7.6 lists the specifications of the solar panels used in the AWAM system. It was made using Polycrystalline Silicon with the maximum power output of 50W. The solar panel was encased in silver / Blk Anodized aluminium casing ensuring its capacity to work under extreme conditions on-site. The research chose the SOLARMO solar panel since its specifications well rest within the intended needs of the system. For each different condition on site that requires additional specifications in the future, there are varieties of solar panels on the market with higher specifications and energy convergence ready to our disposal.

Table 7.6: Solar panel specifications

Name	50W/18V Polycrystalline Solar Panel
Brand	SOLARMO
Model	SM-50W18V-P
Dimensions	565 x 670 x 35 mm
Material	Polycrystalline Silicon
Open Circuit	21V
Short Circuit	2.1A
Max. Power	50w
Max. PowerPoint Voltage	17.5V
Max. PowerPoint Current	2.90A
Number of Cells	36pcs
Solar Panel Frame	Silver/ Blk-Anodized Aluminium
Solar Panels Glass	3.2 mm, High Transmission, AR Coated Tempered Glass

7.4.2.3 Solar Cable

Solar cables are the wired connection from the solar panel to be connected to the solar charge controller in the power station. The AWAM system employs dual-core solar cable with the capacity to resist ultraviolet (UV) light, water, fluids, salt and general weather for the long durations of the slope monitoring. The cable offers high flexibility and high current carrying capacity which is adamant in ensuring the robustness of the AWAM system to carry out monitoring of the slope in harsh climate conditions. Figure 7.15 illustrates the solar cable used in the AWAM system highlighting its insulation of the current conductor.

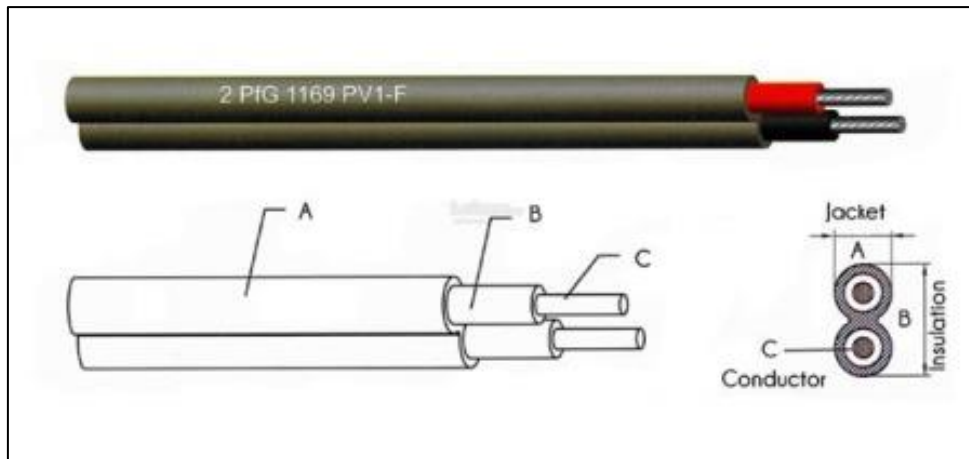


Figure 7.15: Dual-core solar cable used in the AWAM system for transferring current as of the power source

Table 7.7 highlights the specifications of the dual-core solar cable produced by Solarmo (M) Sdn. Bhd. used in the AWAM system. With the diameter of the conductor is double insulated with a Cross-linked polyethylene (XLPE) material, the cable was researched to offer high resistance to UV, ozone, abrasion and all the harsh conditions of the slope monitoring vicinity on-site making it suitable for the AWAM system requirements.

Table 7.7: Solar cable specifications

Name	Solar Cable 2.5 mm ² Dual-core (Black)
Brand	SOLARMO
Model	SM-CA202B-10M
Dimensions	2 x 2.5 mm (double core)
Conductor diameter	2.0 mm
Conductor resistance (Ω/KM)	8.06
Outer diameter	6.20 mm x 9.90 mm
Rated voltage	1000 V DC
Rated current	30A
Temperature range	-40°C ~ +90°C

7.4.2.4 Battery

To power up the power station for the AWAM system, the research chose the ever-reliable, low cost, less maintenance and robustness of the Seal Lead Acid (SLA) rechargeable battery. In addition, its features are researched to be compatible with the power setup of the AWAM system. Although it was considered to have a significant weight to be transported during AWAM system installations, the GP 12 V / 7.2 Ah lead-acid battery was chosen in the comparative studies due to its longevity of usage on-site conditions.

After several trials on-site, it was decided that a dual GP lead battery interconnected together was the ideal setup for the power management of the AWAM system. For the site conditions that are located in the proximity of shades from the surrounding flora, a single battery was unable to sustain its current during the light-off period. Figure 7.16 illustrates the setup of the dual GP seal lead acid battery setup used in the AWAM system.



Figure 7.16: GP Seal Lead Acid (SLA) rechargeable battery used in the power capacity of the AWAM system

Table 7.8 tabulates the specifications of the lead-acid battery used in the storage of the power supply for the power station powering the AWAM system. The system incorporates the usage of the lead battery produced by GP Batteries

International Limited manufactured locally in Malaysia. Its voltage output is 12 V and having the capacity of a 7.0-amp-hour (Ah) per battery ensures the sufficient capacity in powering up the system for a prolonged duration on site. Although there are varieties of solar battery with a much lighter weight compared to the 2.5 kg of the GP lead-acid battery, the research chose to employ the GP battery for its robustness and prolonged usage after the comparison study was made for the battery selection.

Table 7.8: Solar battery specifications

Name	12V/7.0Ah Lead Acid
Brand	GP Battery
Model	SLA-12-70
Dimensions	150 x 63 x 94 mm
Voltage	12V
Capacity	7.0Ah
Weight	2.5 kg

7.4.2.5 Power Relay

Figure 7.17 illustrates the power relay used in the power management of the AWAM system. The power relay was fitted due to its ability to control various appliances and equipment for the power management of the AWAM system. As can be seen from the figure, the power relay utilizes two 5 volts (V) activated relays that is also compatible with a 3.3V input. Two units of opto-isolator IC 817C was built in directly onto the board. The two relays can be independently used to control two devices, should the need for it arises. In addition, the power relay is designed to have a standard interface which can be controlled directly with ease by an Arduino microcontroller.

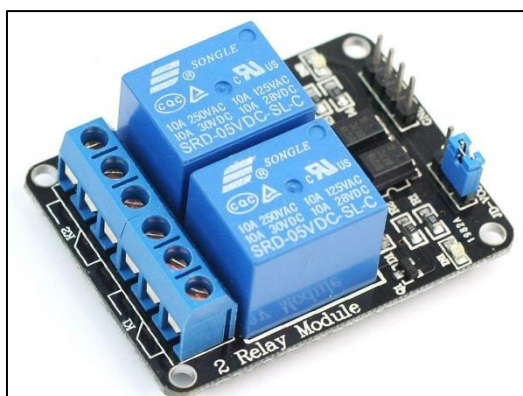


Figure 7.17: Sample of the power relay used to control the current powering the system

Table 7.9 presents the specifications of the power relay used to control the current located in the power station of the AWAM system. The brand Arduino was chosen for the system due to the fact that the power relay was considered to be compatible with the remaining board of the system. In addition, it was also proven to be among the power relay which is opto-isolated which means that it is protected from power surges that may happen due to harsh climate conditions tempering. The power relay would regulate a maximum current rating of 10 amperes (A) with a maximum alternate current (AC) of 250 volts (V) and a direct current of 30V.

Table 7.9: Power relay specifications

Name	Isolator 2 Channel Way 5V Relay Module
Brand	Arduino Opto
Model	2 Channel Relay-1158
Driver current	15-20mA
Relay Details	AC250V 10A, DC30V 10A

7.4.3 Step Down Module

Figure 7.18 shows the LM2596 step-down (buck) module series used in the power management of the AWAM system. A step-down module is used to lowering down the current from the input to the output of an intended system. A step-down module was known to consist of two semiconductors and at least one energy storage element i.e. a capacitor to control the currents running through the module. From the

qualitative study period of the AWAM system development, a step-down (buck) module was used since the power converter efficiency are much superior compared to other modules since the voltages were converted efficiently compared to a simpler circuit that steps down voltage by dissipating power as heat without the option to stepping up the output current.

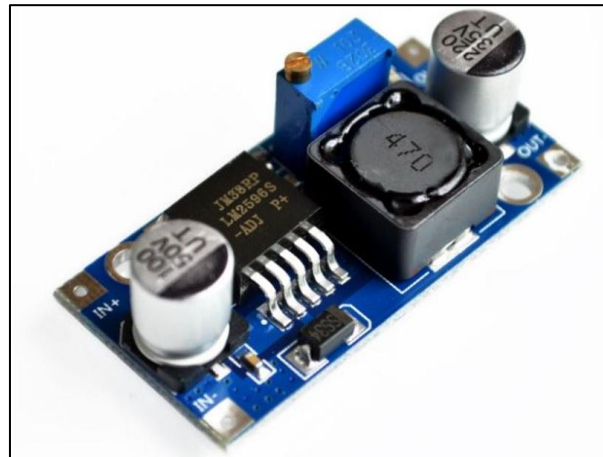


Figure 7.18: The step-down module used in the power management of the AWAM system

Table 7.10 shows the table of the step down (buck) module used in the AWAM system. The brand Arduino was once again chosen due to its compatibility with the current setup of the power management for the AWAM system. Specifically, a step-down module 1260 model was used for the system after a careful selection phase during the comparative studies done to develop the system. The input voltage varies from 3 to 40 V with a conversion output from 1.5 to 35V which rest well within the specifications needed to smoothly run the AWAM system. The conversion rate was recorded to have an efficiency of up to 92% which depends solely on the maximum output voltage required; by that it means that the higher the output voltage is, the higher the efficiency. An onboard current limiting short circuit protection was also an added feature of the module, which in turn would ensure a prolonged duration of efficient power management of the AWAM system with minimal maintenance.

Table 7.10: Step down module specifications

Name	LM2596 Step-Down Module DC-DC Buck Converter Power Supply
Brand	Arduino
Model	Step Down Module-1260
Item size	48 x 22 x 12 mm
Item weight	12g
Input voltage	3-40V
Output voltage	1.5-35V (adjustable)
Output current	Rated current is 2A (maximum 3A)
Conversion efficiency	Up to 92%
Switching frequency	150KHz
Short circuit protection	Current limiting, self-recovery

7.4.4 Data Logging

As specified in the advantages of the AWAM system in automatically log and transmit data to a cloud server, the processes of such feats would be controlled and managed by a combination of circuitry such as a display controller, data transmitter, data transmitter controller and also the date and time logger controller. The following subchapters discuss on the data logging and transfer components of the AWAM system in depth.

7.4.4.1 Controller Display

Figure 7.19 with the red highlighted part displays the on-board LCD controller display used in the data display for the power station of the AWAM system. The display adapter was designed to have a 4-line LCD display to navigate the readings and options model of the data transmission part of the system.

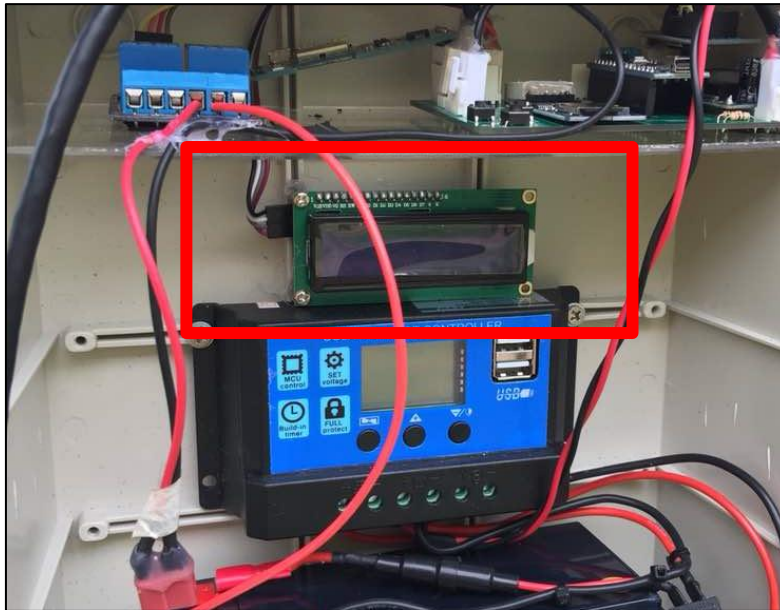


Figure 7.19: Controller display for the data logging status display of the AWAM system

Table 7.11 tabulates the display module specifications for the status display of the data logging by the AWAM system listing its model and dimensions. A simple interface of the display is directly connected to the data logging and transfer of the AWAM system which are controlled by the wireless transmitter controller.

Table 7.11: Controller display specifications

Name	RepRap Smart Controller Display Ramps 1.4 2004 LCD
Brand	kag MAKER
Model	DR142004
Dimensions	150 x 30 mm

7.4.4.2 Wireless Transmitter

The wireless transmitter module is the beacon of the data logging and transmits mechanism of the AWAM system. Since the data would be stored and deciphered on the cloud, the wireless transmitter would be the key to in turn provide the necessary data regularly to establish the slope failure warning signal. Ensuring high quality and dependable board for the wireless transmitter module would result in the efficiency of

the whole AWAM system to provide the warning apparatus to the end-user. A dual-band module connected to both the Global System for Mobile communications (GSM) and General Packet Radio Service (GPRS) network is the core to the selection of the wireless transmission. Having multiple network connections ensures that the data would be transmitted safely if one of the connections experiences failure. Figure 7.20 illustrates the professional version series of GSM/GPRS wireless transmitter module manufactured by Arduino based on an A6 module.



Figure 7.20: Wireless transmitter module manufactured by Arduino Uno for the data transmitting apparatus of the AWAM system

Table 7.12 lists out the specifications of the wireless transmitter module used in the AWAM system. Powered by a GPRS A6 module, the Arduino manufactured transmitter features a compact size and low current consumption. Having the working frequency from 850 to 1900 MHz ensures plenty of width for the data transfer. There is also an onboard sim card holder used to provide the network connection. This would allow for two-way communication via Short Message Service (SMS) if the need for it ever arises. The antenna was fitted through a SMA and IPX connectors, whereby if the systems need upgrading to a higher quality antenna the module will sufficiently allow it. After several tests run on the site, the research opted to install the wireless transmitter for each of the power stations individually with its own sim card network so that any interruptions or network problem from one of the stations would not affect the other devices.

Table 7.12: Wireless transmitter specifications

Name	GPRS A6 Pro Serial GPRS GSM Module Core Development Board
Brand	Arduino Uno
Model	07-06-0-005-00
Working frequency	quad-band network, 850 / 900 / 1800 / 1900MHz
Working voltage	4.8-9VDC
Working Current	maximum of 2A
Sleep Current	5mA
Communication Interface	TTL serial port / RS232 serial port
Baud rate	115200bps / customizable
Interface logic voltage	3.3V
Pin pitch	2.54 mm
On-board antenna interface	SMA and IPX

7.4.4.3 Wireless Transmitter Controller

Figure 7.21 illustrates the controller board used to control the wireless transmitter processes used in the AWAM system whereby the red highlighted box shows the location where the position of the controller on the data logging board. The controller module was developed using an Arduino Nano board which is compact, complete and user-friendly which offers the same connectivity and specifications of the Uno board but in a smaller form. Written program of the Arduino Nano controls the data transmission and logging protocols of the AWAM system where it was programmed using the standard Arduino software.

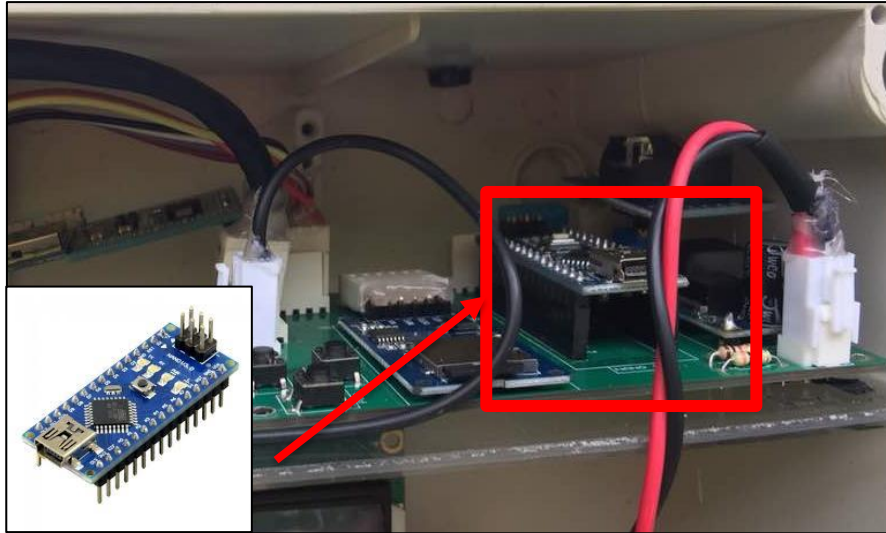


Figure 7.21: The controller board to control the wireless transmitter process used in the AWAM system

Table 7.13 tabulates the wires transmitter controller specifications used in developing the data logging mechanism of the AWAM system. As mentioned above, the controller module was chosen from the Arduino series ATMEGA328-1265 model for its compatibility with the rest of the system. The module was powered by a 9V power supply and having clocking speeds of up to 16 MegaHertz (MHz) which was sufficient in the management of the data logging for the AWAM system.

Table 7.13: Wireless transmitter controller specifications

Name	MicroController Board 3.0 Compatible
Brand	Arduino Nano
Model	ATMEGA328P-1265
8 analogue inputs ports	A0 until A7
14 Digital input / output ports	TX, RX, D2 until D13
6 PWM ports	D3, D5, D6, D9, D10, D11
Power supply	9V battery
Clock Speed	16 MHz

7.4.5 Date and Time Module

Figure 7.22 illustrates the date and time module management board of the AWAM system. The main function of the module is to synchronize the data from the

sensors with a time and date for every reading of the system. The AWAM system utilizes the standard Arduino real-time clock (RTC) module, recording seconds, minutes, hours, days, months and year information accurately with an automatic correction configuration to include leap years. As can be seen from the figure, the module incorporates a battery input that automatically switches to its backup power should the main power supply experiences faulty.



Figure 7.22: The on-board data and time management board for the date and time specifications of the AWAM system

Table 7.14 tabulates the data and time module specifications used in the AWAM system. the module was also chosen from the long line of Arduino boards used in the AWAM system for its capability to be integrated into the overall system. The XPS1-0015 Arduino RTC precision module was considered to be integrated into the system for its capabilities to detect and manage the date and time in harsh conditions where it can be operated even when the main power output is disconnected. This ensures the data for the date and time of the slope monitoring device is intact even when the power station fails to provide power. The module is connected to the Arduino Nano microcontroller mentioned in subchapter 7.4.4.3 and powered using a 3.3 to 5.5 V direct current supplied from the solar power.

Table 7.14: Date and time module specification

Name	DS3231 AT24C32 IIC I2C Module Precision RTC Module
Brand	Arduino
Model	XPS1-0015
Storage capacity	32K
Clock chip	High-precision clock chip DS3231
Memory chips	AT24C32 (storage capacity
Operating voltage	3.3 - 5.5V DC

7.4.6 Security System

The subchapter discusses on the security factor of the AWAM system including the precautions taken to avoid ambient interference and also the onsite alarm signal. Figure 7.23 portrays the casing of the power station in its development stages of the AWAM system. The bolts and nuts used in the system were selected after several trials of the system on-site whereby initially some of the screws were not able to securely protect the on-board circuitry and susceptible to rust when exposed to real site conditions. These security measures would ensure that the casing would be protected from the ambient condition of the AWAM system in harsh climate conditions especially in terms of corrosion. Also shown in the illustration are the red LED bulb casings as an added security measure when the monitored slope is in an alert state. The alert state of the system would be triggered by the same Arduino Nano microcontroller that operates the wireless data transfer mechanism of the AWAM system.



Figure 7.23: The casing of the power station and sensor casings assembled with tightening screw caps to ensure onboard systems are protected.

Table 7.15 presents the specifications of the material and model of the screws used to fasten the power station casing of the AWAM system. The screws were manufactured by KAG MAKER with its model SHSCO508, made from alloy steel with thermal Black Oxide coatings. Its dimensions vary from 80 to 200 mm with a head diameter of 5 mm; depending on the required length of either the power station casing or the sensor casings. These screws were designed to resist corrosion and rusting from harsh conditions on-site and were deemed to have a prolonged lifespan.

Table 7.15: Screw caps specifications

Name	Socket Cap Screws DIN 912 Black Oxide
Brand	KAG MAKER
Model	SHSCO508
Material	Alloy steel with thermal Black Oxide coating
Diameter	5 mm
Dimensions	various lengths of M5 hex socket cap ranging from 80 – 200 mm

Figure 7.24 shows the added security measure of labelling and hoarding the AWAM device on site. These necessary steps were taken to avoid unnecessary tempering while the onsite measuring devices operate. These labelling and hoarding were deemed to be adequate, whilst a more sophisticated and secure parameter of the

device was thought to be necessary for a harsher and prone to wild fauna tampering of the system on remote site locations.



Figure 7.24: The label and hoarding of the research in progress tagging the AWAM system on site

7.4.7 Sensors

As previously mentioned in subchapter 3.5.1.3, Figure 7.25 illustrates the mechanism for the sensors input used in the AWAM system. It was researched that an ArduPilot Mega (APM) 2.8 flight controller used in developing drone navigation system was the perfect candidate in providing input i.e. acting as the combinations of sensory mechanism to provide real-time data monitoring for the deformation of slopes. Its compact design was easily integrated into the series of a system that makes up the AWAM device. Providing data such as accelerometer, gyroscope, Global Positioning System (GPS) coordinate readings would be the heart of the sensory mechanism for the AWAM system.



Figure 7.25: ArduPilot Mega (APM) flight controller used as the sensor mechanism in the AWAM system

Table 7.16 lists out the specifications of the APM 2.8 flight controller used in the sensor mechanism of the AWAM system. Its power supply was produced with a low noise linear (LDO) regulator that requires an input voltage of a minimal 300 mV. The APM 2.8 was fitted with an on-board compass for navigational input and equipped with a multiplexer (MUX) port for multiple sensor data output. The GPS model was developed using a 7M module, supporting 56 channels with an update rate of 10Hz. The APM 2.8 flight controller was also equipped with a rechargeable 3V backup battery in case of power outages. In addition, the GPS module was also backed up by an internal data storage model I2C electrically erasable programmable read-only memory (EEPROM). The EEPROM acts as the hard drive in keeping the instructions (variables) in the event that an Arduino is reset or powered off. The data from the EEPROM can be read, erased and re-written electronically. Finally, the data output per second (Baud) of the module was pre-configured to be around 38,400 Baud for an efficient and precise data output intended for the AWAM system.

Table 7.16: APM 2.8 flight controller sensor specifications

Power Supply / Battery Type	LP2985-3.3
Max voltage	16V
Input voltage	300 mV
Compass	Built-in
Port	Multiplexer (MUX)
GPS model	7M module
GPS Channel	56-channel
GPS update rate	10Hz update rate
Backup battery	Rechargeable 3V
Data storage	I2C EEPROM storage
Data pulses per second (baud)	Pre-configured 38,400 Baud and prams

Similar to the subchapter 3.7.2 whereby the AWAM laboratory-scale device was held into place with a fitted hinged foundation mechanism, the sensor casing for the site AWAM device was also held into the ground. As shown in Figure 7.26, steel rods pinning a hinge mechanism ensured that the sensor casing would only move due to rotation by being in fixed y-axis condition. This was also supported by the fact that from the calibrations of the AWAM in subchapter 4.3.1, the AWAM device sensors would not produce the desired data output if a single axis was not restrained.



Figure 7.26: Hinged foundation mechanism of the AWAM system sensor case

7.4.8 Server and Web Hosting

Figure 7.27 illustrates the main webpage of the web hosting site used in data storage, data analysis and alarm notifier mechanism for the AWAM system.

Originated from one of the Baltic States, Lithuania, the Hostinger International Ltd. company started web hosting back in 2007. The AWAM system utilizes the web hosting service of Hostinger's data centre located in Singapore which was launched in October 2014. As a brief description, web hosting service is a type of internet hosting that allows an individual and organization to create their own webpage accessible via the world wide web. Nowadays, the webpage that was leased to any individual or organization can be freely programmed with sophisticated data analysis and projections of any kind. The research opted to utilize Hostinger.com taking into consideration the perks and values of the web host compared to other sites; such as internet connectivity performance efficiency, the value of cost per annum and the ability to provide a space on the net capable of conducting the AWAM system outputs.

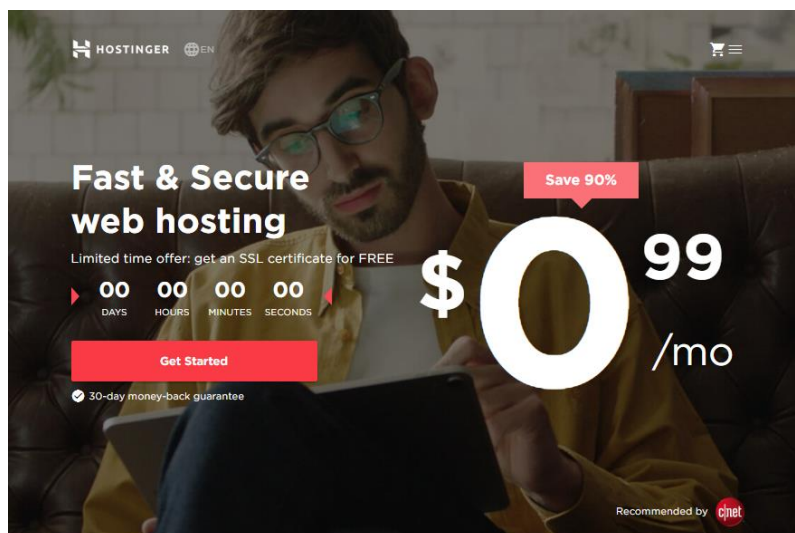


Figure 7.27: Web page Hostinger.com used to host the AWAM system data storage and analysis output algorithms

Table 7.17 shows the specifications of the hostinger.com site in table form. With a server coverage of up to 39 countries world-wide, the hosting site utilizes a simple drag and drop method of web developing. Reaching loading speeds of up as low as 70 mili-second, the site is currently operating under the platform of Linux cloud-based system. The AWAM system leased the awam.my domain for a mere 8 US dollar per month to gain unlimited amount of storage, bandwidth, a number of domains and also email from the hosting site. Incorporating a user-friendly coding script for the host server, this enables the AWAM system code to be written with Java and Hypertext Pre-processors (PHP) languages.

Table 7.17: Web server specifications

Name	Hostinger.com
Coverage	39 countries and more than 29 million customers
Web Builder	drag-and-drop
Page Load Speed	70-80 mili-second
Platform	Linux cloud-based
Business Web Hosting Plan Pricing	\$7.95/month
Scripting & Languages	Java, Hypertext Pre-processors (PHP)
Server Location	USA, UK and Singapore
Storage	unlimited
Bandwidth	unlimited
No of Domains	unlimited
No of Emails	unlimited

7.5 Site Work

The following subchapters depict the site selection and basic fundamental site material and properties testing done initially before AWAM system installations on site.

7.5.1 Site Selection

The site selection for the installation of the AWAM system was divided into two areas of slopes. AWAM device 1 until 3 was installed in the vicinity of the School of Civil Engineering (M47) located at 1°33'44" N 103°38'3" E while two sets of the AWAM device was installed near the vicinity of the Centre for Information and Communication (CICT) located at 1°33'45" N 103°38'14" E. Both sets for the AWAM system slope monitoring were inside the University of Technology, Malaysia area as shown in Figure 7.28. The slope angles vary from 30° to 45° all rest well within the confines of the laboratory scale testing range. The slope span of the area within the School of Civil Engineering was measured to be approximately 18 m, with heights of about 12 m to 18 m. Meanwhile, the two sets installed near the CICT were installed

on a slope having a span of 12 m, with a varied 8 m to 10 m heights for its slopes. Both the slopes were classified as a cut slope with uniform slope geometry.

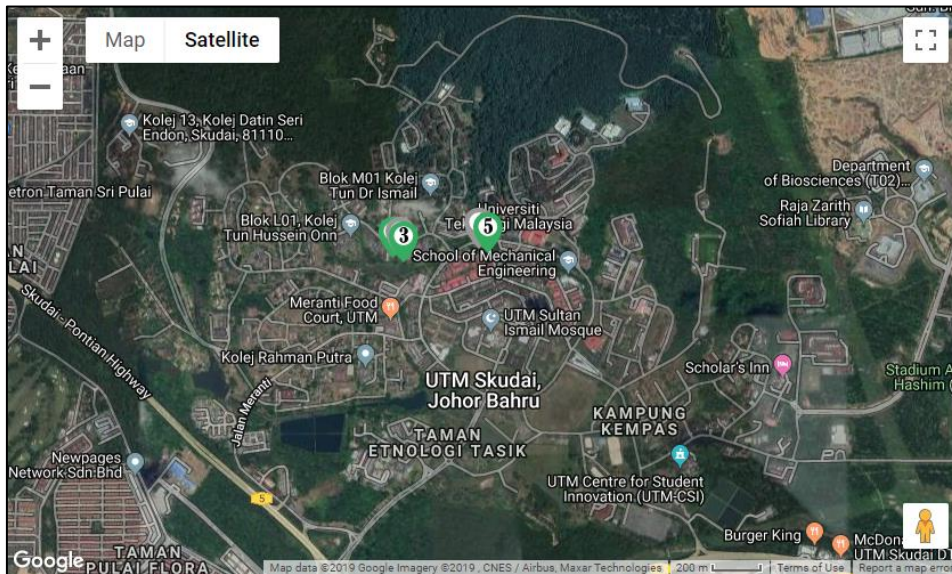


Figure 7.28: Satellite view of AWAM device installation sites through Google maps

Figure 7.29 illustrates the exact location of the AWAM system in the vicinity of the University. The distances from both sites are approximately 350 m apart.

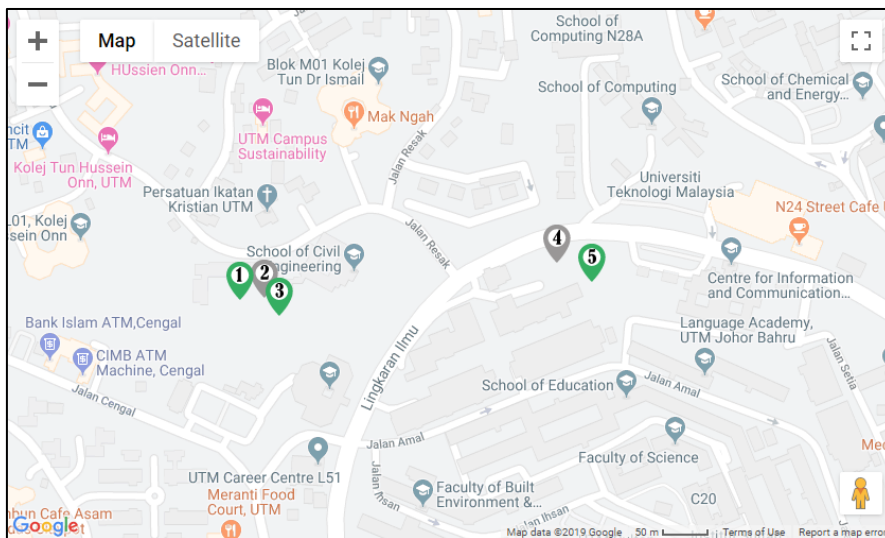


Figure 7.29: Exact location of AWAM device installation inside UTM

Figure 7.30 shows the surrounding for the AWAM system 1 to 3 while Figure 7.31 displays the slope condition for the AWAM system 4 to 5.



Figure 7.30: The aerial overview of the surroundings for the AWAM2.



Figure 7.31: The surrounding location of the AWAM4 and AWAM5

7.5.2 Soil Properties

Over the years, several in situ testing devices have been utilized to characterize, measuring strength and also deformation properties of a site. One of the most commonly used devices is the Mackintosh Probe test, considered to be a faster and cheaper tool especially when the intended site is moderate in-depth and the soil underneath is soft or loose.

7.5.2.1 Mackintosh Probe Test

The research opted to utilize the Mackintosh Probe test since the area of the AWAM system installation is within the range of 15 m depth required for the test and additionally proven to be easier to execute compared to other in situ testing schemes. Outcomes of the test include the bearing capacity and soil properties which are vital to the simulation analysis of the site later on. The Mackintosh Probe test was done according to MS 1056: 2005 which is the method of test for soils for Civil Engineering purposes and an additional test of moisture content using BS 1377: Part 2:1990. Figure 7.32 displays the Mackintosh Probe test in the vicinity of the AWAM system installation.



Figure 7.32: Mackintosh Probe test on site of the AWAM system prepared by research assistants

The result from the Mackintosh Probe test was meant as an initial sub-surface investigation of the site to obtain rough estimations of parameters for geotechnical analysis (Harun, 2019).

7.5.3 Modelling of the Site Slope Stability Analysis

To have a better understanding of the overall behaviour and strategic mobilization of the AWAM device monitoring on the field, a series of numerical modelling was established prior to the installation stage of the system. Geostudio 2012 with its SEEP/W and SLOPE/W components were utilized in this research. Seepage analysis prior to the slope stability analysis for the determination of factor of safety were carefully planned out and executed in modelling the site of the slope monitoring.

7.5.3.1 Modelling of Site Materials

This specialized modelling would include several inputs from the field conditions such as the soil properties, slope geometry, rainfall patterns and also taking into consideration any infrastructure loadings in the vicinity of the site. With the addition of several other factors that may have an impact on the slope stability, computer simulations would serve as an added edge to have as a precautionary step in having a complete and thorough preparation for the effectiveness of the slope stability monitoring system.

As previously stated on the subchapter 6.2, the modelling properties would comprise of several inputs such as; the physical properties, soil-water characteristic curve (SWCC), permeability functions and also a comprehensive geometric study of the slope monitoring site. These values are vital in the simulations of the site and are presented in Table 7.18. Several properties used to model the site was determined in the laboratory after undisturbed sample acquisition using a hand auger and soil sampler was done on-site. The effective shear strength was obtained using Consolidated Isotropic Undrained (CIU) triaxial test resulting in the effective friction angle (ϕ') and effective cohesion (c') as stated. In addition, constant head permeability testing in the lab also provided the permeability values (K) of the soil. Only a single type of soil of up to 6 m was simulated since rainfall-induced slope failure was usually detected as shallow failures (Rahardjo et al., 2005). Rainfall patterns to simulate the real site

conditions were based on the Intensity Duration Frequency (IDF) curve of Johor Bahru discussed in subchapter 5.2.4.

Table 7.18: Physical and mechanical properties of soil samples

	Soil	(w) (%)	G_s	γ_b (kN/m)	c' (kPa)	ϕ' (°)	K (m/s)
Site M47	Sandy silt	19.1	2.65	17.5	7.5	29	5.0×10^{-7}
Site CICT	Sandy silt	43.4	2.65	18.5	7.8	32	5.1×10^{-7}

7.5.3.2 Modelling of the Site Geometry

Subsequently after site selection such as discussed in subchapter 7.5.1, the geometry model of both the sites were prepared on the GeoStudio 2012 simulations. Figure 7.33 shows the overview of the geometric model used in the simulations of the M47 site while Figure 7.34 depicts the overview of the CICT site. The red circle marks the AWAM device location on the slope crest for each of the sites.



Figure 7.33: Overview of the M47 site layout



Figure 7.34: Overview of the CICT site layout

After a successful geometric drawing of both the M47 and CICT sites on the GeoStudio 2012 software, Figure 7.35 and Figure 7.36 were the result of the geometry and boundary conditions that were used in the modelling. The general setting was modelled accordingly as previously discussed in subchapter 6.3.1.



Figure 7.35: Site M47 geometry and boundary conditions



Figure 7.36: Site CICT geometry and boundary conditions

7.5.3.3 Modelling of the Site Initial Condition

The initial condition was established in the beginning stages to simulate initial pore-water pressure very much alike to the real site condition. Initial PWP conditions were setup for a duration of 24 hours. Cell size was set to 0.2 x 1 m resulting in 3204 nodes and 3062 elements for M47 site while the CICT site resulted in 2740 nodes and 2584 elements. Figure 7.37 and Figure 7.38 illustrates the result of the simulation for the initial condition of the M47 and CICT AWAM monitoring site, respectively.

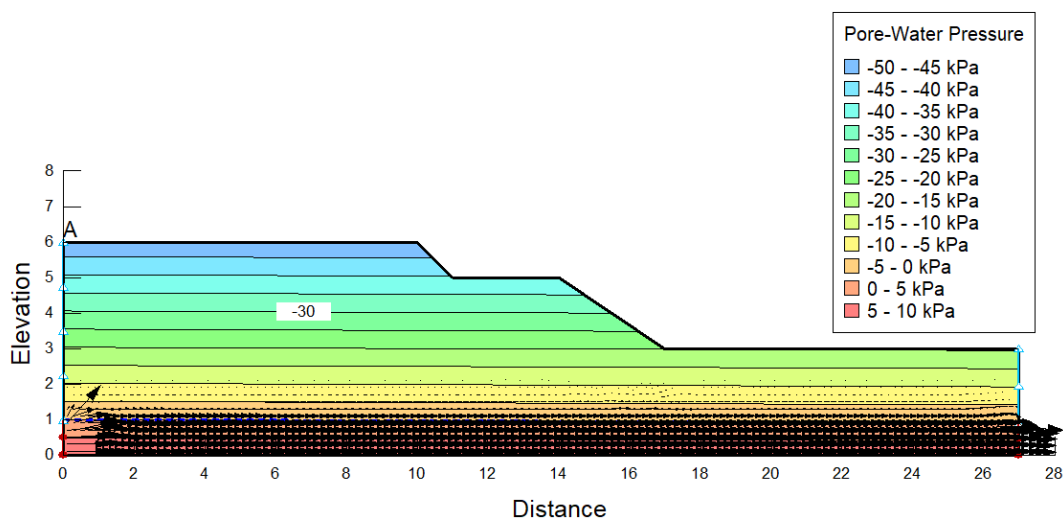


Figure 7.37: SEEP/W initial condition of M47 site

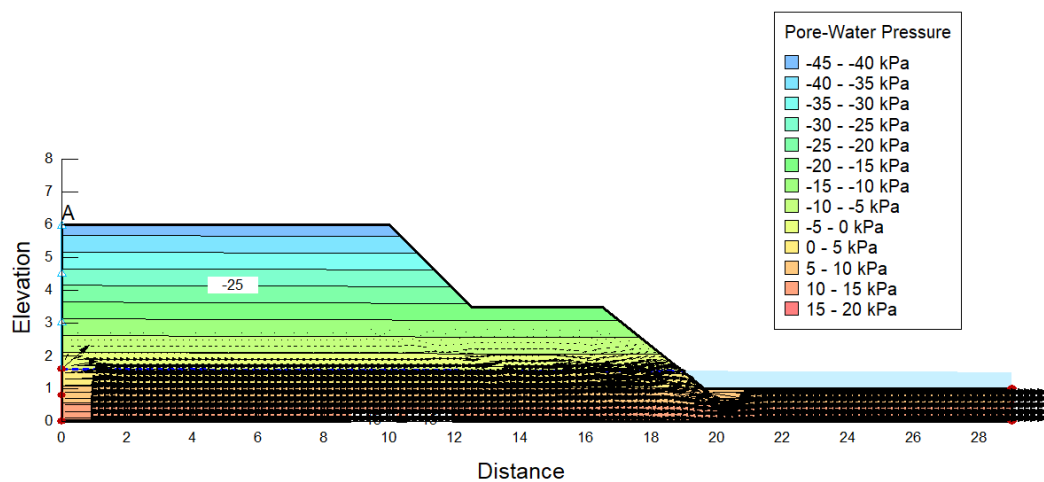


Figure 7.38: SEEP/W initial condition of CICT site

7.5.3.4 Transient Seepage of the Rainfall Simulation for the AWAM Site

After the desired initial conditions were established, the slope model was subjected to intense rainfall over a period of 20 hours. This was based on the research done by Yeh and Tsai (2018) that reported a dramatic decrease in safety coefficient of a modelled slope after an average rainfall duration of 20 hours. The apparent indicator of slope instability is the layer of 0 kPa pore water pressure on the upper layer of the slope model. Since the pore water pressure is registered as nearing 0; these are the indications of the soil to lose shear strength, a briefer time for slope to fail and reduction of the safety of factor for the slope model (Yeh and Tsai, 2018). After analyzing the IDF curve of rainfall intensity as previously mentioned in subchapter 5.2.4, the slope model was subjected to a 20-hour rainfall intensity of 2.82×10^{-7} m/sec.

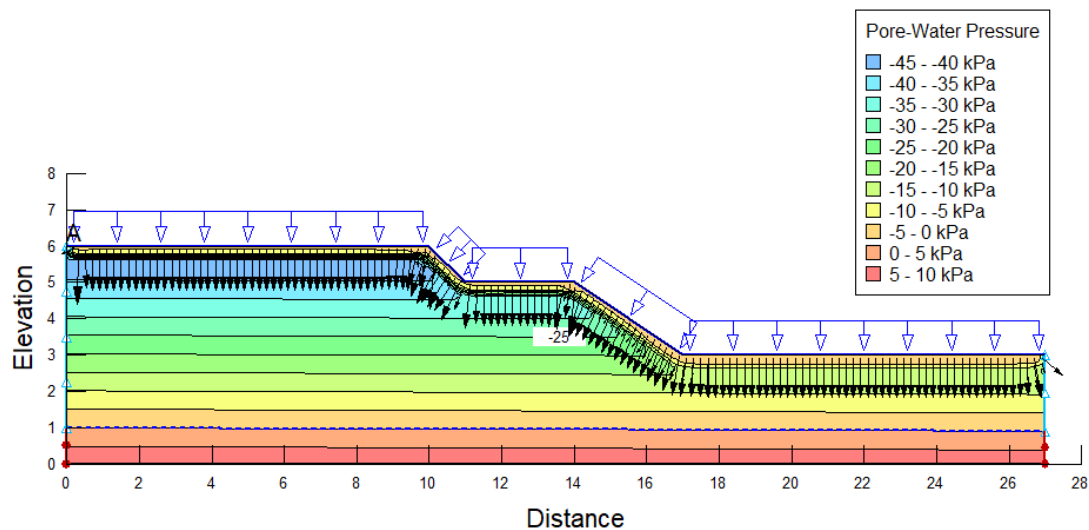


Figure 7.39: Transient seepage simulation condition of M46 site

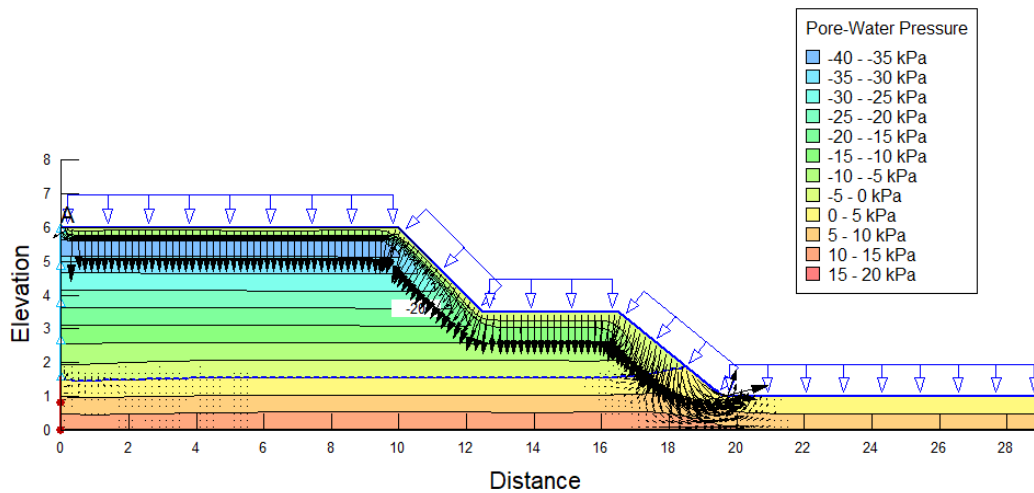


Figure 7.40: Transient seepage simulation condition of CICT site

Figure 7.39 and Figure 7.40 illustrates the result of transient seepage simulation from the SEEP/W analysis of both the sites M46 and CICT. It was observed that the upper layer of the slope monitored both simulated a layer of -5 to 0 kPa pore water pressure suggesting slope instability occurring. Worth to note the thicker layer of pore water pressure nearing 0 kPa on the CICT site suggesting a higher probability of slope instability occurring. The research proceeds to the analysis of the factor of safety difference due to rain duration.

7.5.3.5 Factor of Safety (FOS) vs. Time Simulations for the AWAM Site

Data from the SEEP/W analysis was then further analyzed using SLOPE/W to quantify its slope stability analysis. Morgenstern-Price method of analysis was selected for the analysis type while Entry and Exit Slip Surface Option was opted for the critical slip surface simulations. The factor of safety was determined periodically from initial to its maximum rainfall duration of 20 hours in four separate timeframes as illustrated in the following figures. The final analysis of the 20-hour rainfall simulation was portrayed with an additional Safety Map illustration from the Slip Surfaces Preference option tab in the GeoStudio 2012 software, to measure the distance from the ground surface to the outer rim of the slip surface for the hinged foundation installation as previously mentioned in subchapter 7.4.7.

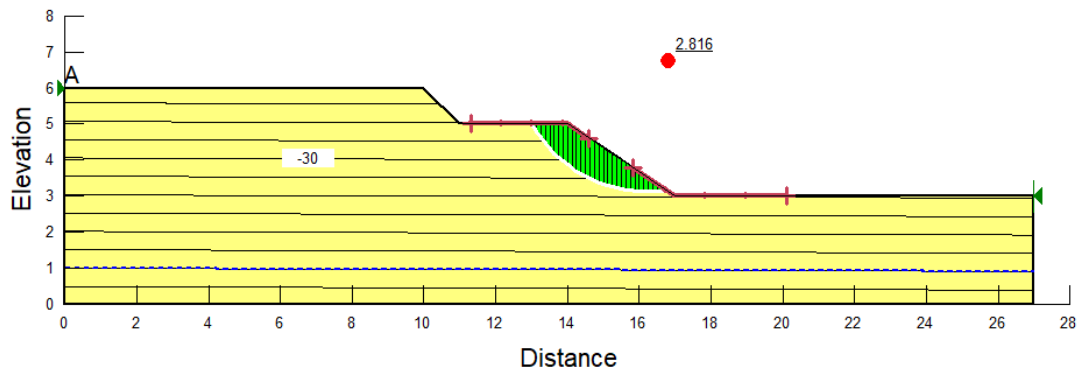


Figure 7.41: SLOPE/W factor of safety analysis of M46 site at 0 hour (initial)

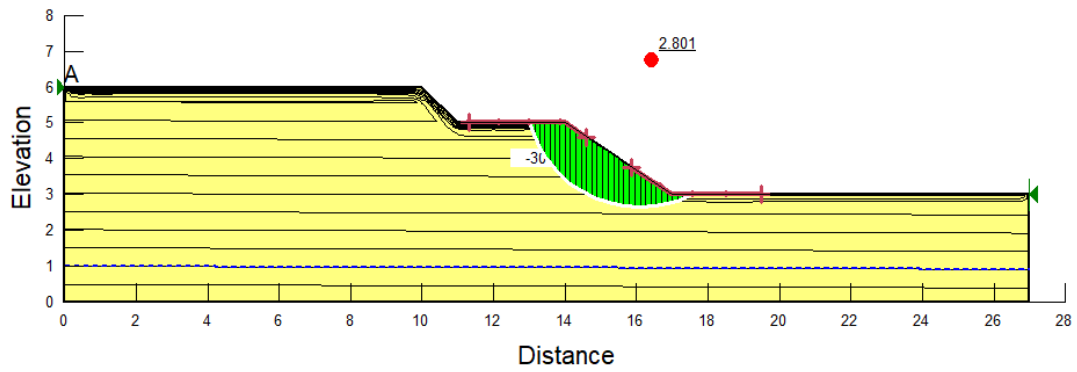


Figure 7.42: SLOPE/W factor of safety analysis of M46 site after 4 hours

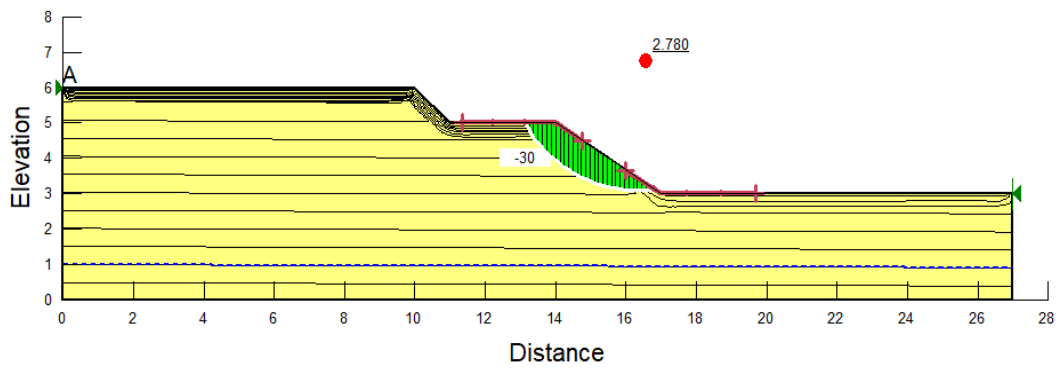


Figure 7.43: SLOPE/W factor of safety analysis of M46 site after 8 hours

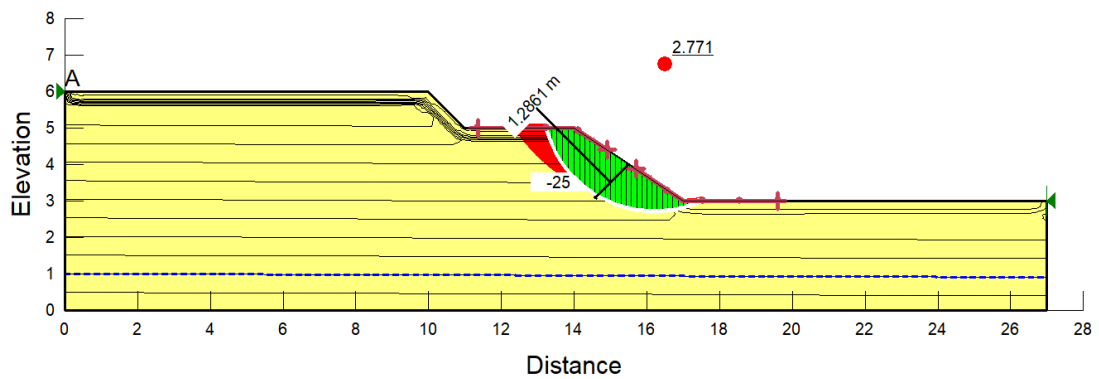


Figure 7.44: SLOPE/W factor of safety analysis of M46 site after 20 hours

Figure 7.41 to Figure 7.44 displayed the SLOPE/W factor of safety analysis for the M46 site. Worth to mention the decrease of factor of safety (FOS) values for the analysis throughout the increase of rainfall duration for the overall SLOPE/W analysis of the M46 site. 2.816 FOS was registered initially and decreased to 2.771 after 20 hours of rainfall. 1.3 m of depth perpendicular to the slope face was determined in Figure 7.44 as the depth needed for the hinged foundation mechanism of the AWAM sensor for the M46 site. The analysis proceeds with the analysis for the CICT site while a thorough analysis of the overall factor of safety with respect to rainfall duration analysis for the sites would be presented in the following subchapter.

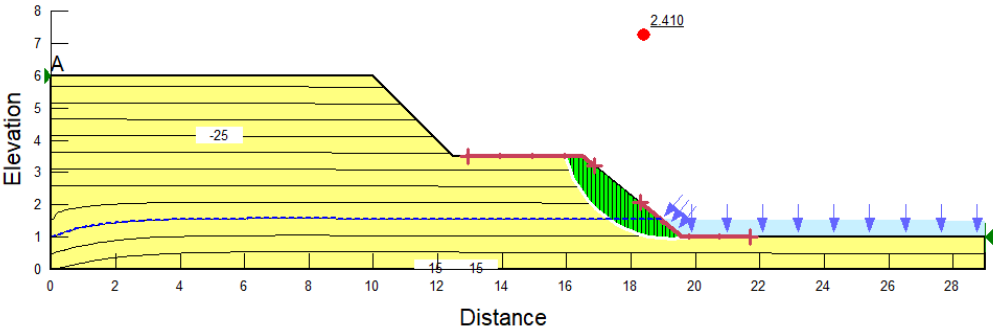


Figure 7.45: SLOPE/W factor of safety analysis of CICT site at 0 hour (initial)

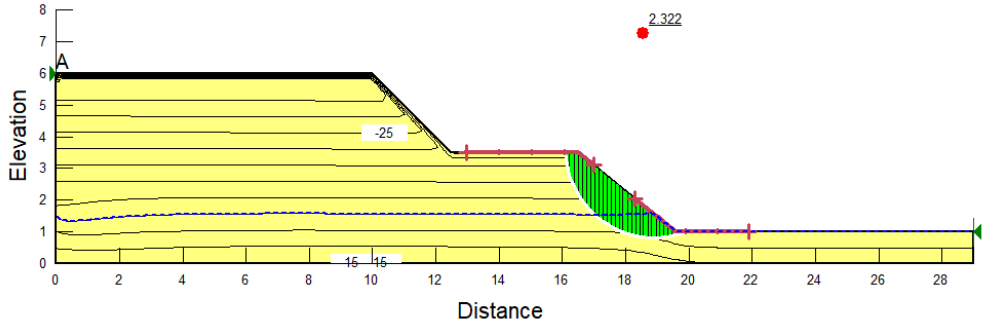


Figure 7.46: SLOPE/W factor of safety analysis of CICT site after 4 hours

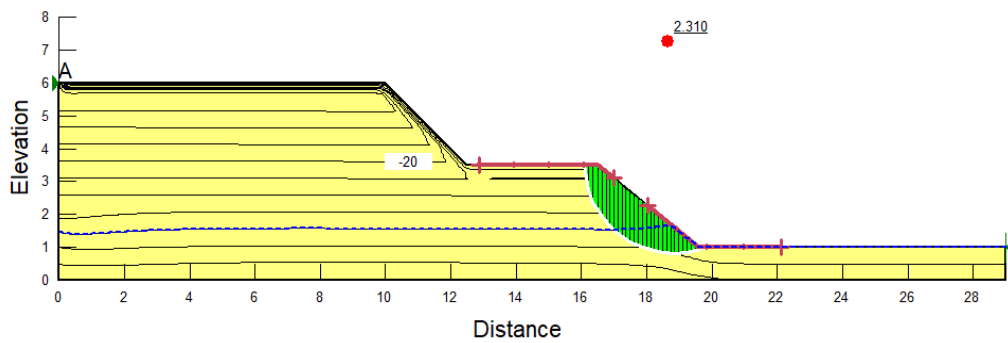


Figure 7.47: SLOPE/W factor of safety analysis of CICT site after 8 hours

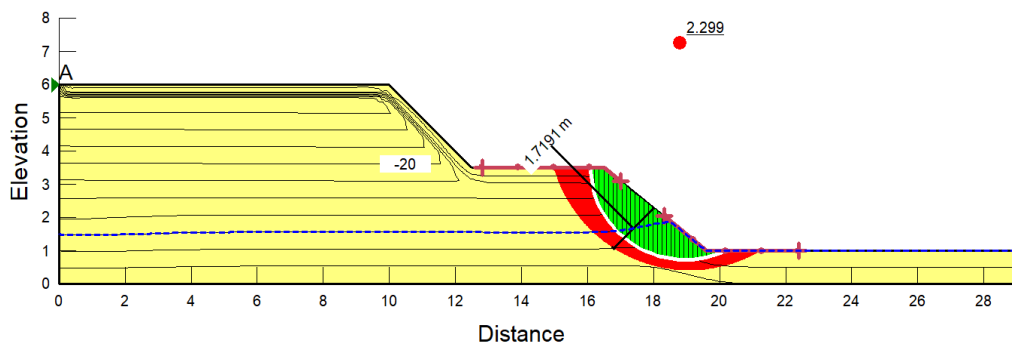


Figure 7.48: SLOPE/W factor of safety analysis of CICT site after 20 hours

Figure 7.45 to Figure 7.48 displayed the SLOPE/W factor of safety analysis for the CICT site. As presented on the analysis for the M46 site, similar behaviour was determined for the result of FOS with respect to the increase of rainfall duration for the CICT site. 2.410 FOS was registered initially and decreased to 2.299 after 20 hours of rainfall. 1.7 m of depth perpendicular to the slope face was determined in Figure 7.48 as the depth needed for the hinged foundation mechanism of the AWAM sensor.

7.5.3.6 Concluding Notes for the Simulations of the AWAM Site

The SEEP/W and SLOPE/W analysis for the AWAM site installations were finalized. The changes in the slope condition from initial slope condition until probable slope instability were illustrated by the changes of the pore water pressure. The factor of safety reduction with respect to rainfall duration was simulated and the probable

slip circle failure was determined. Similar research output was published by Oh and Lu (2015) and Sinarta (2017).

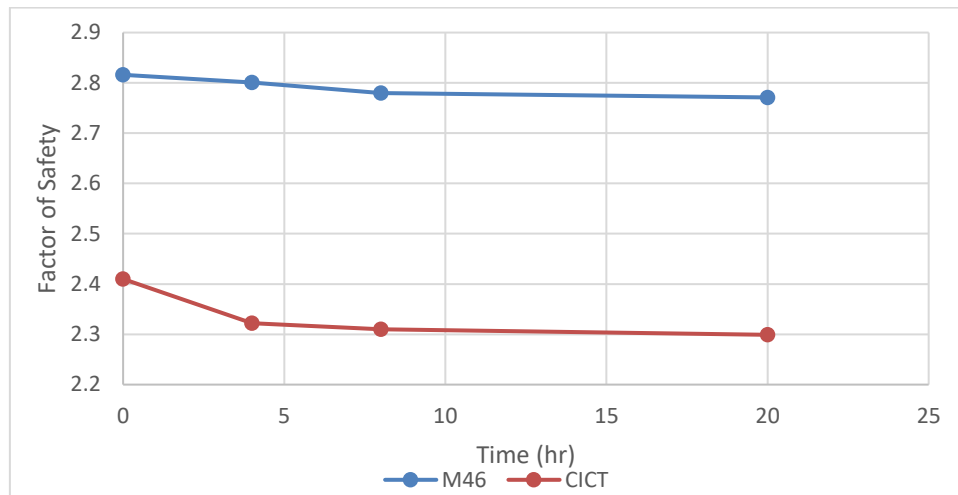


Figure 7.49: Relationship between safety factor and rain period simulations

Figure 7.49 shows the relationship between the FOS and rainfall duration simulations of the AWAM sites M46 and CICT. As illustrated by the figure, the CICT site showed a more drastic difference of values from initial conditions until 20 hours of rainfall simulations. The difference of a factor of safety decrease rate can be explained from the findings of subchapter 7.5.3.4, as it can be seen from the transient seepage simulations whereby a thicker layer of pore water pressure nearing 0 kPa was simulated on the slope face of the CICT site compared to the M46 site. This finding was in line with similar findings by Yeh and Tsai (2018).

The following Table 7.19 summarizes the findings from the SLOPE/W simulations depicted from the Safety Map preference tab for the minimum depth of the AWAM hinged foundation installations.

Table 7.19: Anchor depth summary for AWAM hinged foundation installations

	Site	
	M46	CICT
Anchor Depth (m)	1.3	1.7

Worth to note the difference of the AWAM hinged foundation depth for both the sites M46 and CICT were in correlation with the factor of safety simulated as a higher factor of safety yield a slightly shorter depth of slip circle failure. For future AWAM installation, procedures from 7.5.2 to 7.5.3 would be the standard guidelines as a pre-analysis before AWAM installation commences. Each proposed site would be unique and are required to be analyzed as per recommended by the research findings unless the same conditions and geometry are similar to the one presented.

7.6 Measurement And Warning System Notifier of Slope Monitoring System Through awam.my

The subchapter would entail the measurement method and data interpretation of the slope monitoring system using the awam.my web page. Since the AWAM system employs a web-based data monitoring, subscribers to the system would have the access of the data transmitted by the AWAM devices directly through any web browser attainable via the World Wide Web through personal computers, mobile phones or tablet that has connectivity to the internet. For users without access to the internet but has a subscription to the AWAM system, the global system for mobile communications (GSM) would send a short messaging system (SMS) notification to subscribers to warn them if any high-risk movement of the slope is detected on their specific area of monitoring interest. Fresh data updates every minute for each of the AWAM devices.

7.6.1 awam.my Index Page

The AWAM monitoring systems are fully functional and currently transmitting data from five points all around UTM through web-based platform www.awam.my. Figure 7.50 shows the index page of the webpage which includes a visual representation of AWAM nodes on the Google Map, various page links that drop down for data interpretation and also the device status of all the AWAM nodes.

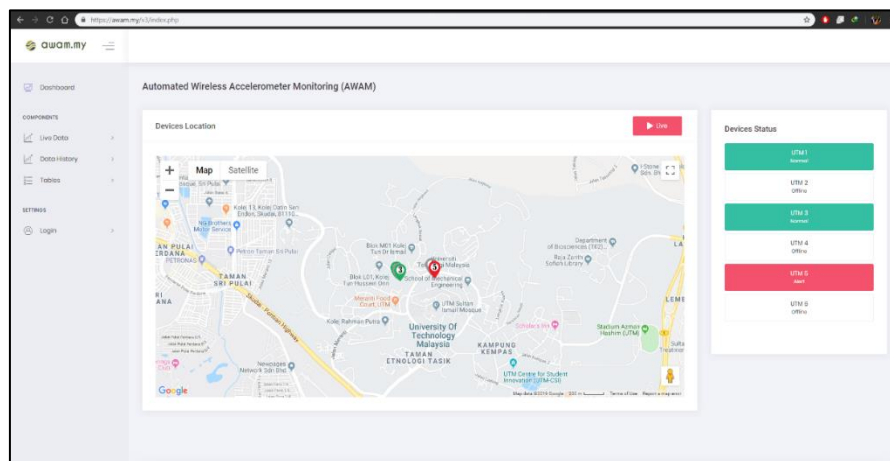


Figure 7.50: AWAM monitoring system webpage

The nodes with a specific AWAM device numbering would be highlighted on the live device location with three distinct representations. Green nodes mean that the device is functioning well and the slope monitored is in a safe condition while red represents the alert status which means that the AWAM system detects movement of the slope and intended subscribers should be wary of such situation. AWAM system personnel and authorities should rush to the alerted site area to do a proper check whether the slope is indeed in a high-risk situation to address the nature of the slope movement. The final representation of the nodes is the grey node that signifies the AWAM device is offline, which can mean dysconnectivity to the AWAM system and in need of technical assistance from AWAM personnel. Figure 7.51 illustrates the awam.my page when all of the AWAM devices from AWAM 1 to 5 are in a green, healthy and operable state.

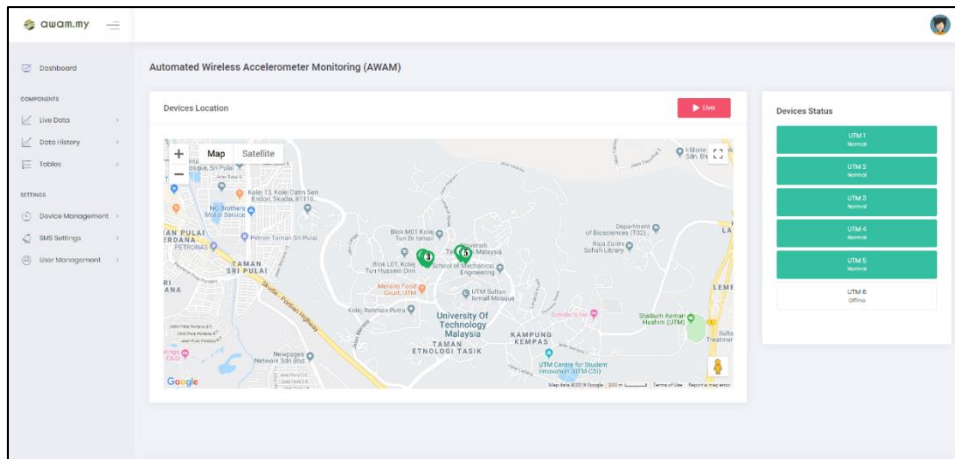


Figure 7.51: awam.my displaying all the healthy status of the AWAM system

7.6.2 awam.my Components

The left side panel of the awam.my webpage includes page navigation to the comprehensive data interpretation of the AWAM system. AWAM system users can navigate the intended slope monitoring data that includes backdated data (data history) in terms of tables or graph representation. Figure 7.52 displays the data table form of the AWAM system complete with a drop-down menu to navigate the required date and device choices.

The screenshot shows the 'Data Table' interface for device '01x0001' on the date '23-10-2019'. It includes filters for 'Date' and 'Devices', and options to view data as 'PDF' or 'Excel'. The table displays 10 rows of data with columns for Date, Time, and acceleration axes (Ax, Ay, Az, Gx, Gy, Gz), along with Temperature and Humidity. A search bar and pagination controls are also visible.

Date	Time	Ax	Ay	Az	Gx	Gy	Gz	Temperature	Humidity
23-10-2019	00:00:02	-133	423	-8.82	0.00	0.00	0.00	28	62
23-10-2019	00:01:02	-134	424	-8.86	0.00	0.00	0.00	28	62
23-10-2019	00:02:02	-133	425	-8.84	0.00	0.00	0.00	28	62
23-10-2019	00:03:02	-134	424	-8.87	0.00	0.00	0.00	28	62
23-10-2019	00:04:02	-132	424	-8.85	0.00	0.00	0.00	28	62
23-10-2019	00:05:02	-134	424	-8.86	0.00	0.00	0.00	28	62
23-10-2019	00:06:02	-135	425	-8.84	0.00	0.00	0.00	28	62
23-10-2019	00:07:02	-134	424	-8.85	0.00	0.00	0.00	28	62
23-10-2019	00:08:02	-133	425	-8.88	0.00	0.00	0.00	28	62
23-10-2019	00:09:02	-136	426	-8.82	0.00	0.00	0.00	28	62

Figure 7.52: awam.my extensive data table display

In addition, the web page also provides data download of the intended device and its date in PDF or Microsoft Excel format. The data is readily available for research purposes and data interpretation for a select date and time. Figure 7.53 shows the sample data that was downloaded from the awam.my website in PDF format for research purposes.

AWAM Automated Wireless Accelerometer Monitoring													
Date	Time	Ax	Ay	Az	Gx	Gy	Gz	Temperature	Humidity	Tempsensor	Climbrate	Voltagenode	Identifier
29-09-2019	00:00:02	-1.29	4.25	-8.86	0.00	0.00	0.00	28	59	37.06	-2.07	12.53	523
29-09-2019	00:01:08	-1.26	4.27	-8.87	0.00	0.00	0.00	28	59	37.06	2.14	12.61	524
29-09-2019	00:02:06	-1.28	4.25	-8.88	0.00	0.00	0.00	28	59	37.06	0.40	12.47	525
29-09-2019	00:03:02	-1.28	4.24	-8.86	0.00	0.00	0.00	28	59	37.07	0.16	12.43	526
29-09-2019	00:04:02	-1.27	4.25	-8.86	0.00	0.00	0.00	28	59	37.07	-1.79	12.59	527
29-09-2019	00:05:02	-1.28	4.26	-8.90	0.00	0.00	0.00	28	59	37.07	-0.70	12.61	528
29-09-2019	00:06:02	-1.29	4.27	-8.88	0.00	0.00	0.00	28	59	37.07	-2.66	12.55	529
29-09-2019	00:07:02	-1.31	4.24	-8.90	0.00	0.00	0.00	28	59	37.08	1.18	12.47	530
29-09-2019	00:08:02	-1.30	4.24	-8.87	0.00	0.00	0.00	28	59	37.08	0.62	12.59	531
29-09-2019	00:09:02	-1.29	4.28	-8.87	0.00	0.00	0.00	28	59	37.08	-2.50	12.47	532
29-09-2019	00:10:02	-1.30	4.25	-8.85	0.00	0.00	0.00	28	59	37.09	-0.62	12.61	533
29-09-2019	00:11:02	-1.30	4.25	-8.86	0.00	0.00	0.00	28	59	37.09	-0.81	12.51	534
29-09-2019	00:12:02	-1.26	4.24	-8.88	0.00	0.00	0.00	28	59	37.09	-0.82	12.61	535
29-09-2019	00:13:02	-1.27	4.25	-8.85	0.00	0.00	0.00	28	59	37.09	1.63	12.41	536
29-09-2019	00:14:02	-1.28	4.23	-8.85	0.00	0.00	0.00	28	58	37.10	-1.01	12.59	537
29-09-2019	00:15:02	-1.28	4.27	-8.86	0.00	0.00	0.00	28	58	37.10	-1.94	12.51	538
29-09-2019	00:16:02	-1.27	4.25	-8.88	0.00	0.00	0.00	28	58	37.10	-2.20	12.49	539
29-09-2019	00:17:04	-1.27	4.21	-8.86	0.00	0.00	0.00	28	58	37.08	-0.01	12.53	540

Figure 7.53: AWAM system data sample downloaded from the awam.my website

7.6.3 awam.my Admin Privilege Page

As a privilege to the admin of the system; an option to set the limiting values, SMS settings and user management are obtainable through signing-in such as shown in Figure 7.54.

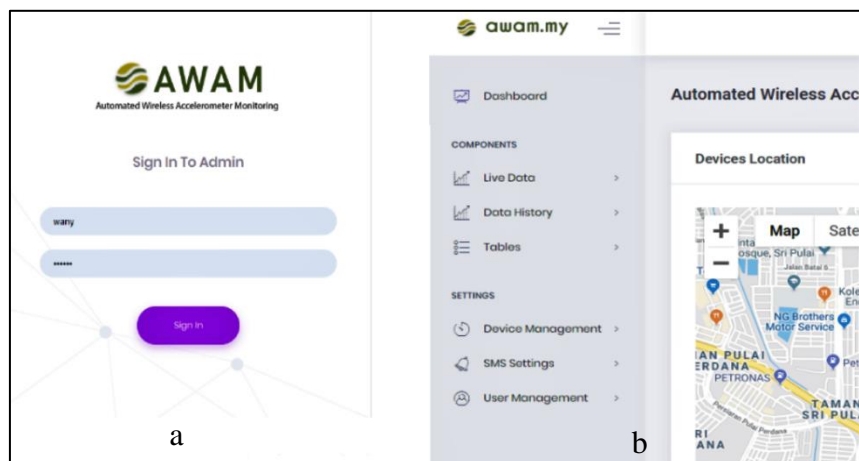
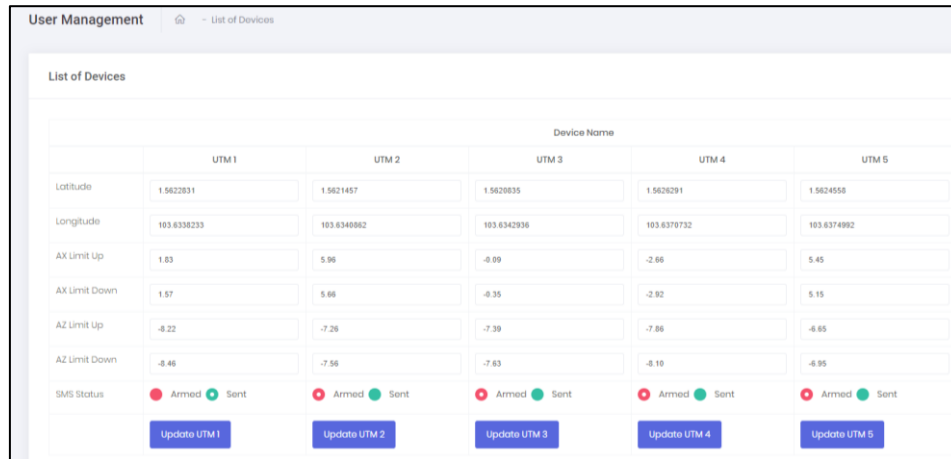


Figure 7.54: a) admin login page and b) settings menu for administration

7.6.4 awam.my Limiting Value Page

Figure 7.55 illustrates the page that sets the limiting value of the accelerometer reading of the AWAM system. There exist two value of limitation which are the upper bound and lower bound. If the reading from the AWAM device exceeds either limit, then a programmed warning signal will be sent to the respective user via SMS.



User Management					
List of Devices					
	Device Name				
	UTM 1	UTM 2	UTM 3	UTM 4	UTM 5
Latitude	1.5622831	1.5621457	1.5620835	1.5620291	1.5624558
Longitude	103.6338233	103.6340862	103.6342936	103.6370732	103.6374892
AX Limit Up	1.63	5.96	-0.09	-2.66	5.45
AX Limit Down	1.57	5.96	-0.35	-2.92	5.15
AZ Limit Up	-8.22	-7.26	-7.39	-7.86	-6.65
AZ Limit Down	-8.46	-7.56	-7.63	-8.10	-6.95
SMS Status	Armed Sent	Armed Sent	Armed Sent	Armed Sent	Armed Sent
	Update UTM 1	Update UTM 2	Update UTM 3	Update UTM 4	Update UTM 5

Figure 7.55: AWAM device data limiting value management

7.6.5 awam.my User Management Page

As an administrator, the AWAM personnel with access to the data management of the system can edit, add or delete the list of users and phone numbers associated with the warning messaging system. Figure 7.56 displays the user management of AWAM system that was used to register SMS user notifier for the system.

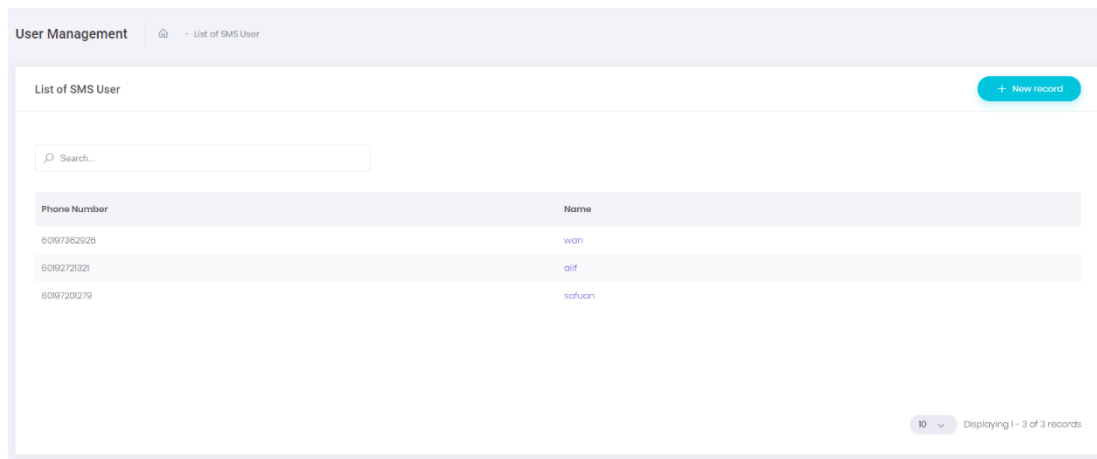


Figure 7.56: User management navigation list for awam.my personnel

In the near future, the awam.my webpage can still be refined to suit the needs of the general public. Amongst the priority is that the web awam.my would be incorporated with the capability to automatically create a user profile for the public allowing direct access to specific AWAM system slope monitoring sites that are intended to the public.

7.7 Installation of AWAM System on the Field

Figure 7.57 shows the installation of the AWAM system that is easily done by a team of 2 to 3 people hand-carrying equipment to installation sites. The first step upon arrival to the installation site should be to clear out any obstacles in installing the AWAM device power station base and sensor case. Following that, the assembly of the power station and sensor case foundation as mentioned in subchapter 7.5 were done using hand tools. All wires from the sensor and solar panel were then connected to the power station module.



Figure 7.57: Preliminary installation stages

After a few hours of setting up procedures such as the networking system, power supply checking and finishing touches on the system such as shown on Figure 7.58, the AWAM system is ready for its intended slope monitoring. In addition, waterproofing procedures were done upon the device for harsh weather condition protections.



Figure 7.58: Setup of the AWAM system on site

Figure 7.59 shows the AWAM monitoring system after the installation was concluded. Through a trial period of 12 months, all the devices that were previously installed maintained its service proving its longevity and performance with minimal maintenance needed.



Figure 7.59: Completed installations of the AWAM system for slope monitoring on site

7.8 Slope Monitoring Result

In this section, the readings of the AWAM monitoring system to access slope movements in the field obtained from awam.my for the entirety of the year 2019 are presented. As mentioned in subchapter 7.6.3, admin privileges are needed to obtain a complete history of data entry for the AWAM system whereas non-admins have limited access to the entirety of the database. The year 2019 was chosen for the documentation of the slope monitoring result since it was the most recent year of data entry prior to the research completion and utilizes an up-to-date version of the system; ensuring a stable and accurate reading of the slope data upon months of fine-tuning and software update for the whole system. The data presented would be an indication of the system's capability to provide a prolonged duration of slope monitoring for the newly developed system.

Though the awam.my provides a huge array of results including accelerometer, gyrometer, temperature, humidity and battery voltage data logging as shown in subchapter 7.6.2, the current subchapter would focus on the acceleration readings since any kind of movement of the slope would be detected through the rate of change for the accelerometer data. The data would be presented in two separate subchapters according to the AWAM system separate locations of M47 and CICT provided by five

sets of data logging from devices AWAM1 to AWAM5. The complete dataset exported from the awam.my website for the slope monitoring field trials are presented in Appendix C.

7.8.1 Slope Monitoring Result for the M47 Site

Figure 7.60 to Figure 7.62 illustrates the actual reading of accelerometer data throughout the year 2019 for the M47 site of AWAM slope monitoring system. The data was collected by AWAM1, AWAM2 and AWAM3 devices obtained from the awam.my website with an average of 10 months readings per device, respectively. The readings of the AWAM devices overall registered a stable and minimal fluctuating readings apart from intentionally scheduled sensor maintenance and device response testing by the research’s team personnel. Several key dates are highlighted in the figures such as the start date of data logging and dates which sensor recalibration procedures were done to the AWAM devices.

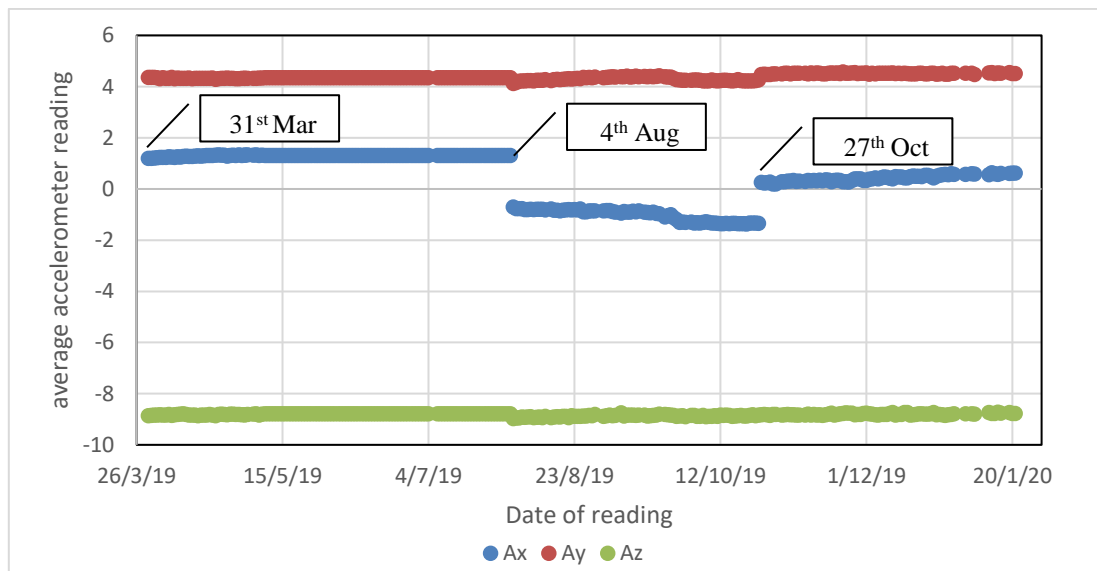


Figure 7.60: AWAM1 device accelerometer readings for the year 2019

Figure 7.60 shows the readings of the AWAM1 device starting from 31st March 2019 until the end of the year 2019. The y and z-axes registered a steady overall of acceleration data throughout the whole span. Meanwhile, on the 4th of August and 27th

October that same year, the value of Ax which originates from accelerometer readings of the x-axis registered a massive fluctuation of reading but remained steady over the course of in between the scheduled sensor recalibrations. The AWAM1 device was put out of commission as the readings of the device ended on January 2020.

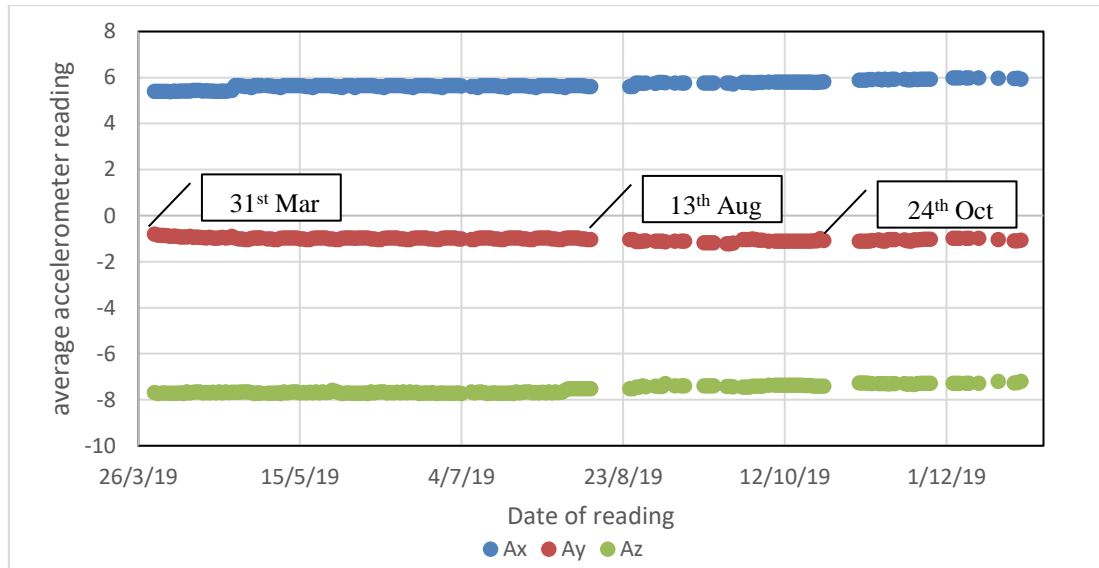


Figure 7.61: AWAM2 device accelerometer readings for the year 2019

Similarly to the AWAM1 device, the start/end date of data logging and scheduled recalibrations of the AWAM2 device was shown in Figure 7.61. It can be observed that apparently, the AWAM2 readings was inherently different in terms of the device needing a few days to become online hence the blank data registered on the 13th August and 24th October subsequently after the scheduled device recalibrations procedures.

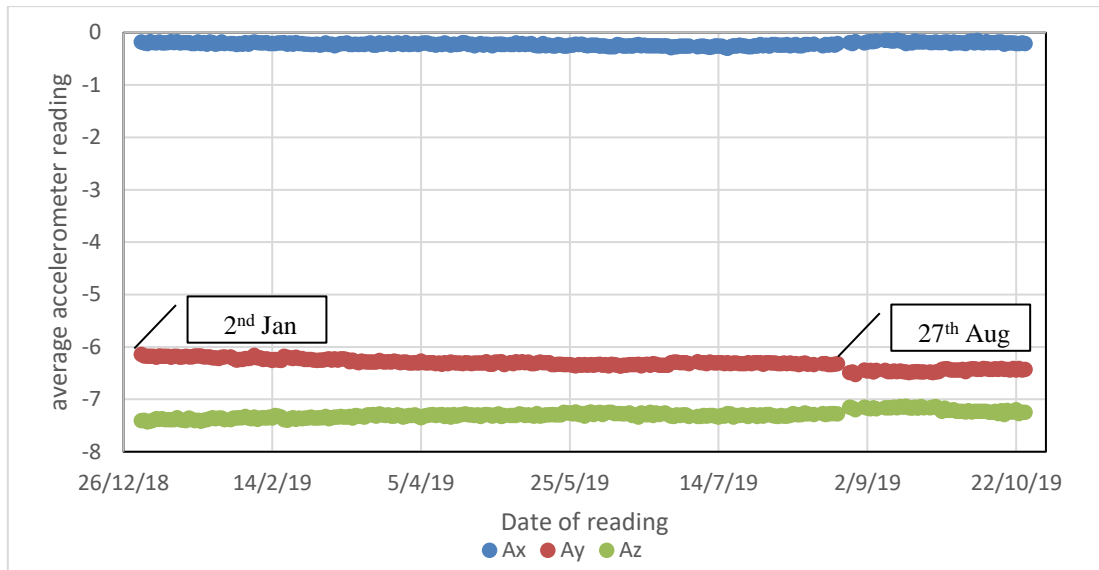


Figure 7.62: AWAM3 device accelerometer readings for the year 2019

The AWAM3 device accelerometer readings were available since the start of the year on the 2nd of January and were put out of commission on the second scheduled sensor recalibration on October the same year as shown in Figure 7.62. Overall readings of the 3-axes fluctuate minimally apart from the device response testing done on the 27th of August.

7.8.2 Slope Monitoring Result for the CICT Site

For the CICT site, Figure 7.63 and Figure 7.64 illustrates the data of accelerometer data for the AWAM4 and AWAM5 devices obtained from the awam.my website with an average span of a similar 10 months data logging for the respective devices.

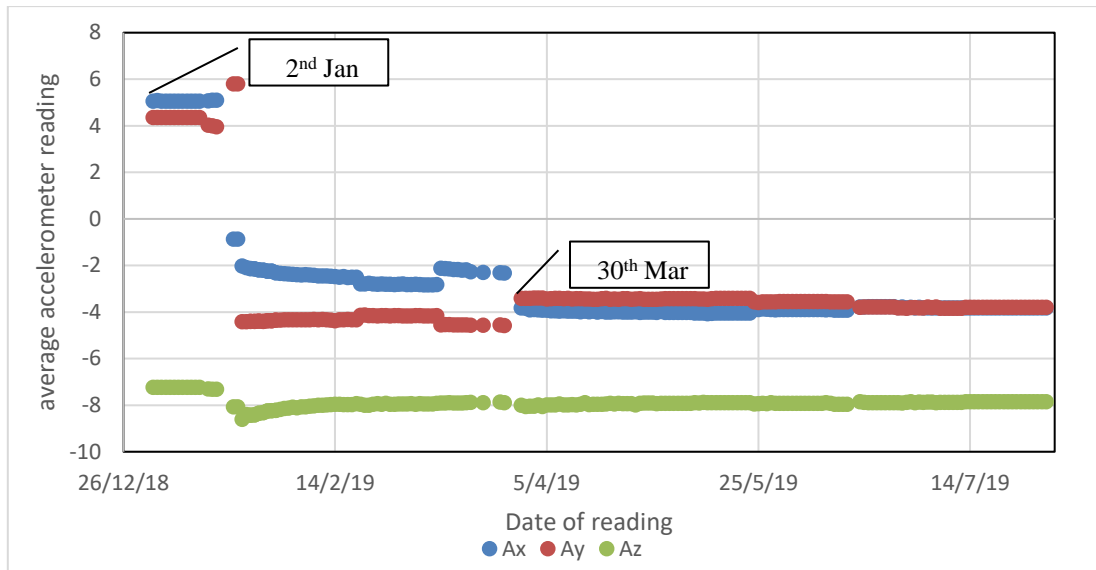


Figure 7.63: AWAM4 device accelerometer readings for the year 2019

Figure 7.63 provides the research with an ample example of the inconsistency of the data logging from the previously tuned version of the AWAM system data logging software as data fluctuates erratically throughout the first four months of the year 2019. Though physical observation of the slope monitored in the CICT site established that the slope remains intact, the AWAM system continued to log inconsistent data hence the need for recalibration and fine-tune procedures. After recalibration procedures were done on the AWAM4 device, the readings registered ever since were deduced to be stable for a period of several months prior to the decommissioning of the AWAM4 device in August later that year. Though it can be observed that the data of the y and x-axes shifted by a small percentage, it was well within the confinements of the limit set by the AWAM system and did not trigger any alarm for slope instability.

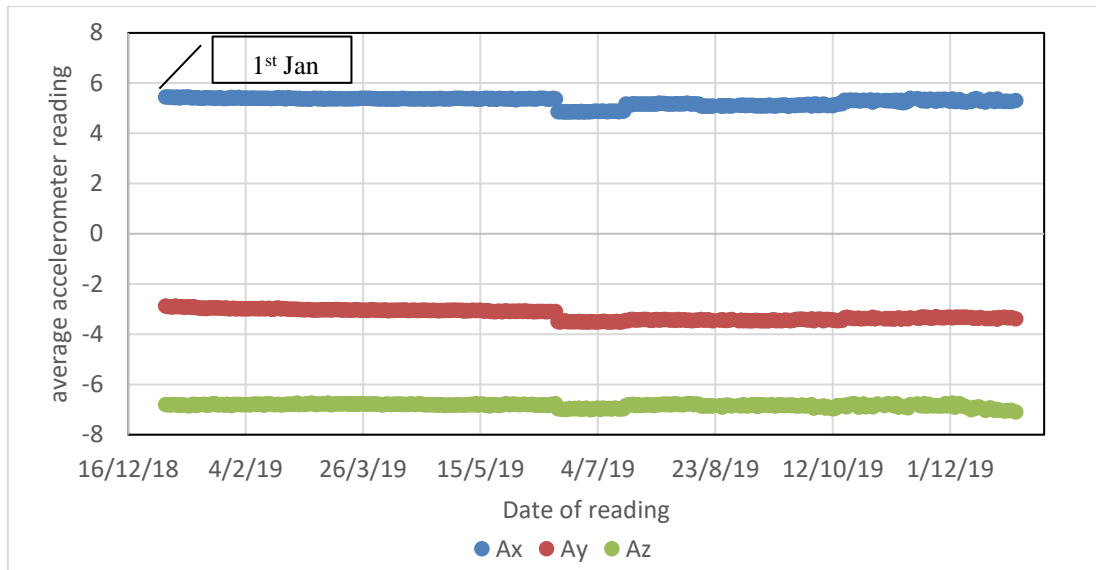


Figure 7.64: AWAM5 device accelerometer readings for the year 2019

Through the entirety of the AWAM system data logging, AWAM5 showed an impressive reading of a completed twelve months of data logging from January 2019 until December 2019 for the CICT site as shown in Figure 7.64. It was observed that the data remained consistent throughout the year until the AWAM5 was decommissioned in December 2019.

7.9 Concluding Remarks

The chapter compiled a complete site work of the Automated Wireless Accelerometer Monitoring (AWAM) system development. The site system envisioned from the laboratory model set onto a more practicable and larger-scale monitoring with guidelines from a collective of previous researches was successfully developed. A thorough and detail component listing for the whole system was documented accordingly throughout subchapter 7.4. A comprehensive assembly of the whole system was thoroughly implemented and later tested for bug fixes before it was ready to be operational on site.

Prior to the installations of the AWAM system on the test site, site selection and several in-situ testing were mobilized on the sites. From the output of the in-situ

testing, a series of numerical modelling was performed to have a better understanding of the overall behaviour and strategic locations for the AWAM system installations. GeoStudio 2012 was utilized in the research particularly using SEEP/W and SLOPE/W limit equilibrium simulations. Pore-water pressure analysis from the initial state until probable slope instability conditions were performed. Probable slope instability was suggested after the SEEP/W simulations projected a layer of slope nearing 0 kPa pore water pressure on the slope surface. Proceeding the pore water pressure simulations, SLOPE/W simulations were utilized to predict the slip failure occurrence on the sites resulting in the factor of safety vs. time simulations. The resulting SLOPE/W simulations would then provide the minimum depth required for the hinged foundation of the AWAM sensor to be installed in each site.

Though preliminary simulations point out that the factor of the proposed site of safety was well above 1.0 value indicating minimal risk of failure, the research opted to proceed with the designated test sites due to restrictions from the timeframe of the research and safety legalities on performing a slope monitoring on a high-risk slope for an untested system. The current focus of the research was to verify the applicability and performance of the AWAM system under real site conditions for a prolonged and minimally maintained system. After several months of slope monitoring on the designated sites, the AWAM system was successfully proven to be operable as envisioned.

Subchapter 7.6 displays the web page navigation of the AWAM system whereby the measurement and warning system notifier resides. Customizable AWAM system locations, numbering, naming, data collection, data frequency and warning triggers were comprehensibly discussed. A closed-circuit privatized slope monitoring was also possible if it is intended by the client, due to the feature of user profile data management as well as the readily available public data interpretation of the awam.my website.

A simple step-by-step installation guide was portrayed in subchapter 7.7 for future AWAM installation procedures, conveniently developed to only require simple hand tools and minimal workforce. Water-proofing procedures were vital in ensuring

the AWAM device would not be affected by the harsh conditions such as heavy rainfall on the site.

Subchapter 7.8 displayed the slope monitoring result for the AWAM system for the entirety of the year 2019. Data was collected solely from the awam.my website with administrative privileges and presented by the 3-axes readings of the accelerometer. Several indications of the system response to artificial alarm triggering movement by the research team were also presented. An added example of the difference between two versions of the system's software was also highlighted in the slope monitoring result from AWAM4 in the CICT site. Finally, it can be concluded that the AWAM system was proven to provide a prolonged duration of slope monitoring data with minimal maintenance in harsh site conditions of the M47 and CICT sites.

The third objective of the research was successfully fulfilled as a measure to assess the performance of the AWAM system in the field. Future endeavours for slope monitoring by the AWAM system would follow the comprehensive guidelines of this chapter such as the preliminary site investigations, system development, site selection, AWAM installations until the report and analysis stage of a specific site monitoring requirements.

CHAPTER 8

SUMMARY, CONCLUSION AND RECOMMENDATIONS

8.1 Summary

Research on the development of a slope monitoring system to predict slope instability using an automated system for the public was reported in the thesis. The system was named Automated Wireless Accelerometer Monitoring system acronymed the AWAM system for short. Ultimately, a system that was tried and tested to provide slope instability warnings optimized for harsh site conditions were the main objectives of the research. In the current chapter, the conclusions of the study were summed up and future recommendations of the study were presented.

As early as the 1960s, researchers have been formulating and devising on systems and devices to study slope instability. Among the many reasons to understand the devastating effects of slope failure is the save lives and properties exposed to the natural phenomenon. Numerous researchers have reported case studies of slope instability using a vast array of surveying techniques such as theodolites and prism, laser monitoring, Global Positioning System, Synthetic Aperture Radar system (SAR), Ground Based Interferometric Synthetic Aperture Radar (GBInSAR) and Automated Robotic Station for slope monitoring (Angeli et al.,2000; Rizzo, 2002; Little, 2006; Herrera et al., 2009; Khan et al., 2010; Fastellini et al., 2011; Blair et al., 1997; Wehr and Lohr, 1999; Jamaluddin and Hussin, 2006; Gili et al., 2000; Malet et al., 2002; Bamler and Hartl, 1998; Berardino et al., 2003; Crosetto et al., 2013; Calo et al.,2014; Jebur et al., 2014; Bozzano et al., 2011; Tarchi et al., 2003; Pierraccini et al., 2003; Bertacchini et al., 2009).

In addition to that, Geotechnical Instrumentation was also widely developed and researched by researchers. Several notable devices such as extensometer, inclinometer and piezometers were used singularly or in tandem with one another

throughout the whole world focused on documenting slope instability (Blair et al., 1997; Ding et al., 2000; Angeli et al., 2000; Fastellini et al., 2011; Herrera et al., 2009; Calo et al., 2014; Little, 2005; Bertacchini et al., 2009; Intrieri et al., 2012). Intrieri et al. (2012) would also then construct a warning level criterion much like a Standard of Operating (SOP) of a system utilizing extensometers to detect tension cracks on an exposed rock slope surface presiding beside a bustling road in Mount Sobasio, Italy. Regarding the warning system, Malet et al. (2002) have forewarned the ability to reliably collect and interpret data for slope instability risk assessment were of the utmost importance in protecting lives and properties in the vicinity of a risky slope. Worth to note the revolutionary innovative concept proven by Dixon et al. (2014), in researching Acoustic Emission (AE) direct relationship with ground displacements using an acoustic sensor planted on slope surfaces. Collectively these researchers have come a long way in providing a safety net for humankind against devastating catastrophe brought by slope failures. The development of the AWAM system in this research was envisioned to provide an extension of alternatives to the current system developed to secure high-risk slopes around the world.

The concept adopted in the AWAM system is the utilization of an accelerometer as a means to measure the motion of a particular slope body. By analyzing the behaviour of movements prior to the failure of a slope, the sensors were connected to a system with the ability to process real-time data that in return would provide early warning slope failure detection. Along with the development of the system, the research was able to compact and attach several other sensors enabling a wider range of slope data logging within the system.

A whole chapter is dedicated as a Standard of Operation (SOP) for future calibrations of the sensors for the AWAM system. Chapter 4 was also constructed to translate the values of the accelerometer readings presented by gravity (g) into slope angle ($^{\circ}$) to assess slope movements in terms of slope angle difference per minute. The value of the slope angle is imperative to quantitatively measure the movement of slope prior to becoming unstable to set the limiting threshold of slope instability.

To achieve a functional, dependable and stable system to monitor slope instability the newly developed system had to be put to the test physically both at the lab and actual field conditions. In addition, numerical studies were established using Particle Image Velocimetry (PIV) procedures and the Geostudios as a means to better understand the mechanics of slope instability and how the system would correspond to the behaviour of the slope during slope instability. In the laboratory-scale testing, a miniaturized AWAM system was tested on a constructed physical model subjected to rainfall imitating the real field conditions. The model was then made to fail all while a variety of systems including the AWAM device, tensiometers and PIV procedures were recording the behaviour of the slope when induced with slope instability process. The laboratory phase of testing conducted with the data collected by the AWAM device provide quantitative criteria of slope instability for slopes constructed within 27° and 45° slope angle and predetermined rainfall intensities. Spikes of the slope movements were detected at 1/2 of the designed load to inflict slope failure for the physical model with a 24-hour duration of rainfall-induced model. In the case of 0 and 1 hour of rainfall simulation on the physical model, the spikes of slope movements were registered at 2/3 of the design load. This proves the pre-cursor movement prior to failure detection ability of the AWAM system were similar to previous researchers in determining the values of designated sensors failure criteria prior to slope instabilities.

As previously mentioned tensiometers were also present for analyzing the effect of rainfall simulation on the physical model. The model was constructed to simulate real site condition and the effects of slope inclination and rainfall intensity on the model's pore water pressure with respect to depth were evidently consistent with previous researchers. To be able to emulate real site conditions were very important in regard to establishing a controlled environment for a slope monitoring system testing.

Besides that, post-processing images from the PIV procedures were successfully interpreted resulting in a clear portrayal of the soil movement and strain development during slope instability. Failure mechanism obtained justifies the efficient placement for the slope monitoring system in the physical model and a prime basis for site installations in the future.

The research proceeds to the numerical modelling stage of the physical model. Transient seepage analysis to construct the Pore Water Pressure (PWP) profile of the model was initially constructed and then the failure mechanism simulation was produced resulting in the Factor of Safety (FOS) overtime analysis. The effects of rainfall intensity and slope inclinations towards the progressive PWP profile and FOS declination overtime was successfully presented. Pre-cursor movement prior to the slope failure detected by the AWAM system was also shown in the FOS vs time analysis, proving a significant gap of the period exist before the failure occurs and would potentially be detected beforehand.

Lastly, the research proceeded to the final stage which is the site trial for slope monitoring. A comprehensive breakdown of the entire system components and data interpretation module was highlighted. Procedures from the physical and numerical model that was applicable to the site trials were replicated and documented as an SOP for future AWAM system installations on site. Simulations for the site condition was deemed essential since it would determine the locality of the slope failure, device installations vicinity and depth as well as the warning trigger value for the early detection of slope instability. Each site was considered unique and in need of a proper preliminary investigation prior to AWAM installations. After a prolonged service of the AWAM system in real site conditions, the data obtained from the 20190 was presented and with it the evidence that the AWAM system was fairly capable in providing a comprehensive slope instability monitoring.

8.2 Conclusion

Three conclusions were drawn after the research concluded with respect to the objectives set upon the research as mentioned in Chapter 1. The conclusions were presented in the following subchapters.

8.2.1 Establishing the AWAM System Mechanics

The AWAM system is a newly developed slope monitoring system to address the need for early warning alarm for slope instability. The automated attribute of the AWAM system depicts the system as a self-sustained device capable of operating without manual data input and with minimal maintenance as the current apparatus available on the market today. In addition, wireless technology was implemented in the system to further implement the innovative feature of the device ever since wireless capabilities of the devices are abundant throughout the years as the expansion of the Internet of Things (IoT). The accelerometer sensing apparatus was used as the main sensor since it can detect movements, vibrations and motion of anybody that is attached to it. Technology advancements have come a long way in miniaturizing movement sensing apparatus. This was vital in the vision to improve slope monitoring systems readily available in the current market.

In order to materialize said vision, the system would have to be put to the test comprehensively and analyzed for its effectiveness. After assembly, it was decided the system would have to be tested methodologically through several stages of laboratory testing. First, the calibration procedure of the system was established. The standard output of the accelerometer used needs to be interpreted to provide information relevant to detect slope movement. After calibration procedures concluded, the device was researched to only provide reading when moving in a tilting position. That said, the anchorage system was introduced to the device whereby a single axis was fixed to the ground while the other two was made to move freely in a tilting manner. In addition, the readings were quantified to provide slope angle difference reading analysis as an interpretation of the slope body movement.

Subsequently, after the calibration procedure, the system needs to be tested in a controlled lab ambience while the system capabilities are justified. A small-scale model of the conditions on site was established and made to fail artificially for the system to detect. Upon completion of the physical model, the researchers concluded that the AWAM system was capable of detecting the pre-cursor movement prior to slope instability. For the range of 27° to 45° of slope angle with rainfall variation of 0,

1 and 24 hours; the AWAM system was determined to detect a huge spike of slope angle over time increase before the slope model undergone instability. For the heavy rainfall simulation of 24 hours; at approximately 1/2 of the loading failure value, the device registered a spike of reading fluctuations while for the light rainfall simulation, the spike of readings was registered during 2/3 of the design load.

The laboratory model was also subjected to several additional data logging procedures such as tensiometers to measure pore water pressure profile and PIV techniques to quantify slope deformation. Both supporting data procedures were proved to validate the slope instability subjected to the model. Proceeding physical model simulations, numerical analysis using the Geostudio software was performed resulting in further validation for the pre-cursor movement prior to slope instability detection by the AWAM system.

8.2.2 Failure Signal Determination for Early Warning Detection

The AWAM device was distinguished to be capable of detecting pre-cursor movement prior to slope instability. For the purpose of providing reliable warning indications prior to the slope failure, a degree of slope change per minute analysis was developed to interpret the trigger limit that would produce an alarm for the user of the slope monitoring system. For the slope angle ranging from 27° to 45° with the simulated dry to heavy rainfall intensity modelling, the AWAM device was concluded to provide a significant reading of slope movement detection prior to slope instability as all six physical models registered spikes of slope degree change per minute in the AWAM result analysis.

In addition, the orientation of movements in the sense of clockwise or counterclockwise of the sensor was determined based on the increment or decrement of the values x and z axes.

8.2.3 Field Testing of AWAM System

The compact size of a particular AWAM unit for site installation was emphasized in the AWAM site installation section of the thesis. The device was shown to be lightweight and easy to install with simple hand tools such that it is possible for a minimal workforce installation job. The performance of the AWAM system on real site conditions was justified to provide continuous, reliable and stable readings for each of the devices installed in the vicinity of the trial sites. Apart from the artificial alarm trigger by the research, the AWAM system proceeded to be operational with minimal maintenance under harsh site conditions for the duration of approximately a year. Moreover, the complete data logging for the presented accelerometer readings throughout the year 2019 was entirely accessed through the cloud database housing of the awam.my website. These features strengthen the standard set upon the AWAM system to provide a dependable, safe and secured slope monitoring service.

8.3 Recommendation for Future Study

The recommendation part of the research is to address future improvements to the study in developing a more advance and sophisticated slope monitoring system, and was subsequently listed in the following points:

- (a) **A system of slope movement detection using triple-axis accelerometer.** A triple-axis accelerometer would offer an easier mode of installation, without any anchorage of the sensor to the ground model. This method of slope movement sensing would require 3 dimensional physical and numerical simulations and an intricate calibration procedure.
- (b) **A system with advance and compact microcontroller governing the slope monitoring system.** Future advancements in the microcontroller industry would offer a substantial upgrade to the existing system such as a more compact and sturdy design capable of withstanding the test of time for future systems.

- (c) **Finite element analysis on the slope failure.** Finite Element Analysis can be opted to assess the failure mechanism of the slope model to provide an advance stress calculation and tackle far more complex problems.
- (d) **Slope model compositions, parameters and scale.** Further experimentation of the physical and numerical model of the slope should be carried out using a variety of other soil compositions. The scale and parameters of the physical model could also be bigger and wider, respectively.

REFERENCES

- Abdel-Aziz, Y., & Karara, H. (1974). Accuracy aspects of non-metric imageries.
- Achache, J., Fruneau, B., & Delacourt, C. (1996). *Applicability of SAR interferometry for monitoring of landslides*. Paper presented at the ERS Applications.
- Adrian, R. J. (1991). Particle-imaging techniques for experimental fluid mechanics. *Annual review of fluid mechanics*, 23(1), 261-304.
- Advance Land Observing Satellite (ALOS). (1997). About ALOS-PALSAR. Retrieved 23 Feb, 2019, from <https://www.eorc.jaxa.jp/ALOS/en/about/palsar.htm>
- Ahmad, F., Kazmi, S. F., & Pervez, T. (2011). Human response to hydro-meteorological disasters: A case study of the 2010 flash floods in Pakistan. *Journal of Geography and Regional Planning*, 4(9), 518.
- Angeli, M.-G., Pasuto, A., & Silvano, S. (2000). A critical review of landslide monitoring experiences. *Engineering Geology*, 55(3), 133-147.
- Antonello, G., Casagli, N., Farina, P., Leva, D., Nico, G., Sieber, A., & Tarchi, D. (2004). Ground-based SAR interferometry for monitoring mass movements. *Landslides*, 1(1), 21-28.
- Atzeni, C., Barla, M., Pieraccini, M., & Antolini, F. (2015). Early warning monitoring of natural and engineered slopes with ground-based synthetic-aperture radar. *Rock Mechanics and Rock Engineering*, 48(1), 235-246.
- Bamler, R., & Hartl, P. (1998). Synthetic aperture radar interferometry. *Inverse problems*, 14(4), R1.
- Bardi, F., Raspini, F., Frodella, W., Lombardi, L., Nocentini, M., Gigli, G., . . . Casagli, N. (2017). Monitoring the rapid-moving reactivation of Earth flows by means of GB-InSAR: the April 2013 Capriglio Landslide (Northern Appennines, Italy). *Remote Sensing*, 9(2), 165.
- Berardino, P., Costantini, M., Franceschetti, G., Iodice, A., Pietranera, L., & Rizzo, V. (2003). Use of differential SAR interferometry in monitoring and modelling large slope instability at Maratea (Basilicata, Italy). *Engineering Geology*, 68(1-2), 31-51.

- Berardino, P., Fornaro, G., Lanari, R., & Sansosti, E. (2002). A new algorithm for surface deformation monitoring based on small baseline differential SAR interferograms. *IEEE Transactions on Geoscience and Remote Sensing*, 40(11), 2375-2383.
- Bertacchini, E., Capitani, A., Capra, A., Castagnetti, C., Corsini, A., Dubbini, M., & Ronchetti, F. (2009). *Integrated surveying system for landslide monitoring, Valoria landslide (Appennines of Modena, Italy)*. Paper presented at the FIG Working Week 2009-Surveyors Key Role in Accelerated Development.
- Blair, S., Sweider, D., Trettenero, S., & Boro, C. (1997). A new reflective optical extensometer (ROX) system for geomechanical deformation measurements. *International Journal of Rock Mechanics and Mining Sciences*, 34(3-4), 29. e21-29. e26.
- Blume, F. (2014). UNAVCO Resources: GNSS Receivers. Retrieved 2019, 25 Feb, from <https://kb.unavco.org/kb/article.php?id=434>
- Boldyrev, G., Melnikov, A., & Barvashov, V. (2012). *Particle image velocimetry and numeric analysis of sand deformations under a test plate*. Paper presented at the The 5th European Geosynthetics Congress.
- Borgatti, L., Corsini, A., Barbieri, M., Sartini, G., Truffelli, G., Caputo, G., & Puglisi, C. (2006). Large reactivated landslides in weak rock masses: a case study from the Northern Apennines (Italy). *Landslides*, 3(2), 115.
- Bozzano, F., Mazzanti, P., Prestininzi, A., & Mugnozza, G. S. (2010). Research and development of advanced technologies for landslide hazard analysis in Italy. *Landslides*, 7(3), 381-385.
- Bunawan, A. R., Mahin, M. A. H., Hezmi, M. A., Kassim, A., & Rashid, A. S. A. (2016). DEVELOPMENT OF SLOPE MONITORING DEVICE USING ACCELEROMETER. *Jurnal Teknologi*, 78(8-5).
- Calò, F., Ardizzone, F., Castaldo, R., Lollino, P., Tizzani, P., Guzzetti, F., . . . Manunta, M. (2014). Enhanced landslide investigations through advanced DInSAR techniques: The Ivancich case study, Assisi, Italy. *Remote Sensing of Environment*, 142, 69-82.
- Carlà, T., Farina, P., Intrieri, E., Botsialas, K., & Casagli, N. (2017). On the monitoring and early-warning of brittle slope failures in hard rock masses: Examples from an open-pit mine. *Engineering Geology*, 228, 71-81.

- Carnec, C., Massonnet, D., & King, C. (1996). Two examples of the use of SAR interferometry on displacement fields of small spatial extent. *Geophysical research letters*, 23(24), 3579-3582.
- Casagli, N., Frodella, W., Morelli, S., Tofani, V., Ciampalini, A., Intrieri, E., Raspini, F., Rossi, F., Tanteri, L., Lu, P. (2017). Spaceborne, UAV and ground-based remote sensing techniques for landslide mapping, monitoring and early warning. *Geoenvironmental Disasters*, 4(1), 9.
- Chowdhury, R., Flentje, P., & Bhattacharya, G. (2009). *Geotechnical slope analysis*: Crc Press.
- Codeglia, D., Dixon, N., Fowmes, G. J., & Marcato, G. (2017). Analysis of acoustic emission patterns for monitoring of rock slope deformation mechanisms. *Engineering Geology*, 219, 21-31.
- Costantini, M., & Rosen, P. A. (1999). *A generalized phase unwrapping approach for sparse data*. Paper presented at the IEEE 1999 International Geoscience and Remote Sensing Symposium. IGARSS'99 (Cat. No. 99CH36293).
- Crosetto, M., Gili, J., Monserrat, O., Cuevas-González, M., Corominas, J., & Serral, D. (2013). Interferometric SAR monitoring of the Vallcebre landslide (Spain) using corner reflectors. *Natural Hazards and Earth System Sciences*, 13(4), 923-933.
- Dick, G. J., Eberhardt, E., Cabrejo-Liévano, A. G., Stead, D., & Rose, N. D. (2014). Development of an early-warning time-of-failure analysis methodology for open-pit mine slopes utilizing ground-based slope stability radar monitoring data. *Canadian Geotechnical Journal*, 52(4), 515-529.
- Ding, X., Ren, D., Montgomery, B., & Swindells, C. (2000). Automatic monitoring of slope deformations using geotechnical instruments. *Journal of Surveying Engineering*, 126(2), 57-68.
- Dixon, N., Moore, R., Spriggs, M., Smith, A., Meldrum, P., & Siddle, R. (2015). Performance of an acoustic emission monitoring system to detect subsurface ground movement at Flat Cliffs, North Yorkshire, UK *Engineering Geology for Society and Territory-Volume 2* (pp. 117-120): Springer.
- Eaton, T. T. (2006). On the importance of geological heterogeneity for flow simulation. *Sedimentary Geology*, 184(3-4), 187-201.

- Fastellini, G., Radicioni, F., & Stoppini, A. (2011). The Assisi landslide monitoring: a multi-year activity based on geomatic techniques. *Applied Geomatics*, 3(2), 91-100.
- Franceschetti, G., & Lanari, R. (1999). *Synthetic aperture radar processing*: CRC press.
- Franceschetti, G., & Lanari, R. (2018). *Synthetic aperture radar processing*: CRC press.
- Ganiyu, A. A. (2016). *INFLUENCE OF AXIALLY LOADED SHAPED PILE ON GEOTECHNICAL CAPACITY*. (Doctoral dissertation), Universiti Teknologi Malaysia, Johor, Malaysia.
- Gili, J. A., Corominas, J., & Rius, J. (2000). Using Global Positioning System techniques in landslide monitoring. *Engineering Geology*, 55(3), 167-192.
- Gofar, N., Lee, M., & Kassim, A. (2008). Response of suction distribution to rainfall infiltration in soil slope. *Electronic Journal of Geotechnical Engineering, EJGE*, 13(E), 1-13.
- Gue, S.-S., & Tan, Y.-C. (2006). Landslides: Abuses of the Prescriptive Method.
- Guerricchio, A., Melidoro, G., & Rizzo, V. (1988). *Instrumental observations of the slope deformations and deep phenomena in Maratea Valley (Italy)*. Paper presented at the Landslides–Glissements de terrains, Proc. 5th Int. Symp. on Landslides, edited by Christophe, B., AA Balkema Publishers.
- Harun, M. (2019). *STABILITY ANALYSIS FOR SLOPE REHABILITATION WORKS AT KM424.80 SOUTH BOUND, NORTH SOUTH EXPRESSWAY*. (Master's thesis), Universiti Teknologi Malaysia, Johor, Malaysia. Retrieved from <http://dms.library.utm.my:8080/vital/access/manager/Repository/vital:125182>
- Heikkila, J., & Silven, O. (1997). *A four-step camera calibration procedure with implicit image correction*. Paper presented at the Proceedings of IEEE computer society conference on computer vision and pattern recognition.
- Herrera, G., Fernández-Merodo, J., Mulas, J., Pastor, M., Luzi, G., & Monserrat, O. (2009). A landslide forecasting model using ground based SAR data: The Portalet case study. *Engineering Geology*, 105(3-4), 220-230.
- Hug, C., & Wehr, A. (1997). Detecting and identifying topographic objects in imaging laser altimeter data. *International archives of photogrammetry and remote sensing*, 32(3 SECT 4W2), 19-26.

- Hutt, C. R., Evans, J. R., Followill, F., Nigbor, R. L., & Wielandt, E. (2009). Guidelines for standardized testing of broadband seismometers and accelerometers. *US Geol. Surv. Open-File Rept, 1295*, 62.
- Intrieri, E., Gigli, G., Mugnai, F., Fanti, R., & Casagli, N. (2012). Design and implementation of a landslide early warning system. *Engineering Geology, 147*, 124-136.
- Iskander, M. G., Liu, J., & Sadek, S. (2002). Transparent amorphous silica to model clay. *Journal of Geotechnical and Geoenvironmental Engineering, 128*(3), 262-273.
- Jamaludin, S., & Hussein, A. N. (2006). Landslide hazard and risk assessment: The Malaysian experience. *Notes*.
- Jebur, M. N., Pradhan, B., & Tehrany, M. S. (2014). Detection of vertical slope movement in highly vegetated tropical area of Gunung pass landslide, Malaysia, using L-band InSAR technique. *Geosciences Journal, 18*(1), 61-68.
- Kalatehjari, R., Arefnia, A., A Rashid, A. S., Ali, N., & Hajihassani, M. (2015). Determination of three-dimensional shape of failure in soil slopes. *Canadian Geotechnical Journal, 52*(9), 1283-1301.
- Kassim, A. (2011). *MODELLING THE EFFECT OF HETEROGENEITIES ON SUCTION DISTRIBUTION BEHAVIOUR IN TROPICAL RESIDUAL SOIL*. (Doctoral dissertation), Universiti Teknologi Malaysia, Johor, Malaysia.
- Khan, Y. A., Lateha, H., Jerfriza, A., & Muhiyuddin, B. (2010). Monitoring of hill-slope movement due to rainfall at Gunung Pass of Cameron Highland district of Peninsular Malaysia. *International Journal of Earth Sciences and Engineering, 3*, 06-12.
- Khatami, H., Deng, A., & Jaksa, M. (2019). An experimental study of the active arching effect in soil using the digital image correlation technique. *Computers and Geotechnics, 108*, 183-196.
- Kristo, C., Rahardjo, H., & Satyanaga, A. (2017). Effect of variations in rainfall intensity on slope stability in Singapore. *International soil and water conservation research, 5*(4), 258-264.
- Kumar, A., & Rathee, R. (2017). Monitoring and evaluating of slope stability for setting out of critical limit at slope stability radar. *International Journal of Geo-Engineering, 8*(1), 18.

- Lacasse, S., & Nadim, F. (2009). Landslide risk assessment and mitigation strategy *Landslides—disaster risk reduction* (pp. 31-61): Springer.
- Lee, L. M., Gofar, N., & Rahardjo, H. (2009). A simple model for preliminary evaluation of rainfall-induced slope instability. *Engineering Geology*, 108(3-4), 272-285.
- Lee, S.-R., Oh, T.-K., Kim, Y.-K., & Kim, H.-C. (2009). Influence of rainfall intensity and saturated permeability on slope stability during rainfall infiltration. *Journal of the Korean Geotechnical Society*, 25(1), 65-76.
- Little, M. (2006). *Slope monitoring strategy at PPRust open pit operation*. Paper presented at the Proceedings of the international symposium on stability of rock slopes in open pit mining and civil engineering.
- Liu, J., & Iskander, M. (2004). Adaptive cross correlation for imaging displacements in soils. *Journal of computing in civil engineering*, 18(1), 46-57.
- Long, J. C., Gilmour, P., & Witherspoon, P. A. (1985). A model for steady fluid flow in random three-dimensional networks of disc-shaped fractures. *Water Resources Research*, 21(8), 1105-1115.
- Malet, J.-P., Maquaire, O., & Calais, E. (2002). The use of Global Positioning System techniques for the continuous monitoring of landslides: application to the Super-Sauze earthflow (Alpes-de-Haute-Provence, France). *Geomorphology*, 43(1-2), 33-54.
- Mametja, T., & Zvarivadza, T. (2017). *Slope stability enhancement through slope monitoring data interpretation*. Paper presented at the 51st US Rock Mechanics/Geomechanics Symposium.
- Medina-Cetina, Z., & Nadim, F. (2008). Stochastic design of an early warning system. *Georisk*, 2(4), 223-236.
- Megawati, K., Pan, T.-C., & Koketsu, K. (2005). Response spectral attenuation relationships for Sumatran-subduction earthquakes and the seismic hazard implications to Singapore and Kuala Lumpur. *Soil Dynamics and Earthquake Engineering*, 25(1), 11-25.
- Ni, Q., Hird, C., & Guymer, I. (2010). Physical modelling of pile penetration in clay using transparent soil and particle image velocimetry. *Géotechnique*, 60(2), 121.
- NOAA. (2018). facts/lidar. Retrieved 23 Feb, 2019, from <https://oceanservice.noaa.gov/facts/lidar.html>

- Oh, S., & Lu, N. (2015). Slope stability analysis under unsaturated conditions: Case studies of rainfall-induced failure of cut slopes. *Engineering Geology*, *184*, 96-103.
- Pieraccini, M., Casagli, N., Luzi, G., Tarchi, D., Mecatti, D., Noferini, L., & Atzeni, C. (2003). Landslide monitoring by ground-based radar interferometry: a field test in Valdarno (Italy). *International Journal of Remote Sensing*, *24*(6), 1385-1391.
- Pieraccini, M., Luzi, G., & Atzeni, C. (2001). Terrain mapping by ground-based interferometric radar. *IEEE Transactions on Geoscience and Remote Sensing*, *39*(10), 2176-2181.
- Rahardjo, H., Li, X., Toll, D. G., & Leong, E. C. (2001). The effect of antecedent rainfall on slope stability *Unsaturated Soil Concepts and Their Application in Geotechnical Practice* (pp. 371-399): Springer.
- Rahardjo, H., Rezaur, R., Hritzuk, K., & Leong, E. (2005). Slope failures in Singapore: Case study of two landslides. *Nanyang Technological University, Singapore*, 59-70.
- Rahardjo, H., Satyanaga, A., & Leong, E.-C. (2013). Effects of flux boundary conditions on pore-water pressure distribution in slope. *Engineering Geology*, *165*, 133-142.
- Ravi, N., Dandekar, N., Mysore, P., & Littman, M. L. (2005). *Activity recognition from accelerometer data*. Paper presented at the Aaai.
- Reilly, P. A., Ashland, F. X., & Fiore, A. R. (2017). Landslide monitoring in the Atlantic Highlands area, New Jersey *Fact Sheet*. Reston, VA.
- Rizzo, V. (1997). Processi morfodinamici e movimenti del suolo nella Valle di Maratea (Basilicata). *Geografia Fisica e Dinamica Quaternaria*, *20*, 119-136.
- Rizzo, V. (2002). GPS monitoring and new data on slope movements in the Maratea Valley (Potenza, Basilicata). *Physics and Chemistry of the Earth, Parts A/B/C*, *27*(36), 1535-1544.
- Ronchetti, F., Borgatti, L., Cervi, F., Lucente, C., Veneziano, M., & Corsini, A. (2007). The Valoria landslide reactivation in 2005–2006 (Northern Apennines, Italy). *Landslides*, *4*(2), 189.
- Rosen, P. A., Hensley, S., Joughin, I. R., Li, F., Madsen, S. N., Rodriguez, E., & Goldstein, R. M. (1998). Synthetic aperture radar interferometry.

- Sagaseta, C., Whittle, A., & Santagata, M. (1997). Deformation analysis of shallow penetration in clay. *International journal for numerical and analytical methods in geomechanics*, 21(10), 687-719.
- Sew, G., & Chin, T. (2006). Landslides: Case Histories, Lessons Learned And Mitigation Measures. *Landslide, Sinkhole, Structure Failure: MYTH or SCIENCE*.
- Simms, P. H., & Yanful, E. K. (2004). Estimation of soil–water characteristic curve of clayey till using measured pore-size distributions. *Journal of Environmental Engineering*, 130(8), 847-854.
- Sinarta, I. N., Rifa'i, A., Fathani, T. F., & Wilopo, W. (2017). LANDSLIDE HAZARDS DUE TO RAINFALL INTENSITY IN THE CALDERA OF MOUNT BATUR BALI. *Wuicace*, 2018, 160-167.
- Smith, A., Dixon, N., Codeglia, D., & Fowmes, G. J. (2016). An acoustic emission slope displacement rate sensor: Comparisons with established instrumentation.
- Smith, A., Dixon, N., & Fowmes, G. J. (2017). Early detection of first-time slope failures using acoustic emission measurements: large-scale physical modelling.
- Smith, A., Dixon, N., Meldrum, P., Haslam, E., & Chambers, J. (2014). Acoustic emission monitoring of a soil slope: Comparisons with continuous deformation measurements. *Géotechnique Letters*, 4(4), 255-261.
- Smith, J. B., Baum, R. L., Mirus, B. B., Michel, A. R., & Stark, B. (2017). Results of hydrologic monitoring on landslide-prone coastal bluffs near Mukilteo, Washington *Open-File Report* (pp. 60). Reston, VA.
- Taha, M. R. (2011). Effectiveness of horizontal drains in improving slope stability: a case study of landslide event in Putra Jaya Precinct 9, Malaysia.
- Take, W. A. (2003). *The influence of seasonal moisture cycles on clay slopes*. University of Cambridge.
- Tarchi, D., Casagli, N., Fanti, R., Leva, D. D., Luzi, G., Pasuto, A., . . . Silvano, S. (2003). Landslide monitoring by using ground-based SAR interferometry: an example of application to the Tessina landslide in Italy. *Engineering Geology*, 68(1-2), 15-30.
- Taylor-Smith, K. (2019). What is a LIDAR Sensor? Retrieved 23 Feb, 2019, from <https://www.azosensors.com/article.aspx?ArticleID=1110>

- Tsaparas, I., Rahardjo, H., Toll, D. G., & Leong, E. C. (2002). Controlling parameters for rainfall-induced landslides. *Computers and Geotechnics*, 29(1), 1-27.
- Wehr, A., & Lohr, U. (1999). Airborne laser scanning—an introduction and overview. *ISPRS Journal of photogrammetry and remote sensing*, 54(2-3), 68-82.
- White, D., Take, W., & Bolton, M. (2003). Soil deformation measurement using particle image velocimetry (PIV) and photogrammetry. *Géotechnique*, 53(7), 619-631.
- Yan, G., Xu, Y., Murgana, V., & Scheuermann, A. (2018). *Application of Image Analysis on Two-Dimensional Experiment of Ground Displacement Under Strip Footing*. Paper presented at the GeoShanghai International Conference.
- Yang, H., Rahardjo, H., Leong, E.-C., & Fredlund, D. G. (2004). Factors affecting drying and wetting soil-water characteristic curves of sandy soils. *Canadian Geotechnical Journal*, 41(5), 908-920.
- Yeh, H.-F., & Tsai, Y.-J. (2018). Effect of variations in long-duration rainfall intensity on unsaturated slope stability. *Water*, 10(4), 479.
- Yeh, H.-F., Wang, J., Shen, K.-L., & Lee, C.-H. (2015). Rainfall characteristics for anisotropic conductivity of unsaturated soil slopes. *Environmental earth sciences*, 73(12), 8669-8681.
- Yusof, M., Khalid, M., Ahmad Tajudin, S. A., Madun, A., & Zainal Abidin, M. H. (2017). Correlation of JKR Probe with Undrained Shear Strength. *MATEC Web of Conferences*, 103, 07009. doi: 10.1051/matecconf/201710307009
- Zebker, H. A., Rosen, P. A., Goldstein, R. M., Gabriel, A., & Werner, C. L. (1994). On the derivation of coseismic displacement fields using differential radar interferometry: The Landers earthquake. *Journal of Geophysical Research*, 99(B10), 19617-19634.

Appendix A Calibration of Instrumentation

Load Cell

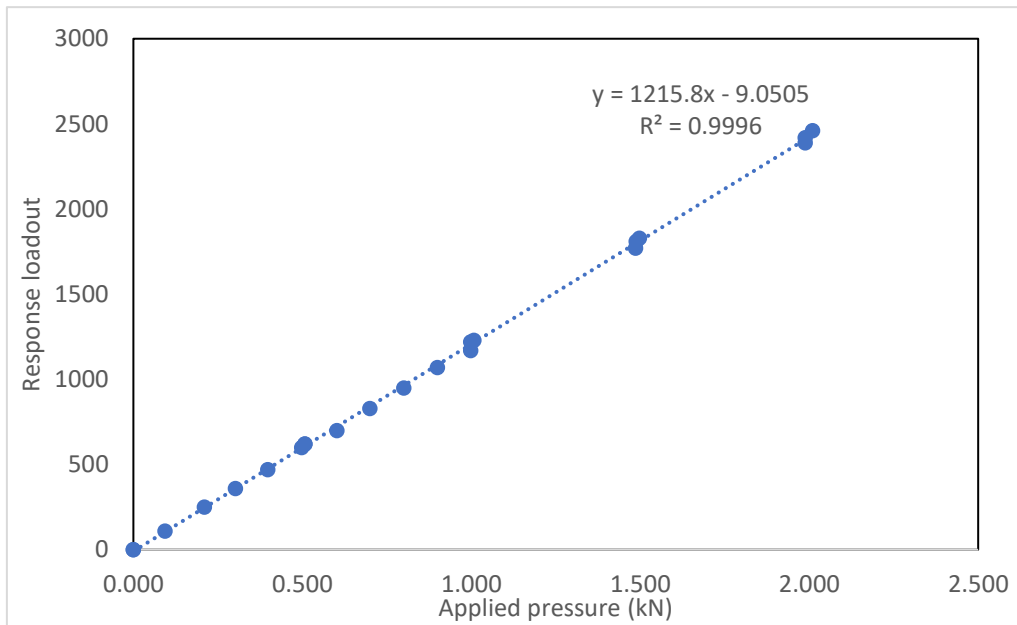


Figure 1: Load cell calibrations

LVDT

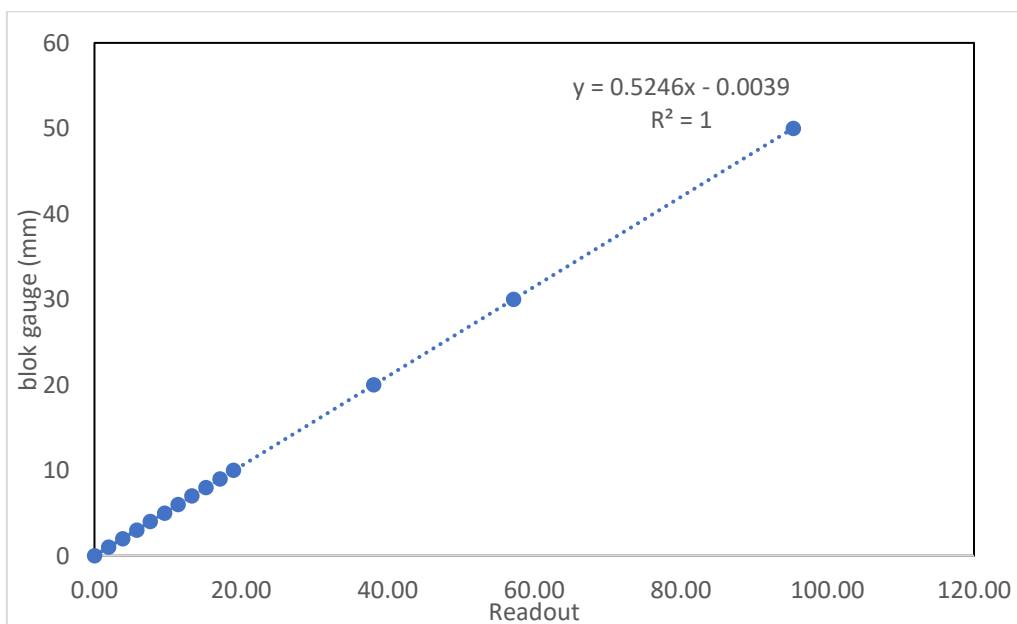


Figure 2: LVDT calibrations

Appendix B MatLab Program for PIV

```

C:\Users\User\alip\piv4\test1\regimlistgen.m
% this file serves as a image list generator.

clear;

imgbegin=input('image start number?')      % begin of image list
imgend=input('image end number?')          % end of image list
step=input('step?')                        % step

fid=fopen('registered_propics_list.txt', 'w');

for i=imgbegin:step:imgend
    k=num2str(i, '%04.0f')
    kk=strcat('DSC_',k, '.jpg')
    fprintf(fid, '%s\n',kk)
end
fclose(fid)
-----
C:\Users\User\alip\piv4\test1\led_launcher
%GeoPIV7 LAUNCHFILE, April 2002, Dave White & Andy Take
%project: Sheffield demo
%task:

%[MESH TO LOAD]
MESH_example3.txt 0                      %filename of initial mesh

%[PIV ANALYSIS]
searchzonepixels 5 %PIV search zone, smax. (<max disp).

show_mesh 1                               %Show PIV mesh during analysis.
show_patch 1                               %Show each PIV patch during analysis.
show_quiver 1                              %Show quiver plot during analysis.
show_vector 1                              %Print vector magnitude during
analysis.

spare_A 0                                  %Spare. For future use.
spare_B 0                                  %Spare. For future use.
spare_C 0                                  %Spare. For future use.
spare_D 0                                  %Spare. For future use.
spare_E 0                                  %Spare. For future use.

C:\Users\User\alip\piv4\test1 %Location of image files

leapfrog 1                                 %Leapfrog flag

subpixelmeth 1                             %FFT on/off boolean

%[IMAGES]

DSC_0966.jpg
DSC_0967.jpg
DSC_0968.jpg
DSC_0969.jpg
DSC_0970.jpg
DSC_0971.jpg
DSC_0972.jpg
DSC_0973.jpg

```

DSC_0974.jpg
 DSC_0975.jpg
 DSC_0976.jpg
 DSC_0977.jpg
 DSC_0978.jpg
 DSC_0979.jpg
 DSC_0980.jpg
 DSC_0981.jpg
 DSC_0982.jpg
 DSC_0983.jpg
 DSC_0984.jpg
 DSC_0985.jpg
 DSC_0986.jpg
 DSC_0987.jpg
 DSC_0988.jpg
 DSC_0989.jpg
 DSC_0990.jpg
 DSC_0991.jpg
 DSC_0992.jpg
 DSC_0993.jpg
 DSC_0994.jpg
 DSC_0995.jpg
 DSC_0996.jpg
 DSC_0997.jpg
 DSC_0998.jpg
 DSC_0999.jpg
 DSC_1000.jpg
 DSC_1001.jpg
 DSC_1002.jpg
 DSC_1003.jpg
 DSC_1004.jpg
 DSC_1005.jpg
 DSC_1006.jpg
 DSC_1007.jpg
 DSC_1008.jpg
 DSC_1009.jpg
 DSC_1010.jpg
 DSC_1011.jpg
 DSC_1012.jpg
 DSC_1013.jpg
 DSC_1014.jpg

```
-----
C:\Users\User\alip\piv4\test1\fmeshing.m
function fmeshing(filename,meshfile,size)
%function fmeshing(filename,meshfile,size); size of meshes
im=imread(strcat(filename, '.jpg'));
imagesc(im);axis image;
[x,y]=ginput;
xi=x(1,1); xf=x(2,1);
yi=y(1,1); yf=y(2,1);
Lx=xf-xi; Ly=yf-yi;
nx=ceil(Lx/size); ny=ceil(Ly/size);
meshfileout=strcat('mesh',meshfile, '.txt')
fid=fopen(meshfileout, 'w');
fprintf(fid, '%patch    uo  vo  uf  vf  du  dv  size  desc\n');
patch=0;
uo=0;
vo=0;
du=0;
dv=0;
desc=0;
```

```

for c=1:nx,
    for r=1:ny,
        patch=patch+1;
        x(r,c)=xi-size/2+c*size;
        y(r,c)=yi-size/2+r*size;
        fprintf(fid,'%4g %9.2f %9.2f %9.2f %9.2f %9.2f %9.2f %9.2f
%9.2f\n', patch,uo,vo, x(r,c), y(r,c),du,dv,size,desc);
    end
end
end
fclose(fid);
%data1=load(meshfileout);
%data2=load('cptargets.txt');
%data=cat(1,data1,data2)
%dlmwrite(strcat('mesh',meshfile,'.tgt'),data,'\t')
imagesc(im);axis image
hold on
plot(x,y,'+y');axis ij
hold off

```

C:\Users\User\alip\piv4\test1\targetmarker\XYCoordinate

%No	X	Y
1	0.0000	0.0000
2	40.0000	0.0000
3	80.0000	0.0000
4	120.0000	0.0000
5	160.0000	0.0000
6	200.0000	0.0000
7	240.0000	0.0000
8	0.0000	40.0000
9	40.0000	40.0000
10	80.0000	40.0000
11	120.0000	40.0000
12	160.0000	40.0000
13	200.0000	40.0000
14	240.0000	40.0000
15	0.0000	80.0000
16	40.0000	80.0000
17	80.0000	80.0000
18	120.0000	80.0000
19	160.0000	80.0000
20	200.0000	80.0000
21	240.0000	80.0000
22	0.0000	120.0000
23	40.0000	120.0000
24	80.0000	120.0000
25	120.0000	120.0000
26	160.0000	120.0000
27	200.0000	120.0000
28	240.0000	120.0000
29	0.0000	160.0000
30	40.0000	160.0000
31	80.0000	160.0000
32	120.0000	160.0000
33	160.0000	160.0000
34	200.0000	160.0000
35	240.0000	160.0000
36	0.0000	200.0000
37	40.0000	200.0000
38	80.0000	200.0000
39	120.0000	200.0000
40	160.0000	200.0000

```

41         200.0000      200.0000
42         240.0000      200.0000
43          0.0000      240.0000
44         40.0000      240.0000
45         80.0000      240.0000
46        120.0000      240.0000
47        160.0000      240.0000
48        200.0000      240.0000
49        240.0000      240.0000
-----
C:\Users\User\alip\piv4\test1\consolidate8.m
function patchpositions=consolidate8

% Post-PIV assembly of patch trajectories.
% GeoPIV8 creates text files PIV_imagename1_imagename2.txt
% consolidate8.m draws in these files and constructs a matrix of u,v
coordinate movement through time
% This version can assemble data from PIV runs in which the leapfrog
flag has been used
% Dave White

%LOAD IMAGE LIST
[filename,pathname]=uigetfile('*.txt','Open launch file (.txt
format)');
cd (pathname);

%imagefilenames=textread(filename,'%q');
%[numberofimages,pointlessvariable]=size(imagefilenames)
[s_launch
f_launch]=textread(filename,'%s%f','commentstyle','matlab');
[numberofimages,pointlessvariable]=size(s_launch);
numberofimages=numberofimages-14;
imagefilenames=s_launch(15:(numberofimages+14));
leapfrog=f_launch(13); %leapfrog flag. Number of images between
updates of initial image.

sequence=1;
leapfrogprogress=leapfrog-1;
%LOAD SEQUENCE OF PATCH POSITIONS
for currentimagenumber=1:sequence:(numberofimages-sequence);

    leapfrogprogress=leapfrogprogress+sequence;

    if (leapfrogprogress-leapfrog)>=0
% do update image 1: draw in new filename1
        filename1=char(imagefilenames(currentimagenumber));
        leapfrogprogress=sequence-1;
    else
% don't update image 1
    end

        filename2=char(imagefilenames(currentimagenumber+sequence));

        piv_outfile = strcat('PIV_',filename1(1:length(filename1)-
4), '_',filename2(1:length(filename2)-4), '.txt')
        piv_data=load(piv_outfile);

        if currentimagenumber==1
            %pull in patch numbers and u coordinates
            patchpositions(:, :, 1)=piv_data(:, 1:2);
            %pull in patch numbers and v coordinates

```

```

patchpositions(:,1:3,2)=piv_data(:,1:3);
patchpositions(:,2,2)=patchpositions(:,3,2);
%pull in u coordinates of 2nd image
patchpositions(:,3,1)=piv_data(:,4);
%pull in v coordinates of 2nd image
patchpositions(:,3,2)=piv_data(:,5);

else

    currentimagenumber;
    a=((currentimagenumber-1)/sequence)+2;
    %pull in u coordinates
    patchpositions(:,(currentimagenumber-
1)/sequence)+3,1)=piv_data(:,4);
    %pull in v coordinates
    patchpositions(:,(currentimagenumber-
1)/sequence)+3,2)=piv_data(:,5);

end

end

-----
C:\Users\User\alip\piv4\test1\targetmarker\LEDcentroiding.m
function LEDcentroiding(filename)
%filename (in string 'qoute') is the name of the image file without
extension (e.g. 'JPG',
%'TIF')
im=imread(strcat(filename, '.JPG'));
imgray=rgb2gray(im);

n=25; % initial cropping area

cp=load(strcat('mesh',filename, '.txt')); % loading estimated
centroids
%cp=load('cpRefraction_01.txt'); % loading estimated centroids
x=cp(:,4);
y=cp(:,5);
cp=[x y];

fid=fopen(strcat('tg',filename, '.txt'),'w'); % preparing to write
the file of resulting centroids

itarget=length(x);

for i=1:itarget

y(i)=floor(y(i));
x(i)=floor(x(i));
impat0=im((y(i)-n):(y(i)+n),(x(i)-n):(x(i)+n));
impatgray=impat0;
impat0dbl=double(impat0);

[imconvpatch, ttop, tbottom]=fG(impat0);
%function of convolution the target, for smoothing the noise on the
top and the bottom of the target .

t=ttop*(1-.10); %initial threshold taken 10% from top.

[xc(i), yc(i)]=fthird(im, x(i), y(i), n, t); % centroiding

```

```

to=round((tbottom+ttop)/2); % taking threshold in middle of target
y-axis cross section

trange=floor((ttop-tbottom)*.9/2);

if trange>50
    dt=50;
else
    dt=trange;
end

ncrop=15; % to crop the surrounding region close to the target.

%AVERAGING AND WEIGHTED AVERAGING thresholds over the target y-axis
cross
%section:
[xcw(i),ycw(i),xcav(i),ycav(i)]=fcrossing(im,xc(i),yc(i),ncrop,to,dt
);

%fprintf(fid,'%9.2f %9.2f %9.2f %9.2f %9.2f %9.2f\n',
xc(i),yc(i),xcw(i),ycw(i),xcav(i),ycav(i));
fprintf(fid,'%9.2f %9.2f\n',xcav(i),ycav(i));

%subplot(5,2,i),surf(imconvpatch);view(90,0)

yf(i)=floor(ycw(i));
xf(i)=floor(xcw(i));

%impatchfinal=im((yf(i)-ncrop):(yf(i)+ncrop),(xf(i)-
ncrop):(xf(i)+ncrop));
%subplot(5,2,i), surf(double(impatchfinal))
%title(['Target no. ',num2str(i)])

end
fclose(fid);

controlpoint=load (strcat('tg',filename,'.txt')); %loading the file
of the resulting centroids
dcp=cp-controlpoint % calculation of the offset from the referred
image ('SF10_001.JPG')

%PLOTTING
figure, imagesc(im);axis image;
hold on
plot(xc, yc,'ro', ...
'MarkerSize',10)

%plot(xcw, ycw,'ko', ...
%'MarkerSize',100)
plot(xcav, ycav,'b+', ...
'MarkerSize',10)
titletext=strcat(filename,'.JPG');
title(titletext)
hold off

cp=load(strcat('mesh',filename,'.txt'));

```

```

    cp(:,4)=controlpoint(:,1);cp(:,5)=controlpoint(:,2);
    fid=fopen(strcat('newmesh',filename,'.txt'),'w');
    fprintf(fid,'%patch    uo  vo  uf  vf  du  dv  size    desc\n');
    for i=1:itarget
    fprintf(fid, '%4g \t %9.4f \t %9.4f \t %9.4f \t %9.4f \t %8.4f \t
    %8.4f \t %8.2f\t %8.2f\n', cp(i,1:9));
    end
    fclose (fid)
-----
C:\Users\User\alip\piv4\test1\qq.m
function qq(data,frame1,frame2,scale)

% qq(data,frame1,frame2,scale)
% Plots quiver plot of PIV data.
% Use consolidate8.m to assemble matrix 'data'
% scale passes value to quiver command to scale arrow length

diffx=data(:,frame2+1,1)-data(:,frame1+1,1);
diffy=data(:,frame2+1,2)-data(:,frame1+1,2);

%diff=(diffx.^2+diffy.^2).^0.5;
%maxvector=max(max(diff));
%stderror=std(diff)
%hist(diff)

figure(1)
quiver(data(:,frame1+1,1),data(:,frame1+1,2),diffx*scale,diffy*scale
,0,'k')
set(gca,'DataAspectRatio',[1 1 1],'YDir','reverse') %axis ij; axis
equal;

% Add this line if you want to show the patch numbers
%text(data(:,frame2,1),data(:,frame2,2),num2str(data(:,1,1)),'Fontsi
ze',8)
xlabel('Horizontal direction (mm)')
ylabel('Vertical direction (mm)')
colormap cool

axis ([-100 500 0 350])
axis ij
line ([-80 150],[50 50],'Color','r','LineWidth',2);
line ([150 480],[50 190],'Color','r','LineWidth',2);
%line ([900 1000],[400 400],'Color','r','LineWidth',2);
rectangle ('position',[-25,40,150,10]);
text (130,45,'Soil surface')
text (50,35,'Load','horizontalAlignment','center');
-----
C:\Users\User\alip\piv4\test1\cntr.m
function cntr(data,frame1,frame2,scale)

% qq(data,frame1,frame2,scale)
% Plots quiver plot of PIV data.
% Use consolidate8.m to assemble matrix 'data'
% scale passes value to quiver command to scale arrow length

diffx=data(:,frame2+1,1)-data(:,frame1+1,1);
diffy=data(:,frame2+1,2)-data(:,frame1+1,2);
x = data(:,frame1+1,1)
y = data(:,frame1+1,2);
%diff=(diffx.^2+diffy.^2).^0.5;

```

```

%maxvector=max(max(diff));
%stderror=std(diff)
%hist(diff)

%figure(1)
%quiver(data(:,frame1+1,1),data(:,frame1+1,2),diffx*scale,diffy*scale,0,'k')
%set(gca,'DataAspectRatio',[1 1 1],'YDir','reverse') %axis ij; axis
equal;

% Add this line if you want to show the patch numbers
%text(data(:,frame2,1),data(:,frame2,2),num2str(data(:,1,1)),'FontSize',8)

ndata=length(x)
rows=1
while (x(rows+1)-x(rows))<1
    rows=rows+1
end

k=1;
l=1:rows
cols=ndata/rows

for i=1:cols
    for j=1:rows
        xa(j,i)=x(k);
        ya(j,i)=y(k);
        va(j,i)=diffy(k);
        k=k+1;
    end
end
%im=imread(strcat(filename1,'.JPG'));
%im=imread('sf10_001.JPG');
%imagesc(im); colormap(gray);axis image
%hold on
v = ([-10,-8,-6,-4,-2,2,4,6,8]);
[C,h] = contour(xa,ya,va,v);
set(h,'ShowText','on','TextStep',get(h,'LevelStep')*1)
xlabel('Horizontal direction (mm)')
ylabel('Vertical direction (mm)')
colormap cool

axis ([-100 800 -200 250])
axis ij
line ([-100 200],[-125 -125],'Color','r','LineWidth',2);
line ([200 800],[-125 175],'Color','r','LineWidth',2);
%line ([900 1000],[175 250],'Color','r','LineWidth',2);
rectangle ('position',[-25,-135,150,10]);
text (130,-135,'Soil surface')
text (50,-145,'Load','horizontalAlignment','center');
%axis ([-50 400 0 300]);
%axis ij;
%line ([-9.84 374],[60.6 60.6],'Color','r','LineWidth',2);
%text (-11.5,54.6,'sample surface')
%rectangle ('position',[130 50.6 100 10]);
%text (180,40.6,'FOOTING','horizontalAlignment','center');
%axis ([43 430 0 290]);
%axis ij;
%line ([43 430],[92.3 92.3]);
%text (43,86.3,'sample surface')

```



```

%rectangle ('position',[183 82.3 100 10]);
%text(233,77.3,'FOOTING','horizontalAlignment','center');
-----
C:\Users\User\alip\piv4\test1\plotstrains.m
function plotstrains(strains,frame,quantity)

% Plotting of strain data produced by geoSTRAIN8
% strains:  output from geoSTRAIN8
% frame:    final frame of interest (total strains plotted between
start and this frame)
% quantity: 1- total maximum shear strain, 2- total volumetric
strain, 3- incremental maximum shear strain (linear strains see
below)
% strains displayed in %.
% NOTE: YOU WILL NEED TO EDIT LINES 25 & 26 TO SET THE COARSENESS OF
THE PLOT
% DJW 27/2/05

ele_x=strains(:,frame,2); % X coordinate
ele_y=strains(:,frame,3); % Y coordinate

ele_exx=strains(:,frame,4+1)*100; % total XX strain
ele_eyy=strains(:,frame,5+1)*100; % total YY strain
if quantity==1
    ele_strain=strains(:,frame,9+1)*100; %
elseif quantity==2
    ele_strain=strains(:,frame,11+1)*100;
elseif quantity==3
    ele_strain=strains(:,frame,22+1)*100;
end

% SET COARSENESS OF PLOT
xxi=-50:10:4000;
yyi=0:10:300;
[xi,yi]=meshgrid(xxi,yyi);
zi=griddata(ele_x,ele_y,ele_strain,xi,yi);

%[PLOT OUTPUT TO SCREEN]
%figure(20);
%clf
%surf(xi,yi,zi);
%contour(xi,yi,zi);
v = ([20, 40, 80, 120, 160, 200, 240, 280, 320]);
[C,h] = contour(xi,yi,zi,v);axis ij; %axis ([100 350 100 220]);
set(h,'ShowText','on','TextStep',get(h,'LevelStep')*1)
xlabel('Horizontal direction (mm)')
ylabel('Vertical direction (mm)')
colormap cool

axis ([-50 400 0 300])
axis ij
line ([-80 150],[60 60],'Color','r','LineWidth',2);
line ([150 480],[60 190],'Color','r','LineWidth',2);
%line ([900 1000],[400 400],'Color','r','LineWidth',2);
rectangle ('position',[-25,50,150,10]);
text (130,55,'Soil surface')
text (50,45,'Load','horizontalAlignment','center');
%shading flat;
%hold on;
%view(0,90)
%shading interp

```

```
%  
%caxis([-1 1])  
%axis equal  
%axis([0 375 0 300])  
%colorbar;  
%grid off  
axis ij
```

Appendix C awam.my datalogging for AWAM system for the year 2019

Date	Ax	Ay	Az	Gx	Gy	Gz	Temperature
AWAM1							
21/1/2020	0.62	4.51	-8.77	0	0	0	27
20/1/2020	0.62	4.51	-8.77	0	0	0	27
19/1/2020	0.61	4.55	-8.74	0	0	0	29
16/1/2020	0.61	4.52	-8.76	0	0	0	29
15/1/2020	0.57	4.54	-8.72	0	0	0	27
14/1/2020	0.6	4.51	-8.77	0	0	0	30
13/1/2020	0.63	4.55	-8.77	0	0	0	33
12/1/2020	0.56	4.54	-8.74	0	0	0	27
7/1/2020	0.58	4.48	-8.8	0	0	0	31
6/1/2020	0.6	4.52	-8.79	0	0	0	29
4/1/2020	0.57	4.53	-8.79	0	0	0	29
31/12/2019	0.57	4.52	-8.79	0	-0.01	0	35
30/12/2019	0.6	4.52	-8.81	0	-0.01	0	35
29/12/2019	0.56	4.49	-8.82	0	0	0	34
28/12/2019	0.57	4.49	-8.85	0	-0.01	0	36
27/12/2019	0.56	4.52	-8.82	0	0	0	36
26/12/2019	0.53	4.5	-8.81	0	0	0	36
25/12/2019	0.5	4.49	-8.82	0	0	0	30
24/12/2019	0.44	4.53	-8.74	0	0	0	0
23/12/2019	0.5	4.52	-8.79	0	0	0	29
22/12/2019	0.53	4.5	-8.8	0	-0.01	0	39
21/12/2019	0.53	4.5	-8.8	0	-0.01	0	39
20/12/2019	0.49	4.52	-8.78	0	0	0	28
19/12/2019	0.5	4.52	-8.79	0	0	0	37
18/12/2019	0.5	4.5	-8.81	0	0	0	37
17/12/2019	0.51	4.5	-8.82	0	0	0	28
16/12/2019	0.48	4.5	-8.83	0	0	0	38
15/12/2019	0.43	4.51	-8.73	0	0	0	0
14/12/2019	0.43	4.52	-8.74	0	0	0	26
13/12/2019	0.47	4.51	-8.81	0	0	0	28
12/12/2019	0.47	4.52	-8.81	0	0	0	32
11/12/2019	0.49	4.51	-8.84	0	0	0	29
10/12/2019	0.4	4.54	-8.74	0	0	0	0
9/12/2019	0.42	4.53	-8.77	0	0	0	27
8/12/2019	0.46	4.52	-8.81	0	0	0	35
7/12/2019	0.47	4.53	-8.81	0	0	0	35
6/12/2019	0.43	4.52	-8.81	0	0	0	29

5/12/2019	0.4	4.52	-8.83	0	0	0	29
4/12/2019	0.44	4.5	-8.82	0	0	0	36
3/12/2019	0.4	4.52	-8.8	0	0	0	29
2/12/2019	0.39	4.49	-8.79	0	0	0	28
1/12/2019	0.33	4.54	-8.76	0	0	0	27
30/11/2019	0.33	4.53	-8.77	0	0	0	0
29/11/2019	0.4	4.52	-8.81	0	0	0	29
28/11/2019	0.4	4.51	-8.81	0	0	0	35
27/11/2019	0.4	4.55	-8.82	0	0	0	29
26/11/2019	0.33	4.54	-8.76	0	0	0	0
25/11/2019	0.27	4.52	-8.76	0	0	0	0
24/11/2019	0.28	4.52	-8.75	0	0	0	25
23/11/2019	0.28	4.57	-8.77	0	0	0	0
22/11/2019	0.33	4.51	-8.78	0	0	0	28
21/11/2019	0.35	4.54	-8.81	0	0	0	34
20/11/2019	0.34	4.52	-8.83	0	0	0	28
19/11/2019	0.29	4.54	-8.76	0	0	0	0
18/11/2019	0.35	4.53	-8.8	0	0	0	28
17/11/2019	0.36	4.5	-8.82	0	0	0	41
16/11/2019	0.32	4.5	-8.85	0	0	0	29
15/11/2019	0.35	4.52	-8.82	0	0	0	29
14/11/2019	0.32	4.54	-8.83	0	0	0	29
13/11/2019	0.33	4.51	-8.81	0	0	0	30
12/11/2019	0.32	4.54	-8.84	0	0	0	30
11/11/2019	0.33	4.5	-8.8	0	-0.01	0	29
10/11/2019	0.3	4.52	-8.83	0	0	0	31
8/11/2019	0.31	4.52	-8.83	0	0	0	31
7/11/2019	0.3	4.52	-8.83	0	0	0	29
6/11/2019	0.34	4.53	-8.82	0	0	0	30
5/11/2019	0.31	4.5	-8.82	0	0	0	29
4/11/2019	0.31	4.52	-8.81	0	0	0	29
3/11/2019	0.29	4.52	-8.82	0	0	0	30
2/11/2019	0.29	4.5	-8.84	0	-0.01	0	40
31/10/2019	0.2	4.5	-8.81	0	0	0	32
30/10/2019	0.2	4.5	-8.81	0	0	0	32
29/10/2019	0.27	4.48	-8.85	0	0	0	29
28/10/2019	0.25	4.47	-8.82	0	0	0	35
27/10/2019	0.23	4.49	-8.81	0	-0.01	0	28
26/10/2019	0.26	4.48	-8.82	0	0	0	28
25/10/2019	-1.34	4.26	-8.84	0	0	0	29
24/10/2019	-1.33	4.24	-8.86	0	0	0	29

23/10/2019	-1.33	4.23	-8.82	0	0	0	29
22/10/2019	-1.33	4.23	-8.85	0	-0.01	0	29
21/10/2019	-1.37	4.22	-8.87	0	-0.01	0	29
20/10/2019	-1.36	4.22	-8.87	0	-0.01	0	29
19/10/2019	-1.36	4.24	-8.85	0	-0.01	0	30
18/10/2019	-1.36	4.27	-8.86	0	0	0	28
17/10/2019	-1.34	4.24	-8.87	0	-0.01	0	28
16/10/2019	-1.34	4.23	-8.89	0	-0.01	0	29
15/10/2019	-1.36	4.24	-8.85	0	0	0	28
14/10/2019	-1.34	4.25	-8.84	0	-0.01	0	28
13/10/2019	-1.35	4.25	-8.85	0	0	0	28
12/10/2019	-1.35	4.24	-8.84	0	-0.01	0	28
11/10/2019	-1.34	4.23	-8.88	0	0	0	27
10/10/2019	-1.33	4.24	-8.86	0	0	0	28
9/10/2019	-1.33	4.26	-8.89	0.01	0	0	27
8/10/2019	-1.3	4.23	-8.88	0	0	0	37
7/10/2019	-1.28	4.23	-8.9	0	-0.01	0	39
6/10/2019	-1.3	4.22	-8.85	0	-0.01	0	34
5/10/2019	-1.33	4.25	-8.89	0	0	0	28
4/10/2019	-1.32	4.26	-8.89	0	0	0	28
3/10/2019	-1.33	4.26	-8.85	0	-0.01	0	32
2/10/2019	-1.29	4.25	-8.85	0	0	0	32
30/9/2019	-1.31	4.25	-8.9	0	-0.01	0	28
29/9/2019	-1.29	4.25	-8.86	0	0	0	28
28/9/2019	-1.3	4.26	-8.87	0	0	0	28
27/9/2019	-1.19	4.27	-8.89	0	0	0	29
26/9/2019	-1.12	4.32	-8.85	0	0	0	29
25/9/2019	-1.01	4.37	-8.84	0	0	0	31
24/9/2019	-1.04	4.38	-8.82	0	-0.01	0	29
23/9/2019	-1.09	4.39	-8.81	0	0	0	0
21/9/2019	-0.97	4.42	-8.8	0	0	0	26
20/9/2019	-0.96	4.4	-8.84	0	-0.01	0	30
19/9/2019	-0.91	4.39	-8.85	0	-0.01	0	30
18/9/2019	-0.93	4.4	-8.86	0	-0.01	0	30
17/9/2019	-0.92	4.39	-8.87	0	-0.01	0	29
16/9/2019	-0.91	4.4	-8.84	0	-0.01	0	34
14/9/2019	-0.86	4.39	-8.84	0	-0.01	0	31
13/9/2019	-0.89	4.41	-8.85	0	0	0	28
12/9/2019	-0.87	4.39	-8.84	0	0	0	29
11/9/2019	-0.9	4.38	-8.84	0	-0.01	0	29
10/9/2019	-0.91	4.41	-8.83	0	-0.01	0	29

9/9/2019	-0.88	4.39	-8.87	0	0	0	30
8/9/2019	-0.94	4.39	-8.75	0	0	0	31
6/9/2019	-0.9	4.38	-8.85	0	-0.01	0	30
5/9/2019	-0.88	4.39	-8.86	0	-0.01	0	29
4/9/2019	-0.84	4.38	-8.84	0	-0.01	0	30
3/9/2019	-0.84	4.36	-8.86	0	-0.01	0	31
2/9/2019	-0.85	4.35	-8.88	0.01	-0.01	0	38
30/8/2019	-0.85	4.37	-8.81	0	-0.01	0	30
29/8/2019	-0.85	4.35	-8.86	0	-0.01	0	29
28/8/2019	-0.86	4.36	-8.85	0	-0.01	0	29
27/8/2019	-0.89	4.35	-8.87	0	-0.01	0	28
26/8/2019	-0.89	4.36	-8.87	0	0	0	28
25/8/2019	-0.78	4.31	-8.89	0	0	0	35
24/8/2019	-0.82	4.32	-8.89	0	0	0	29
23/8/2019	-0.8	4.31	-8.88	0	0	0	34
22/8/2019	-0.82	4.3	-8.86	0	0	0	30
21/8/2019	-0.81	4.31	-8.94	0	0	0	37
20/8/2019	-0.82	4.3	-8.89	0	0	0	29
19/8/2019	-0.83	4.29	-8.88	0	0	0	28
18/8/2019	-0.85	4.27	-8.91	0	0	0	30
17/8/2019	-0.83	4.29	-8.9	0	0	0	29
16/8/2019	-0.83	4.27	-8.91	0	0	0	29
15/8/2019	-0.78	4.24	-8.93	0	0	0	37
13/8/2019	-0.82	4.27	-8.88	0	0	0	30
12/8/2019	-0.79	4.25	-8.93	0	0	0	30
11/8/2019	-0.79	4.25	-8.91	0	0	0	31
10/8/2019	-0.79	4.25	-8.92	0	0	0	30
9/8/2019	-0.81	4.22	-8.93	0	0	0	31
8/8/2019	-0.79	4.24	-8.9	0	0	0	30
7/8/2019	-0.8	4.24	-8.91	0	0	0	29
6/8/2019	-0.8	4.23	-8.92	0	0	0	28
5/8/2019	-0.77	4.23	-8.91	0	0	0	28
4/8/2019	-0.77	4.21	-8.95	0	0	0	29
3/8/2019	-0.77	4.16	-8.95	0	0	0	29
2/8/2019	-0.7	4.13	-8.97	0	0	0	28
1/8/2019	1.31	4.35	-8.78	0	0	0	29
31/7/2019	1.31	4.35	-8.78	0	0	0	29
30/7/2019	1.31	4.35	-8.78	0	0	0	29
29/7/2019	1.31	4.35	-8.78	0	0	0	29
28/7/2019	1.31	4.35	-8.78	0	0	0	29
27/7/2019	1.31	4.35	-8.78	0	0	0	29

26/7/2019	1.31	4.35	-8.78	0	0	0	29
25/7/2019	1.31	4.35	-8.78	0	0	0	29
24/7/2019	1.31	4.35	-8.78	0	0	0	29
23/7/2019	1.31	4.35	-8.78	0	0	0	29
22/7/2019	1.31	4.35	-8.78	0	0	0	29
21/7/2019	1.31	4.35	-8.78	0	0	0	29
20/7/2019	1.31	4.35	-8.78	0	0	0	29
19/7/2019	1.31	4.35	-8.78	0	0	0	29
18/7/2019	1.31	4.35	-8.78	0	0	0	29
17/7/2019	1.31	4.35	-8.78	0	0	0	29
16/7/2019	1.31	4.35	-8.78	0	0	0	29
15/7/2019	1.31	4.35	-8.78	0	0	0	29
14/7/2019	1.31	4.35	-8.78	0	0	0	29
13/7/2019	1.31	4.35	-8.78	0	0	0	29
12/7/2019	1.31	4.35	-8.78	0	0	0	29
11/7/2019	1.31	4.35	-8.78	0	0	0	29
10/7/2019	1.31	4.35	-8.78	0	0	0	29
9/7/2019	1.31	4.35	-8.78	0	0	0	29
8/7/2019	1.31	4.35	-8.78	0	0	0	29
7/7/2019	1.31	4.35	-8.78	0	0	0	29
4/7/2019	1.31	4.35	-8.78	0	0	0	29
3/7/2019	1.31	4.35	-8.78	0	0	0	29
2/7/2019	1.31	4.35	-8.78	0	0	0	29
1/7/2019	1.31	4.35	-8.78	0	0	0	29
30/6/2019	1.31	4.35	-8.78	0	0	0	29
29/6/2019	1.31	4.35	-8.78	0	0	0	29
28/6/2019	1.31	4.35	-8.78	0	0	0	29
27/6/2019	1.31	4.35	-8.78	0	0	0	29
26/6/2019	1.31	4.35	-8.78	0	0	0	29
25/6/2019	1.31	4.35	-8.78	0	0	0	29
24/6/2019	1.31	4.35	-8.78	0	0	0	29
23/6/2019	1.31	4.35	-8.78	0	0	0	29
22/6/2019	1.31	4.35	-8.78	0	0	0	29
21/6/2019	1.31	4.35	-8.78	0	0	0	29
20/6/2019	1.31	4.35	-8.78	0	0	0	29
19/6/2019	1.31	4.35	-8.78	0	0	0	29
18/6/2019	1.31	4.35	-8.78	0	0	0	29
17/6/2019	1.31	4.35	-8.78	0	0	0	29
16/6/2019	1.31	4.35	-8.78	0	0	0	29
15/6/2019	1.31	4.35	-8.78	0	0	0	29
14/6/2019	1.31	4.35	-8.78	0	0	0	29

13/6/2019	1.31	4.35	-8.78	0	0	0	29
12/6/2019	1.31	4.35	-8.78	0	0	0	29
11/6/2019	1.31	4.35	-8.78	0	0	0	29
10/6/2019	1.31	4.35	-8.78	0	0	0	29
9/6/2019	1.31	4.35	-8.78	0	0	0	29
8/6/2019	1.31	4.35	-8.78	0	0	0	29
7/6/2019	1.31	4.35	-8.78	0	0	0	29
6/6/2019	1.31	4.35	-8.78	0	0	0	29
5/6/2019	1.31	4.35	-8.78	0	0	0	29
4/6/2019	1.31	4.35	-8.78	0	0	0	29
3/6/2019	1.31	4.35	-8.78	0	0	0	29
2/6/2019	1.31	4.35	-8.78	0	0	0	29
1/6/2019	1.31	4.35	-8.78	0	0	0	29
31/5/2019	1.31	4.35	-8.78	0	0	0	29
30/5/2019	1.31	4.35	-8.78	0	0	0	29
29/5/2019	1.31	4.35	-8.78	0	0	0	29
28/5/2019	1.31	4.35	-8.78	0	0	0	29
27/5/2019	1.31	4.35	-8.78	0	0	0	29
26/5/2019	1.31	4.35	-8.78	0	0	0	29
25/5/2019	1.31	4.35	-8.78	0	0	0	29
24/5/2019	1.31	4.35	-8.78	0	0	0	29
23/5/2019	1.31	4.35	-8.78	0	0	0	29
22/5/2019	1.31	4.35	-8.78	0	0	0	29
21/5/2019	1.31	4.35	-8.78	0	0	0	29
20/5/2019	1.31	4.35	-8.78	0	0	0	29
19/5/2019	1.31	4.35	-8.78	0	0	0	29
18/5/2019	1.31	4.35	-8.78	0	0	0	29
17/5/2019	1.31	4.35	-8.78	0	0	0	29
16/5/2019	1.31	4.35	-8.78	0	0	0	29
15/5/2019	1.31	4.35	-8.78	0	0	0	29
14/5/2019	1.31	4.35	-8.78	0	0	0	29
13/5/2019	1.31	4.35	-8.78	0	0	0	29
12/5/2019	1.31	4.35	-8.78	0	0	0	29
11/5/2019	1.31	4.35	-8.78	0	0	0	29
10/5/2019	1.31	4.35	-8.78	0	0	0	29
9/5/2019	1.31	4.35	-8.78	0	0	0	29
8/5/2019	1.32	4.34	-8.8	0	0	0	31
7/5/2019	1.31	4.34	-8.83	0	0	0	30
6/5/2019	1.33	4.33	-8.79	0	0	0	31
5/5/2019	1.32	4.33	-8.8	0	0	0	31
3/5/2019	1.33	4.32	-8.81	0	0	0	31

2/5/2019	1.32	4.33	-8.82	0	0	0	31
2/5/2019	1.32	4.33	-8.82	0	0	0	31
1/5/2019	1.31	4.32	-8.82	0	0	0	29
30/4/2019	1.34	4.31	-8.81	0	0	0	42
29/4/2019	1.31	4.31	-8.81	0	0	0	32
28/4/2019	1.32	4.32	-8.8	0	0	0	30
27/4/2019	1.31	4.32	-8.8	0	0	0	33
26/4/2019	1.28	4.34	-8.82	0	0	0	30
25/4/2019	1.32	4.32	-8.81	0	0	0	29
24/4/2019	1.32	4.33	-8.8	0	0	0	29
23/4/2019	1.33	4.31	-8.81	0	0	0	29
22/4/2019	1.32	4.29	-8.86	0	0	0	31
21/4/2019	1.31	4.34	-8.84	0	0	0	29
20/4/2019	1.31	4.32	-8.81	0	0	0	29
19/4/2019	1.31	4.33	-8.84	0	0	0	31
18/4/2019	1.3	4.32	-8.84	0	0	0	30
17/4/2019	1.29	4.32	-8.84	0	0	0	29
16/4/2019	1.3	4.32	-8.86	0	0	0	29
15/4/2019	1.28	4.33	-8.83	0	0	0	29
14/4/2019	1.27	4.31	-8.83	0	0	0	29
13/4/2019	1.27	4.34	-8.83	0	0	0	28
12/4/2019	1.28	4.33	-8.81	0	0	0	29
11/4/2019	1.27	4.33	-8.79	0	0	0	29
10/4/2019	1.25	4.32	-8.8	0	0	0	29
9/4/2019	1.26	4.34	-8.81	0	0	0	30
8/4/2019	1.23	4.31	-8.82	0	0	0	30
7/4/2019	1.25	4.36	-8.85	0	0	0	28
6/4/2019	1.26	4.32	-8.81	0	0	0	29
5/4/2019	1.24	4.32	-8.83	0	0	0	30
4/4/2019	1.24	4.35	-8.83	0	0	0	29
3/4/2019	1.23	4.31	-8.82	0	0	0	29
2/4/2019	1.22	4.35	-8.83	0	0	0	29
1/4/2019	1.21	4.36	-8.84	0	0	0	30
31/3/2019	1.2	4.36	-8.85	0	0	0	30
30/3/2019	1.2	4.36	-8.86	0	0	0	30
AWAM2							
24/12/2019	5.93	-1.07	-7.2	0	0	0	0
23/12/2019	5.97	-1.1	-7.26	0	0	0.01	30
22/12/2019	5.95	-1.1	-7.27	0	0	0	31
17/12/2019	5.96	-1.04	-7.21	0	0	0	37
11/12/2019	5.98	-0.99	-7.29	0	0	0	29

8/12/2019	5.98	-0.99	-7.29	0	0	0	29
7/12/2019	5.98	-0.99	-7.29	0	0	0	29
5/12/2019	5.98	-0.99	-7.29	0	0	0	29
4/12/2019	5.98	-0.99	-7.29	0	0	0	29
3/12/2019	5.98	-0.99	-7.29	0	0	0	29
26/11/2019	5.92	-1.03	-7.29	0	0	0	29
25/11/2019	5.92	-1.03	-7.29	0	0	0	29
24/11/2019	5.92	-1.03	-7.29	0	0	0	29
23/11/2019	5.92	-1.04	-7.29	0	0	0	29
22/11/2019	5.91	-1.06	-7.31	0	0	0	29
21/11/2019	5.93	-1.06	-7.34	0	0	0	29
20/11/2019	5.9	-1.11	-7.32	0	0	0	29
19/11/2019	5.9	-1.1	-7.33	0	0	0	28
18/11/2019	5.92	-1.06	-7.31	0	0	0	28
15/11/2019	5.92	-1.04	-7.3	0	0	0	29
14/11/2019	5.92	-1.04	-7.3	0	0	0	29
13/11/2019	5.9	-1.04	-7.32	0	0	0	28
12/11/2019	5.93	-1.11	-7.31	0	0	0	30
11/11/2019	5.9	-1.1	-7.3	0	0	0	29
10/11/2019	5.92	-1.06	-7.3	0	0	0	32
8/11/2019	5.91	-1.08	-7.31	0	0	0	31
7/11/2019	5.91	-1.12	-7.29	0	0	0	31
6/11/2019	5.88	-1.12	-7.28	0	0	0	34
5/11/2019	5.88	-1.12	-7.28	0	0	0	34
4/11/2019	5.88	-1.12	-7.28	0	0	0	34
24/10/2019	5.81	-1.09	-7.41	0	0	0	41
23/10/2019	5.8	-1	-7.41	0	0	0	29
22/10/2019	5.79	-1.1	-7.41	0	0	0	35
21/10/2019	5.79	-1.1	-7.41	0	0	0	35
20/10/2019	5.8	-1.12	-7.38	0	0	0	39
19/10/2019	5.8	-1.12	-7.38	0	0	0	39
18/10/2019	5.8	-1.12	-7.38	0	0	0	39
17/10/2019	5.8	-1.11	-7.37	0	0	0	41
16/10/2019	5.8	-1.11	-7.37	0	0	0	41
15/10/2019	5.8	-1.11	-7.37	0	0	0	41
14/10/2019	5.8	-1.11	-7.37	0	0	0	41
13/10/2019	5.8	-1.11	-7.37	0	0	0	41
12/10/2019	5.8	-1.11	-7.37	0	0	0	41
11/10/2019	5.8	-1.11	-7.37	0	0	0	41
10/10/2019	5.8	-1.11	-7.37	0	0	0	41
9/10/2019	5.8	-1.11	-7.37	0	0	0	41

7/10/2019	5.8	-1.11	-7.37	0	0	0	41
5/10/2019	5.78	-1.07	-7.41	0	0	0	39
4/10/2019	5.78	-1.07	-7.41	0	0	0	39
3/10/2019	5.77	-1.04	-7.42	0	0	0	27
2/10/2019	5.76	-1.02	-7.42	0	0	0	28
1/10/2019	5.79	-1.04	-7.45	0	0	0	29
30/9/2019	5.79	-1.04	-7.45	0	0	0	29
29/9/2019	5.79	-1.04	-7.45	0	0	0	29
26/9/2019	5.71	-1.2	-7.44	0	0	0	34
25/9/2019	5.76	-1.23	-7.43	0	0	0	42
24/9/2019	5.76	-1.23	-7.43	0	0	0	42
20/9/2019	5.75	-1.18	-7.4	0	0	0	40
19/9/2019	5.75	-1.18	-7.4	0	0	0	40
18/9/2019	5.75	-1.18	-7.4	0	0	0	40
17/9/2019	5.75	-1.18	-7.4	0	0	0	40
11/9/2019	5.76	-1.12	-7.4	0	0	0	28
10/9/2019	5.76	-1.12	-7.4	0	0	0	28
8/9/2019	5.76	-1.12	-7.4	0	0	0	28
5/9/2019	5.77	-1.14	-7.3	0	0	0	41
4/9/2019	5.78	-1.12	-7.43	0	0	0	38
3/9/2019	5.78	-1.12	-7.43	0	0	0	38
2/9/2019	5.74	-1.12	-7.42	0	0	0	32
30/8/2019	5.75	-1.1	-7.44	0	0	0	31
29/8/2019	5.74	-1.12	-7.4	0	0	0	30
28/8/2019	5.76	-1.13	-7.45	0	0	0	38
27/8/2019	5.76	-1.13	-7.45	0	0	0	38
26/8/2019	5.61	-1.04	-7.52	0	0	0	36
25/8/2019	5.61	-1.04	-7.52	0	0	0	36
13/8/2019	5.61	-1.04	-7.52	0	0	0	36
12/8/2019	5.61	-1.04	-7.52	0	0	0	36
11/8/2019	5.63	-1.01	-7.52	0	0	0	32
10/8/2019	5.65	-1.02	-7.53	0	0	0	37
9/8/2019	5.64	-0.98	-7.52	0	0	0	34
8/8/2019	5.64	-0.98	-7.52	0	0	0	34
7/8/2019	5.64	-0.98	-7.52	0	0	0	34
6/8/2019	5.64	-0.98	-7.52	0	0	0	34
5/8/2019	5.56	-0.99	-7.6	0	0	0	31
4/8/2019	5.61	-1.04	-7.68	0	6	0	29
3/8/2019	5.61	-1.04	-7.69	0	6	0	29
2/8/2019	5.63	-1.01	-7.66	0	6	0	29
1/8/2019	5.65	-1.02	-7.7	0	6	0	29

31/7/2019	5.64	-0.98	-7.66	0	6	0	29
30/7/2019	5.64	-0.98	-7.71	0	6	0	29
29/7/2019	5.64	-0.98	-7.68	0	6	0	29
28/7/2019	5.64	-0.98	-7.7	0	6	0	29
27/7/2019	5.56	-0.99	-7.69	0	6	0	29
26/7/2019	5.61	-1.04	-7.7	0	6	0	29
25/7/2019	5.61	-1.04	-7.67	0	6	0	29
24/7/2019	5.63	-1.01	-7.67	0	6	0	29
23/7/2019	5.65	-1.02	-7.68	0	6	0	29
22/7/2019	5.64	-0.98	-7.71	0	6	0	29
21/7/2019	5.64	-0.98	-7.67	0	6	0	29
20/7/2019	5.64	-0.98	-7.73	0	6	0	29
19/7/2019	5.64	-0.98	-7.7	0	6	0	29
18/7/2019	5.56	-0.99	-7.72	0	6	0	29
17/7/2019	5.61	-1.04	-7.72	0	6	0	29
16/7/2019	5.61	-1.04	-7.72	0	6	0	29
15/7/2019	5.63	-1.01	-7.72	0	6	0	29
14/7/2019	5.65	-1.02	-7.71	0	6	0	29
13/7/2019	5.64	-0.98	-7.72	0	6	0	29
12/7/2019	5.64	-0.98	-7.74	0	6	0	29
11/7/2019	5.64	-0.98	-7.69	0	6	0	29
10/7/2019	5.64	-0.98	-7.67	0	6	0	29
9/7/2019	5.56	-0.99	-7.68	0	6	0	29
8/7/2019	5.61	-1.04	-7.71	0	6	0	29
7/7/2019	5.61	-1.04	-7.67	0	6	0	29
4/7/2019	5.63	-1.01	-7.73	0	6	0	29
3/7/2019	5.65	-1.02	-7.7	0	6	0	29
2/7/2019	5.64	-0.98	-7.72	0	6	0	29
1/7/2019	5.64	-0.98	-7.72	0	6	0	29
30/6/2019	5.64	-0.98	-7.72	0	6	0	29
29/6/2019	5.64	-0.98	-7.72	0	6	0	29
28/6/2019	5.56	-0.99	-7.71	0	6	0	29
27/6/2019	5.61	-1.04	-7.72	0	6	0	29
26/6/2019	5.61	-1.04	-7.74	0	6	0	29
25/6/2019	5.63	-1.01	-7.69	0	6	0	29
24/6/2019	5.65	-1.02	-7.72	0	6	0	29
23/6/2019	5.64	-0.98	-7.71	0	6	0	29
22/6/2019	5.64	-0.98	-7.72	0	6	0	29
21/6/2019	5.64	-0.98	-7.74	0	6	0	29
20/6/2019	5.64	-0.98	-7.68	0	6	0	29
19/6/2019	5.56	-0.99	-7.69	0	6	0	29

18/6/2019	5.61	-1.04	-7.66	0	6	0	29
17/6/2019	5.61	-1.04	-7.7	0	6	0	29
16/6/2019	5.63	-1.01	-7.66	0	6	0	29
15/6/2019	5.65	-1.02	-7.71	0	6	0	29
14/6/2019	5.64	-0.98	-7.68	0	6	0	29
13/6/2019	5.64	-0.98	-7.7	0	6	0	29
12/6/2019	5.64	-0.98	-7.69	0	6	0	29
11/6/2019	5.64	-0.98	-7.7	0	6	0	29
10/6/2019	5.56	-0.99	-7.67	0	6	0	29
9/6/2019	5.61	-1.04	-7.67	0	6	0	29
8/6/2019	5.61	-1.04	-7.68	0	6	0	29
7/6/2019	5.63	-1.01	-7.71	0	6	0	29
6/6/2019	5.65	-1.02	-7.67	0	6	0	29
5/6/2019	5.64	-0.98	-7.73	0	6	0	29
4/6/2019	5.64	-0.98	-7.7	0	6	0	29
3/6/2019	5.64	-0.98	-7.72	0	6	0	29
2/6/2019	5.64	-0.98	-7.72	0	6	0	29
1/6/2019	5.56	-0.99	-7.72	0	6	0	29
31/5/2019	5.64	-0.98	-7.72	0	6	0	29
30/5/2019	5.64	-0.98	-7.71	0	6	0	29
29/5/2019	5.64	-0.98	-7.72	0	6	0	29
28/5/2019	5.56	-0.99	-7.74	0	6	0	29
27/5/2019	5.61	-1.04	-7.69	0	6	0	29
26/5/2019	5.61	-1.04	-7.64	0	6	0	29
25/5/2019	5.63	-1.01	-7.59	0	6	0	29
24/5/2019	5.65	-1.02	-7.68	0	6	0	29
23/5/2019	5.64	-0.98	-7.69	0	6	0	29
22/5/2019	5.64	-0.98	-7.66	0	6	0	29
21/5/2019	5.64	-0.98	-7.7	0	6	0	29
20/5/2019	5.64	-0.98	-7.66	0	6	0	29
19/5/2019	5.56	-0.99	-7.71	0	6	0	29
18/5/2019	5.61	-1.04	-7.68	0	6	0	29
17/5/2019	5.61	-1.04	-7.7	0	6	0	29
16/5/2019	5.63	-1.01	-7.69	0	6	0	29
15/5/2019	5.65	-1.02	-7.7	0	6	0	29
14/5/2019	5.64	-0.98	-7.67	0	6	0	29
13/5/2019	5.64	-0.98	-7.67	0	6	0	29
12/5/2019	5.64	-0.98	-7.68	0	6	0	29
11/5/2019	5.64	-0.98	-7.71	0	6	0	29
10/5/2019	5.64	-0.98	-7.67	0	6	0	29
9/5/2019	5.56	-0.99	-7.73	0	6	0	29

8/5/2019	5.61	-1.04	-7.7	0	6	0	29
7/5/2019	5.61	-1.04	-7.72	0	6	0	29
6/5/2019	5.63	-1.01	-7.72	0	6	0	29
5/5/2019	5.65	-1.02	-7.72	0	6	0	29
3/5/2019	5.64	-0.98	-7.72	0	6	0	29
2/5/2019	5.64	-0.98	-7.71	0	6	0	29
2/5/2019	5.64	-0.98	-7.72	0	6	0	29
1/5/2019	5.64	-0.98	-7.74	0	6	0	29
30/4/2019	5.56	-0.99	-7.69	0	6	0	29
29/4/2019	5.61	-1.04	-7.663	0	6	0	29
28/4/2019	5.61	-1.04	-7.666	0	6	0	29
27/4/2019	5.63	-1.01	-7.669	0	6	0	29
26/4/2019	5.65	-1.02	-7.672	0	6	0	29
25/4/2019	5.64	-0.98	-7.675	0	6	0	29
24/4/2019	5.43	-0.9	-7.68	0	0	0	31
23/4/2019	5.42	-0.96	-7.69	0	0	0	30
22/4/2019	5.4	-0.97	-7.66	0	0	0	31
21/4/2019	5.41	-0.95	-7.7	0	0	0	29
20/4/2019	5.4	-0.98	-7.66	0	0	0	30
19/4/2019	5.4	-0.99	-7.71	0	0	0	31
18/4/2019	5.41	-0.97	-7.68	1	62	0	30
17/4/2019	5.41	-0.95	-7.7	0	0	0	30
16/4/2019	5.42	-0.97	-7.69	0	0	0	30
15/4/2019	5.41	-0.96	-7.7	0	0	0	30
14/4/2019	5.43	-0.95	-7.67	0	0	0	30
13/4/2019	5.43	-0.94	-7.67	0	0	0	29
12/4/2019	5.43	-0.95	-7.68	0	0	0	30
11/4/2019	5.41	-0.91	-7.71	0	0	0	29
10/4/2019	5.41	-0.93	-7.67	0	0	0	29
9/4/2019	5.41	-0.93	-7.73	0	0	0	30
8/4/2019	5.41	-0.93	-7.7	0	0	0	30
7/4/2019	5.4	-0.91	-7.72	0	0	0	29
6/4/2019	5.41	-0.89	-7.72	0	0	0	29
5/4/2019	5.38	-0.9	-7.72	0	0	0	31
4/4/2019	5.39	-0.88	-7.72	0	0	0	29
3/4/2019	5.4	-0.87	-7.71	0	0	0	29
2/4/2019	5.39	-0.86	-7.72	0	0	0	30
1/4/2019	5.39	-0.85	-7.74	0	0	0	30
31/3/2019	5.4	-0.81	-7.69	0	0	0	38

AWAM3

Date	Ax	Ay	Az	Gx	Gy	Gz	Temperature
25/10/2019	-0.21	-6.43	-7.25	0	0	0	30
24/10/2019	-0.2	-6.44	-7.25	0	0	0	30
23/10/2019	-0.21	-6.41	-7.27	0	0	0	29
22/10/2019	-0.21	-6.44	-7.2	0	0	0	30
21/10/2019	-0.2	-6.41	-7.24	0	0	0	30
20/10/2019	-0.2	-6.44	-7.24	0	0	0	30
19/10/2019	-0.2	-6.43	-7.21	0	0	0	30
18/10/2019	-0.22	-6.43	-7.29	0	0	0	31
17/10/2019	-0.18	-6.41	-7.22	0	0	0	29
16/10/2019	-0.18	-6.43	-7.27	0	0	0	30
15/10/2019	-0.19	-6.42	-7.23	0	0	0	29
14/10/2019	-0.19	-6.43	-7.25	0	0	0	29
13/10/2019	-0.19	-6.43	-7.25	0	0	0	29
12/10/2019	-0.17	-6.42	-7.23	0	0	0	29
11/10/2019	-0.2	-6.41	-7.23	0	0	0	28
10/10/2019	-0.19	-6.43	-7.23	0	0	0	29
9/10/2019	-0.15	-6.43	-7.23	0	0	0	29
8/10/2019	-0.2	-6.42	-7.23	0	0	0	30
7/10/2019	-0.16	-6.42	-7.24	0	0	0	29
6/10/2019	-0.17	-6.43	-7.22	0	0	0	29
5/10/2019	-0.21	-6.47	-7.24	0	0	0	29
4/10/2019	-0.2	-6.43	-7.23	0	0	0	29
3/10/2019	-0.19	-6.44	-7.23	0	0	0	27
2/10/2019	-0.2	-6.44	-7.23	0	0	0	29
1/10/2019	-0.18	-6.44	-7.2	0	0	0	29
30/9/2019	-0.21	-6.44	-7.21	0	0	0	29
29/9/2019	-0.18	-6.42	-7.21	0	0	0	29
28/9/2019	-0.18	-6.42	-7.17	0	0	0	30
27/9/2019	-0.19	-6.43	-7.23	0	0	0	30
26/9/2019	-0.19	-6.47	-7.17	0	0	0	33
25/9/2019	-0.18	-6.48	-7.14	0	0	0	31
24/9/2019	-0.19	-6.49	-7.15	0	0	0	31
23/9/2019	-0.19	-6.48	-7.16	0	0	0	29
21/9/2019	-0.18	-6.48	-7.16	0	0	0	34
20/9/2019	-0.18	-6.48	-7.14	0	0	0	30
19/9/2019	-0.18	-6.47	-7.17	0	0	0	31
18/9/2019	-0.16	-6.47	-7.15	0	0	0	31
17/9/2019	-0.2	-6.48	-7.17	0	0	0	29
16/9/2019	-0.19	-6.49	-7.16	0	0	0	30

15/9/2019	-0.21	-6.48	-7.13	0	0	0	30
14/9/2019	-0.17	-6.47	-7.15	0	0	0	32
13/9/2019	-0.16	-6.46	-7.14	0	0	0	29
12/9/2019	-0.14	-6.47	-7.16	0	0	0	30
11/9/2019	-0.16	-6.46	-7.15	0	0	0	30
10/9/2019	-0.16	-6.47	-7.16	0	0	0	31
9/9/2019	-0.15	-6.47	-7.16	0	0	0	30
8/9/2019	-0.15	-6.45	-7.16	0	0	0	29
5/9/2019	-0.16	-6.45	-7.18	0	0	0	30
4/9/2019	-0.17	-6.48	-7.16	0	0	0	31
3/9/2019	-0.17	-6.45	-7.18	0	0	0	32
2/9/2019	-0.18	-6.46	-7.17	0	0	0	34
1/9/2019	-0.2	-6.44	-7.15	0	0	0	37
29/8/2019	-0.17	-6.53	-7.2	0	0	0	42
28/8/2019	-0.21	-6.48	-7.17	0	0	0	36
27/8/2019	-0.19	-6.49	-7.15	0	0	0	42
23/8/2019	-0.21	-6.32	-7.28	0	0	0	30
22/8/2019	-0.24	-6.33	-7.27	0	0	0	30
21/8/2019	-0.22	-6.34	-7.27	0	0	0	32
20/8/2019	-0.24	-6.34	-7.28	0	0	0	31
19/8/2019	-0.23	-6.32	-7.29	0	0	0	29
18/8/2019	-0.25	-6.32	-7.27	0	0	0	30
15/8/2019	-0.22	-6.34	-7.29	0	0	0	39
13/8/2019	-0.23	-6.33	-7.28	0	0	0	31
12/8/2019	-0.23	-6.31	-7.26	0	0	0	31
11/8/2019	-0.25	-6.32	-7.29	0	0	0	32
10/8/2019	-0.25	-6.34	-7.3	0	0	0	32
9/8/2019	-0.23	-6.32	-7.29	0	0	0	32
8/8/2019	-0.24	-6.32	-7.27	0	0	0	31
7/8/2019	-0.25	-6.31	-7.31	0	0	0	31
6/8/2019	-0.23	-6.32	-7.32	0	0	0	29
5/8/2019	-0.24	-6.31	-7.32	0	0	0	29
4/8/2019	-0.24	-6.32	-7.31	0	0	0	30
3/8/2019	-0.24	-6.32	-7.33	0	0	0	30
2/8/2019	-0.23	-6.31	-7.32	0	0	0	29
1/8/2019	-0.23	-6.31	-7.31	0	0	0	29
31/7/2019	-0.26	-6.3	-7.29	0	0	0	30
30/7/2019	-0.24	-6.3	-7.29	0	0	0	30
29/7/2019	-0.25	-6.33	-7.32	0	0	0	32
28/7/2019	-0.23	-6.3	-7.3	0	0	0	29
27/7/2019	-0.26	-6.3	-7.33	0	0	0	30

26/7/2019	-0.25	-6.3	-7.3	0	0	0	29
25/7/2019	-0.27	-6.32	-7.3	0	-0.01	0	31
24/7/2019	-0.27	-6.3	-7.33	0	0	0	29
23/7/2019	-0.26	-6.32	-7.31	0	0	0	28
22/7/2019	-0.25	-6.32	-7.3	0	0	0	30
21/7/2019	-0.24	-6.32	-7.31	0	0	0	30
20/7/2019	-0.26	-6.31	-7.31	0	0	0	29
19/7/2019	-0.25	-6.31	-7.34	0	0	0	29
18/7/2019	-0.27	-6.32	-7.28	0	0	0	29
17/7/2019	-0.3	-6.3	-7.27	0	-0.01	0	29
16/7/2019	-0.28	-6.32	-7.32	0	0	0	29
15/7/2019	-0.26	-6.3	-7.31	0	0	0	31
14/7/2019	-0.26	-6.3	-7.34	0	-0.01	0	31
13/7/2019	-0.25	-6.31	-7.32	0	-0.01	0	30
12/7/2019	-0.27	-6.3	-7.31	0	0	0	29
11/7/2019	-0.28	-6.29	-7.31	0	0	0	31
10/7/2019	-0.27	-6.32	-7.32	0	-0.01	0	30
9/7/2019	-0.26	-6.3	-7.31	0	0	0	29
8/7/2019	-0.26	-6.3	-7.33	0	0	0	29
7/7/2019	-0.27	-6.28	-7.33	0	0	0	30
4/7/2019	-0.26	-6.32	-7.33	0	0	0	29
3/7/2019	-0.26	-6.3	-7.3	0	0	0	31
2/7/2019	-0.26	-6.3	-7.3	0	0	0	30
1/7/2019	-0.26	-6.3	-7.31	0	0	0	30
30/6/2019	-0.27	-6.29	-7.3	0	0	0	31
29/6/2019	-0.27	-6.29	-7.33	0	0	0	31
28/6/2019	-0.29	-6.3	-7.32	0	0	0	31
27/6/2019	-0.26	-6.35	-7.29	0	-0.01	0	29
26/6/2019	-0.25	-6.35	-7.26	0	-0.01	0	33
25/6/2019	-0.26	-6.35	-7.27	0	0	0	30
24/6/2019	-0.25	-6.35	-7.29	0	-0.01	0	31
23/6/2019	-0.25	-6.33	-7.26	0	0	0	29
22/6/2019	-0.25	-6.32	-7.31	0	0	0	31
21/6/2019	-0.25	-6.35	-7.25	0	-0.01	0	30
20/6/2019	-0.25	-6.33	-7.3	0	-0.01	0	31
19/6/2019	-0.24	-6.34	-7.28	0	0	0	31
18/6/2019	-0.25	-6.36	-7.26	0	0	0	31
17/6/2019	-0.23	-6.33	-7.34	0	-0.01	0	31
16/6/2019	-0.24	-6.34	-7.3	0	0	0	30
15/6/2019	-0.26	-6.34	-7.31	0	-0.01	0	32
14/6/2019	-0.25	-6.34	-7.26	0	-0.01	0	32

13/6/2019	-0.26	-6.35	-7.27	0	-0.01	0	30
12/6/2019	-0.26	-6.35	-7.28	0	0	0	31
11/6/2019	-0.24	-6.37	-7.27	0	-0.01	0	32
10/6/2019	-0.23	-6.35	-7.27	0	-0.01	0	31
9/6/2019	-0.27	-6.34	-7.27	0	-0.01	0	31
8/6/2019	-0.27	-6.33	-7.25	0	-0.01	0	30
7/6/2019	-0.27	-6.36	-7.25	0	0	0	31
6/6/2019	-0.26	-6.34	-7.26	0	-0.01	0	31
5/6/2019	-0.25	-6.35	-7.29	0	-0.01	0	31
4/6/2019	-0.26	-6.33	-7.25	0	-0.01	0	31
3/6/2019	-0.24	-6.34	-7.26	0	0	0	31
2/6/2019	-0.24	-6.35	-7.29	0	0	0	30
1/6/2019	-0.24	-6.34	-7.24	0	0	0	30
31/5/2019	-0.25	-6.35	-7.26	0	0	0	30
30/5/2019	-0.24	-6.34	-7.32	0	0	0	30
29/5/2019	-0.22	-6.35	-7.27	0	0	0	31
28/5/2019	-0.23	-6.34	-7.29	0	0	0	31
27/5/2019	-0.22	-6.36	-7.24	0	0	0	30
26/5/2019	-0.24	-6.35	-7.28	0	0	0	31
25/5/2019	-0.24	-6.34	-7.26	0	0	0	30
24/5/2019	-0.26	-6.34	-7.26	0	0	0	30
23/5/2019	-0.26	-6.34	-7.25	0	-0.01	0	29
22/5/2019	-0.24	-6.33	-7.3	0	0	0	29
21/5/2019	-0.23	-6.33	-7.3	0	-0.01	0	30
20/5/2019	-0.26	-6.34	-7.3	0	-0.01	0	31
19/5/2019	-0.25	-6.34	-7.29	0	-0.01	0	31
18/5/2019	-0.24	-6.3	-7.3	0	0	0	30
17/5/2019	-0.25	-6.3	-7.3	0	-0.01	0	31
16/5/2019	-0.21	-6.3	-7.31	0	-0.01	0	31
15/5/2019	-0.25	-6.29	-7.32	0	-0.01	0	30
14/5/2019	-0.25	-6.31	-7.27	0	0	0	30
13/5/2019	-0.24	-6.32	-7.32	0	0	0	31
12/5/2019	-0.21	-6.32	-7.31	0	-0.01	0	39
11/5/2019	-0.22	-6.29	-7.3	0	0	0	31
10/5/2019	-0.23	-6.3	-7.31	0	0	0	31
9/5/2019	-0.21	-6.28	-7.29	0	-0.01	0	31
8/5/2019	-0.23	-6.3	-7.28	0	0	0	32
7/5/2019	-0.2	-6.28	-7.31	0	0	0	31
6/5/2019	-0.23	-6.32	-7.31	0	0	0	33
5/5/2019	-0.23	-6.3	-7.31	0	0	0	31
3/5/2019	-0.23	-6.34	-7.31	0	0	0	30

2/5/2019	-0.22	-6.3	-7.32	0	0	0	32
2/5/2019	-0.23	-6.28	-7.33	0	0	0	32
1/5/2019	-0.22	-6.29	-7.28	0	0	0	31
30/4/2019	-0.22	-6.29	-7.3	0	0	0	2
29/4/2019	-0.25	-6.33	-7.32	0	-0.01	0	33
28/4/2019	-0.23	-6.33	-7.3	0	-0.01	0	31
27/4/2019	-0.22	-6.28	-7.29	0	0	0	30
26/4/2019	-0.24	-6.31	-7.3	0	-0.01	0	32
25/4/2019	-0.21	-6.31	-7.33	0	0	0	31
24/4/2019	-0.23	-6.31	-7.3	0	0	0	31
23/4/2019	-0.25	-6.31	-7.31	0	0	0	30
22/4/2019	-0.22	-6.32	-7.3	0	0	0	32
21/4/2019	-0.23	-6.31	-7.3	0	0	0	30
20/4/2019	-0.2	-6.3	-7.28	0	0	0	30
19/4/2019	-0.19	-6.32	-7.29	0	0	0	32
18/4/2019	-0.22	-6.31	-7.3	0	0	0	31
17/4/2019	-0.23	-6.31	-7.32	0	0	0	30
16/4/2019	-0.22	-6.3	-7.29	0	0	0	31
15/4/2019	-0.24	-6.29	-7.34	0	0	0	31
14/4/2019	-0.22	-6.32	-7.3	0	0	0	31
13/4/2019	-0.2	-6.3	-7.33	0	0	0	30
12/4/2019	-0.23	-6.33	-7.29	0	0	0	31
11/4/2019	-0.22	-6.31	-7.3	0	0	0	30
10/4/2019	-0.24	-6.32	-7.31	0	0	0	30
9/4/2019	-0.22	-6.3	-7.29	0	0	0	35
8/4/2019	-0.22	-6.3	-7.3	0	0	0	32
7/4/2019	-0.2	-6.31	-7.31	0	0	0	29
6/4/2019	-0.2	-6.3	-7.32	0	0	0	30
5/4/2019	-0.21	-6.27	-7.35	0	0	0	31
4/4/2019	-0.23	-6.31	-7.33	0	0	0	30
3/4/2019	-0.21	-6.3	-7.3	0	0	0	30
2/4/2019	-0.22	-6.31	-7.31	0	0	0	31
1/4/2019	-0.23	-6.31	-7.31	0	0	0	31
31/3/2019	-0.19	-6.29	-7.32	0	0	0	31
30/3/2019	-0.23	-6.29	-7.34	0	0	0	32
29/3/2019	-0.21	-6.3	-7.31	0	0	0	29
28/3/2019	-0.2	-6.28	-7.3	0	0	0	32
27/3/2019	-0.22	-6.27	-7.32	0	0	0	31
26/3/2019	-0.23	-6.29	-7.32	0	0	0	31
25/3/2019	-0.2	-6.28	-7.3	0	0	0	30
24/3/2019	-0.21	-6.29	-7.31	0	0	0	31

23/3/2019	-0.22	-6.28	-7.3	0	0	0	31
22/3/2019	-0.2	-6.26	-7.28	0	0	0	30
21/3/2019	-0.24	-6.29	-7.32	0	0	0	32
20/3/2019	-0.24	-6.29	-7.29	0	0	0	31
19/3/2019	-0.2	-6.29	-7.3	0	0	0	29
18/3/2019	-0.21	-6.29	-7.3	0	0	0	29
17/3/2019	-0.23	-6.28	-7.34	0	0	0	30
16/3/2019	-0.22	-6.27	-7.33	0	0	0	28
15/3/2019	-0.23	-6.3	-7.32	0	0	0	29
14/3/2019	-0.22	-6.28	-7.31	0	0	0	30
13/3/2019	-0.23	-6.25	-7.36	0	0	0	30
12/3/2019	-0.23	-6.28	-7.33	0	0	0	29
11/3/2019	-0.2	-6.24	-7.34	0	0	0	29
10/3/2019	-0.21	-6.23	-7.34	0	0	0	29
9/3/2019	-0.21	-6.23	-7.33	0	0	0	31
8/3/2019	-0.23	-6.25	-7.34	0	0	0	30
7/3/2019	-0.25	-6.23	-7.34	0	0	0	31
6/3/2019	-0.22	-6.25	-7.35	0	0	0	31
5/3/2019	-0.23	-6.23	-7.37	0	0	0	33
4/3/2019	-0.2	-6.24	-7.33	0	0	0	30
3/3/2019	-0.23	-6.25	-7.35	0	0	0	29
2/3/2019	-0.24	-6.25	-7.35	0	0	0	31
1/3/2019	-0.22	-6.26	-7.36	0	0	0	30
28/2/2019	-0.23	-6.25	-7.36	0	0	0	31
27/2/2019	-0.23	-6.24	-7.34	0	0	0	31
26/2/2019	-0.22	-6.24	-7.36	0	0	0	31
25/2/2019	-0.22	-6.24	-7.36	0	0	0	30
24/2/2019	-0.21	-6.22	-7.37	0	0	0	30
23/2/2019	-0.21	-6.22	-7.36	0	0	0	30
22/2/2019	-0.19	-6.2	-7.38	0	0	0	30
21/2/2019	-0.22	-6.22	-7.35	0	0	0	30
20/2/2019	-0.2	-6.21	-7.37	0	0	0	30
19/2/2019	-0.22	-6.2	-7.4	0	0	0	30
18/2/2019	-0.19	-6.18	-7.39	0	0	0	29
17/2/2019	-0.2	-6.26	-7.34	0	0	0	31
16/2/2019	-0.2	-6.25	-7.32	0	0	0	30
15/2/2019	-0.21	-6.24	-7.31	0	0	0	31
14/2/2019	-0.21	-6.26	-7.36	0	0	0	31
13/2/2019	-0.21	-6.24	-7.34	0	0	0	31
12/2/2019	-0.19	-6.23	-7.36	0	0	0	29
11/2/2019	-0.2	-6.24	-7.35	0	0	0	30

10/2/2019	-0.2	-6.21	-7.36	0	0	0	31
9/2/2019	-0.19	-6.21	-7.38	0	0	0	30
8/2/2019	-0.18	-6.16	-7.34	0	0	0	29
7/2/2019	-0.19	-6.21	-7.37	0	0	0	29
6/2/2019	-0.22	-6.22	-7.36	0	0	0	30
5/2/2019	-0.19	-6.22	-7.33	0	0	0	30
4/2/2019	-0.22	-6.24	-7.35	0	0	0	31
3/2/2019	-0.21	-6.24	-7.35	0	0	0	31
2/2/2019	-0.23	-6.25	-7.36	0	0	0	31
1/2/2019	-0.21	-6.22	-7.36	0	0	0	30
31/1/2019	-0.21	-6.19	-7.39	0	0	0	32
29/1/2019	-0.21	-6.19	-7.39	0	0.01	0	30
28/1/2019	-0.18	-6.2	-7.36	0	0.01	0	32
27/1/2019	-0.21	-6.22	-7.36	0	0.01	0	30
26/1/2019	-0.22	-6.21	-7.37	0	0.01	0	30
25/1/2019	-0.19	-6.21	-7.35	0	0.01	0	30
24/1/2019	-0.18	-6.19	-7.37	0	0.01	0	29
23/1/2019	-0.22	-6.19	-7.39	0	0.01	0	31
22/1/2019	-0.19	-6.19	-7.4	0	0.01	0	30
21/1/2019	-0.21	-6.17	-7.42	0	0.01	0	31
20/1/2019	-0.18	-6.17	-7.4	0	0.01	0	30
19/1/2019	-0.21	-6.17	-7.41	0	0.01	0	29
18/1/2019	-0.21	-6.19	-7.38	0	0.01	0	30
17/1/2019	-0.19	-6.19	-7.36	0	0.01	0	31
16/1/2019	-0.19	-6.18	-7.41	0	0.01	0	29
15/1/2019	-0.19	-6.19	-7.4	0	0.01	0	31
14/1/2019	-0.2	-6.2	-7.39	0	0.01	0	31
13/1/2019	-0.17	-6.18	-7.35	0	0.01	0	30
12/1/2019	-0.19	-6.18	-7.39	0	0.01	0	30
11/1/2019	-0.17	-6.2	-7.39	0	0.01	0	31
10/1/2019	-0.19	-6.18	-7.39	0	0.01	0	30
9/1/2019	-0.2	-6.18	-7.39	0	0.01	0	31
8/1/2019	-0.2	-6.18	-7.37	0	0.01	0	31
7/1/2019	-0.18	-6.17	-7.38	0	0.01	0	31
6/1/2019	-0.2	-6.2	-7.37	0	0.01	0	31
5/1/2019	-0.19	-6.18	-7.4	0	0.01	0	31
4/1/2019	-0.17	-6.18	-7.42	0	0.01	0	32
3/1/2019	-0.21	-6.18	-7.43	0	0	0	31
2/1/2019	-0.2	-6.17	-7.4	0	0.01	0	31
1/1/2019	-0.18	-6.14	-7.41	0	0.01	0	30

AWAM4

2/1/2019	5.06	4.36	-7.24	0	0	0	39
3/1/2019	5.08	4.36	-7.24	0	0	0	31
4/1/2019	5.06	4.36	-7.24	0	-0.01	0	31
5/1/2019	5.06	4.36	-7.24	0	0	0	29
6/1/2019	5.05	4.36	-7.24	0	0	0	30
7/1/2019	5.06	4.36	-7.24	0	0	0	30
8/1/2019	5.06	4.36	-7.24	0	0	0	31
9/1/2019	5.06	4.36	-7.24	0	0	0	32
10/1/2019	5.06	4.36	-7.24	0	0	0	30
11/1/2019	5.06	4.36	-7.24	0	0	0	31
12/1/2019	5.06	4.36	-7.24	0	0	0	31
13/1/2019	5.06	4.36	-7.24	0	0	0	31
15/1/2019	5.07	4.02	-7.31	0	0	0	31
16/1/2019	5.09	3.99	-7.32	0	0	0	31
17/1/2019	5.1	3.95	-7.32	0	0	0	31
21/1/2019	-0.87	5.8	-8.07	0	0	0	41
22/1/2019	-0.87	5.8	-8.07	0	0	0	31
23/1/2019	-2.03	-4.42	-8.61	0	-0.01	0	31
24/1/2019	-2.09	-4.42	-8.41	0	0	0	29
25/1/2019	-2.13	-4.41	-8.43	0	0	0	30
26/1/2019	-2.15	-4.4	-8.42	0	0	0	30
27/1/2019	-2.19	-4.39	-8.35	0	0	0	31
28/1/2019	-2.2	-4.4	-8.32	0	0	0	32
29/1/2019	-2.24	-4.37	-8.25	0	0	0	30
30/1/2019	-2.24	-4.37	-8.24	0	0	0	31
31/1/2019	-2.31	-4.35	-8.22	0	0	0	31
1/2/2019	-2.34	-4.35	-8.19	0	0	0	31
2/2/2019	-2.36	-4.33	-8.14	0	0	0	31
3/2/2019	-2.37	-4.33	-8.13	0	0	0	31
4/2/2019	-2.38	-4.33	-8.09	0	0	0	31
5/2/2019	-2.39	-4.34	-8.11	0.01	0	0	31
6/2/2019	-2.41	-4.33	-8.07	0.01	0	-0.01	31
7/2/2019	-2.4	-4.34	-8.08	0	-0.01	0	29
8/2/2019	-2.41	-4.33	-8.05	0.01	0	0	29
9/2/2019	-2.43	-4.32	-8.03	0.01	-0.01	0	30
10/2/2019	-2.45	-4.34	-8.01	0.01	0	0	31
11/2/2019	-2.45	-4.32	-8	0.01	0	0	30
12/2/2019	-2.45	-4.34	-7.99	0.01	0	-0.01	29
13/2/2019	-2.46	-4.35	-7.98	0.01	-0.01	0	32
14/2/2019	-2.48	-4.37	-7.97	0.01	-0.01	0	31
15/2/2019	-2.51	-4.33	-7.97	0.01	-0.01	0	31

16/2/2019	-2.48	-4.34	-7.98	0.01	-0.01	0	30
17/2/2019	-2.52	-4.32	-7.98	0.01	-0.01	0	31
18/2/2019	-2.5	-4.34	-7.98	0.01	0	-0.01	29
19/2/2019	-2.5	-4.33	-7.94	0.01	-0.01	0	31
20/2/2019	-2.79	-4.14	-7.97	0.01	-0.01	0	30
21/2/2019	-2.8	-4.13	-8.01	0.01	-0.01	0	30
22/2/2019	-2.77	-4.15	-8	0.01	-0.01	0	31
23/2/2019	-2.79	-4.16	-7.97	0.01	-0.01	0	31
24/2/2019	-2.81	-4.17	-7.94	0.01	-0.01	0	30
25/2/2019	-2.8	-4.15	-7.97	0.01	-0.01	0	30
26/2/2019	-2.81	-4.15	-7.93	0.01	-0.01	0	32
27/2/2019	-2.81	-4.17	-7.97	0.01	-0.01	0	32
28/2/2019	-2.82	-4.15	-7.96	0.01	-0.01	0	31
1/3/2019	-2.81	-4.15	-7.95	0.01	-0.01	0	31
2/3/2019	-2.8	-4.17	-7.95	0.01	-0.01	0	31
3/3/2019	-2.82	-4.17	-7.95	0.01	-0.01	-0.01	29
4/3/2019	-2.82	-4.17	-7.94	0.01	-0.01	-0.01	30
5/3/2019	-2.81	-4.16	-7.97	0.01	-0.01	-0.01	29
6/3/2019	-2.82	-4.16	-7.94	0.01	-0.01	0	31
7/3/2019	-2.84	-4.17	-7.95	0.01	-0.01	0	31
8/3/2019	-2.84	-4.17	-7.95	0.01	-0.01	0	30
9/3/2019	-2.83	-4.17	-7.95	0.01	-0.01	0	30
10/3/2019	-2.82	-4.15	-7.93	0.01	-0.01	-0.01	29
11/3/2019	-2.12	-4.56	-7.91	0.01	-0.01	0	29
12/3/2019	-2.14	-4.54	-7.91	0.01	-0.01	0	30
13/3/2019	-2.15	-4.54	-7.89	0.01	-0.01	-0.01	31
14/3/2019	-2.17	-4.55	-7.91	0.01	-0.01	0	31
15/3/2019	-2.18	-4.55	-7.91	0.01	-0.01	0	29
16/3/2019	-2.2	-4.55	-7.91	0.01	-0.01	-0.01	28
17/3/2019	-2.19	-4.56	-7.9	0.01	-0.01	0	31
18/3/2019	-2.27	-4.57	-7.88	0.01	-0.01	-0.01	29
21/3/2019	-2.3	-4.57	-7.89	0.01	-0.01	-0.01	29
25/3/2019	-2.32	-4.55	-7.87	0.01	-0.01	-0.01	29
26/3/2019	-2.33	-4.58	-7.9	-0.01	0	0	31
30/3/2019	-3.82	-3.42	-8.01	0	0	0	42
31/3/2019	-3.84	-3.41	-8.06	0	0	0	31
1/4/2019	-3.91	-3.42	-8.05	0	0	0	32
2/4/2019	-3.89	-3.4	-8.05	0	0	0	30
3/4/2019	-3.91	-3.4	-7.99	0	0	0	30
4/4/2019	-3.92	-3.4	-8.06	0	0	0	31
5/4/2019	-3.92	-3.44	-7.99	0	0	0	31

6/4/2019	-3.95	-3.43	-7.99	0	0	0	30
7/4/2019	-3.95	-3.42	-7.99	0	0	0	29
8/4/2019	-3.96	-3.42	-7.95	0	0	0	32
9/4/2019	-3.95	-3.43	-7.99	0	0	0	31
10/4/2019	-3.97	-3.41	-7.99	0	0	0	31
11/4/2019	-3.96	-3.44	-7.98	0	0	0	30
12/4/2019	-3.96	-3.43	-7.99	0	0	0	31
13/4/2019	-3.99	-3.43	-7.97	0	0	0	30
14/4/2019	-3.97	-3.44	-7.89	0	0	0	32
15/4/2019	-3.99	-3.44	-7.98	0	0	0	31
16/4/2019	-3.97	-3.45	-7.96	0	0	0	32
17/4/2019	-4	-3.45	-7.96	0	0	0	31
18/4/2019	-3.98	-3.43	-7.96	0	0	0	31
19/4/2019	-4	-3.42	-7.95	0	0	0	32
20/4/2019	-4	-3.46	-7.92	0	0	0	31
21/4/2019	-3.99	-3.44	-7.95	0	0	0	31
22/4/2019	-3.99	-3.45	-7.93	0	0	0	32
23/4/2019	-4.01	-3.43	-7.94	0	0	0	31
24/4/2019	-4	-3.43	-7.94	0	0	0	31
25/4/2019	-4	-3.46	-7.94	0	0	0	31
26/4/2019	-3.99	-3.44	-7.99	0	0	0	34
27/4/2019	-4.02	-3.43	-7.92	0	0	0	31
28/4/2019	-4.01	-3.45	-7.91	0	0	0	30
29/4/2019	-4.01	-3.45	-7.91	0	0	0	30
30/4/2019	-4.01	-3.45	-7.91	0	0	0	30
1/5/2019	-4.02	-3.45	-7.94	0	0	0	32
2/5/2019	-3.98	-3.44	-7.92	0	0	0	43
3/5/2019	-4.02	-3.43	-7.93	0	0	0	32
4/5/2019	-4.02	-3.43	-7.93	0	0	0	32
5/5/2019	-4.02	-3.43	-7.93	0	0	0	32
6/5/2019	-4.02	-3.43	-7.93	0	0	0	32
7/5/2019	-4.02	-3.43	-7.93	0	0	0	32
8/5/2019	-4.02	-3.43	-7.93	0	0	0	29
9/5/2019	-4.02	-3.43	-7.93	0	0	0	29
10/5/2019	-4.05	-3.43	-7.9	0	0	0	32
11/5/2019	-4.04	-3.44	-7.91	0	0	0	31
12/5/2019	-4.05	-3.44	-7.88	0	0	0	32
13/5/2019	-4.08	-3.45	-7.89	0	0	0	31
14/5/2019	-4.06	-3.43	-7.9	0	0	0	30
15/5/2019	-4.04	-3.42	-7.89	0	0	0	30
16/5/2019	-4.04	-3.42	-7.89	0	0	0	30

17/5/2019	-4.04	-3.42	-7.89	0	0	0	30
18/5/2019	-4.04	-3.42	-7.89	0	0	0	30
19/5/2019	-4.04	-3.42	-7.89	0	0	0	30
20/5/2019	-4.04	-3.42	-7.89	0	0	0	30
21/5/2019	-4.04	-3.42	-7.89	0	0	0	30
22/5/2019	-4.04	-3.42	-7.89	0	0	0	30
23/5/2019	-4.04	-3.42	-7.89	0	0	3	29
24/5/2019	-3.89	-3.56	-7.95	0	0	0	31
25/5/2019	-3.9	-3.59	-7.94	0	0	0	31
26/5/2019	-3.87	-3.56	-7.93	0	0	0	31
27/5/2019	-3.88	-3.57	-7.94	0	0	0	31
28/5/2019	-3.89	-3.56	-7.9	0	0	0	32
29/5/2019	-3.91	-3.56	-7.92	0	0	0	32
30/5/2019	-3.89	-3.55	-7.92	0	0	0	31
31/5/2019	-3.89	-3.55	-7.92	0	0	0	31
1/6/2019	-3.89	-3.55	-7.92	0	0	0	31
2/6/2019	-3.89	-3.55	-7.92	0	0	0	31
3/6/2019	-3.89	-3.55	-7.92	0	0	0	31
4/6/2019	-3.89	-3.55	-7.92	0	0	0	31
5/6/2019	-3.89	-3.55	-7.92	0	0	0	31
6/6/2019	-3.89	-3.55	-7.92	0	0	0	31
7/6/2019	-3.89	-3.55	-7.92	0	0	0	31
8/6/2019	-3.89	-3.55	-7.92	0	0	0	31
9/6/2019	-3.89	-3.55	-7.92	0	0	0	31
10/6/2019	-3.91	-3.55	-7.9	0	0	0	31
11/6/2019	-3.9	-3.57	-7.93	0	0	0	32
12/6/2019	-3.92	-3.56	-7.96	0	0	0	36
13/6/2019	-3.92	-3.56	-7.96	0	0	0	36
14/6/2019	-3.92	-3.56	-7.96	0	0	0	36
15/6/2019	-3.92	-3.56	-7.96	0	0	0	36
18/6/2019	-3.79	-3.8	-7.86	0	0	0	32
19/6/2019	-3.78	-3.79	-7.88	0	0	0	32
20/6/2019	-3.77	-3.79	-7.9	0	0	0	32
21/6/2019	-3.77	-3.79	-7.9	0	0	0	32
22/6/2019	-3.77	-3.79	-7.9	0	0	0	32
23/6/2019	-3.77	-3.79	-7.9	0	0	0	32
24/6/2019	-3.77	-3.79	-7.9	0	0	0	32
25/6/2019	-3.77	-3.79	-7.9	0	0	0	32
26/6/2019	-3.77	-3.79	-7.9	0	0	0	32
27/6/2019	-3.81	-3.82	-7.9	0	0	0	30
28/6/2019	-3.79	-3.83	-7.91	0	0	0	31

29/6/2019	-3.82	-3.84	-7.88	0	0	0	32
30/6/2019	-3.8	-3.81	-7.86	0	0	-0.01	31
1/7/2019	-3.82	-3.81	-7.89	0	0	0	31
2/7/2019	-3.8	-3.82	-7.87	0	0	0	30
3/7/2019	-3.82	-3.83	-7.88	0	0	0	31
4/7/2019	-3.82	-3.79	-7.87	0	0	0	30
5/7/2019	-3.83	-3.81	-7.87	0	0	0	30
6/7/2019	-3.83	-3.78	-7.89	0	0	-0.01	29
7/7/2019	-3.83	-3.84	-7.88	0	0	0	33
8/7/2019	-3.83	-3.84	-7.88	0	0	0	33
9/7/2019	-3.83	-3.84	-7.88	0	0	0	33
10/7/2019	-3.83	-3.84	-7.88	0	0	0	33
11/7/2019	-3.83	-3.84	-7.88	0	0	0	33
12/7/2019	-3.83	-3.84	-7.88	0	0	0	33
13/7/2019	-3.82	-3.8	-7.85	0	0	0	30
14/7/2019	-3.82	-3.8	-7.85	0	0	0	30
15/7/2019	-3.82	-3.8	-7.85	0	0	0	30
16/7/2019	-3.82	-3.8	-7.85	0	0	0	30
17/7/2019	-3.82	-3.8	-7.85	0	0	0	30
18/7/2019	-3.82	-3.8	-7.85	0	0	0	30
19/7/2019	-3.82	-3.8	-7.85	0	0	0	30
20/7/2019	-3.82	-3.8	-7.85	0	0	0	30
21/7/2019	-3.82	-3.8	-7.85	0	0	0	30
22/7/2019	-3.82	-3.8	-7.85	0	0	0	30
23/7/2019	-3.82	-3.8	-7.85	0	0	0	30
24/7/2019	-3.82	-3.8	-7.85	0	0	0	30
25/7/2019	-3.82	-3.8	-7.85	0	0	0	30
26/7/2019	-3.82	-3.8	-7.85	0	0	0	30
27/7/2019	-3.82	-3.8	-7.85	0	0	0	30
28/7/2019	-3.82	-3.8	-7.85	0	0	0	30
29/7/2019	-3.82	-3.8	-7.85	0	0	0	30
30/7/2019	-3.82	-3.8	-7.85	0	0	0	30
31/7/2019	-3.82	-3.8	-7.85	0	0	0	30
1/8/2019	-3.82	-3.8	-7.85	0	0	0	30
AWAM5							
Date	Ax	Ay	Az	Gx	Gy	Gz	Temperature
1/1/2019	5.44	-2.88	-6.81	0	0.01	0	30
2/1/2019	5.44	-2.91	-6.82	-0.01	0.01	0	30
3/1/2019	5.43	-2.91	-6.82	-0.01	0.01	0	32
4/1/2019	5.45	-2.92	-6.8	-0.01	0.01	0	31

5/1/2019	5.42	-2.88	-6.81	-0.01	0.01	0	30
6/1/2019	5.44	-2.91	-6.82	-0.01	0	0	30
7/1/2019	5.41	-2.91	-6.83	-0.01	0.01	0	30
8/1/2019	5.44	-2.91	-6.8	0	0.01	0	31
9/1/2019	5.43	-2.93	-6.83	0	0.01	0	30
10/1/2019	5.44	-2.92	-6.84	-0.01	0.01	0	30
11/1/2019	5.44	-2.91	-6.86	0	0.01	0	30
12/1/2019	5.41	-2.93	-6.81	0	0.01	0	29
13/1/2019	5.42	-2.91	-6.79	0	0.01	0	29
14/1/2019	5.42	-2.94	-6.84	0	0.01	0	30
15/1/2019	5.41	-2.96	-6.8	-0.01	0.01	0	30
16/1/2019	5.4	-2.97	-6.8	-0.01	0.01	0	29
17/1/2019	5.39	-2.96	-6.79	0	0.01	0	30
18/1/2019	5.42	-2.98	-6.82	-0.01	0.01	0	29
19/1/2019	5.42	-2.95	-6.83	-0.01	0.01	0	29
20/1/2019	5.41	-2.95	-6.81	-0.01	0.01	0	30
21/1/2019	5.41	-2.94	-6.77	-0.01	0.01	0	30
22/1/2019	5.4	-2.96	-6.76	-0.01	0.01	0	30
23/1/2019	5.41	-2.96	-6.82	0	0.01	0	30
24/1/2019	5.42	-2.96	-6.81	0	0.01	0	29
25/1/2019	5.4	-2.97	-6.8	-0.01	0.01	0	29
26/1/2019	5.38	-2.97	-6.83	0	0.01	0	30
27/1/2019	5.39	-2.96	-6.79	-0.01	0.01	0	30
28/1/2019	5.39	-2.99	-6.82	-0.01	0.01	0	31
29/1/2019	5.43	-2.98	-6.84	-0.01	0.01	0	30
30/1/2019	5.4	-2.97	-6.79	-0.01	0.01	0	30
31/1/2019	5.41	-2.99	-6.81	-0.01	0.01	0	30
1/2/2019	5.43	-2.98	-6.79	-0.01	0.01	0	30
2/2/2019	5.39	-2.98	-6.81	-0.01	0.01	0	30
3/2/2019	5.39	-2.99	-6.8	-0.01	0.01	0	30
4/2/2019	5.41	-2.98	-6.81	-0.01	0.01	0	31
5/2/2019	5.39	-2.99	-6.8	-0.01	0.01	0	30
6/2/2019	5.4	-2.98	-6.82	-0.01	0.01	0	30
7/2/2019	5.41	-2.98	-6.79	-0.01	0.01	0	29
8/2/2019	5.4	-2.98	-6.78	0	0	0	28
9/2/2019	5.4	-2.98	-6.79	-0.01	0.01	0	29
10/2/2019	5.4	-2.99	-6.79	0	0.01	0	31
11/2/2019	5.39	-2.97	-6.79	0	0.01	0	30
12/2/2019	5.4	-2.99	-6.83	-0.01	0.01	0	29
13/2/2019	5.4	-2.98	-6.77	-0.01	0.01	0	31
14/2/2019	5.39	-2.97	-6.78	-0.01	0.01	0	30

15/2/2019	5.38	-3	-6.78	-0.01	0.01	0	31
16/2/2019	5.39	-3	-6.8	-0.01	0.01	0	30
17/2/2019	5.39	-2.97	-6.8	-0.01	0.01	0	30
18/2/2019	5.42	-2.96	-6.79	-0.01	0.01	0	29
19/2/2019	5.39	-2.99	-6.82	0	0	0	0
20/2/2019	5.41	-2.98	-6.81	0	0	0	29
21/2/2019	5.37	-2.98	-6.81	0	0	0	29
22/2/2019	5.42	-3.01	-6.78	0	0	0	30
23/2/2019	5.39	-3	-6.79	0	0	0	30
24/2/2019	5.39	-3	-6.79	0	0	0	30
25/2/2019	5.39	-3.01	-6.78	0	0	0	29
26/2/2019	5.37	-3	-6.74	0	0	0	31
27/2/2019	5.4	-3.02	-6.8	0	0	0	31
28/2/2019	5.36	-3.02	-6.79	0	0	0	30
1/3/2019	5.38	-3.03	-6.81	0	0	0	30
2/3/2019	5.37	-3.02	-6.77	0	0	0	30
3/3/2019	5.36	-3.02	-6.78	0	0	0	29
4/3/2019	5.37	-3.03	-6.74	0	0	0	29
5/3/2019	5.39	-3.04	-6.76	0	0	0	29
6/3/2019	5.39	-3.04	-6.8	0	0	0	37
7/3/2019	5.37	-3.03	-6.78	0	0	0	31
8/3/2019	5.39	-3.03	-6.78	0	0	0	30
9/3/2019	5.36	-3.02	-6.77	0	0	0	30
10/3/2019	5.38	-3.03	-6.78	0	0	0	29
11/3/2019	5.37	-3.02	-6.74	0	0	0	28
12/3/2019	5.4	-3.03	-6.8	0	0	0	29
13/3/2019	5.37	-3.03	-6.8	0	0	0	30
14/3/2019	5.38	-3.02	-6.78	0	0	0	30
15/3/2019	5.37	-3.02	-6.76	0	0	0	29
16/3/2019	5.38	-3.02	-6.78	0	0	0	28
17/3/2019	5.38	-3.04	-6.78	0	0	0	30
18/3/2019	5.37	-3.03	-6.77	0	0	0	28
19/3/2019	5.37	-3.03	-6.77	0	0	0	28
20/3/2019	5.38	-3.04	-6.79	0	0	0	31
21/3/2019	5.37	-3.05	-6.77	0	0	0	31
22/3/2019	5.38	-3.05	-6.79	0	0	0	30
23/3/2019	5.38	-3.02	-6.76	0	0	0	31
24/3/2019	5.38	-3.03	-6.79	0	0	0	31
25/3/2019	5.4	-3.04	-6.76	0	0	0	29
26/3/2019	5.39	-3.04	-6.77	0	0	0	30
27/3/2019	5.4	-3.05	-6.78	0	0	0	31

28/3/2019	5.39	-3.06	-6.79	0	0	0	31
29/3/2019	5.39	-3.03	-6.78	0	0	0	28
30/3/2019	5.38	-3.02	-6.78	0	0	0	31
31/3/2019	5.38	-3.04	-6.77	0	0	0	30
1/4/2019	5.37	-3.04	-6.79	0	0	0	31
2/4/2019	5.37	-3.05	-6.79	0	0	0	30
3/4/2019	5.37	-3.06	-6.82	0	0	0	30
4/4/2019	5.38	-3.03	-6.81	0	0	0	30
5/4/2019	5.35	-3.04	-6.78	0	0	0	31
6/4/2019	5.38	-3.07	-6.79	0	0	0	30
7/4/2019	5.35	-3.04	-6.8	0	0	0	29
8/4/2019	5.38	-3.06	-6.79	0	0	0	31
9/4/2019	5.35	-3.05	-6.78	0	0	0	30
10/4/2019	5.37	-3.05	-6.79	0	0	0	29
11/4/2019	5.38	-3.05	-6.78	0	0	0	29
12/4/2019	5.39	-3.05	-6.81	0	0	0	30
13/4/2019	5.38	-3.03	-6.79	0	0	0	29
14/4/2019	5.38	-3.06	-6.8	0	0	0	30
15/4/2019	5.37	-3.06	-6.78	0	0	0	30
16/4/2019	5.37	-3.04	-6.78	0	0	0	30
17/4/2019	5.37	-3.04	-6.8	0	0	0	30
18/4/2019	5.37	-3.06	-6.79	0	0	0	31
19/4/2019	5.38	-3.06	-6.76	0	0	0	32
20/4/2019	5.37	-3.04	-6.79	0	0	0	30
21/4/2019	5.36	-3.04	-6.81	0	0	0	30
22/4/2019	5.38	-3.04	-6.82	0	0	0	31
23/4/2019	5.38	-3.06	-6.81	0	0	0	30
24/4/2019	5.36	-3.06	-6.8	0	0	0	30
25/4/2019	5.38	-3.04	-6.82	0	0	0	30
26/4/2019	5.37	-3.06	-6.81	0	0	0	31
27/4/2019	5.38	-3.07	-6.83	0	0	0	29
28/4/2019	5.39	-3.06	-6.81	0	0	0	30
29/4/2019	5.37	-3.06	-6.82	0	0	0	32
30/4/2019	5.37	-3.06	-6.84	0	0	0	29
1/5/2019	5.37	-3.04	-6.82	0	0	0	30
2/5/2019	5.37	-3.06	-6.82	0	0	0	31
3/5/2019	5.38	-3.04	-6.83	0	0	0	31
4/5/2019	5.39	-3.05	-6.83	0	0	0	30
5/5/2019	5.4	-3.05	-6.81	0	0	0	30
6/5/2019	5.39	-3.06	-6.82	0	0	0	32
7/5/2019	5.4	-3.05	-6.82	0	0	0	31

8/5/2019	5.38	-3.08	-6.83	0	0	0	31
9/5/2019	5.38	-3.06	-6.81	0	0	0	30
10/5/2019	5.38	-3.07	-6.82	0	0	0	31
11/5/2019	5.38	-3.06	-6.79	0	0	0	31
12/5/2019	5.39	-3.05	-6.82	0	0	0	31
13/5/2019	5.36	-3.06	-6.77	0	0	0	30
14/5/2019	5.37	-3.06	-6.83	0	0	0	30
15/5/2019	5.36	-3.04	-6.79	0	0	0	30
16/5/2019	5.38	-3.07	-6.78	0	0	0	31
17/5/2019	5.4	-3.08	-6.83	0	0	0	31
18/5/2019	5.39	-3.06	-6.8	0	0	0	30
19/5/2019	5.36	-3.09	-6.85	0	0	0	31
20/5/2019	5.4	-3.09	-6.8	0	0	0	30
21/5/2019	5.36	-3.11	-6.81	0	0	0	30
22/5/2019	5.36	-3.09	-6.82	0	0	0	29
23/5/2019	5.39	-3.08	-6.84	0	0	0	29
24/5/2019	5.38	-3.11	-6.82	0	0	0	30
25/5/2019	5.37	-3.08	-6.79	0	0	0	30
26/5/2019	5.38	-3.07	-6.77	0	0	0	30
27/5/2019	5.36	-3.09	-6.8	0	0	0	30
28/5/2019	5.4	-3.09	-6.81	0	0	0	31
29/5/2019	5.36	-3.08	-6.78	0	0	0	31
30/5/2019	5.33	-3.09	-6.79	0	0	0	30
31/5/2019	5.37	-3.08	-6.8	0	0	0	30
1/6/2019	5.38	-3.08	-6.8	0	0	0	30
2/6/2019	5.37	-3.09	-6.79	0	0	0	30
3/6/2019	5.38	-3.07	-6.79	0	0	0	30
4/6/2019	5.37	-3.09	-6.81	0	0	0	30
5/6/2019	5.4	-3.09	-6.81	0	0	0	31
6/6/2019	5.37	-3.09	-6.79	0	0	0	30
7/6/2019	5.37	-3.11	-6.82	0	0	0	31
8/6/2019	5.37	-3.1	-6.83	0	0	0	30
9/6/2019	5.39	-3.1	-6.82	0	0	0	31
10/6/2019	5.39	-3.1	-6.83	0	0	0	31
11/6/2019	5.39	-3.1	-6.81	0	0	0	31
12/6/2019	5.37	-3.11	-6.83	0	0	0	31
13/6/2019	5.36	-3.09	-6.84	0	0	0	30
14/6/2019	5.37	-3.09	-6.79	0	0	0	31
15/6/2019	5.39	-3.11	-6.82	0	0	0	32
16/6/2019	5.37	-3.09	-6.77	0	0	0	30
17/6/2019	4.86	-3.5	-6.97	0	0	0	31

18/6/2019	4.86	-3.51	-6.97	0	0	0	31
19/6/2019	4.86	-3.49	-7	0	0	0	31
20/6/2019	4.85	-3.47	-6.99	0	0	0	30
21/6/2019	4.86	-3.5	-7	0	0	0	30
22/6/2019	4.84	-3.5	-6.96	0	0	0	30
23/6/2019	4.86	-3.5	-6.97	0	0	0	29
24/6/2019	4.86	-3.5	-6.96	0	0	0	31
25/6/2019	4.86	-3.5	-6.97	0	0	0	30
26/6/2019	4.85	-3.49	-6.94	0	0	0	32
27/6/2019	4.87	-3.51	-6.99	0	0	0	29
28/6/2019	4.84	-3.5	-6.98	0	0	0	31
29/6/2019	4.86	-3.51	-6.94	0	0	0	31
30/6/2019	4.86	-3.51	-6.97	0	0	0	31
1/7/2019	4.86	-3.5	-7.01	0	0	0	30
2/7/2019	4.87	-3.5	-6.98	0	0	0	30
3/7/2019	4.88	-3.51	-6.96	0	0	0	31
4/7/2019	4.87	-3.52	-6.95	0	0	0	29
5/7/2019	4.87	-3.5	-7	0	0	0	30
6/7/2019	4.88	-3.49	-6.95	0	0	0	29
7/7/2019	4.87	-3.49	-6.96	0	0	0	29
8/7/2019	4.86	-3.52	-6.97	0	0	0	29
9/7/2019	4.88	-3.52	-6.96	0	0	0	28
10/7/2019	4.88	-3.52	-6.98	0	0	0	30
11/7/2019	4.87	-3.5	-6.95	0	0	0	30
12/7/2019	4.89	-3.49	-6.96	0	0	0	29
13/7/2019	4.86	-3.51	-6.98	0	0	0	30
14/7/2019	4.88	-3.52	-6.97	0	0	0	31
15/7/2019	4.89	-3.49	-6.97	0	0	0	31
16/7/2019	5.16	-3.45	-6.84	0	0	0	29
17/7/2019	5.15	-3.46	-6.81	0	0	0	29
18/7/2019	5.13	-3.41	-6.82	0	0	0	29
19/7/2019	5.18	-3.42	-6.79	0	0	0	29
20/7/2019	5.17	-3.44	-6.84	0	0	0	29
21/7/2019	5.16	-3.43	-6.8	0	0	0	30
22/7/2019	5.16	-3.43	-6.84	0	0	0	29
23/7/2019	5.17	-3.42	-6.83	0	0	0	28
24/7/2019	5.16	-3.41	-6.83	0	0	0	29
25/7/2019	5.17	-3.41	-6.81	0	0	0	30
26/7/2019	5.16	-3.44	-6.82	0	0	0	29
27/7/2019	5.16	-3.45	-6.82	0	0	0	30
28/7/2019	5.17	-3.43	-6.84	0	0	0	29

29/7/2019	5.16	-3.41	-6.8	0	0	0	31
30/7/2019	5.2	-3.44	-6.81	0	0	0	30
31/7/2019	5.19	-3.43	-6.8	0	0	0	30
1/8/2019	5.19	-3.42	-6.78	0	0	0	29
2/8/2019	5.18	-3.42	-6.81	0	0	0	29
3/8/2019	5.17	-3.43	-6.78	0	0	0	30
4/8/2019	5.17	-3.44	-6.82	0	0	0	30
5/8/2019	5.17	-3.43	-6.79	0	0	0	29
6/8/2019	5.18	-3.45	-6.77	0	0	0	29
7/8/2019	5.18	-3.42	-6.81	0	0	0	30
8/8/2019	5.17	-3.44	-6.79	0	0	0	30
9/8/2019	5.18	-3.43	-6.82	0	0	0	31
10/8/2019	5.18	-3.43	-6.79	0	0	0	31
11/8/2019	5.2	-3.45	-6.77	0	0	0	31
12/8/2019	5.18	-3.44	-6.78	0	0	0	31
13/8/2019	5.16	-3.47	-6.77	0	0	0	30
14/8/2019	5.18	-3.45	-6.8	0	0	0	31
15/8/2019	5.16	-3.44	-6.78	0	0	0	30
16/8/2019	5.17	-3.44	-6.79	0	0	0	30
17/8/2019	5.09	-3.42	-6.86	0	0	0	32
18/8/2019	5.08	-3.44	-6.87	0	0	0	30
19/8/2019	5.09	-3.44	-6.84	0	0	0	29
20/8/2019	5.08	-3.43	-6.86	0	0	0	30
21/8/2019	5.07	-3.45	-6.86	0	0	0	32
22/8/2019	5.09	-3.46	-6.86	0	0	0	30
25/8/2019	5.1	-3.44	-6.84	0	0	0	32
26/8/2019	5.08	-3.43	-6.9	0	0	0	29
27/8/2019	5.1	-3.45	-6.84	0	0	0	33
28/8/2019	5.1	-3.45	-6.82	0	0	0	30
29/8/2019	5.09	-3.44	-6.84	0	0	0	30
30/8/2019	5.09	-3.42	-6.85	0	0	0	31
2/9/2019	5.11	-3.46	-6.84	0	0	0	37
3/9/2019	5.11	-3.44	-6.85	0	0	0	31
4/9/2019	5.12	-3.46	-6.8	0	0	0	31
5/9/2019	5.1	-3.45	-6.85	0	0	0	30
6/9/2019	5.11	-3.46	-6.85	0	0	0	30
7/9/2019	5.11	-3.47	-6.82	0	0	0	30
8/9/2019	5.11	-3.47	-6.82	0	0	0	30
9/9/2019	5.09	-3.45	-6.8	0	0	0	30
10/9/2019	5.1	-3.45	-6.88	0	0	0	37
11/9/2019	5.09	-3.46	-6.81	0	0	0	30

12/9/2019	5.09	-3.47	-6.82	0	0	0	30
13/9/2019	5.1	-3.46	-6.82	0	0	0	29
14/9/2019	5.09	-3.47	-6.83	0	0	0	31
15/9/2019	5.13	-3.47	-6.84	0	0	0	37
16/9/2019	5.1	-3.44	-6.81	0	0	0	30
17/9/2019	5.09	-3.43	-6.85	0	0	0	30
18/9/2019	5.09	-3.46	-6.85	0	0	0	31
19/9/2019	5.11	-3.45	-6.81	0	0	0	31
20/9/2019	5.11	-3.46	-6.82	0	0	0	30
21/9/2019	5.12	-3.45	-6.83	0	0	0	30
22/9/2019	5.12	-3.44	-6.84	0	0	0	29
23/9/2019	5.08	-3.45	-6.82	0	0	0	31
24/9/2019	5.1	-3.46	-6.84	0	0	0	30
25/9/2019	5.11	-3.45	-6.82	0	0	0	32
26/9/2019	5.1	-3.42	-6.86	0	0	0	30
27/9/2019	5.13	-3.42	-6.86	0	0	0	29
28/9/2019	5.12	-3.4	-6.85	0	0	0	28
29/9/2019	5.12	-3.4	-6.82	0	0	0	29
30/9/2019	5.13	-3.42	-6.86	0	0	0	29
1/10/2019	5.15	-3.43	-6.85	0	0	0	28
2/10/2019	5.15	-3.44	-6.84	0	0	0	28
3/10/2019	5.09	-3.39	-6.81	0	0	0	23
4/10/2019	5.17	-3.46	-6.95	0	0	0	33
5/10/2019	5.16	-3.42	-6.89	0	0	0	32
6/10/2019	5.1	-3.4	-6.91	0	0	0	27
7/10/2019	5.11	-3.4	-6.88	0	0	0	0
8/10/2019	5.16	-3.47	-6.85	0	0.01	0	29
9/10/2019	5.13	-3.41	-6.95	0	0	0	28
10/10/2019	5.1	-3.41	-6.89	0	0	0	0
11/10/2019	5.11	-3.43	-6.95	0	0	0	32
12/10/2019	5.1	-3.43	-6.97	0	0	0	29
13/10/2019	5.14	-3.45	-6.96	0	0	0	31
14/10/2019	5.15	-3.47	-6.84	0	0.01	0	29
15/10/2019	5.19	-3.45	-6.86	0	0.01	0	29
16/10/2019	5.18	-3.45	-6.85	0	0.01	0	30
17/10/2019	5.32	-3.35	-6.83	0	0.01	0	30
18/10/2019	5.26	-3.33	-6.89	0	0	0	28
19/10/2019	5.32	-3.35	-6.79	0	0.01	0	30
20/10/2019	5.32	-3.36	-6.79	0	0.01	0	30
21/10/2019	5.31	-3.37	-6.77	0	0.01	0	30
22/10/2019	5.32	-3.37	-6.79	0	0.01	0	31

23/10/2019	5.29	-3.36	-6.9	0	0	0	32
24/10/2019	5.29	-3.39	-6.85	0	0	0	37
25/10/2019	5.32	-3.37	-6.78	0	0.01	0	31
26/10/2019	5.3	-3.38	-6.89	0	0	0	34
28/10/2019	5.33	-3.37	-6.83	0	0.01	0	37
29/10/2019	5.24	-3.33	-6.89	0	0	0	27
30/10/2019	5.31	-3.39	-6.84	0	0.01	0	41
31/10/2019	5.32	-3.36	-6.78	0	0.01	0	30
3/11/2019	5.31	-3.39	-6.84	0	0	0	37
4/11/2019	5.3	-3.37	-6.78	0	0.01	0.01	31
5/11/2019	5.29	-3.39	-6.77	0	0.01	0	31
6/11/2019	5.31	-3.38	-6.81	0	0.01	0	32
7/11/2019	5.28	-3.4	-6.86	0	0	0	35
8/11/2019	5.32	-3.38	-6.76	0	0.01	0	33
9/11/2019	5.24	-3.35	-6.9	0	0	0	27
10/11/2019	5.32	-3.4	-6.87	0	0	0.01	43
11/11/2019	5.22	-3.38	-6.88	0	0	0	30
12/11/2019	5.24	-3.37	-6.91	0	0	0	31
13/11/2019	5.28	-3.39	-6.93	0	0	0	35
14/11/2019	5.39	-3.35	-6.81	0	0.01	0	36
17/11/2019	5.38	-3.36	-6.78	0	0.01	0.01	43
18/11/2019	5.35	-3.36	-6.84	0	0	0	35
19/11/2019	5.29	-3.31	-6.86	0	0	0	31
20/11/2019	5.35	-3.33	-6.76	0	0.01	0	30
21/11/2019	5.28	-3.32	-6.87	0	0	0	28
22/11/2019	5.36	-3.35	-6.79	0	0.01	0.01	30
23/11/2019	5.35	-3.36	-6.84	0	0	0	33
24/11/2019	5.3	-3.35	-6.86	0	0	0	31
25/11/2019	5.28	-3.3	-6.84	0	0	0	25
26/11/2019	5.35	-3.34	-6.85	0	0	0	32
27/11/2019	5.3	-3.34	-6.86	0	0	0	29
28/11/2019	5.35	-3.35	-6.85	0	0	0	34
29/11/2019	5.35	-3.34	-6.76	0	0.01	0	31
30/11/2019	5.3	-3.33	-6.85	0	0	0	28
1/12/2019	5.28	-3.33	-6.84	0	0	0	28
2/12/2019	5.37	-3.35	-6.74	0	0.01	0	30
3/12/2019	5.27	-3.33	-6.9	0	0	0	29
4/12/2019	5.27	-3.32	-6.84	0	0	0	26
5/12/2019	5.34	-3.33	-6.76	0	0.01	0	31
6/12/2019	5.25	-3.33	-6.86	0	0	0	26
7/12/2019	5.27	-3.33	-6.85	0	0	0	0

8/12/2019	5.24	-3.32	-6.9	0	0	0	27
10/12/2019	5.26	-3.34	-7.01	0	0	0	29
11/12/2019	5.36	-3.36	-6.92	0	0	0	30
12/12/2019	5.38	-3.36	-6.94	0	0	0	33
13/12/2019	5.35	-3.36	-6.89	0	0.01	0	31
14/12/2019	5.28	-3.34	-6.92	0	0	0	26
16/12/2019	5.24	-3.37	-7.03	0	0	0	0
17/12/2019	5.31	-3.38	-6.99	0	0	0	29
18/12/2019	5.35	-3.38	-6.93	0	0	0	34
19/12/2019	5.29	-3.37	-6.97	0	0	0	26
20/12/2019	5.27	-3.35	-7.04	0	0	0	27
21/12/2019	5.37	-3.4	-7	0	0	0	34
22/12/2019	5.28	-3.34	-7.03	0	0	0	27
24/12/2019	5.27	-3.33	-7.06	0	0	0	27
25/12/2019	5.28	-3.34	-7.05	0	0	0	25
26/12/2019	5.27	-3.35	-7.05	0	0	0	29
27/12/2019	5.27	-3.34	-7.03	0	0	0	25
29/12/2019	5.31	-3.39	-7.1	0	0	0	31